1.1 LIST OF PUBLICATIONS

Publication included as a part of this doctoral thesis

1. Heneberg P., Dráberová L., **Bambousková M.**, Pompach P., Dráber P.: Down regulation of protein-tyrosine phosphatases activated an immune receptor in absence of its translocation into lipid rafts. *J. Biol. Chem.* **285**(17):12787-802, 2010.

2. Bugajev V., **Bambousková M.**, Dráberová L., Dráber P.: What precedes the initial tyrosine phosphorylation of the high affinity IgE receptor in antigen-activated mast cells? *FEBS Lett.* **84**(24):4949-55, 2010.

3. Hálová I., Dráberová L., **Bambousková M.**, Machyna M., Stegurová L., Smrž D., Dráber P.: Cross-talk between tetraspanin CD9 and transmembrane adaptor protein non-T-cell activation linker (NTAL) in mast cell activation and chemotaxis. *J. Biol. Chem.* **288**(14):9801-14, 2013.

4. Dráberová L., Bugajev V., Potůčková L., Hálová I., **Bambousková M.**, Polakovičová I., Xavier R. J., Seed B., Dráber P.: Transmembrane adaptor protein PAG/CBP is involved in both positive and negative regulation of mast cell signaling. *Mol. Cell. Biol.* **34**(23):4285-300, 2014.

5. Bugajev V., Hálová I., Dráberová L., **Bambousková M.**, Potůčková L., Dráberová H., Paulenda T., Junyent S., Dráber P.: Negative regulatory roles of ORMDL3 in FcεRI-triggered expression of proinflammatory mediators and chemotactic response in murine mast cells. *Cell. Mol. Life Sci.* **73**(6):1265-85, 2016.

6. Dráberová L., Paulenda T., Hálová I., Potůčková L., Bugajev V., **Bambousková M.**, Tůmová M., Dráber P.: Ethanol inhibits high-affinity immunoglobulin E (FcεRI) signaling in mast cells by suppressing the function of FcεRI-cholesterol signalosomes. *PLoS One*. **10**(12):e0144596, 2015.

7. **Bambousková M.**, Polakovičová I., Hálová I., Goel G., Dráberová L., Bugajev V., Doan A., Utěkal P., Gardet A., Xavier R. J., Dráber P.: New regulatory roles of galectin-3 in high-affinity IgE receptor signaling. *Mol. Cell. Biol*. **36**(9):1366-82, 2016.

Publications not included as a part of this doctoral thesis

1. **Bambousková M.**, Hájková Z., Dráber P., Dráber P.: Microscopy assays for evaluation of mast cell migration and chemotaxis. *Basophils and Mast cells: Methods in molecular biology* (**Gibbs**, B. F., and **Falcone**, F. eds.), Springer New York, New York, NY. pp *161-176*, 2014.

2. Potůčková L., Franko F., **Bambousková M.**, Dráber P.: Rapid and sensitive detection of cytokines using functionalized gold nanoparticle-based immune-PCR, comparison with immuno-PCR and ELISA. *J. Immunol. Methods.* **371**(1-2):38-47, 2011.

3. Klein O., Nyekel F. N., Stefanache T., Torres R., Salomonsson M., Hallgren J., Rådinger M., **Bambousková** M., Campbell M., Cohen-Mor S., Dema B., Rose C. G., Abrink M., Charles N., Ainooson G., Paivandy A., Pavlova V. G., Serrano-Candelas E., Yu Y., Hellman L., Jensen B. M., Van Anrooij B., Grootens J., Gura H. K., Stylianou M., Tobio A., Blank U., Öhrvik H., Maurer M,.: Identification of biological and pharmaceutical mast cell and basophil related targets. *Scand. J. Immunol.* Article in press, 2016.

1.2 DOWN REGULATION OF PROTEIN-TYROSINE PHOSPHATASES ACTIVATES AN IMMUNE RECEPTOR IN ABSENCE OF ITS TRANSLOCATION INTO LIPID RAFTS

J Biol Chem. 285(17):12787-802, 2010.

In this work we studied the FcεRI signaling initiation upon inhibition of PTPs by pervanadate (Pv). We found that FcεRI subunits get phosphorylated even in the absence of extensive aggregation and translocation to the lipid rafts, suggesting balance in PTP-PTK activities is a crucial mechanism controlling FcεRI triggering. Using monoclonal Ab specific for oxidized state of PTPs we confirmed that PTPs undergo redox regulation after mast cell activation and identified several redox-regulated PTPs in activated mast cells. We also identified contribution of actin cytoskeleton as a potential regulator of balance in the activities of PTPs and PTKs in mast cells.

THE JOURNAL OF BIOLOGICAL CHEMISTRY VOL. 285, NO. 17, pp. 12787–12802, April 23, 2010

Down-regulation of Protein-tyrosine Phosphatases Activates an Immune Receptor in the Absence of Its Translocation into Lipid Rafts*[S]

Received for publication, August 5, 2009, and in revised form, February 11, 2010 Published, JBC Papers in Press, February 15, 2010, DOI 10.1074/jbc.M109.052555

Petr Heneberg[‡1,2], **Lubica Dráberová**[‡1], **Monika Bambousková**[‡], **Petr Pompach**[§], **and Petr Dráber**[‡3]

From the [‡]*Laboratory of Signal Transduction, Institute of Molecular Genetics, and* [§]*Institute of Microbiology, Academy of Sciences of the Czech Republic, CZ-142 20 Prague 4, Czech Republic*

The earliest known biochemical step that occurs after ligand binding to the multichain immune recognition receptor is tyrosine phosphorylation of the receptor subunits. In mast cells and basophils activated by multivalent antigen-IgE complexes, this step is mediated by Src family kinase Lyn, which phosphorylates the high affinity IgE receptor (FcεRI). However, the exact molecular mechanism of this phosphorylation step is incompletely understood. In this study, we tested the hypothesis that changes in activity and/or topography of protein-tyrosine phosphatases (PTPs) could play a major role in the FcεRI triggering. We found that exposure of rat basophilic leukemia cells or mouse bone marrow-derived mast cells to PTP inhibitors, H_2O_2 or pervanadate, induced phosphorylation of the FcεRI subunits, similarly as FcεRI triggering. Interestingly, and in sharp contrast to antigen-induced activation, neither H_2O_2 nor pervanadate induced any changes in the association of FcεRI with detergent-resistant membranes and in the topography of FcεRI detectable by electron microscopy on isolated plasma membrane sheets. In cells stimulated with pervanadate, H_2O_2 or antigen, enhanced oxidation of active site cysteine of several PTPs was detected. Unexpectedly, most of oxidized phosphatases bound to the plasma membrane were associated with the actin cytoskeleton. Several PTPs (SHP-1, SHP-2, hematopoietic PTP, and PTP-MEG2) showed changes in their enzymatic activity and/or oxidation state during activation. Based on these and other data, we propose that down-regulation of enzymatic activity of PTPs and/or changes in their accessibility to the substrates play a key role in initial tyrosine phosphorylation of the FcεRI and other multichain immune receptors.

Multichain immune recognition receptors (MIRRs),[4] such as T- and B-cell receptors, NK receptors, and Fc receptors are transmembrane multiprotein complexes that are activated by binding of their ligands. The first detectable biochemical step after ligand binding is phosphorylation of tyrosine residues in the cytoplasmic domain of the receptor by protein-tyrosine kinases (PTKs) of the Src family. Signal propagation and termination are spatiotemporally regulated by proper interplay between a wide range of PTKs and protein-tyrosine phosphatases (PTPs). Even though the role of PTKs in the MIRRs signaling has been intensively studied (1, 2), the exact involvement of PTPs remains still enigmatic and only partially understood (3–5).

Most members of the PTP family are characterized by a signature motif (I/V)HC*XXGXX*R(S/T) in their catalytic domain. An invariant Cys residue present in this motif is essential for catalysis. Because this Cys has low pK_a value, it is present as a thiolate anion at neutral pH, which strengthens its ability to act in nucleophilic attack on the phosphate group in potential substrates. However, the low pK_a value also renders this residue highly susceptible to oxidation, which is followed by sharp inhibition of PTP activity (6), a part of which was found to be reversible *in vivo* (7).

Application of oxidative agents was shown to induce cellular activation independent of receptor triggering. In mast cells, exposure to pervanadate (a mixture of vanadate and H_2O_2 (8, 9)) was found to stimulate tyrosine phosphorylation of various proteins, followed by enhanced calcium uptake and degranulation (10, 11). Pervanadate causes oxidation and subsequent inactivation of PTPs (12). However, it is not known whether the key mast cell immunoreceptor, the high affinity IgE receptor (FcεRI), is tyrosine-phosphorylated in pervanadate-treated cells similarly to antigen-activated cells and, if so, whether this phosphorylation is due to a transfer of FcεRI into lipid rafts, as predicted by the lipid raft model (see below). Furthermore, it is

* This work was supported in part by Projects 301/09/1826 and P302/10/1759 from Grant Agency of the Czech Republic, Center of Molecular and Cellular Immunology 1M0506, Projects LC-545 and 1M0505 from the Ministry of Education, Youth, and Sports of the Czech Republic, Grants KAN200520701 and M200520901 from the Academy of Sciences of the Czech Republic, and Institutional Project AVOZ50520514.

[S] The on-line version of this article (available at http://www.jbc.org) contains supplemental Figs. S1 and S2 and Tables S1 and S2.

[1] Both authors contributed equally to this work.

[2] Supported by Research Goal MSM0021620814 from the 3rd Faculty of Medicine, Charles University, Prague, Czech Republic, and by a Canadian Institute of Health Research fellowship.

[3] To whom correspondence should be addressed: Laboratory of Signal Transduction, Institute of Molecular Genetics, Academy of Sciences of the Czech Republic, Videnska 1083, CZ-142 20 Prague 4, Czech Republic. Tel.: 420-241062468; Fax: 420-241062214; E-mail: draberpe@img.cas.cz.

[4] The abbreviations used are: MIRR, multichain immune recognition receptor; PTK, protein-tyrosine kinase; PTP, protein-tyrosine phosphatase; FcεRI, high affinity IgE receptor; ITAM, immunoreceptor tyrosine-based activation motif; DRM, detergent-resistant membrane; ROS, reactive oxide species; RBL, rat basophilic leukemia; FCS, fetal calf serum; BMMC, bone marrow mast cell; IL-3, interleukin-3; SCF, stem cell factor; TNP, trinitrophenyl; BSA, bovine serum albumin; mAb, monoclonal antibody; DNP, dinitrophenyl; SHP, Src homology 2 domain-containing phosphatase; HRP, horseradish peroxidase; GαMIgG, goat anti-mouse IgG; GαRIgG, goat anti-rabbit IgG; PCF, pair correlation function; IAA, iodoacetic acid; FDP, 3,6-fluorescein diphosphate; oxPTP, oxidized PTP; Pv, pervanadate; MALDI, matrix-assisted laser desorption ionization; HePTP, hematopoietic PTP.

not known whether or not FcεRI triggering leads to decreased activity of PTPs, an effect that would partly explain the enhanced tyrosine phosphorylation of FcεRI.

In mast cells and basophils activated by binding of multivalent antigen to IgE anchored to the FcεRI, initial tyrosine phosphorylation of the FcεRI β and γ subunits is catalyzed by the Src family kinase Lyn (13). The mechanism by which Lyn initiates phosphorylation of the FcεRI subunits has been extensively studied; two major models are being considered.

The transphosphorylation model is based on observation that a small fraction of Lyn is constitutively bound to FcεRI in the absence of immunoreceptor tyrosine-based activation motif (ITAM) phosphorylation. When FcεRI becomes aggregated, Lyn bound to one receptor can phosphorylate ITAMs on the adjacent receptor and thus initiate the signaling pathway (14). This model was recently supported by studies using trivalent ligands connected to DNA spacers of varying lengths, showing that phosphorylation of the receptor subunits and subsequent activation events require appropriate spatial organization of the FcεRI clusters (15). Furthermore, transfection of cDNA coding for the Lyn N-terminal domain, responsible for association of Lyn with nonaggregated FcεRI, has been shown to inhibit FcεRI β and γ subunits phosphorylation; this inhibition probably reflects a competition between endogenous Lyn kinase constitutively associated with FcεRI β and exogenous Lyn unique domain (16). Finally, electron microscopy studies of immunolabeled plasma membrane sheets demonstrated a colocalization of Lyn kinase with ~25% of FcεRI clusters in unstimulated cells (17).

The alternative model postulates that Lyn kinase is not preassociated with FcεRI but instead is separated from it into membrane microdomains called lipid rafts; this prevents Lyn-mediated FcεRI phosphorylation in nonactivated cells (18, 19). After activation, the aggregated (but not monomeric) FcεRI associates with membrane rafts, and only this pool of the FcεRI is tyrosine-phosphorylated after cross-linking. This model is supported by the experiments of Baird and co-workers (18, 19), who showed that Lyn kinase and FcεRI are located, respectively, in low and high density fractions of sucrose gradient after ultracentrifugation of lysates from nonactivated cells solubilized with Triton X-100. However, when FcεRI-activated cells were used and analyzed under the same conditions, the majority of both Lyn and FcεRI was found in low density fractions (18, 19). Although other plasma membrane receptors exhibit similar density-related changes after ligand-mediated triggering (20), most interpretations of these experiments presume that detergent-resistant membranes (DRMs) are equal to lipid rafts, an assumption that is probably incorrect (21, 22). Furthermore, electron microscopy studies indicated that FcεRI triggering did not lead to enhanced association of FcεRI aggregates with Lyn and some other presumable lipid raft markers (17). It should be mentioned in this connection that dimerization of FcεRI results in increased association of the receptor with DRMs without enhanced formation of large FcεRI aggregates (23). Furthermore, we found that genetic removal of the Lyn kinase palmitoylation site resulting in a release of Lyn from DRMs (but not plasma membrane) failed to inhibit Lyn-mediated FcεRI phosphorylation (24). Thus, the molecular mechanisms of initial stages of FcεRI signaling still remain unclear.

This study is focused on the role of PTPs in the regulation of cell signaling following external addition of reactive oxide species (ROS) or after FcεRI triggering. We investigated the oxidation state and enzymatic activity of various PTPs after exposure of mast cells to ROS at various concentrations, including those observed under physiological conditions in a close vicinity to activated macrophages, where cell-released ROS serve as mast cell proinflammatory agents (25). Because several PTPs are known to be involved in FcεRI signaling (3, 26–29), we also examined the influence of ROS on tyrosine phosphorylation of FcεRI and fine topography of FcεRI and oxidized PTPs. The findings indicate that ROS-induced inhibition of PTPs could lead to tyrosine phosphorylation of FcεRI in the absence of FcεRI movement into DRMs. This led us to postulate a third model of FcεRI signaling, which also takes PTPs into account.

EXPERIMENTAL PROCEDURES

Cells—Rat basophilic leukemia (RBL) cells, clone 2H3 (30), were kindly provided by H. Metzger. They were maintained as monolayers in culture medium consisting of a 1:1 mixture of RPMI 1640 and minimum essential medium supplemented with nonessential amino acids, 3 mM L-glutamine and 1 mM sodium pyruvate. This medium was further supplemented with antibiotics (penicillin (100 units/ml) and streptomycin (100 μg/ml)), extra D-glucose (2.5 mg/ml), and 10% (v/v) heat-inactivated fetal calf serum (FCS). The cultures were maintained at 37 °C in humidified atmosphere of 5% CO_2 in air. Cells grown as monolayers were dissociated with 0.2% EDTA in phosphate-buffered saline (PBS), pH 7.4, and subcultured 2 times a week.

Bone marrow mast cells (BMMCs) were isolated from the femurs and tibias of 6–10-week-old C57BL/6J mice. The cells were incubated for 6–8 weeks in suspension cultures in freshly prepared culture media (Iscove's medium containing 10% FCS and antibiotics) supplemented with interleukin-3 (IL-3; 20 ng/ml; PeproTech EC, London, UK) and stem cell factor (SCF; 40 ng/ml; PeproTech EC). Before activation, BMMCs were cultured for 16 h in culture medium without SCF, followed by incubation for 3–4 h in SCF- and IL-3-free medium supplemented with trinitrophenyl (TNP)-specific IgE (1 μg/ml). The cells were then washed in buffered saline solution (BSS: 20 mM HEPES, pH 7.4, 135 mM NaCl, 5 mM KCl, 1.8 mM $CaCl_2$, 5.6 mM glucose, 1 mM $MgCl_2$) supplemented with 0.1% bovine serum albumin (BSA) and challenged with various concentrations of TNP-BSA conjugate. Alternatively, cells were cultured for 16 h in culture medium without SCF, followed by incubation for 3–4 h in SCF- and IL-3-free medium, and activated with various concentrations of H_2O_2 or pervanadate as indicated under "Results." Cell cultures were mycoplasma-free as confirmed by the Hoechst staining method (31).

Antibodies and Reagents—The following mouse monoclonal antibodies (mAbs) were used: TNP-specific IgE (IGEL b4 1) (32), dinitrophenyl (DNP)-specific IgE (33), anti-oxidized PTP active site (oxPTP; clone 335636, R&D Systems, Minneapolis, MN), anti-Lyn (34), and anti-FcεRI β subunit (JRK) (35). Rabbit polyclonal antibodies specific for Src homology 2 domain-containing phosphatase (SHP)-1 (C-19), SHP-2 (C-18), hematopoi-

etic PTP (HePTP) (H-80), and PTP-MEG2 (H-300), the corresponding blocking peptide for SHP-2 antibody (sc-280 P), and a negative control peptide (sc-287 P) were obtained from Santa Cruz Biotechnology (Santa Cruz, CA). Phospho-Tyr-specific mAb (PY20), conjugated to horseradish peroxidase (HRP), was purchased from BD Transduction Laboratories (Lexington, KY). IgE-specific antibody was prepared by immunization of rabbits with isolated IGEL b4 1, followed by immunoaffinity purification of the rabbit anti-mouse IgE on immobilized IgE. Goat anti-mouse IgG (GαMIgG) affinity-purified secondary antibody conjugated to 5-nm colloidal gold particles were obtained from Amersham Biosciences. Goat anti-rabbit IgG (GαRIgG) affinity-purified antibodies conjugated to 6- or 12-nm gold particles were obtained from Jackson ImmunoResearch (West Grove, PA). EM streptavidin conjugated with 5-nm colloidal gold particles was obtained from BBInternational (Cardiff, UK). [γ-^{32}P]ATP was purchased from ICN (Irvine, CA). Nickel electron microscopy grids (300 mesh), OsO_4, and Pioloform were obtained from Christine Gröpl Elektronenmikroskopie (Tulln, Austria). Poly(Glu_4Tyr)$_n$ and all other chemicals were from Sigma. Pervanadate was prepared by mixing sodium orthovanadate solution with H_2O_2 to get a concentration of 10 mM for both components. After 15 min at 20 °C, the pervanadate solution was diluted 1:50 directly into solutions used for cell activation.

A peptide VHCSAG surrounding the catalytic site cysteine shared by all known catalytically active classical PTP domains was used in competition experiments to verify the specificity of oxPTP mAb (36). This and other peptides (see below) were obtained from GenScript (Piscataway, NJ). The sulfhydryl group of the cysteine was oxidized to sulfonic acid (–SO_3H) as described previously (37) with minor modifications. Briefly, performic acid was freshly prepared by mixing 88% formic acid with 30% H_2O_2 at a ratio 9:1. The peptide (7 mg) was dissolved in 100 μl of ice-cold 88% formic acid and mixed with 1.5 ml of performic acid. After 1 h of incubation on ice, 15 ml of water was added, and the mixture was freeze-dried. The peptide was dissolved in 2 ml of PBS, aliquoted, and stored at −70 °C. Control VHASAG peptide was treated in the same way. Other controls involved peptides VHCSAG and VHASAG treated with formic acid but not oxidized with performic acid. All peptides were analyzed by electrospray ionization/Fourier transformation mass spectrometry. The peptides were dissolved in solvent composed of 50% methanol in water and 0.1% formic acid. Thirteen picomolar solution of each peptide was used for the analysis. Peptides were ionized by electrospray Dual II ion source (Bruker Daltonics, Billerica, MA). Mass spectra were acquired on APEX-Qe Fourier transformation mass spectrometry instrument equipped with a 9.4 tesla superconducting magnet (Bruker Daltonics). The cell was opened for 4 ms, and accumulation time was set at 0.8 s; on average, one experiment consisted of 12 spectra. The acquisition data set size was set to 512,000 points with the mass range starting at m/z 200 atomic mass units. The instrument was externally calibrated by using arginine clusters resulting in mass error above 1 ppm. After a clean selection of the desired precursor, peptides have been confirmed by dropping the potential of the collision cell. Mass spectrometry confirmed complete oxidation of the peptide and the presence of three forms possessing 0–2 sodium ions (supplemental Fig. S1, *A* and *B*). The peptides were used for determining the specificity of oxPTP mAb. Immunoblotting studies showed that the binding of oxPTP mAb to the PTPs from pervanadate-oxidized cells was inhibited by the VHCSAG peptide only slightly yet strongly by the oxidized peptide, even though incompletely (supplemental Fig. S1*C*). VHASAG peptide treated with formic acid exhibited no change in molecular mass. Neither was the binding of oxPTP mAb to its targets inhibited. Importantly, oxPTP mAb bound only weakly to PTPs from nonactivated cells (see "Results").

Electron Microscopy of Immunogold-labeled Membrane Sheets—Ultraclean glass coverslips (15 mm in diameter) used for isolation of plasma membrane sheets were prepared as described previously (38). Coverslips used for attachment of BMMCs were coated in 24-well plates by overnight incubation at 4 °C with fibronectin (50 μg/ml in 0.43 M $NaHCO_3$), followed by washing with distilled water, and used immediately.

BMMCs (4×10^6/ml) were cultured in Iscove's medium with FCS, IL-3, and DNP-specific IgE (1 μg/ml). After 16–18 h, the cells were centrifuged and resuspended at a concentration of 10^7/ml in 1:4 mixture of PBS and Iscove's medium with FCS but without SCF, IL-3, and IgE. The suspension (0.2 ml) was transferred on fibronectin-coated coverslips in 24-well plates and incubated for 1 h at 37 °C. RBL cells were harvested by exposure to EDTA in PBS, counted, resuspended to 5×10^5 cells in 0.5 ml of complete culture medium supplemented with anti-DNP IgE (1 μg/ml), and transferred into wells of 24-well plate containing ultraclean glass coverslips.

The cells were washed with PBS, and FcεRI was aggregated by incubation with DNP-BSA (1 μg/ml) in a 4:1 mixture of PBS and culture medium for 5 min at 37 °C. Alternatively, the cells were activated by addition of 0.2 mM pervanadate at 37 °C. Cell activation was stopped by rapid washing out of the activators and immersing the coverslips with attached cells in ice-cold HEPES buffer (25 mM HEPES, pH 7.0, 25 mM KCl, 2.5 mM magnesium acetate). For surface labeling of FcεRI, IgE-sensitized cells were washed three times with ice-cold PBS and exposed on ice to rabbit anti-mouse IgE (1:200 diluted in PBS + 0.1% BSA, 10 min), followed by GαRIgG conjugated with 12 nm gold (10-fold diluted). Plasma membrane sheets were isolated immediately after activation, fixed by ice-cold 2% paraformaldehyde in HEPES buffer (10 min), and transferred into PBS where they were floated for 5–30 min. Labeling of the intracellular leaflet component was performed by incubation of the grids with membranes on drops of antibodies diluted in PBS + 0.1% BSA (30 min), followed by four 5-min washes with PBS. FcεRI β subunit and oxidized PTPs were labeled by sequential incubation of the membranes with primary mAb JRK (2 μg/ml) and oxPTP (5 μg/ml), respectively, followed by GαMIgG conjugated with 5 nm gold (20-fold diluted). In some experiments, anti-oxPTP mAb was diluted in PBS/BSA containing 2.5× diluted VHCSAG or ox-VHCSAG and incubated for 20 min at 25 °C before use.

SHP-2 was detected with anti-SHP-2 antibody, followed by GαRIgG conjugated to 6- or 12-nm gold particles. Specificity of anti-SHP-2 antibody was verified by inhibition of the binding

with SHP-2 blocking peptide (sc-280 P) but not negative control peptide (sc-287 P). The specimens were post-fixed with 2.5% glutaraldehyde in PBS for 10 min and washed with PBS for 30 min. They were then stained for 10 min with 1% OsO_4 in cacodylate buffer, washed three times for 5 min in water, incubated for 10 min with 1% aqueous tannic acid, washed three times for 5 min in water, and stained for 10 min with 1% aqueous uranyl acetate. Finally, samples were washed twice with water for 5 min, air-dried, and observed with FEI Morgagni 268 electron microscope (FEI Czech Republic, Brno, Czech Republic) operating at 80 kV. Typically, 10–20 micrographs covering 22.2–44.4 μm^2 of the cell surface were obtained from each grid; three independent experiments were made for each condition tested.

The coordinates of gold particles were determined by means of ImageJ (National Institutes of Health). Statistical evaluation of particles clustering of the same type was based on program Gold (39) using pair correlation function (PCF), which expresses the ratio of the density of gold particles at a given distance from a typical particle to the average density of such particles.

Immunoprecipitation and Immunoblotting—Cells were harvested, resuspended in culture medium to a concentration 1 × 10^6 cells/ml, and sensitized or not with IgE (IGEL b4 1; ascites diluted 1:1000). After 60 min at 37 °C the cells were washed in BSS/BSA and challenged with antigen (TNP/BSA) for the indicated time intervals. Alternatively, unsensitized cells were activated by externally added H_2O_2 at the indicated concentrations and time interval or by addition of 0.2 mM pervanadate. Toward the end of the activation period, the cells were briefly centrifuged, and the cell pellets were lysed in ice-cold lysis buffer (25 mM Tris-HCl, pH 7.5, 140 mM NaCl, 2 mM EDTA, 1 mM Na_3VO_4, protease inhibitor mixture, and 0.2% Triton X-100). When indicated, 0.5% Brij 96, 1% Triton X-100 or a mixture of 1% *n*-dodecyl β-D-maltoside, 1% Nonidet P-40 was used instead of 0.2% Triton X-100.

To release free cytoplasmic molecules, the cells were permeabilized by incubation for 5 min on ice in PBS supplemented with 0.1% saponin, 5 mM $MgCl_2$ and 1 mM Na_3VO_4; cytoplasmic components released into the supernatant were removed, and the cell "ghosts" were then extracted for 15 min on ice in lysis buffer supplemented with 1% Triton X-100 (34, 40). Cell lysates were centrifuged at 16,000 × *g* for 1 min at 4 °C, and postnuclear supernatants were directly analyzed by SDS-PAGE and immunoblotting. Alternatively, the proteins of interest in postnuclear supernatants were immunoprecipitated for 2 h at 4 °C using antibodies bound to UltraLink-immobilized protein A or protein G (Pierce). The beads were then washed with lysis buffer, and the bound proteins were eluted by boiling in Laemmli SDS-PAGE sample buffer.

To detect sulfenic and sulfinic acid forms of active PTP sites, an alkylation step was inserted before elution of the immunoprecipitated proteins as described previously (41). Briefly, 100 mM iodoacetic acid (IAA) in lysis buffer without detergents was added to the washed beads with immunoprecipitates for 30 min at room temperature in the dark. Following incubation with IAA, the immunoprecipitates were washed three times and incubated with 100 mM dithiothreitol. After 30 min, dithiothreitol was washed out, and the beads were incubated with pervanadate for 60 min. The beads were then washed, and the proteins were eluted and size-fractionated by SDS-PAGE. Immunoblotting was performed with selected concentrations of primary and HRP-labeled secondary antibodies or with HRP-labeled PY-20. Immunoblots were quantified by Luminescent Image Analyzer LAS-3000 (Fuji Photo Film Co., Tokyo, Japan).

Identification of Oxidized PTPs by Mass Spectrometry—BMMCs were activated by pervanadate (0.2 mM, 15 min) and then lysed in ice-cold lysis buffer supplemented with 5 mM iodoacetamide. The nuclei were removed by centrifugation, and postnuclear supernatant was supplemented with SDS (final concentration 0.5%). After heating at 95 °C for 5 min and centrifugation at 4 °C for 5 min at 14,000 × *g*, the supernatant was supplemented with 4 volumes of cold lysis buffer with 1% Nonidet P-40. Oxidized PTPs were immunoprecipitated by adding oxPTP mAb-armed protein G. Immunoprecipitated material was released from the beads by heating (95 °C, 5 min) in SDS-PAGE sample buffer. The proteins were then size-fractionated by SDS-PAGE. The spots of interest were cut from the gel, destained by a mixture of 100 mM ethylmorpholine acetate buffer and acetonitrile (1:1), and reduced by tris(2-carboxyethyl)phosphine hydrochloride. Reduced cysteines were then alkylated by 50 mM IAA. Gel pieces were washed three times with acetonitrile and water. Trypsin protease was added to the gel in digestion buffer (50 mM ethylmorpholine acetate buffer, 10% acetonitrile, pH 8.3). After overnight incubation, tryptic peptides were extracted from the gel by addition of 80% acetonitrile, 0.1% trifluoroacetic acid.

Extracted peptides were desalted by using Peptide Microtrap in the off-line holder (MichromBioresources, Auburn, CA). Each sample was spotted on one position of the 384 ground steel position MALDI plate (Bruker Daltonics, Billerica, MA). α-Cyano-4-hydroxycinnamic acid was used as a matrix (Bruker Daltonics). Samples were ionized by matrix-assisted laser desorption ionization (MALDI) using Dual II ion source (Bruker Daltonics). Mass spectra were acquired on a APEX-Qe Fourier transformation mass spectrometry instrument equipped with a 9.4 tesla superconducting magnet (Bruker Daltonics). The cell was opened for 4 ms; accumulation time was set at 0.2 s, and one experiment consists of the average of four spectra. The acquisition data set size was set to 512,000 points with the mass range starting at m/z 600 atomic mass units. The instrument was externally calibrated by using Bruker Daltonics calibration standard II resulting in mass error above 1 ppm. The spectra were processed by Data Analysis 4.0 software (Bruker Daltonics) and searched by Mascot search engine against the data base (SwissProt) created from all known *Mus musculus* proteins.

Density Gradient Fractionation—This method was performed as described before (24) with some modifications. Cells (2×10^7) were sensitized in suspension with ^{125}I-labeled TNP-specific IgE and activated or not as described in the legend to Fig. 1, *F* and *G*. The cells were lysed on ice in 0.8 ml of lysis buffer (10 mM Tris-HCl, pH 8.0, 50 mM NaCl, 10 mM EDTA, 1 mM Na_3VO_4, 10 mM glycerophosphate, protease inhibitor mixture for mammalian tissues (Sigma), 1 mM PMSF, and 0.06% Triton X-100). After 15 min, the lysate was homogenized by passing it

10 times through a 27-gauge needle and adjusted to 40% (w/v) sucrose by adding an equal amount of 80% sucrose. The gradient was formed by dispensing 0.2 ml of 80% sucrose to the bottom of the polyallomer tube 13 × 51 mm (Beckman Instruments, Palo Alto, CA), followed by 0.5 ml of 60% sucrose, 1.5 ml of 40% sucrose containing the cell lysate, and successive addition of 0.8 ml of 35% and 0.5-ml aliquots of 30, 25, 20, and 15% sucrose. The loaded tubes were centrifuged for 4 h at 200,000 × *g* using an SW 55 Ti rotor (Beckman Instruments). Twenty five 0.2-ml fractions were collected from the top of the gradient.

Association of oxidized PTPs with DRMs was determined by lysing the cells (2×10^7) in 0.8 ml of ice-cold lysis buffer as above containing 0.2% Triton X-100. Gradient was formed by adding 0.5 ml of 80% sucrose stock solution to the bottom of the tube, followed by 1.5 ml of 40% sucrose containing the cell lysate, 2 ml of 30% sucrose, and 1 ml of 5% sucrose. The tubes were centrifuged as above. Ten 0.5-ml fractions were collected. All but the most dense fraction were mixed with an equal amount of 2× SDS sample buffer without (RBL cells) or with (BMMCs) 2-mercaptoethanol and analyzed by SDS-PAGE.

In-tube and In-gel Phosphatase Assays—To detect the enzymatic activity of PTPs, we used in-tube SensoLyte phosphatase assay kit obtained from AnaSpec (San Jose, CA). Briefly, 3,6-fluorescein diphosphate (FDP) was used as a fluorogenic phosphatase substrate. Immunoprecipitates were incubated for 30 min in buffer containing FDP according to the manufacturer's instructions. The phosphatase activity was determined by means of Tecan Infinite M200 monochromator-based microplate reader (Tecan Austria, Grödig/Salzburg, Austria) with excitation at 485/9 nm and emission at 528/20 nm.

Changes in enzymatic activity of nonreceptor PTPs were detected by means of phosphatase in-gel assay (42). Compared with the in-tube assay, the in-gel PTP assay allows detection of PTP activity related to the molecules of specific molecular weight, which is helpful in analysis of both whole lysates and immunoprecipitates. However, it detects activity changes caused by covalent modifications (such as phosphorylation) only. Briefly, poly(Glu_4Tyr)$_n$ radiolabeled with [γ-^{32}P]ATP using recombinant human c-Src served as a substrate. It was incorporated in 10% SDS-polyacrylamide gel. Following electrophoresis, the SDS was removed from the gel, and the proteins in the gel were renatured by sequential treatment with 6 M guanidine hydrochloride, 0.04% Tween 20, and 0.3% 2-mercaptoethanol in renaturation buffers. PTP activity was determined in autoradiographs of dried gels as areas from which ^{32}P had been selectively removed. Fuji Bio-Imaging Analyzer Bas 5000 was used for quantification.

RESULTS

Tyrosine Phosphorylation of FcεRI in the Absence of Its Association with DRM—As shown previously, exposure of mast cells to pervanadate inhibited the enzymatic activity of PTPs and led to dramatically enhanced tyrosine phosphorylation of PTK substrates (10, 11, 43, 44). Importantly, most of the PTK substrates did not become phosphorylated if pervanadate was added to the cell lysates instead of intact cells (45). These data suggested that there exist preformed signaling assemblies containing PTKs, PTPs, and their substrates and that these complexes are destroyed after detergent solubilization of the cells (45, 46).

In the first series of experiments, we therefore addressed the question whether FcεRI β and γ subunits are tyrosine-phosphorylated in pervanadate-activated cells, similarly to antigen-activated cells, and whether this activation reflects an association of the FcεRI with DRMs. IgE-sensitized RBL cells were activated by exposure to antigen or pervanadate and solubilized in different detergents, and IgE-FcεRI complexes were immunoprecipitated from postnuclear supernatants. Data presented in Fig. 1, *A* and *B*, indicate that only weak tyrosine phosphorylation of the FcεRI β and γ subunits is detectable in nonactivated cells. After antigen-mediated triggering, β and γ subunits of the FcεRI exhibited enhanced phosphorylation. As expected, the extent of tyrosine phosphorylation depended on the detergent used. The strongest phosphorylation was observed in cells solubilized in 0.2% Triton X-100. Lower tyrosine phosphorylation of the FcεRI subunits was observed in cells lysed with 1% Triton X-100, 0.5% Brij 96, or a mixture of 1% lauryl maltoside and 1% Nonidet P-40. IgE immunoprecipitates also contained some coprecipitated proteins; the extent of their amount and/or phosphorylation was largely dependent on the detergent used for cell solubilization (Fig. 1*A*).

IgE immunocomplexes from pervanadate-activated cells likewise showed strong tyrosine phosphorylation of FcεRI β and γ subunits (Fig. 1*B*). Similarly to antigen-activated cells, the use of various detergents was decisive for the appearance of different tyrosine-phosphorylated proteins coprecipitating with IgE. Strong tyrosine phosphorylation of FcεRI β and γ subunits was also observed in cells activated by H_2O_2, but only at relatively high concentrations of the activator (≥5 mM; Fig. 1*C*). As H_2O_2 forms a gradient across the plasma membrane, the intracellular concentrations causing FcεRI β and γ phosphorylation are expected to be ~7 times lower (47). H_2O_2-induced phosphorylation of the FcεRI subunits was transient, as indicated by higher phosphorylation at 5 min compared with 15 min. Because RBL cells are neoplastic cells, we also subjected nontransformed mouse BMMCs to the same analysis. Data presented in Fig. 1, *D* and *E*, indicate that both cell types exhibited similar dynamics of FcεRI tyrosine phosphorylation after activation by antigen. In cells activated with pervanadate, the onset of phosphorylation was slower, but the extent of phosphorylation was higher compared with antigen-induced FcεRI phosphorylation.

The observed tyrosine phosphorylation of FcεRI subunits in H_2O_2- or pervanadate-treated cells could reflect the existence of preformed signaling assemblies containing PTKs, PTPs, and FcεRI as their substrate. Thus, inhibition of PTPs by H_2O_2 or pervanadate could change the equilibrium between PTKs and PTPs and phosphorylation of the receptor. Alternatively, both H_2O_2 and pervanadate could induce movement of FcεRI into lipid rafts where it could be phosphorylated by Lyn kinase, as proposed by the lipid raft hypothesis (see Introduction). Next, we analyzed properties of IgE-FcεRI complexes from antigen- or pervanadate-activated cells. The cells were solubilized with 0.06% Triton X-100 and fractionated by discontinuous sucrose density gradient centrifugation. The results confirmed previously published data that most of FcεRI from nonactivated RBL

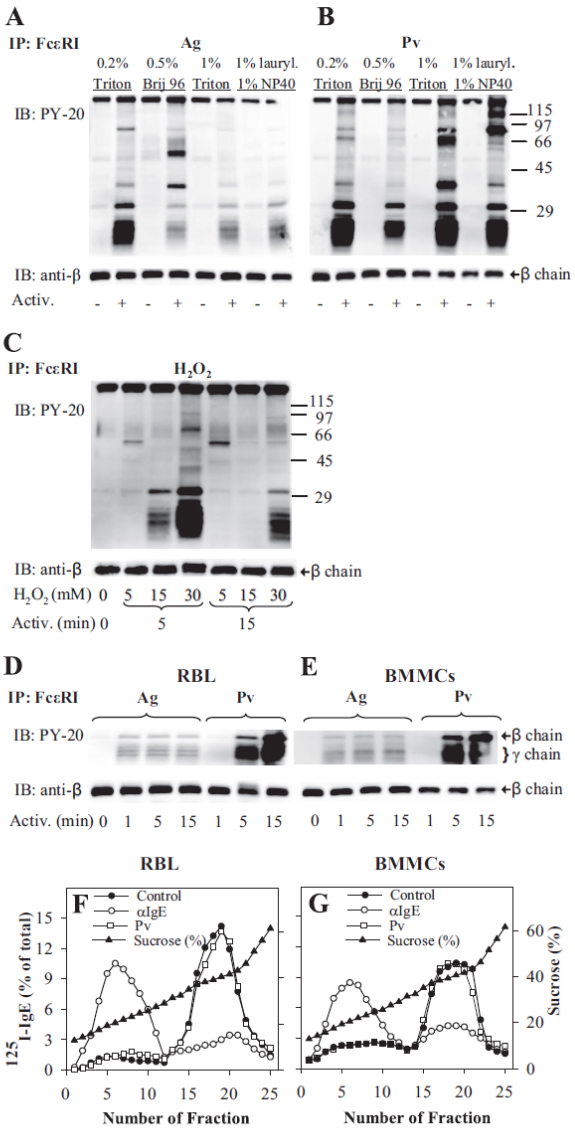

FIGURE 1. **Tyrosine phosphorylation of FcεRI in the absence of its association with DRMs.** *A*, IgE-sensitized RBL cells were activated (*Activ.*; +) or not (−) for 5 min with 0.5 μg/ml TNP-BSA (*Ag*). After activation, the cells were solubilized in lysis buffers containing 0.2% Triton X-100 (*Triton*), 0.5% Brij 96, 1% Triton X-100, or 1% *n*-dodecyl β-D-maltoside (*lauryl.*) and 1% Nonidet P-40 (*NP-40*). FcεRI receptor was immunoprecipitated (*IP*) from postnuclear supernatant using anti-IgE-armed protein A beads. The immunocomplexes were size-fractionated by SDS-PAGE and analyzed by immunoblotting (*IB*) with phosphotyrosine-specific antibody-HRP conjugates (*PY-20*). After stripping, the membranes were probed with antibody specific for FcεRI-β subunit (anti-β), which served as a loading control. *B*, IgE-sensitized RBL cells were activated (+) or not (−) for 5 min with 0.2 mM Pervanadate (Pv), solubilized, and analyzed as in *A*. *Numbers* on the *right* indicate positions of molecular mass markers (kDa). *C*, IgE-sensitized RBL cells were either not activated (0 min) or activated for 5 or 15 min with different concentrations (5–30 mM) of H_2O_2, then solubilized in lysis buffer containing 0.2% Triton X-100, and analyzed as in *A*. *D*, IgE-sensitized RBL cells were activated for different time intervals with 0.5 μg/ml TNP-BSA (*Ag*) or 0.2 mM Pv, then solubilized in lysis buffer containing 0.5% Triton X-100, and analyzed as in *A*. *E*, IgE-sensitized BMMCs were treated and analyzed as in *D*; only FcεRI β and γ subunits are shown (on the *right*). *F* and *G*, sucrose gradient ultracentrifugation of cell lysates. ^{125}I-IgE-sensitized RBL cells (*F*) and BMMCs (*G*) were exposed to anti-IgE (αIgE), 0.2 mM Pv, or BSS/BSA alone (*Control*). After 5 min, the cells were solubilized in lysis buffer containing 0.06% Triton X-100. Lysates were then diluted 1:1 with 80% sucrose buffer, loaded into sucrose step gradients, and ultracentrifuged. After fractionation, 0.2-ml aliquots were collected from the top of the gradient, and the distribution of ^{125}I-IgE-FcεRI complexes was expressed as percentage of total radioactivity present in individual fractions. Percentage of sucrose in the fractions was determined with Abbe refractometer. Representative data from two (*C*) or three (all other) experiments are shown.

cells is detergent-soluble and is found in high density fractions of sucrose gradient (fractions 15–25), whereas most of aggregated FcεRI localizes to low density fractions containing DRMs (fractions 1–12; Fig. 1*F*). In pervanadate-treated cells, most of FcεRI remained in the high density fractions, and no enhanced localization of the receptor in DRMs was observed. Similar results were obtained with BMMCs (Fig. 1*G*). Likewise, no movement of FcεRI into DRMs was observed in RBL cells or BMMCs activated for 5 min with 5 or 30 mM H_2O_2 (not shown). Thus, using two different cell types, we show that in pervanadate- or H_2O_2-activated cells FcεRI can be phosphorylated in the absence of its association with DRMs.

Topography of FcεRI—Previous studies showed that antigen-mediated activation of mast cells was accompanied by the formation of FcεRI aggregates in osmiophilic regions of the plasma membrane; it has been proposed that these aggregates could represent signaling assemblies required for initiation of FcεRI signaling (17, 48, 49). To find out whether or not there are any changes in topography of FcεRI observable after activation with pervanadate, RBL cells and BMMCs were activated by antigen-IgE complexes or pervanadate, and the distribution of the FcεRI β subunit was determined. Data presented in Fig. 2, *A* and *B*, confirm previous results that FcεRI in nonactivated cells is mostly distributed in small clusters in both RBL cells (17, 38) and BMMCs (38). In antigen-activated RBL cells or BMMCs, FcεRI accumulated in osmiophilic regions (Fig. 2, *C* and *D*). Contrary to that, when the cells were activated with pervanadate, FcεRI remained scattered in small clusters (Fig. 2, *E* and *F*) similar to those found in control nonactivated cells. These observations were confirmed by evaluation of particle clustering using PCF; in both RBL cells (Fig. 2*G*) and BMMCs (Fig. 2*H*), particle clustering was not affected by pervanadate treatment. Thus, phosphorylation of FcεRI can occur in the absence of association of FcεRI with DRMs and FcεRI clustering.

Enhanced Oxidation of PTPs in Activated Mast Cells—Pervanadate and H_2O_2 are known to inhibit the enzymatic activity of phosphatases by oxidation of their active site cysteine (50–52). Oxidation of reactive catalytic cysteine yields a reversibly oxidized sulfenic acid that is susceptible to further oxidation to sulfinic and sulfonic species. Oxidized forms of active site cysteine residue, especially the sulfinic and sulfonic species, can be detected with oxPTP antibody (53). In addition, reversibly oxidized forms of PTPs can be detected with oxPTP antibody after treatment of the lysates with IAA and pervanadate (41, 53).

To determine whether mast cell activation results in the formation of oxidized forms of phosphatases, we analyzed lysates of RBL cells by immunoblotting with oxPTP antibody. Interestingly, the antibody reacted with several phosphatases even in nonactivated cells (Fig. 3*A*, *Control*). Treatment of the cells

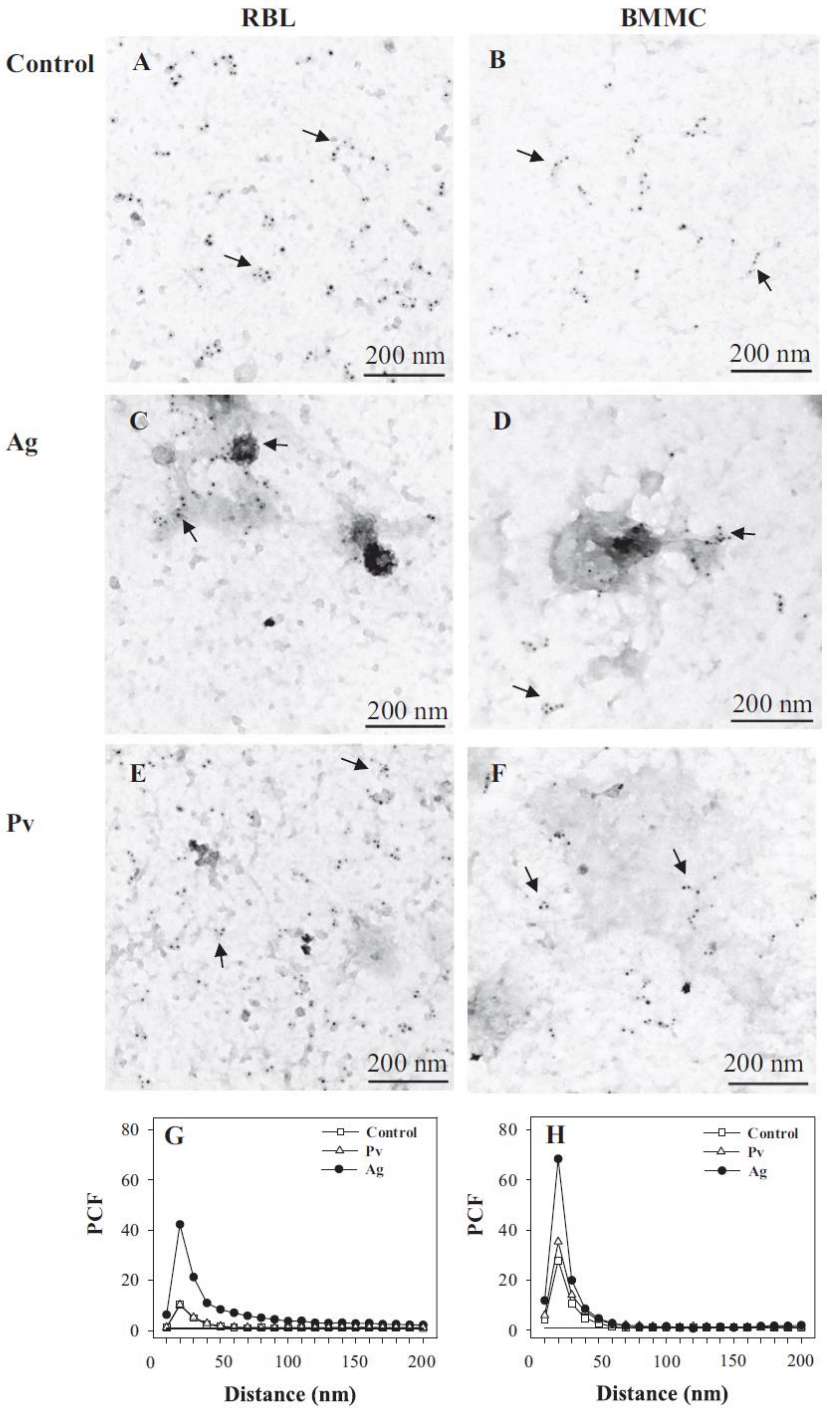

FIGURE 2. **Membrane topography of FcεRI-β subunit.** *A–F*, IgE-sensitized RBL cells (*A*, *C*, and *E*) or BMMCs (*B*, *D*, and *F*) were nonactivated (*Control*; *A* and *B*) or activated for 5 min with 1 μg/ml DNP/BSA (*Ag*; *C* and *D*) or 0.2 mM Pv (*E* and *F*). Membrane sheets were prepared and labeled from the cytoplasmic side for FcεRI-β subunit using JRK mAb followed by GαMIgG conjugated with 5-nm gold particles. *Arrows* indicate small clusters of FcεRI. *G* and *H*, clustering of FcεRI as determined by electron microscopy on membrane sheets (see above). PCF indicates clustering when it reaches the values higher than 1 arbitrary unit. Random distribution of gold particles (PCF = 1) is depicted by a *solid line*.

with H_2O_2 (5 mM, 15 min) enhanced the binding of oxPTP antibody to some of the PTPs, namely those with a relative molecular mass of 40–50 kDa. In pervanadate-activated cells (0.2 mM, 15 min), the antibody reacted more strongly with these PTPs and recently with PTPs of ~90 and 130–150 kDa. Antigen-mediated activation (0.5 μg/ml TNP/BSA, 15 min) enhanced the formation of oxidized forms to an extent similar to that induced by external addition of H_2O_2.

Partially different pattern of oxidized phosphatases was observed with BMMCs, and again the strongest binding of the antibody was seen in lysates from pervanadate-activated cells (Fig. 3*B*). Interestingly, each of the three stimuli led to comparably enhanced oxidation of PTP of about 95 kDa.

When RBL cells were exposed to 1.6 mM H_2O_2, the extent of oxidation of several PTPs rose in time following H_2O_2 addition (Fig. 3*C*). PTP oxidation also increased with a rising dose of H_2O_2 (Fig. 3*D*). Lysis of the cells before exposure to H_2O_2 also led to the formation of oxidized forms of PTPs, but the extent of this oxidation was lower than in intact cells (compare Fig. 3, *D* and *E*), suggesting that the proper regulation of enzymatic activity of phosphatases by ROS requires intact cellular environment. If BMMCs were exposed to various concentrations of H_2O_2, a dose-dependent increase in PTPs oxidation was also observed (Fig. 3*F*). It should be noted that H_2O_2 at all concentrations and time intervals analyzed was not toxic to the cells as determined by trypan blue exclusion test.

In an attempt to identify which PTPs were oxidized, we employed immunoprecipitation with oxPTP mAb, followed by size fractionation of the proteins by SDS-PAGE and mass spectrometry. Because oxPTP mAb does not precipitate native PTPs, the lysates were denatured by boiling with SDS and then "neutralized" with Nonidet P-40. Under these conditions, we were able to identify by mass spectrometry two

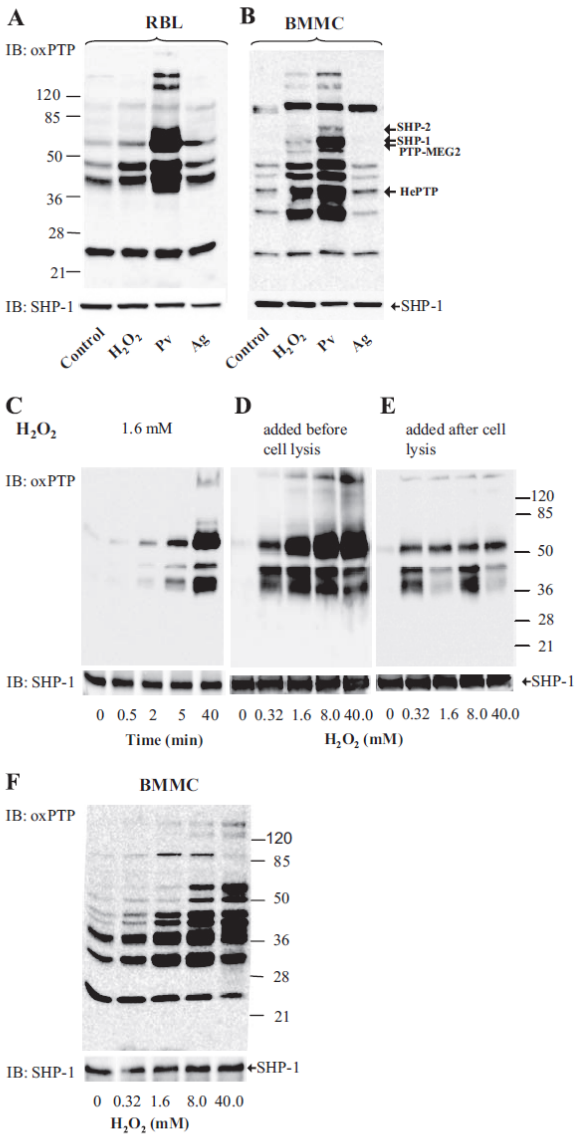

FIGURE 3. **Numerous PTPs are oxidized in the course of mast cell activation.** *A* and *B*, IgE-sensitized RBL cells (*A*) or BMMCs (*B*) were nonactivated (*Control*) or activated with 5 mM H_2O_2, 0.2 mM Pv, or TNP/BSA (*Ag*; 0.5 μg/ml). After 15 min, the cells were solubilized in lysis buffer containing 0.2% Triton X-100. Postnuclear supernatants were size-fractionated by SDS-PAGE and analyzed by immunoblotting (*IB*) with mAb specific for the oxidized PTP active site. After stripping, the membranes were probed with anti-SHP-1 antibody as a loading control (SHP-1). *Numbers* on the *left* and *right* indicate, respectively, position of molecular mass markers (in kDa) and localization of phosphatases as identified by immunoprecipitation and/or mass spectrometry (see supplemental Fig. S2 and Tables S1 and S2). *C*, RBL cells were activated with 1.6 mM H_2O_2 for the indicated time intervals. The cells were lysed and processed as in *A*. *D*, RBL cells were activated for 40 min with different concentrations of H_2O_2. Subsequently, the cells were lysed in 0.2% Triton X-100 and processed as in *A*. *E*, RBL cells were first lysed with 0.2% Triton X-100, and the postnuclear supernatants were exposed to H_2O_2 at the indicated concentrations. After 40 min, the lysates were fractionated by SDS-PAGE and analyzed as in *A*. *F*, BMMCs were activated for 40 min with different concentrations of H_2O_2. Subsequently, the cells were lysed in 0.2% Triton X-100 and processed as in *A*. Typical experiments from at least three performed are shown.

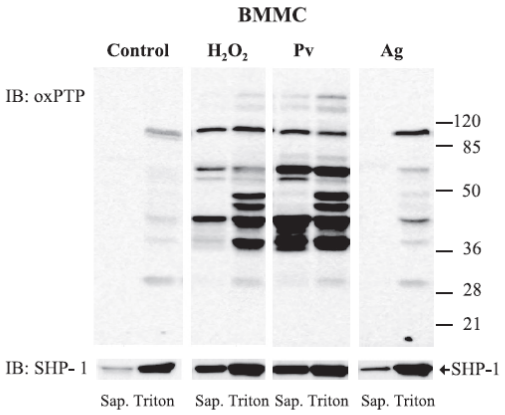

FIGURE 4. **Most of oxidized PTPs are associated with large molecular assemblies.** BMMCs were either nonactivated (*Control*) or activated with 5 mM H_2O_2, 0.2 mM Pv, or TNP/BSA (*Ag*; 0.5 μg/ml). After 5 min, the cells were permeabilized with 0.1% saponin, and the material released from the cells was removed (*Sap.*). The cell ghosts were then extracted for 15 min on ice in lysis buffer supplemented with 1% Triton X-100, and the postnuclear supernatant (*Triton*) was harvested. Both supernatants, saponin and Triton, were size-fractionated by SDS-PAGE and analyzed by immunoblotting (*IB*) with oxPTP mAb and after stripping with anti-SHP-1 antibody to check for the amount of this phosphatase (*bottom, arrow*). Representative data from three experiments are shown. *Numbers* on the *right* indicate positions of molecular mass markers (kDa).

oxidized PTPs as follows: SHP-1 (supplemental Table S1) and SHP-2 (supplemental Table S2). We also performed reverse experiments in which various PTPs were immunoprecipitated with the corresponding antibodies, and their oxidized forms were identified by immunoblotting with oxPTP mAb. By using this approach, we confirmed oxidation of the above-mentioned two PTPs and found two new ones, HePTP and PTP-MEG2 (supplemental Fig. S2). The position of the oxidized PTPs is indicated in Fig. 3*B*.

Subcellular Distribution of Oxidized Phosphatases—It is still unclear what are the phosphatases directly involved in the regulation of FcεRI phosphorylation. PTPs can be divided into cytosolic PTPs and receptor PTPs. To determine whether oxidized PTPs are freely moving in cytosol, or rather participate in the formation of large signaling assemblies, we employed a simple method based on the release of free cytoplasmic components from the cells permeabilized with the cholesterol-sequestering reagent saponin (42). Saponin-treated cells were first washed to remove free cytoplasmic components, then treated with Triton-X-100 to completely solubilize all membrane components, including DRMs, and subjected to immunoblotting analysis. By using this procedure, we found that almost all oxidized PTPs in nonactivated cells were localized to large molecular assemblies not released from the saponin-permeabilized cells but made soluble by the subsequent Triton X-100 solubilization step (Fig. 4, *Control*). In H_2O_2- or pervanadate-activated cells, a fraction of oxidized PTPs was found to be released from saponin-permeabilized cells. Some other PTPs, such as those of 40 and 45–50 kDa, were mostly associated with saponin-resistant cell ghosts, suggesting that they are part of large complexes. Antigen-induced activation led to enhanced oxidation of phosphatases of 45, 50, 70, and 90 kDa, all of which were

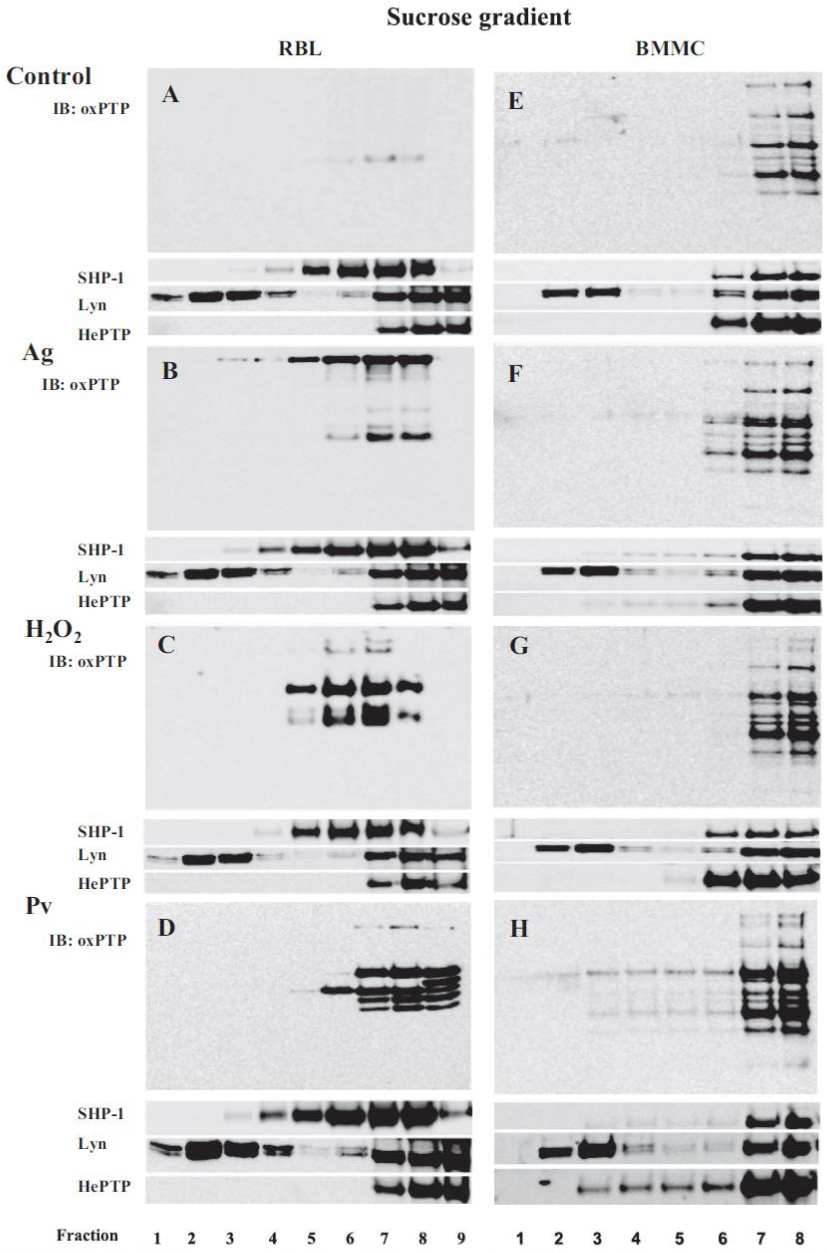

FIGURE 5. **Oxidized PTPs are excluded from DRMs.** *A*, nonactivated RBL cells (*Control*) were lysed in 0.2% Triton X-100 and then subjected to sucrose density gradient ultracentrifugation. Individual fractions were collected from the top and analyzed with oxPTP mAb by immunoblotting (*IB*) for the presence of oxidized PTP. *B*, IgE-sensitized RBL cells were activated for 5 min with TNP/BSA (*Ag*; 0.5 μg/ml) and then analyzed as in *A*. *C*, RBL cells were activated with 1.6 mM H_2O_2 for 40 min and then analyzed as in *A*. *D*, RBL cells were activated with 0.2 mM Pv for 5 min and then analyzed as in *A*. *E–H*, BMMCs were nonactivated (*E*) or activated by antigen (*F*), H_2O_2 (*G*), or pervanadate (*H*) as RBL cells (see above). Distribution in individual fractions of Lyn kinase (a marker of membrane rafts), SHP-1, and HePTP is also shown. Representative data from three experiments are shown.

associated with large signaling assemblies. The same samples were also used to determine the distribution of SHP-1. In nonactivated cells most of SHP-1 was associated with large signaling assemblies and was not released from saponin-permeabilized cells. After FcεRI triggering, and especially after treatment with H_2O_2 or pervanadate, more SHP-1 was released from permeabilized cells. It seems to indicate that SHP-1 was released from submembrane signaling complexes into the cytoplasm as a consequence of changes in affinity to a wide range of substrates, as in the case of the SHP-1 Cys/Ser mutant (54, 55).

Next, we studied the association of PTPs and their oxidized forms with DRMs. RBL cells and BMMCs were solubilized with 0.2% Triton X-100, followed by sucrose density gradient ultracentrifugation. Individual fractions were probed by immunoblotting with oxPTP mAb or antibodies specific for SHP-1, Lyn kinase, or HePTP. Data presented in Fig. 5, *A–H*, indicate that a significant fraction of Lyn kinase was localized as expected in DRMs (fractions 2–4), whereas SHP-1 and HePTP were found mostly in the high density fractions and only a minor part (0–5%, $n = 3$) in low density fractions. In nonactivated RBL cells, only a small fraction of PTPs was oxidized, and all were detected in the high density fractions (Fig. 5*A*). Antigen-mediated activation resulted in enhanced oxidation of several phosphatases, and again, all of them were in the high density fractions (Fig. 5*B*); the observed staining of the high molecular weight proteins, those located even in low density fractions, reflects the reactivity of the secondary HRP-labeled antibody with IgE bound to FcεRI. After treatment with H_2O_2 (Fig. 5*C*) or pervanadate (Fig. 5*D*), oxidized forms were again found only in the high density fractions. When BMMCs were analyzed, an enhanced amount of oxidized PTPs after activation with antigen, H_2O_2, or pervanadate was observed mainly in the high density fractions (Fig. 5, *E–H*). These data indicate that oxidized forms of PTPs are not associated with DRMs or that 0.2% Triton X-100 removes them from these regions, similarly as Syk is stripped off from FcεRI in antigen-activated cells (56).

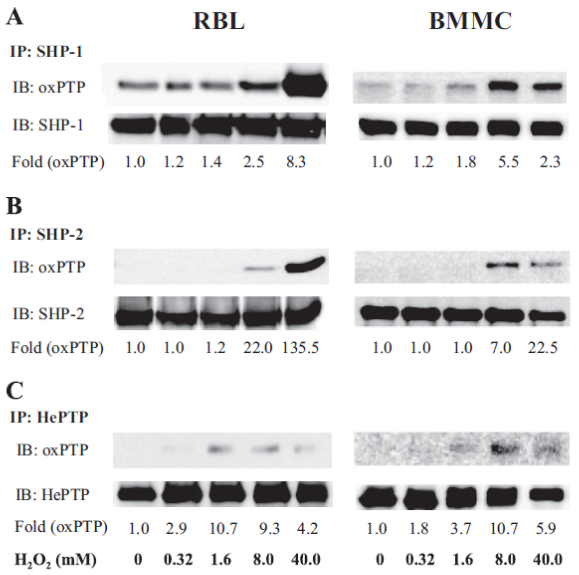

FIGURE 6. **Changes in oxidation of selected PTPs in H_2O_2-activated cells.** *A–C*, RBL cells (*left*) and BMMCs (*right*) were activated with the indicated concentrations of H_2O_2. After 40 min, the cells were lysed in 0.2% Triton X-100, and SHP-1 (*A*), SHP-2 (*B*) and HePTP (*C*) were immunoprecipitated (*IP*) from the postnuclear supernatants with the corresponding antibodies. After size fractionation by SDS-PAGE, the samples were subjected to immunoblotting (*IB*) with oxPTP mAb and subsequently, after stripping, with the respective antibodies as loading controls. The amounts of immunoprecipitated phosphatases and their oxidized forms were quantified by densitometry, and oxPTP signals were normalized to nonactivated cells and amount of the phosphatases (*Fold* (*oxPTP*)). Representative data from three experiments are shown.

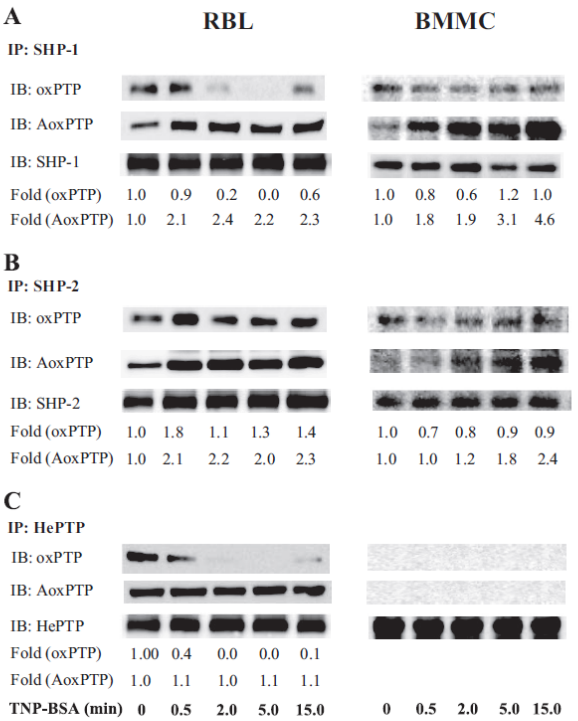

FIGURE 7. **Changes in oxidation of selected PTPs in cells activated by FcεRI triggering.** *A–C*, IgE-sensitized RBL cells (*left*) and BMMCs (*right*) were activated with 1 μg/ml TNP/BSA. After the indicated time intervals, the cells were lysed in 0.2% Triton X-100, and SHP-1 (*A*), SHP-2 (*B*), or HePTP (*C*) were immunoprecipitated (*IP*) from the postnuclear supernatants. After size fractionation by SDS-PAGE, the samples were analyzed by immunoblotting (*IB*) with oxPTP mAb (oxPTP, irreversibly oxidized). In parallel, another set of the immunoprecipitates was subjected to alkylation by IAA, followed by reduction of the reversibly oxidized PTPs with dithiothreitol, and by final oxidation with pervanadate (*IB*, AoxPTP, reversibly oxidized). After stripping the membranes were analyzed by immunoblotting with the corresponding antibodies (loading controls). The amounts of immunoprecipitated phosphatases and their oxidized forms were quantified by densitometry, and oxPTP and AoxPTP signals were normalized as in Fig. 6. Representative data from three experiments are shown.

Differences in Redox Regulation of Selected PTPs—The experiments just described showed that mast cells possess oxidized PTPs and that their amount increases in the course of cell activation. In further studies we investigated the redox regulation of phosphatases known to be involved in FcεRI signaling, namely SHP-1, SHP-2, and HePTP (26–29). In the first series of experiments, the phosphatases were immunoprecipitated from nonactivated or H_2O_2-treated RBL cells or BMMCs, and their oxidation was determined by immunoblotting with oxPTP antibody. Binding of PTP-specific antibodies served as loading controls. We found that a fraction of SHP-1 was oxidized even in nonactivated cells. After exposure to H_2O_2, especially at higher concentrations (8 and 40 mM), this oxidation was enhanced in both cell types (Fig. 6*A*). The closely related phosphatase SHP-2 showed no oxidation in quiescent cells and rising oxidation at higher concentrations of H_2O_2 (Fig. 6*B*). The maximum oxidation level of the active site Cys in SHP-2 was lower when compared with SHP-1. Finally, we also estimated the redox regulation of the active site of nonreceptor phosphatase HePTP, which reached a plateau of oxidation in RBL cells at 1.6 mM H_2O_2 and in BMMCs at 8.0 mM H_2O_2 (Fig. 6*C*). The maxima of HePTP oxidation were low, close to the detection limits. Thus, different PTPs in different cell types exhibit different basal levels of oxidation and sensitivity to redox regulation.

FcεRI Triggering Results in Changes of Redox State of Mast Cell PTPs—Similar experiments as above were performed with cells activated by antigen-induced aggregation of FcεRI. Because the oxPTP antibody reacts preferentially with the sulfonic acid form of the PTP active site, we also employed alkylation of the oxidized active sites to determine the sulfenic and sulfinic acid forms. Alkylation using IAA, followed by incubation in buffer containing dithiothreitol, and subsequently in buffer with pervanadate, resulted in a somewhat different pattern than in previous experiments. When SHP-1 was isolated from RBL cells activated for various time intervals with antigen, a substantial decrease of sulfonic acid form was observed, reaching the minimum at 5 min after triggering and returning back at 15 min (Fig. 7*A*, *IB: oxPTP*). This decrease could reflect the calpain-mediated degradation of oxidized forms of the PTPs (57). Unlike that, the levels of reversibly inactivated SHP-1 showed a rapid increase (within 30 s) after triggering with antigen, followed by constant levels between 0.5 and 15 min (Fig. 7*A*, *IB: AoxPTP*). The amount of irreversibly oxidized phosphatases in BMMCs only slightly decreased, whereas the amount of reversibly oxidized phosphatases steadily increased up to 15 min.

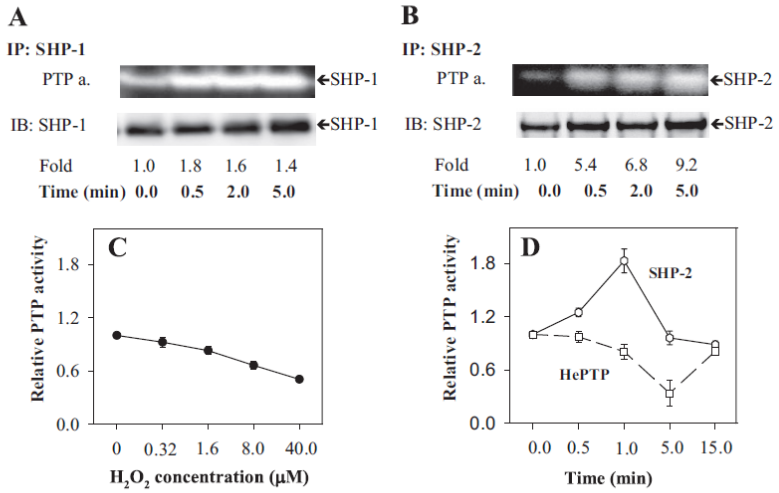

FIGURE 8. **Changes in activity of PTPs in activated cells.** *A* and *B*, IgE-sensitized RBL cells were activated with 1 μg/ml TNP/BSA for the indicated time intervals. After activation, the cells were permeabilized with saponin, and cell ghosts were subsequently lysed in lysis buffer supplemented with 1% Triton X-100. SHP-1 (*A*) and SHP-2 (*B*) were immunoprecipitated (*IP*) from the postnuclear supernatants, size-fractionated by SDS-PAGE, and subjected to the PTP in-gel assay (*PTP a.*). In parallel, the immunoprecipitated PTPs were also analyzed by immunoblotting (*IB*) with the corresponding antibodies as loading controls. The signals were evaluated by densitometry, and the enzymatic activity at each given time interval was normalized to nonactivated cells and amount of protein (*Fold*). Representative data from three independent experiments are shown. *C*, RBL cells were activated for 40 min with the indicated concentrations of externally added H_2O_2. Relative activity of total cellular PTPs was determined by fluorometry after addition of FDP to intact cells. *D*, IgE-sensitized RBL cells were activated with antigen (1 μg/ml TNP/BSA) for the indicated time intervals and lysed in 0.2% Triton X-100. Subsequently SHP-2 (*solid line*) and HePTP (*dashed line*) were immunoprecipitated, and relative activity of PTPs was determined by measuring FDP fluorescence. Averages ± S.D. from three to four experiments are shown.

Some irreversibly oxidized forms were observed in SHP-2 immunoprecipitates from nonactivated RBL cells and BMMCs. This is probably caused by a sensitization process because SHP-2 in nonsensitized and nonactivated cells did not react with oxPTP (Fig. 6*B*; H_2O_2 untreated cells). After activation with antigen, an increase in the number of sulfonic acid forms was observed 30 s after triggering in RBL cells; in BMMCs, a small decrease rather than increase of this form was observed (Fig. 7*B*, *IB: oxPTP*). The levels of reversibly oxidized SHP-2 increased within 30 s after activation and remained higher up to 15 min in both cell types (Fig. 7*B*, *AoxPTP*). When immunoprecipitated HePTP was analyzed, a reduction of its Cys-SO_3H form to almost undetectable levels was observed within 2 and 5 min after triggering in RBL cells. In BMMC, neither binding of IgE (sensitization) nor antigen triggering led to any detectable sulfonic acid (Fig. 7*C*, *IB: oxPTP*). HePTP from IgE-sensitized RBL cells carried some reversibly oxidized cysteine, and their levels remained constant in the course of activation, whereas this form was undetectable in BMMCs (Fig. 7*C*, *IB: AoxPTP*). These data indicate that FcεRI-induced activation of the cells initiates changes in the oxidation state of active site cysteine in SHP-1 and SHP-2 in both RBL cells and BMMCs. Some changes in redox state of HePTP were observed only in RBL cells in connection with cell sensitization.

Changes in Activity of Selected PTPs in Response to FcεRI Triggering—The observed changes of the redox state of PTPs in the course of cell activation suggested that their enzymatic activity is affected. To verify this hypothesis, we next assayed the enzymatic activity of several phosphatases by means of two assays, phosphatase in-gel assay using [γ-^{32}P]ATP and phosphatase in-tube assay employing fluorogenic phosphatase substrate FDP. When SHP-1 was immunoprecipitated from large signaling assemblies of saponin-permeabilized nonactivated cells (0 min), the basal level of phosphatase activity was determined. After FcεRI triggering, the enzymatic activity of SHP-1 slightly increased peaking at 30 s (Fig. 8*A*). Enzymatic activity of SHP-2 exhibited a more rapid increase (Fig. 8*B*).

The regulation of PTPs by oxidation, conformational changes, and/or phosphorylation may sometimes act against each other. We have confirmed the previous observations (12) that application of H_2O_2 to the cells leads to a substantial decrease in overall PTP activity detected at the level of FDP fluorescence (Fig. 8*C*). However, individual phosphatases may behave differently in the course of cellular activation induced by MIRRs, where the redox regulation is just one of several contributors. Using the in-tube FDP assay, we next compared the phosphatase activity of two selected nonreceptor PTPs, SHP-2 and HePTP isolated from total cell lysates, in the course of FcεRI activation. SHP-2 showed a substantial rapid transient increase of its activity (peaking at 1 min after triggering), whereas HePTP exhibited a clear decrease with the minimum at 5 min after activation (Fig. 8*D*). Thus, cell activation affects differentially the redox state, phosphorylation, and activity of PTPs.

Fine Topography of Oxidized PTPs—The finding that oxidized PTPs are part of the large signaling assemblies associated with saponin-permeabilized cells suggested that they are bound to the plasma membrane. This assumption was tested experimentally. When plasma membrane sheets were isolated from nonactivated cells and probed on the cytoplasmic side for oxidized PTPs, a limited number of particles (~2/μm^2) was observed (Fig. 9, *A* and *G*). An increased number of oxidized PTPs was detected in antigen-activated cells, thus supporting the previous results (Fig. 4) and extending them by localizing the phosphatases on the plasma membrane. Interestingly, oxidized forms of PTPs were mostly localized in distinct membrane cytoskeleton-like structures (Fig. 9, *B* and *G*). In cells activated by pervanadate, the number of membrane-associated particles was dramatically enhanced, and again, most of them were associated with the membrane cytoskeleton-like structures (Fig. 9, *C* and *G*). Although the ox-VHCSAG peptide was a suboptimal inhibitor of the binding of oxPTP mAb to oxidized phosphatases (see "Experimental Procedures"), this peptide, compared with nonoxidized control peptide, significantly

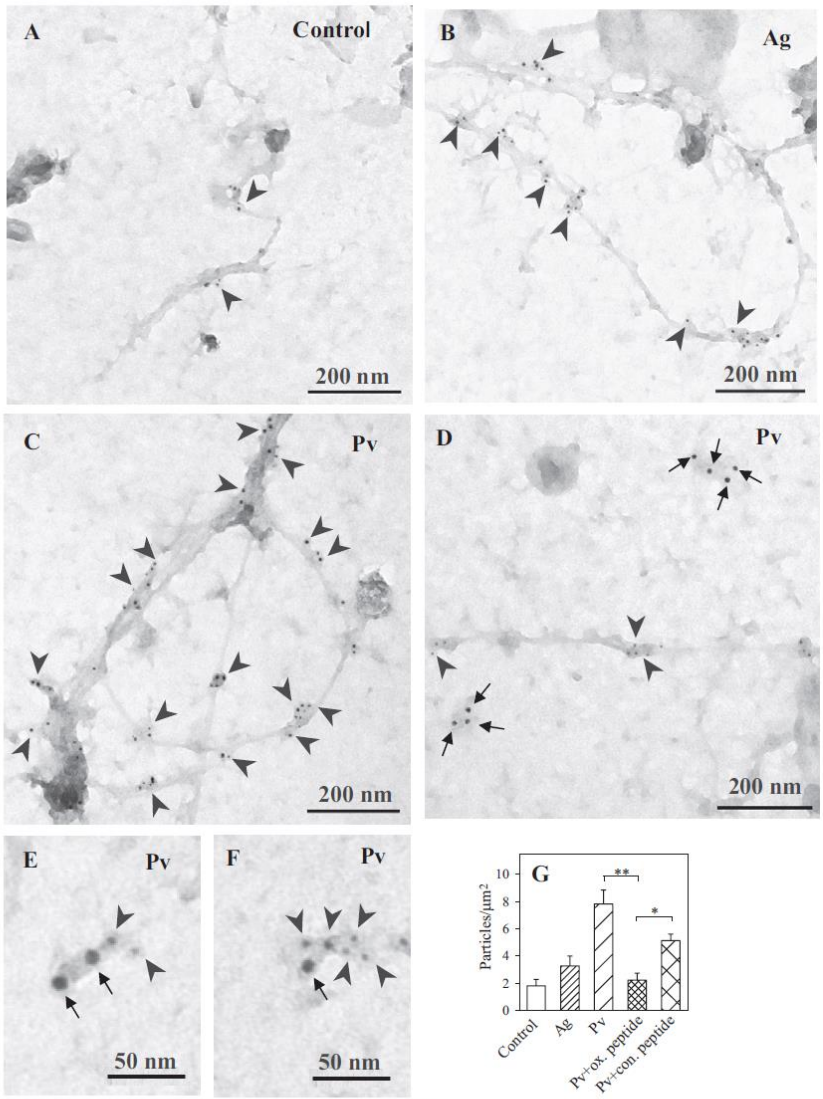

FIGURE 9. **Membrane topography of oxidized PTPs.** Plasma membrane sheets were isolated from nonactivated (control) IgE-sensitized (*A*), antigen (*Ag*)-activated (*B*; 1 μg/ml DNP-BSA, 5 min) or Pv-activated (*C*; 0.2 mM, 5 min) BMMCs. Membrane sheets were labeled from the cytoplasmic side with oxPTP mAb followed by GαMIgG conjugated with 5-nm gold particles (*arrowheads*). *D–F*, IgE bound to FcεRI was visualized by labeling whole cells (kept on ice) with rabbit anti-mouse IgE (*RαMIgE*), followed by GαRIgG conjugated with 12-nm gold (*arrows*); plasma membrane sheets were then isolated, and oxidized PTPs were detected as above. *G*, quantitative analysis of oxidized PTPs (numbers of gold particles per μm^2) in control cells or antigen (*Ag*)- or Pv-activated cells. Binding of oxPTP mAb to membrane sheets from Pv-activated cells in the presence of control (*con.*) peptide (VHCSAG) or the same peptide with Cys oxidized to sulfonic acid (*ox. peptide*) is also shown. Means ± S.D. were calculated from three independent experiments, each 22.2 mm^2. Statistical significance of intergroup differences was calculated using Student's *t* test: *, $p < 0.01$; **, $p < 0.0001$.

inhibited the binding of the oxPTP mAb to membrane sheets from pervanadate-activated cells (Fig. 9*G*), confirming the specificity of this interaction.

To determine whether oxidized PTPs are co-localized with FcεRI, the FcεRI and oxidized phosphatases were labeled on the extracellular and cytoplasmic sides, respectively, of the plasma membrane sheets isolated from pervanadate-activated cells. Under these conditions, most of FcεRI was located in distinct osmiophilic regions, whereas oxidized phosphatases were associated with membrane cytoskeleton-like structures (Fig. 9*D*). However, in a small fraction of FcεRI clusters, oxidized phosphatases were also present (Fig. 9, *E* and *F*), suggesting a functional link.

In an attempt to identify whether oxidized phosphatases are associated with actin cytoskeleton, plasma membrane sheets were labeled on the cytoplasmic side simultaneously with biotin-labeled phalloidin, which specifically reacts with F-actin (58–60), and oxPTP mAb. Data presented in Fig. 10*A* indicate that osmiophilic cytoskeleton-like structures possess both oxidized PTPs and F-actin. These data suggest that oxidized phosphatases associate with actin cytoskeleton.

One of the phosphatases detectable on isolated plasma membrane sheets is SHP-2 (Fig. 10*B*). This phosphatase was, however, localized outside osmiophilic cytoskeleton-like structures carrying oxidized phosphatases. In nonactivated as well as activated cells, SHP-2 was found mostly in areas different from those containing FcεRI (data not shown). Interestingly, a clear co-localization was occasionally observed (Fig. 10, *C* and *D*). Quantitative analysis revealed that in the course of pervanadate-mediated activation, the number of gold particles associated with SHP-2 significantly increased (Fig. 10*E*). This increase reflected specific binding of anti-SHP-2 antibody to the target antigen, because the binding was significantly reduced by addition of the corresponding blocking peptide (sc-280 P) but not negative control peptide (sc-287 P). An increased binding of oxPTP mAb to membrane sheets was also observed in antigen-activated cells; however, due to variations, this increase was insignificant.

DISCUSSION

The binding of a multivalent antigen to IgE-FcεRI complexes induces tyrosine phosphorylation of the receptor subunits. However, it is not exactly clear how the binding is communicated across the plasma membrane to the cellular interior as the

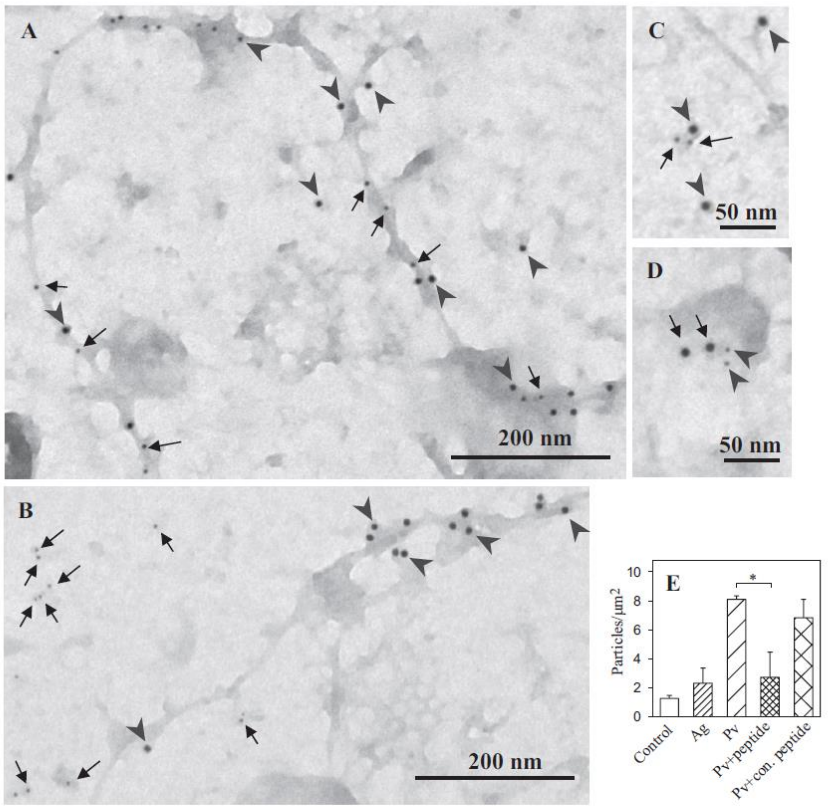

FIGURE 10. **Association of PTPs with actin cytoskeleton and FcεRI.** *A*, plasma membrane sheets were isolated from pervanadate-activated (0.2 mM, 5 min) BMMCs. The sheets were labeled from the cytoplasmic side for oxidized PTPs with oxPTP mAb followed by GαMIgG conjugated with 12-nm gold particles (*arrowheads*) and for F-actin with biotin-labeled phalloidin, followed by streptavidin conjugated with 5-nm gold particles (*arrows*). *B*, BMMCs were activated with pervanadate (as in *A*), and plasma membrane sheets were labeled with oxPTP mAb (12 nm gold, *arrowheads*) and rabbit anti-SHP-2 Ab (6 nm gold, *arrows*). *C*, plasma membrane sheets were isolated from resting cells and stained on cytoplasmic side with mouse anti-FcεRI-β mAb followed by GαMIgG conjugated with 12-nm gold particles (*arrowheads*), and rabbit anti-SHP-2 Ab followed by GαRIgG conjugated with 6-nm gold particles (*arrows*). *D*, alternatively, plasma membrane sheets were isolated from resting cells and stained on cytoplasmic side with mouse anti-FcεRI-β mAb (6 nm gold; *arrowheads*) and rabbit anti-SHP-2 Ab (12 nm gold; *arrows*). *Scale bars* are shown at the *bottom*. *E*, quantitative analysis of SHP-2 (numbers of gold particles per μm^2) in control cells or antigen (Ag)- or Pv-activated cells. Binding of SHP-2 antibody to the membrane sheets from Pv-activated cells in the presence of SHP-2 blocking peptide (*peptide*) or negative control (*con.*) peptide is also shown. Means ± S.D. were calculated from three independent experiments; each 22.2 μm^2. Statistical significance of intergroup differences was calculated using Student's *t* test, *, $p < 0.01$.

two models, which have been proposed (see Introduction and Fig. 11, *A* and *B*), are not capable of completely explaining all current observations, including those presented in this study.

To better understand the early activation events in all their complexities, we studied the role of PTPs in mast cell triggering. The oxidative agent pervanadate is known to induce protein tyrosine phosphorylation, formation of inositol 1,4,5-trisphosphate, an increase in calcium influx, and histamine secretion (11, 61). Several lines of evidence presented in this study indicate that pervanadate and H_2O_2 initiate FcεRI tyrosine phosphorylation by a mechanism that is different from the previously postulated models of FcεRI triggering.

First, exposure of the cells to the PTP inhibitor pervanadate induced tyrosine phosphorylation of FcεRI in the absence of the receptor aggregation, as evidenced by electron microscopy on isolated plasma membrane sheets. Thus, it is unlikely that tyrosine phosphorylation of the receptor subunits in pervanadate-stimulated cells is mediated by enhanced aggregation of FcεRI and associated Lyn kinase, as proposed by the transphosphorylation model (14). It is in line with previous data showing that dimerization of FcεRI leads to tyrosine phosphorylation in the absence of extensive receptor clustering (23). Thus, formation of large aggregates of multivalent antigen-IgE-FcεRI complexes within osmiophilic regions containing other signaling molecules (phospholipase Cγ2, phosphatidylinositol 3-kinase, Gab2, and Grb2) (62) is not a necessary condition for initiation of FcεRI signaling.

Second, in unstimulated cells lysed in Triton X-100, most of FcεRI is soluble and is localized in high density fractions after sucrose density gradient ultracentrifugation. Following FcεRI aggregation (by multivalent antigen-IgE complexes, antibodies against FcεRI, or biotinylated IgE-streptavidin complexes), the major part of FcεRI is associated with low density fractions (19, 24, 63). Because the same fractions also possess Lyn kinase and other signaling molecules, including some adaptor proteins (24, 64, 65), it was postulated that coalescence of FcεRI with lipid rafts is the key step for tyrosine phosphorylation of FcεRI β and γ subunits (see lipid raft model, Fig. 11*B*). However, our data indicate that exposure of mast cells to pervanadate leads to rapid tyrosine phosphorylation of the FcεRI (Fig. 1, *D* and *E*) without enhanced association of the receptor with Lyn kinase-containing DRMs (Fig. 1, *F* and *G*).

Third, the transphosphorylation model postulates that a fraction of Lyn is preassociated with FcεRI in quiescent cells (14). However, when detergent-solubilized nonactivated cells are fractionated by density gradient centrifugation, most of Lyn is found associated with DRMs in low density fractions, whereas FcεRI is found mostly in separate high density fractions (Fig. 1*F*). The latter data are in conflict with the results of electron microscopy studies indicating preassociation of a fraction of Lyn with FcεRI clusters (17), as well as with immunochemical studies detecting Lyn in immunocomplexes of FcεRI in quiescent cells (14, 16). These discrepancies can be explained by removal of Lyn from FcεRI complexes during density gradi-

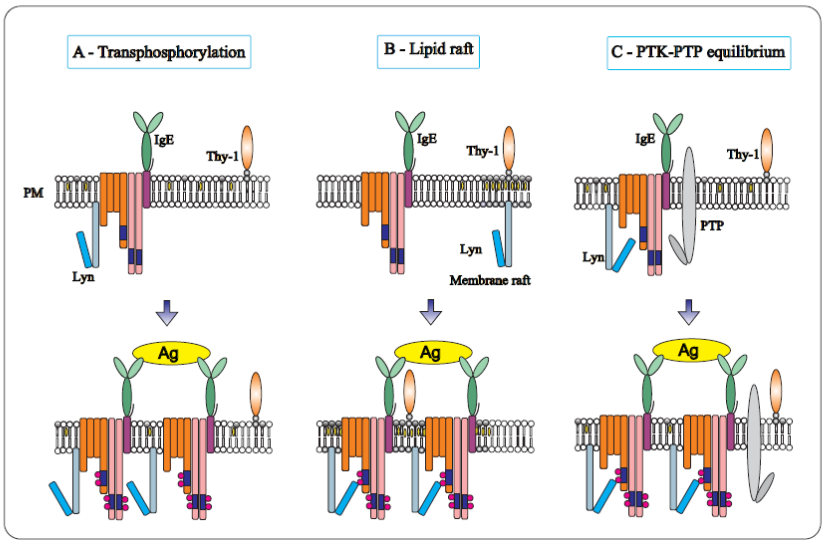

FIGURE 11. **Models of the initial tyrosine phosphorylation of the FcεRI.** *A*, according to the "transphosphorylation model," a fraction of the tetrameric FcεRI ($\alpha\beta2\gamma$) in the plasma membrane (*PM*) is associated with Lyn kinase. After binding of the IgE to the FcεRI α subunit, the receptor remains randomly distributed at the plasma membrane. Stimulation with bivalent or multivalent antigen (*Ag*) leads to receptor dimerization or multimerization. Only in the clusters can the Lyn kinases phosphorylate ITAMs of the neighboring receptors. Monovalent ligands do not cluster the receptors and therefore do not induce phosphorylation and activation. *B*, "lipid raft model" proposes that Lyn kinase is not bound to FcεRI but is separated instead into membrane regions (lipid rafts), which are enriched with cholesterol and glycosphingolipids. These domains possess some other lipid-anchored molecules, like glycosylphosphatidylinositol-anchored Thy-1 glycoprotein. After antigen-mediated FcεRI clustering, the receptors are recruited into lipid rafts where their ITAMs are phosphorylated by Lyn. *C*, according to "PTK-PTP equilibrium model," a fraction of Lyn kinase in resting cells is associated with FcεRI and phosphorylates it. This activity is counterbalanced by the action of PTPs, resulting in the formation of a basal equilibrium in quiescent cells. Perturbation of this equilibrium by inhibiting the enzymatic activity of the PTPs or by clustering-induced allosteric changes in the receptor shifts the balance between phosphorylation and dephosphorylation resulting in a net increase in tyrosine phosphorylation of the receptor.

ent fractionation of detergent-solubilized cells. Our results showing that various detergents have different effects on the binding of several tyrosine-phosphorylated proteins to the FcεRI immunocomplexes (Fig. 1*A*) support this explanation. The combined data indicate that transphosphorylation and the lipid raft model do not fully comply with all data on the mechanism of FcεRI tyrosine phosphorylation gathered under some particular conditions and that phosphatases obviously play a key role at initial stage of the activation process.

Based on these data we propose a third model for FcεRI triggering (Fig. 11*C*). According to this PTK-PTP equilibrium model, FcεRI in quiescent cells is functionally associated with PTKs and PTPs that are in equilibrium, and therefore, no net phosphorylation of FcεRI is observed. When the cell is activated, this equilibrium is disturbed, and a shift occurs in favor of kinases; consequently, FcεRI becomes phosphorylated. The first step of the activation sequence according to this model is inhibition of enzymatic activity of PTPs. ROS produced by macrophages in the close vicinity of mast cells could represent potent inhibitors of PTPs (25). ROS are also produced in the course of FcεRI triggering by mast cells, but because they are not necessary for cell triggering (66), the role of intracellular ROS production in cell activation is unclear. An alternative possibility is that activation induces conformational changes in the receptor subunits (67), either impairing (PTPs) or enhancing (PTKs) access of the enzymes to the ITAMs of the receptor, leading thus to a change in equilibrium between PTKs and PTPs and to enhanced tyrosine phosphorylation. It should be mentioned that the regulatory role of PTPs and ROS has been proposed during activation in other MIRRs (45, 68). However, our data prove for the first time that FcεRI in ROS-treated cells does not aggregate and that extensive phosphorylation of the receptor does not require its associate with Lyn-containing DRMs.

An analysis of binding motifs in nonphosphorylated FcεRI β and γ chains did not reveal any binding sites for phosphatases besides the phosphotyrosine motifs. Furthermore, we failed in attempts to co-immunoprecipitate PTPs associated with FcεRI from nonactivated cells.[5] This could reflect weak association and sensitivity to detergents used for cell solubilization. Similarly, Syk kinase, for example, which clearly interacts with FcεRI γ chain, does not co-precipitate with the receptor (56). The vicinity of FcεRI phosphotyrosine motifs may be sufficient to stimulate substrate-specific binding of PTPs. Barr *et al.* (69) provided convincing evidence that, despite the largely conserved fold, surface properties of PTP phosphatase domains are strikingly diverse. The activity of individual PTP catalytic domains against various phosphopeptides, including substrates commonly found in mast cells, such as c-Kit, WASP, or Csk, varied at least by 2 orders of magnitude. Interestingly, the reaction rates did not correlate with the specific activity of each PTP domain toward general PTP substrate 6,8-difluoro-4-methylumbelliferyl phosphate. Thus, it is possible that the PTPs in the vicinity of FcεRI recognize specific phosphorylation sites in the absence of another binding motif.

Using mAb specific for the oxidized active site cysteine of PTPs, we found a dramatic increase of oxidized phosphatases in pervanadate-treated cells. PTPs were also oxidized in both H_2O_2- and antigen-activated cells, although to lesser extent. Interestingly, most of oxidized PTPs were found in the high density fractions of sucrose gradients, suggesting that they are separated from signaling assemblies during cell solubilization and/or density gradient fractionation. It is possible that oxidation of the PTPs modifies their physical properties and contributes to their relocation to actin cytoskeleton (see below) and cytoplasm.

[5] P. Heneberg, L. Dráberová, and P. Dráber, unpublished data.

DRMs are known to host only a fraction of total membrane and submembrane PTPs. Peirce and Metzger (56) suggested that tyrosine phosphorylation of substrates located in DRMs is favored by both the enrichment of kinases and the paucity of phosphatases; however, several pieces of evidence do not support such model. Only a limited fraction of PTPs (see *e.g. SHP-1* in Fig. 5) is associated with DRMs. Furthermore, membrane proteins located outside DRMs are dephosphorylated with the similar kinetics as phosphoproteins residing in DRMs (56). Finally, the DRM-associated pool of PTPs is largely in reduced form (Fig. 5), allowing its higher enzymatic activity and faster fine-tuning by phosphorylation and/or conformational changes. Therefore, it is possible that plasma membrane hosts a fraction of PTPs, which undergo strict regulation of their activity in activated cells. Alternatively, oxidation leads to the removal of PTPs from DRMs, contributing to the observed deficiency of oxidized PTPs in DRMs (56, 70).

Does FcεRI triggering resemble signaling via the growth factor receptors (7, 53, 53, 71) and does it also lead to inactivation of PTPs via ROS species? Our results, as well as data from others (25, 66, 72), clearly show that there is an increase in the amount of oxidized PTPs in antigen-activated mast cells. However, the results presented here also indicate that despite the fact that a fraction of phosphatases is oxidized and thus inactivated, the net enzymatic activity is not necessarily reduced and is largely dependent on other ways of regulation, leading to either an increase (SHP-2) or a decrease (HePTP) in their enzymatic activity after FcεRI triggering. It is therefore likely that under physiological conditions only a limited fraction of PTPs is inactivated by oxidation. This corresponds with the findings that physiological concentrations of ROS are not capable of inducing oxidation of the whole pool of particular PTPs (73). Thus, in the course of MIRRs or growth factor receptor activation, cells may retain a pool of PTPs with reduced active site cysteines that undergo versatile regulation based on conformational and/or phosphorylation changes leading to a further increase or decrease of their enzymatic activity by several orders of magnitude (74).

The unexpected finding reported here is the association of PTPs recognized by oxPTP mAb predominantly with plasma membrane actin cytoskeleton. Although detailed identification of the target phosphatases will require further studies, it is possible that actin cytoskeleton is involved in early activation events by regulating the topography of phosphatases. Interestingly, FcεRI was only rarely co-localized with PTPs or their oxidized forms. However, such co-localization was occasionally observed (Fig. 9, *E* and *F*, and Fig. 10, *C* and *D*), confirming a physical and functional link between PTPs and FcεRI.

In summary, we propose an alternative pathway of an initial stage of FcεRI triggering based on the existence of preformed complexes containing FcεRI, PTKs, and PTPs, where the latter two components are in equilibrium in quiescent cells. Activation-induced down-regulation of the enzymatic activity of PTPs by oxidation of their active site cysteine and/or changes in their accessibility to the receptor subunits lead to disturbance of the equilibrium and subsequently enhanced tyrosine phosphorylation of the receptor subunits.

Acknowledgments—We thank Hana Mrázová and Romana Budovičová for expert technical assistance.

REFERENCES

1. Gilfillan, A. M., and Tkaczyk, C. (2006) *Nat. Rev. Immunol.* **6,** 218–230
2. Gilfillan, A. M., and Rivera, J. (2009) *Immunol. Rev.* **228,** 149–169
3. Heneberg, P., and Dráber, P. (2002) *Int. Arch. Allergy Immunol.* **128,** 253–263
4. Pao, L. I., Badour, K., Siminovitch, K. A., and Neel, B. G. (2007) *Annu. Rev. Immunol.* **25,** 473–523
5. Vang, T., Miletic, A. V., Arimura, Y., Tautz, L., Rickert, R. C., and Mustelin, T. (2008) *Annu. Rev. Immunol.* **26,** 29–55
6. Denu, J. M., and Tanner, K. G. (1998) *Biochemistry* **37,** 5633–5642
7. Meng, T. C., Fukada, T., and Tonks, N. K. (2002) *Mol. Cell* **9,** 387–399
8. Zick, Y., and Sagi-Eisenberg, R. (1990) *Biochemistry* **29,** 10240–10245
9. Heffetz, D., Bushkin, I., Dror, R., and Zick, Y. (1990) *J. Biol. Chem.* **265,** 2896–2902
10. Teshima, R., Ikebuchi, H., Nakanishi, M., and Sawada, J. (1994) *Biochem. J.* **302,** 867–874
11. Amoui, M., Dráberová, L., Tolar, P., and Dráber, P. (1997) *Eur. J. Immunol.* **27,** 321–328
12. Huyer, G., Liu, S., Kelly, J., Moffat, J., Payette, P., Kennedy, B., Tsaprailis, G., Gresser, M. J., and Ramachandran, C. (1997) *J. Biol. Chem.* **272,** 843–851
13. Eiseman, E., and Bolen, J. B. (1992) *Nature* **355,** 78–80
14. Pribluda, V. S., Pribluda, C., and Metzger, H. (1994) *Proc. Natl. Acad. Sci. U.S.A.* **91,** 11246–11250
15. Sil, D., Lee, J. B., Luo, D., Holowka, D., and Baird, B. (2007) *ACS Chem. Biol.* **2,** 674–684
16. Vonakis, B. M., Gibbons, S. P., Jr., Rotté, M. J., Brothers, E. A., Kim, S. C., Chichester, K., and MacDonald, S. M. (2005) *J. Immunol.* **175,** 4543–4554
17. Wilson, B. S., Pfeiffer, J. R., and Oliver, J. M. (2000) *J. Cell Biol.* **149,** 1131–1142
18. Field, K. A., Holowka, D., and Baird, B. (1995) *Proc. Natl. Acad. Sci. U.S.A.* **92,** 9201–9205
19. Field, K. A., Holowka, D., and Baird, B. (1997) *J. Biol. Chem.* **272,** 4276–4280
20. Simons, K., and Toomre, D. (2000) *Nat. Rev. Mol. Cell Biol.* **1,** 31–39
21. Munro, S. (2003) *Cell* **115,** 377–388
22. Brown, D. A. (2006) *Physiology* **21,** 430–439
23. Dráberová, L., Lebduška, P., Hálová, I., Tolar, P., Štokrová, J., Tolarová, H., Korb, J., and Dráber, P. (2004) *Eur. J. Immunol.* **34,** 2209–2219
24. Kovářová, M., Tolar, P., Arudchandran, R., Dráberová, L., Rivera, J., and Dráber, P. (2001) *Mol. Cell. Biol.* **21,** 8318–8328
25. Swindle, E. J., Hunt, J. A., and Coleman, J. W. (2002) *J. Immunol.* **169,** 5866–5873
26. Swieter, M., Berenstein, E. H., Swaim, W. D., and Siraganian, R. P. (1995) *J. Biol. Chem.* **270,** 21902–21906
27. Xie, Z. H., Zhang, J., and Siraganian, R. P. (2000) *J. Immunol.* **164,** 1521–1528
28. Kimura, T., Zhang, J., Sagawa, K., Sakaguchi, K., Appella, E., and Siraganian, R. P. (1997) *J. Immunol.* **159,** 4426–4434
29. Nakata, K., Yoshimaru, T., Suzuki, Y., Inoue, T., Ra, C., Yakura, H., and Mizuno, K. (2008) *J. Immunol.* **181,** 5414–5424
30. Barsumian, E. L., Isersky, C., Petrino, M. G., and Siraganian, R. P. (1981) *Eur. J. Immunol.* **11,** 317–323
31. Chen, T. R. (1977) *Exp. Cell Res.* **104,** 255–262
32. Rudolph, A. K., Burrows, P. D., and Wabl, M. R. (1981) *Eur. J. Immunol.* **11,** 527–529
33. Liu, F. T., Bohn, J. W., Ferry, E. L., Yamamoto, H., Molinaro, C. A., Sherman, L. A., Klinman, N. R., and Katz, D. H. (1980) *J. Immunol.* **124,** 2728–2737
34. Dráberová, L., Amoui, M., and Dráber, P. (1996) *Immunology* **87,** 141–148
35. Rivera, J., Kinet, J. P., Kim, J., Pucillo, C., and Metzger, H. (1988) *Mol. Immunol.* **25,** 647–661
36. Andersen, J. N., Mortensen, O. H., Peters, G. H., Drake, P. G., Iversen, L. F.,

Olsen, O. H., Jansen, P. G., Andersen, H. S., Tonks, N. K., and Møller, N. P. (2001) *Mol. Cell. Biol.* **21,** 7117–7136
37. Persson, C., Kappert, K., Engström, U., Östman, A., and Sjöblom, T. (2005) *Methods* **35,** 37–43
38. Lebduška, P., Korb, J., Tůmová, M., Heneberg, P., and Dráber, P. (2007) *J. Immunol. Methods* **328,** 139–151
39. Philimonenko, A. A., Janáček, J., and Hozák, P. (2000) *J. Struct. Biol.* **132,** 201–210
40. Dráberová, L., Dudková, L., Boubelík, M., Tolarová, H., Šmíd, F., and Dráber, P. (2003) *J. Immunol.* **171,** 3585–3593
41. Weibrecht, I., Böhmer, S. A., Dagnell, M., Kappert, K., Östman, A., and Böhmer, F. D. (2007) *Free Radic. Biol. Med.* **43,** 100–110
42. Tolarová, H., Dráberová, L., Heneberg, P., and Dráber, P. (2004) *Eur. J. Immunol.* **34,** 1627–1636
43. Suzuki, Y., Yoshimaru, T., Matsui, T., Inoue, T., Niide, O., Nunomura, S., and Ra, C. (2003) *J. Immunol.* **171,** 6119–6127
44. O'Shea, J. J., McVicar, D. W., Bailey, T. L., Burns, C., and Smyth, M. J. (1992) *Proc. Natl. Acad. Sci. U.S.A.* **89,** 10306–10310
45. Wienands, J., Larbolette, O., and Reth, M. (1996) *Proc. Natl. Acad. Sci. U.S.A.* **93,** 7865–7870
46. Dráber, P., Dráberová, L., Heneberg, P., Šmíd, F., Farghali, H., and Dráber, P. (2007) *Cell. Signal.* **19,** 2400–2412
47. Antunes, F., and Cadenas, E. (2000) *FEBS Lett.* **475,** 121–126
48. Wilson, B. S., Pfeiffer, J. R., Surviladze, Z., Gaudet, E. A., and Oliver, J. M. (2001) *J. Cell Biol.* **154,** 645–658
49. Surviladze, Z., Harrison, K. A., Murphy, R. C., and Wilson, B. S. (2007) *J. Lipid Res.* **48,** 1325–1335
50. Mikalsen, S. O., and Kaalhus, O. (1998) *J. Biol. Chem.* **273,** 10036–10045
51. Heneberg, P., and Dráber, P. (2005) *Curr. Med. Chem.* **12,** 1859–1871
52. Tonks, N. K. (2005) *Cell* **121,** 667–670
53. Persson, C., Sjöblom, T., Groen, A., Kappert, K., Engström, U., Hellman, U., Heldin, C. H., den Hertog, J., and Östman, A. (2004) *Proc. Natl. Acad. Sci. U.S.A.* **101,** 1886–1891
54. Keilhack, H., Müller, M., Böhmer, S. A., Frank, C., Weidner, K. M., Birchmeier, W., Ligensa, T., Berndt, A., Kosmehl, H., Günther, B., Müller, T., Birchmeier, C., and Böhmer, F. D. (2001) *J. Cell Biol.* **152,** 325–334
55. Simoneau, M., Boulanger, J., Coulombe, G., Renaud, M. A., Duchesne, C., and Rivard, N. (2008) *J. Biol. Chem.* **283,** 25544–25556
56. Peirce, M., and Metzger, H. (2000) *J. Biol. Chem.* **275,** 34976–34982
57. Gulati, P., Markova, B., Göttlicher, M., Böhmer, F. D., and Herrlich, P. A. (2004) *EMBO Rep.* **5,** 812–817
58. Wulf, E., Deboben, A., Bautz, F. A., Faulstich, H., and Wieland, T. (1979) *Proc. Natl. Acad. Sci. U.S.A.* **76,** 4498–4502
59. Lachapelle, M., and Aldrich, H. C. (1988) *J. Histochem. Cytochem.* **36,** 1197–1202
60. Steinmetz, M. O., Stoffler, D., Müller, S. A., Jahn, W., Wolpensinger, B., Goldie, K. N., Engel, A., Faulstich, H., and Aebi, U. (1998) *J. Mol. Biol.* **276,** 1–6
61. den Hertog, J., Groen, A., and van der Wijk, T. (2005) *Arch. Biochem. Biophys.* **434,** 11–15
62. Wilson, B. S., Pfeiffer, J. R., and Oliver, J. M. (2002) *Mol. Immunol.* **38,** 1259–1268
63. Field, K. A., Holowka, D., and Baird, B. (1999) *J. Biol. Chem.* **274,** 1753–1758
64. Volná, P., Lebduška, P., Dráberová, L., Šímová, S., Heneberg, P., Boubelík, M., Bugajev, V., Malissen, B., Wilson, B. S., Hořejší, V., Malissen, M., and Dráber, P. (2004) *J. Exp. Med.* **200,** 1001–1013
65. Zhang, W., Sloan-Lancaster, J., Kitchen, J., Trible, R. P., and Samelson, L. E. (1998) *Cell* **92,** 83–92
66. Swindle, E. J., Coleman, J. W., DeLeo, F. R., and Metcalfe, D. D. (2007) *J. Immunol.* **179,** 7059–7071
67. Tolar, P., Sohn, H. W., and Pierce, S. K. (2005) *Nat. Immunol.* **6,** 1168–1176
68. Reth, M. (2002) *Nat. Immunol.* **3,** 1129–1134
69. Barr, A. J., Ugochukwu, E., Lee, W. H., King, O. N., Filippakopoulos, P., Alfano, I., Savitsky, P., Burgess-Brown, N. A., Müller, S., and Knapp, S. (2009) *Cell* **136,** 352–363
70. Stauffer, T. P., and Meyer, T. (1997) *J. Cell Biol.* **139,** 1447–1454
71. Chen, C. H., Cheng, T. H., Lin, H., Shih, N. L., Chen, Y. L., Chen, Y. S., Cheng, C. F., Lian, W. S., Meng, T. C., Chiu, W. T., and Chen, J. J. (2006) *Mol. Pharmacol.* **69,** 1347–1355
72. Swindle, E. J., Metcalfe, D. D., and Coleman, J. W. (2004) *J. Biol. Chem.* **279,** 48751–48759
73. Lou, Y. W., Chen, Y. Y., Hsu, S. F., Chen, R. K., Lee, C. L., Khoo, K. H., Tonks, N. K., and Meng, T. C. (2008) *FEBS J.* **275,** 69–88
74. Barford, D., and Neel, B. G. (1998) *Structure* **6,** 249–254

1.3 WHAT PRECEDES THE INITIAL TYROSINE PHOSPHORYLATION OF THE HIGH AFFINITY IGE RECEPTOR IN ANTIGEN-ACTIVATED MAST CELLS?

FEBS Lett. 84(24):4949-55, 2010.

In this review we evaluated current models of FcεRI signaling initiation.

FEBS Letters 584 (2010) 4949–4955

journal homepage: www.FEBSLetters.org

Review

What precedes the initial tyrosine phosphorylation of the high affinity IgE receptor in antigen-activated mast cell?

Viktor Bugajev, Monika Bambousková, Lubica Dráberová, Petr Dráber*

Laboratory of Signal Transduction, Institute of Molecular Genetics, Academy of Sciences of the Czech Republic, CZ-142 20 Prague 4, Czech Republic

ARTICLE INFO

Article history:
Received 21 July 2010
Revised 23 August 2010
Accepted 31 August 2010
Available online 7 September 2010

Edited by Israel Pecht

Keywords:
Mast cell
Immunoreceptor
Cell signaling
Protein tyrosine kinase
Protein tyrosine phosphatase
Plasma membrane

ABSTRACT

An interaction of multivalent antigen with its IgE bound to the high-affinity IgE receptor (FcεRI) on the surface of mast cells or basophils initiates a series of signaling events leading to degranulation and release of inflammatory mediators. Earlier studies showed that the first biochemically defined step in this signaling cascade is tyrosine phosphorylation of the FcεRI β subunit by Src family kinase Lyn. However, the processes affecting this step remained elusive. In this review we critically evaluate three current models (transphosphorylation, lipid raft, and our preferential protein tyrosine kinase–protein tyrosine phosphatase interplay model) substantiating three different mechanisms of FcεRI phosphorylation.

1. Introduction

Activation of mast cells and basophils through the high-affinity IgE receptor (FcεRI) leads to the release of pro-inflammatory mediators involved in inflammation and allergy disorders [1]. FcεRI, which belongs to the multichain immune recognition receptor (MIRR) family is a tetrameric complex formed by an IgE-binding α-subunit, a signal-amplifying β-subunit, and a homodimer of disulphide-linked γ-subunits. Each FcεRI β- and γ-subunit contains one immunoreceptor tyrosine-based activation motif (ITAM) which, after tyrosine phosphorylation, serves as a docking site for other signaling molecules such as Src homology 2 (SH2) domain-containing Src family kinase Lyn or Syk/Zap family kinase Syk [1]. Several models have been proposed to explain mechanistically how the FcεRI becomes phosphorylated by protein tyrosine kinase (PTK) Lyn. The models differ in their perception of the spatiotemporal relationship between Lyn kinase and FcεRI, and of the role of protein tyrosine phosphatases (PTPs) at initial tyrosine phosphorylation of the receptor.

2. Models of FcεRI phosphorylation

2.1. Transphosphorylation model

This model assumes that FcεRI in quiescent cells is non-covalently associated through its non-phosphorylated β subunit with Lyn kinase which is unable to phosphorylate its carrier receptor (Fig. 1). Aggregation of the IgE–FcεRI complexes with multivalent antigen initiates Lyn-dependent phosphorylation of the neighboring receptors within the aggregate [2]. This process is known as transphosphorylation and was suggested to play a role in the signal transduction in several other systems [3]. It is corroborated by several experimental findings. First, when biochemically crosslinked, at least 3–4% of the non-aggregated FcεRI was found to be directly associated with Lyn [4]. Second, Vonakis et al. [5] showed that Lyn binds through its unique domain to β subunit of FcεRI, irrespective of phosphorylation of the ITAM. This binding does not involve Lyn SH2 domain which interacts with phosphorylated ITAM, serving to amplify the initial activation signal. Third, transfection of Lyn unique domain into rat basophilic leukemia (RBL) cells inhibited antigen-induced phosphorylation of FcεRI β and γ subunit; this

Abbreviations: FcεRI, high-affinity IgE receptor; MIRR, multichain immune recognition receptor; ITAM, immunoreceptor tyrosine-based activation motif; SH2, Src homology 2; PTK, protein tyrosine kinase; PTP, protein tyrosine phosphatase; RBL, rat basophilic leukemia; EGFP, enhanced green fluorescent protein; DRM, detergent-resistant membrane; MBCD, methyl-β-cyclodextrin; ROS, reactive oxygen species; NADPH, nicotinamide adenine dinucleotide phosphate; BMMC, bone marrow-derived mast cell; LAT, linker of activated T cell; PLC, phospholipase; NTAL, non-T cell activation linker

* Corresponding author. Address: Laboratory of Signal Transduction, Institute of Molecular Genetics, Academy of Sciences of the Czech Republic, Vídeňská 1083, Prague 4, CZ 142 20, Czech Republic. Fax: +420 241062214.
E-mail address: draberpe@img.cas.cz (P. Dráber).

0014-5793/$36.00 © 2010 Federation of European Biochemical Societies. Published by Elsevier B.V. All rights reserved.
doi:10.1016/j.febslet.2010.08.045

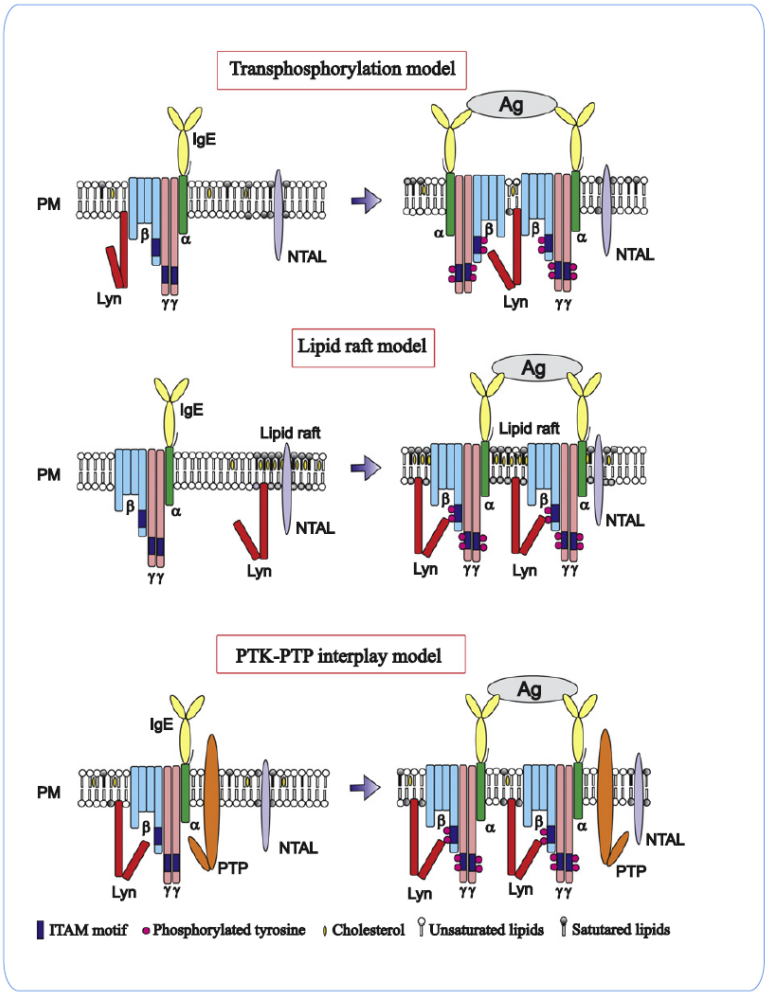

Fig. 1. Models of FcεRI phosphorylation. Transphosphorylation model presumes that active Lyn is constitutively associated with non-phosphorylated FcεRI; upon FcεRI aggregation, Lyn phosphorylates adjacent receptors in the aggregate. Lipid raft model postulates that FcεRI and Lyn are localized in different plasma membrane microdomains; after aggregation FcεRI is translocated to lipid rafts where it is phosphorylated by lipid raft-associated Lyn kinase. PTK–PTP interplay model assumes that PTPs set the threshold of FcεRI tyrosine phosphorylation; after FcεRI triggering there is a shift in the PTK–PTP steady state in favor of PTKs.

suggests a competition for FcεRI as a substrate between endogenous Lyn and the transfected Lyn unique domain [6]. Fourth, studies with Chinese hamster ovary fibroblasts expressing FcεRI and various amounts of Lyn showed a direct correlation between amount of Lyn and tyrosine phosphorylation of the FcεRI. Detailed mathematic analysis demonstrated that one Lyn molecule is capable of phosphorylating numerous adjacent FcεRIs [7]. Fifth, Lyn was found to colocalize with FcεRI as detected by transmission electron microscopy on plasma membrane sheets isolated from RBL cells. In non-stimulated cells about 25% of randomly dispersed FcεRI was associated with one or a few Lyn molecules [8]. Sixth, Lyn kinase in quiescent mast cells is enzymatically active and its activity is not further enhanced after FcεRI triggering [9]. A mutation of the C terminal tyrosine, responsible for inhibition of Lyn kinase activity, led to a weak constitutive tyrosine phosphorylation of several substrates including β and γ subunits of FcεRI and Syk kinase in non-stimulated cells [9]. Seventh, aggregation of FcεRI with trivalent ligands bound in defined distance to a symmetric DNA scaffold, resulted in phosphorylation of the FcεRI β and γ subunits depending on the length of DNA spacer; more potent trivalent ligands were those with shorter spacer [10]. Similarly, it has been suggested that dominant factor affecting signaling capacity of various anti-FcεRI monoclonal antibodies is the orientational element [11]. Eight, simultaneous observation of FcεRI marked with various quantum dot-labeled IgE revealed that aggregates of at least three crosslinked FcεRI remained mobile, showed prolonged diffusion and exhibited phosphorylation of the FcεRI β subunit and β-glucuronidase release [12]. Finally, fluorescence correlation spectroscopy of Lyn-enhanced green fluorescent protein (EGFP) and fluorescently labeled IgE bound to FcεRI confirmed that a small fraction of FcεRI in non-activated cells colocalized with Lyn [13]. Taken together, the results from the studies applying different methods provide a strong support for the hypothesis that a fraction of Lyn binds to unphosphorylated FcεRI, and strengthen the notion that transphosphorylation could be the first step in FcεRI signaling. However, some data are in conflict with this hypothesis. For exam-

ple, aggregated FcεRI becomes tyrosine phosphorylated even in the absence of β subunit [14]. Furthermore, chimeric receptors containing only the γ cytoplasmic tail become tyrosine phosphorylated upon their aggregation [15]. Alternative models had been therefore proposed.

2.2. Lipid raft model

Lipid raft membrane microdomains were conceived as a mechanism for intracellular trafficking of lipids and lipid-anchored proteins. The model assumes that biological membranes possess microdomains having a lipidic structure with properties of lipid order phase. These domains are rich in cholesterol and sphingomyelin, and possess a limited set of proteins, including those anchored to the membrane via glycolipids (e.g. glycophosphatidylinositol) or acyl groups (e.g. palmitoyl or myristoyl), and also some acylated proteins with transmembrane domain. They are surrounded by membranes with lipid structure resembling lipid disorder phase possessing phosphatidylinositols and a majority of the transmembrane proteins [16]. Cholesterol plays a crucial role in the formation of lipid rafts, and cholesterol-depletion experiments have been used in lipid raft function studies. Membrane domains with properties of lipid rafts are often isolated as membranes resistant to solubilization with non-ionic detergents, such as Triton X-100 at low temperature. Thus, the lipid raft hypothesis is in part based on studies presuming that detergent-resistant membranes (DRMs) correspond to lipid rafts, an assumption which is probably incorrect [16]. On the other hand, the lipid raft model is supported by experiments showing that aggregation of FcεRI and some other membrane proteins leads to a decreased detergent solubility as can be documented by density gradient ultracentrifugation. From the FcεRI perspective, lipid raft model postulates that in quiescent cells FcεRI is physically separated from active Lyn residing in lipid raft domains [17]. After aggregation, FcεRI is translocated into these domains and is phosphorylated there by Lyn (Fig. 1). Decreased detergent solubility was observed not just in extensively aggregated FcεRI, but even upon FcεRI dimerization, although the activation was delayed and more sustained [18]. Furthermore, it has been shown that cholesterol depletion with methyl-β-cyclodextrin (MBCD) reduced phosphorylation of the FcεRI subunits as well as other proteins. The tyrosine phosphorylation of FcεRI was rescued when cholesterol was added [19]. These data were taken as evidence that FcεRI cannot be phosphorylated in the cells in which lipid rafts are destroyed. Removal of cholesterol with MBCD, however, led to a decreased expression of FcεRI and had some other effects on mast cell physiology [20]; therefore, these experiments cannot simply be interpreted as supporting the role of lipid rafts in FcεRI signaling.

Recent studies based on advanced microscopy methods revealed that membrane domains in quiescent cells are highly dynamic and small in size (less than 10 nm). They can transiently coalesce after ligand-induced aggregation of membrane proteins and form larger domains [21]. In antigen-stimulated mast cells, transient increase of FcεRI in specialized cholesterol-rich domains, peaking at 5 min after receptor aggregation has been described [22]. However, it remains to be determined whether these changes reflect either an association of FcεRI with cholesterol-enriched lipid rafts possessing sequestered Lyn, or rather changes leading to removal of aggregated FcεRI. In fact, experiments with N-palmitoylation-site deficient Lyn show that anchor of the Lyn to the plasma membrane but not to DRMs is important for proper tyrosine phosphorylation of the FcεRI [23]. Furthermore, Lyn-EGFP mobility within the plasma membrane decreased upon FcεRI triggering, and association of the kinase with FcεRI was increased. However, no change in association of aggregated FcεRI with EGFP anchored to the plasma membrane through Lyn acylation site was observed [13]. Thus, lipid raft localization of Lyn is not sufficient for its interaction with aggregated FcεRI.

2.3. PTK–PTP interplay model

The key player in the transphosphorylation and lipid raft models in antigen-activated mast cells is the PTK Lyn utilizing FcεRI ITAM as a substrate. However, the extent of phosphorylation of the immunoreceptors and other substrates depends not only on enzymatic activity of the PTKs, but, at least partly, also on the activity of PTPs. As an attempt to explain some conflicting experimental data which were inconsistent with lipid raft model, the PTK–PTP interplay model was coined (Fig. 1). Initially, the model was elaborated in studies of immunoreceptor signaling in B cells. Reth and co-workers [24] showed that the B cell receptor, belonging to the MIRR family, forms a complex with PTKs and PTPs; this complex is indispensable for reactive oxygen species (ROS)-induced phosphorylation. Also, ROS encompassing superoxide or hydrogen peroxide are known inhibitors of PTPs and are capable of initiating early FcεRI-induced signaling events in mast cells. Despite a growing list of confirmed PTPs present in mast cells, their contribution to cell signaling regulation is still poorly understood [25,26]. One possible way of regulation of the PTP activity is reversible oxidation of Cys residue in a conserved signature motif (I/

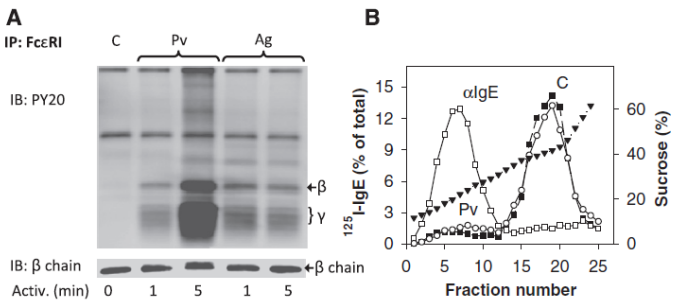

Fig. 2. Phosphorylation of FcεRI does not require its translocation into lipid rafts. (A) IgE-senzitized BMMCs were non-activated (C, 0 min) or activated for 1 or 5 min with pervanadate (Pv) or antigen (Ag). The cells were solubilized and the FcεRI complexes were immunoprecipitated (IP) and analyzed by immunoblotting (IB) with antibodies specific for phosphotyrosine (PY20) or FcεRI β chain (loading control). Positions of FcεRI β and γ chains are indicated. (B) Density gradient fractionation of cell lysates. The cells were sensitized with ^{125}I-IgE and then left non-activated (C; filled squares) or activated with pervanadate (Pv; open circles) or anti-IgE (αIgE; open squares). After 5 min the cells were solubilized and fractionated by sucrose density gradient ultracentrifugation. Radioactivity in individual fractions was determined and expressed as percentage of the total radioactivity recovered. Percentage of sucrose in individual fractions is also shown (filled triangles). Methodological details can be found elsewhere [32].

V)HCxxGxxR(S/T) in the catalytic domain. The proximity of Arg in the signature motif makes it possible for an invariant Cys to form a thiolate anion at physiological pH (p*Ka* <6.0) that can act in nucleophilic attack on the phosphate group. However, the same Cys residue can be oxidized by ROS to catalytically inactive Cys-sulphenic acid, a mechanism that is fully reversible by action of glutathione or other thiols [27]. ROS are produced under physiological conditions by the activity of specialized enzymes such as nicotinamide adenine dinucleotide phosphate (NADPH)-oxidase [28,29]. Strong oxidants like pervanadate (a mixture of vanadate and H_2O_2) irreversibly inactivate PTPs by the formation of Cys-sulphonic acid residues [30]. Exposure of mast cells to pervanadate leads to activation events which resemble those induced by physiological activators [31,32].

The PTK–PTP interplay model is supported by several lines of evidence. First, exposure of RBL or bone marrow-derived mast cells (BMMCs) to pervanadate or H_2O_2 induced robust tyrosine phosphorylation of the FcεRI subunits in the absence of receptor migration into DRMs, as determined by solubilization of the cells in Triton X-100 followed by sucrose density gradient ultracentrifugation. This was in sharp contrast to antigen- or anti-IgE antibody-induced activation which led to the movement of FcεRI into DRMs (Fig. 2). Such data indicate that association of FcεRI with DRMs is not required for receptor phosphorylation. Second, electron microscopy studies on isolated plasma membrane sheets showed that FcεRI in pervanadate-activated cells was distributed in the same way as the receptor in non-activated cells. Thus, enhanced receptor clustering is not required for tyrosine phosphorylation

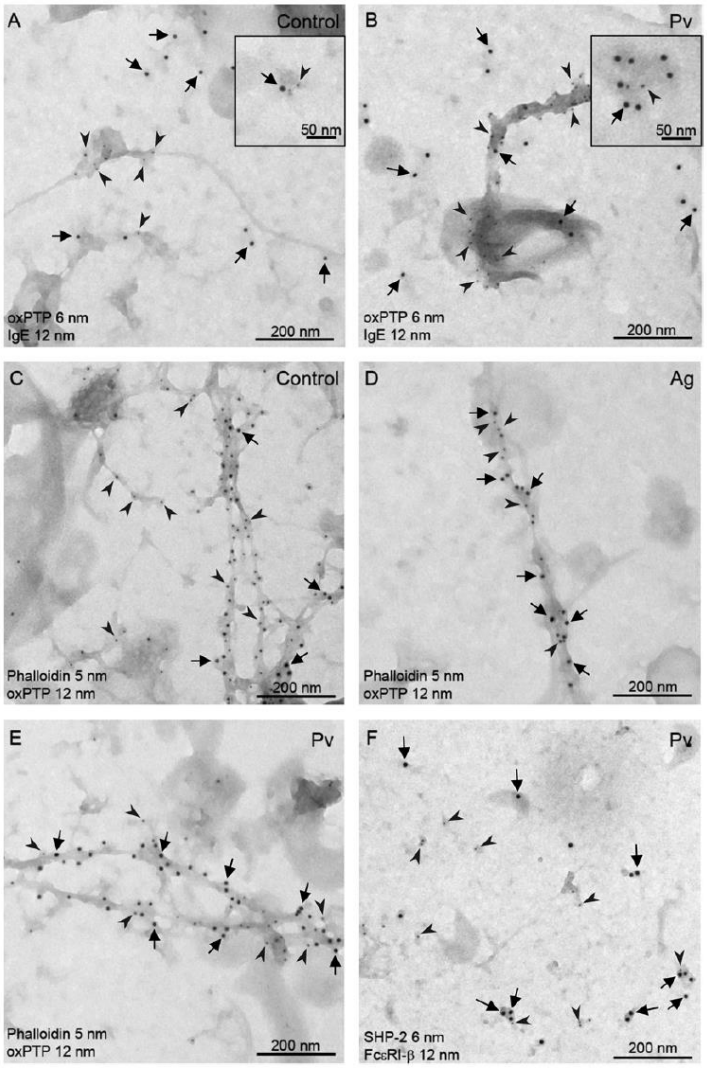

Fig. 3. Membrane topography of phosphatases, actin and FcεRI. Plasma membrane sheets were prepared from non-activated (Control; A and C), pervanadate-activated (Pv; B, E, and F) or antigen-activated (Ag; D) BMMCs and after two-step labeling procedure were analyzed by electron microscopy. FcεRI was labeled extracellularly using IgE (12 nm gold; A and B) or from cytoplasmic side using anti-FcεRI β chain (12 nm gold; F). Oxidized phosphatases were labeled with oxPTP monoclonal antibody marked with 6 nm (A and B) or 12 nm gold particles (C–E). F-Actin or SHP-2 were labeled with phalloidin (5 nm gold; C–E) or anti-SHP-2 antibody (6 nm gold; F), respectively. Gold particles of 5–6 nm are indicated by arrowheads and those of 12 nm by arrows. Inlets in A and B show higher magnification. Experimental procedure details have been described [32].

of FcεRI [32]. Third, using a monoclonal antibody (oxPTP) recognizing oxidized Cys residue in catalytic domain of PTPs, enzymatically inactive PTPs were detectable in a time- and dose-dependent manner in cells activated with pervanadate, H_2O_2 or antigen [32]. Fourth, most of PTK substrates are not phosphorylated if pervanadate is added to cell lysates instead of intact cells [24]. Similarly, lysates prepared from non-activated mast cells and treated with H_2O_2 or pervanadate exhibited a lower amount of oxidized PTPs than lysates prepared from cells activated with H_2O_2 or pervanadate before lysis [32]. These data suggest that solubilization of the cells with detergents destroys preformed signaling assemblies containing PTKs, PTPs, and their substrates. Fifth, pretreatment of activated cells with saponine, leading to cell permeabilization and release of the majority of free cytoplasmic components, resulted in association of the majority of oxidized PTPs with cellular ghosts [32]. This indicates that oxidized PTPs are not freely moving in cytosol, but rather form large complexes. In fact, FcεRI on plasma membrane sheets isolated from non-activated (Fig. 3A) or activated (Fig. 3B) cells occasionally colocalizes with oxidized PTPs. Interestingly, fraction of oxidized PTPs was associated with membrane-bound actin cytoskeleton, especially after activation (Fig. 3C–E). Finally, activation of the cells with antigen leads to decreased enzymatic activity of HePTP (PTPN7) and some other PTPs, and exposure of the cells to H_2O_2 leads to a substantial decrease in overall phosphatase activity [32].

An important task is the identification of PTPs directly involved in regulating the tyrosine phosphorylation of the receptor. Using a modified immunoprecipitation procedure with oxPTP antibody, followed by mass spectrometry analysis of the immunoprecipitated proteins, we found that several PTPs are oxidized in activated

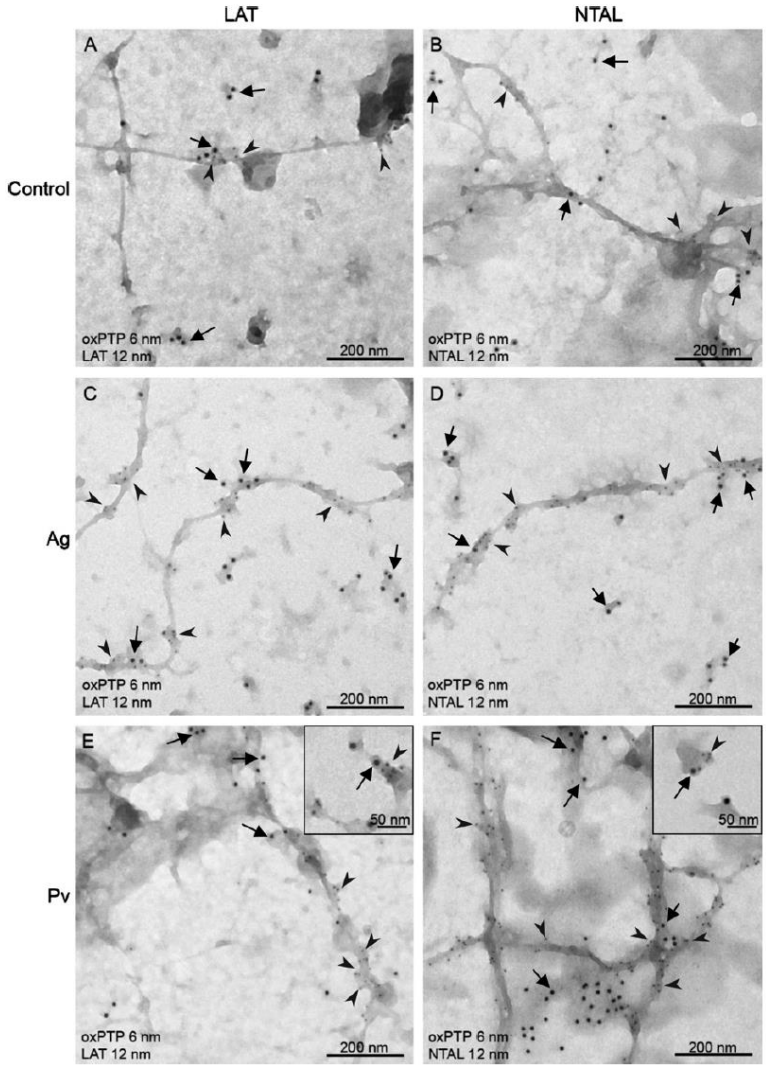

Fig. 4. Topography of oxidized phosphatases and transmembrane adaptor proteins. Plasma membrane sheets were prepared from non-activated (Control; A and B), antigen-activated (Ag; C and D) and pervanadate-activated (Pv; E and F) BMMCs and labeled for oxidized PTPs with 6 nm gold (A–F) or for LAT (A, C, and E) or NTAL (B, D, and F) with 12 nm gold. Gold particles of 6 or 12 nm in size are indicated with arrowheads or arrows, respectively. Inlets in E and F show higher magnification. Experimental procedure details have been described [32,38].

mast cells; they include SHP-1 (PTPN6), SHP-2 (PTPN11), PTP-MEG2 (PTPN9) and HePTP. However, we failed to co-immunoprecipitate the PTPs with FcεRI and we found no binding motifs in FcεRI β and γ subunits for the phosphatases, except for the phosphotyrosine motifs. Interestingly, it has been found that SHP-2 occasionally colocalizes with FcεRI (Fig. 3F), and that FcεRI is pre-associated in non-activated cells with SHP-1 [33]; these phosphatases exhibited enhanced enzymatic activity after FcεRI triggering [32]. The finding that a fraction of these phosphatases was reversibly oxidized in their active sites [32], suggests that there are spatiotemporal differences in enzymatic activity of the phosphatases. It is possible that the enzyme molecules in the vicinity of the receptor in submembraneous region have different enzymatic activity immediately after receptor triggering than the rest of molecules in the cell. Another PTP, the HePTP, also oxidized in activated mast cells, exhibited a decreased enzymatic activity after FcεRI triggering, and could thus contribute to an enhanced phosphorylation in activated cells.

How could the PTPs become inactivated under physiological conditions? Production of ROS either intracellularly [28] or by adjacent macrophages [34] influences mast cell activation. It has been shown that ROS produced by NADPH oxidase is crucial for phosphorylation of many substrates [linker of activated T cells (LAT), phospholipase (PLC)γ1 and (PLC)γ2], but NADPH oxidase alone is dependent on the activity of Src family kinases and PI3-kinase [28]. In one recent study, however, abrogation of FcεRI-dependent ROS production had no effect on degranulation or cytokine production [29]; this would suggest that antigen-induced conformational changes in FcεRI and resulting impaired access of PTPs to their substrates could be more important for enhanced FcεRI β and γ subunits phosphorylation than inhibition of enzymatic activity of the PTPs by ROS. Conformational changes in activated MIRRs have already been described [35,36]. It is possible that a similar change could lead to a shift in PTK–PTP steady state phosphorylation level of FcεRI after mast cells triggering. The combined data suggests, that non-activated mast cells possess preformed signaling assemblies containing immunoreceptors, and PTKs and PTPs which are in steady state. The binding of a multivalent antigen could cause a change in conformation of FcεRI which would be followed by a change in the steady state in favor of PTKs.

3. Topography of signaling molecules

Electron microscopy studies showed that most of the plasma membrane-bound molecules are associated with osmiophilic regions of the membrane [37]. Interestingly, molecules which were expected to be localized in lipid rafts, such as non-T cell activation linker (NTAL) and LAT, were localized individually or in small clusters and were not intermixed [38]. This suggests that lipid rafts, if they exist, are smaller than previously thought, and could be restricted to individual proteins or their clusters and surrounding lipids. Small size of signaling domains was documented in studies in which FcεRI dimers were capable of initiating signaling cascades without any dramatic changes in their redistribution in the plasma membrane [12,18]. Signalosomes of dimerized FcεRI persisted at the membrane longer than large aggregates formed by binding of multivalent antigen to IgE–FcεRI complexes. Thus, formation of large FcεRI aggregates is important for more potent removal of the membrane signalosomes at later stages of signaling.

Interesting data were obtained in studies analyzing the topography of membrane-bound PTPs. Antibody specific for oxidized phosphatases reacted mostly with cytoskeleton-like structures in non-activated mast cells [32]. Enhanced association of oxidized phosphatases with these structures was observed in cells activated by antigen and especially by pervanadate. The same structures were labeled with phalloidin (Fig. 3C–E), indicating that oxidized phosphatases are preferentially associated with actin cytoskeleton. These data suggest that actin cytoskeleton is involved in early signaling events by regulating the topography of phosphatases. Alternatively, actin could play a role in sequestering and/or scavenging irreversibly oxidized PTPs. In this connection it should be mentioned that actin probably plays a role in sequestering Lyn kinase to the periphery of large FcεRI aggregates which are consequently internalized [8].

Further studies showed that PTPs could also play a role in activation-induced tyrosine phosphorylation of the transmembrane adaptor protein NTAL and LAT, which in phosphorylated state serve as docking sites for molecules involved in FcεRI signaling [1]. Although both LAT and NTAL are detergent-resistant proteins, they exhibited enhanced colocalization with oxidized PTPs after FcεRI triggering and even more so after treatment with pervanadate (Fig. 4). Nevertheless, oxidized phosphatases have not been found in DRMs [32]. Similarly, Syk was detected in FcεRI clusters on plasma membrane sheets isolated from activated mast cells [8], in spite of the fact that only FcεRI, was associated with DRMs [39]. Moreover, experiments with disaggregated FcεRI clusters showed that the rate of their dephosphorylation was the same as that of other proteins [39]. These data indicate that proteins in DRMs are not protected from phosphatase activity and that even typical DRM proteins could be phosphorylated as proposed by the PTK–PTP interplay model.

4. Conclusions

We evaluated three models which have been proposed to explain the molecular mechanism whereby aggregation of the FcεRI initiates the first biochemically defined step in the antigen-mediated signaling in mast cells – tyrosine phosphorylation of the FcεRI β subunit by Lyn kinase. Although the transphosphorylation and lipid raft models are supported by numerous studies that are not limited to immunoreceptor signaling, they do not satisfactorily explain all activation events, such as tyrosine phosphorylation by ROS. This necessitated the introduction of PTK–PTP interplay model based on an assumption that PTKs and PTPs are in steady state in quiescent cells and activation disturbs this steady state in favor of kinases. Considering the fact that the turnover rate of active PTPs is 100- to 1000-times higher than that of PTKs [40], one can hypothesize that the PTK–PTP steady state in quiescent cell is set to override PTK, a process that could serve as a threshold of FcεRI signaling. Local ROS production or conformational changes of FcεRI leading to inactivation of the enzymatic activity of PTPs or their inaccessibility to the substrate could precede tyrosine phosphorylation of the FcεRI.

New approaches and methods are required to understand in detail the initiation of FcεRI phosphorylation and spatiotemporal coordination of the FcεRI signalosome formation. Better understanding of these events is expected from the introduction of new real-time methodologies with nanoscale resolution. Promising are approaches analyzing immunoreceptor signaling in cell-free systems with defined composition of lipid bilayers and properly accommodated signaling molecules. Genetic approaches will no doubt play a major role in deciphering signaling events in a complex cellular environment. Detailed analysis of properties of cells with knock-out of selected genes and restored with various mutant forms of the gene (knock-in approach) could still lead to the discovery of new players involved in initial stages of FcεRI signaling. These, in turn, could become targets for new drugs, and thus contribute to new rational approaches to therapy of mast cell mediated diseases.

Acknowledgements

This work was supported by Project 1M6837805001 (Center of Molecular and Cellular Immunology), LC-545, and a stipend to M.B. from Ministry of Education, Youth and Sports of the Czech Republic, Grants 204/05/H023, 301/09/1826 and P302/10/1759 from the Grant Agency of the Czech Republic, and Institutional project AVOZ50520514. M. B. was also supported by a specific Research Project No. 33779266 from Charles University, Prague.

References

[1] Kraft, S. and Kinet, J.P. (2007) New developments in FcεRI regulation, function and inhibition. Nat. Rev. Immunol. 7, 365–378.
[2] Pribluda, V.S., Pribluda, C. and Metzger, H. (1994) Transphosphorylation as the mechanism by which the high-affinity receptor for IgE is phosphorylated upon aggregation. Proc. Natl. Acad. Sci. USA 91, 11246–11250.
[3] Tamir, I. and Cambier, J.C. (1998) Antigen receptor signaling: integration of protein tyrosine kinase functions. Oncogene 17, 1353–1364.
[4] Yamashita, T., Mao, S.-Y. and Metzger, H. (1994) Aggregation of the high-affinity IgE receptor and enhanced activity of p53/p56^{lyn} protein-tyrosine kinase. Proc. Natl. Acad. Sci. USA 91, 11251–11255.
[5] Vonakis, B.M., Chen, H., Haleem-Smith, H. and Metzger, H. (1997) The unique domain as the site on Lyn kinase for its constitutive association with the high affinity receptor for IgE. J. Biol. Chem. 272, 24072–24080.
[6] Vonakis, B.M., Gibbons Jr., S.P., Rotté, M.J., Brothers, E.A., Kim, S.C., Chichester, K. and MacDonald, S.M. (2005) Regulation of rat basophilic leukemia-2H3 mast cell secretion by a constitutive Lyn kinase interaction with the high affinity IgE receptor (FcεRI). J. Immunol. 175, 4543–4554.
[7] Wofsy, C., Vonakis, B.M., Metzger, H. and Goldstein, B. (1999) One lyn molecule is sufficient to initiate phosphorylation of aggregated high-affinity IgE receptors. Proc. Natl. Acad. Sci. USA 96, 8615–8620.
[8] Wilson, B.S., Pfeiffer, J.R. and Oliver, J.M. (2000) Observing FcεRI signaling from the inside of the mast cell membrane. J. Cell Biol. 149, 1131–1142.
[9] Tolar, P., Dráberová, L., Tolarová, H. and Dráber, P. (2004) Positive and negative regulation of Fcε receptor I-mediated signaling events by Lyn kinase C-terminal tyrosine phosphorylation. Eur. J. Immunol. 34, 1136–1145.
[10] Sil, D., Lee, J.B., Luo, D., Holowka, D. and Baird, B. (2007) Trivalent ligands with rigid DNA spacers reveal structural requirements for IgE receptor signaling in RBL mast cells. ACS Chem. Biol. 2, 674–684.
[11] Ortega, E., Schweitzer-Stenner, R. and Pecht, I. (1988) Possible orientational constraints determine secretory signals induced by aggregation of IgE receptors on mast cells. EMBO J. 7, 4101–4109.
[12] Andrews, N.L., Pfeiffer, J.R., Martinez, A.M., Haaland, D.M., Davis, R.W., Kawakami, T., Oliver, J.M., Wilson, B.S. and Lidke, D.S. (2009) Small, mobile FcεRI receptor aggregates are signaling competent. Immunity 31, 469–479.
[13] Larson, D.R., Gosse, J.A., Holowka, D.A., Baird, B.A. and Webb, W.W. (2005) Temporally resolved interactions between antigen-stimulated IgE receptors and Lyn kinase on living cells. J. Cell Biol. 171, 527–536.
[14] Lin, S., Cicala, C., Scharenberg, A.M. and Kinet, J.P. (1996) The FcεRIβ subunit functions as an amplifier of FcεRIγ-mediated cell activation signals. Cell 85, 985–995.
[15] Eiseman, E. and Bolen, J.B. (1992) Signal transduction by the cytoplasmic domains of FcεRI-γ and TCR-ζ in rat basophilic leukemia cells. J. Biol. Chem. 267, 21027–21032.
[16] Brown, D.A. (2006) Lipid rafts, detergent-resistant membranes, and raft targeting signals. Physiology 21, 430–439.
[17] Field, K.A., Holowka, D. and Baird, B. (1997) Compartmentalized activation of the high affinity immunoglobulin E receptor within membrane domains. J. Biol. Chem. 272, 4276–4280.
[18] Dráberová, L., Lebduška, P., Hálová, I., Tolar, P., Štokrová, J., Tolarová, H., Korb, J. and Dráber, P. (2004) Signaling assemblies formed in mast cells activated via Fcε receptor I dimers. Eur. J. Immunol. 34, 2209–2219.
[19] Sheets, E.D., Holowka, D. and Baird, B. (1999) Critical role for cholesterol in Lyn-mediated tyrosine phosphorylation of FcεRI and their association with detergent-resistant membranes. J. Cell Biol. 145, 877–887.
[20] Surviladze, Z., Dráberová, L., Kovářová, M., Boubelík, M. and Dráber, P. (2001) Differential sensitivity to acute cholesterol lowering of activation mediated via the high-affinity IgE receptor and Thy-1 glycoprotein. Eur. J. Immunol. 31, 1–10.
[21] Kusumi, A. and Suzuki, K. (2005) Toward understanding the dynamics of membrane-raft-based molecular interactions. Biochim. Biophys. Acta 1746, 234–251.
[22] Davey, A.M., Krise, K.M., Sheets, E.D. and Heikal, A.A. (2008) Molecular perspective of antigen-mediated mast cell signaling. J. Biol. Chem. 283, 7117–7127.
[23] Kovářová, M., Tolar, P., Arudchandran, R., Dráberová, L., Rivera, J. and Dráber, P. (2001) Structure-function analysis of Lyn kinase association with lipid rafts and initiation of early signaling events after Fcε receptor I aggregation. Mol. Cell Biol. 21, 8318–8328.
[24] Wienands, J., Larbolette, O. and Reth, M. (1996) Evidence for a preformed transducer complex organized by the B cell antigen receptor. Proc. Natl. Acad. Sci. USA 93, 7865–7870.
[25] Heneberg, P. and Dráber, P. (2002) Nonreceptor protein tyrosine and lipid phosphatases in type I Fcε receptor-mediated activation of mast cells and basophils. Int. Arch. Allergy Immunol. 128, 253–263.
[26] Zhang, J., Mendoza, M., Guiraldelli, M.F., Barbu, E.A. and Siraganian, R.P. (2010) Small interfering RNA screen for phosphatases involved in IgE-mediated mast cell degranulation. J. Immunol. 184, 7178–7185.
[27] Denu, J.M. and Tanner, K.G. (1998) Specific and reversible inactivation of protein tyrosine phosphatases by hydrogen peroxide: evidence for a sulfenic acid intermediate and implications for redox regulation. Biochemistry 37, 5633–5642.
[28] Suzuki, Y., Yoshimaru, T., Matsui, T., Inoue, T., Niide, O., Nunomura, S. and Ra, C. (2003) FcεRI signaling of mast cells activates intracellular production of hydrogen peroxide: role in the regulation of calcium signals. J. Immunol. 171, 6119–6127.
[29] Swindle, E.J., Coleman, J.W., DeLeo, F.R. and Metcalfe, D.D. (2007) FcεRI- and Fcγ receptor-mediated production of reactive oxygen species by mast cells is lipoxygenase- and cyclooxygenase-dependent and NADPH oxidase-independent. J. Immunol. 179, 7059–7071.
[30] Barrett, W.C., DeGnore, J.P., König, S., Fales, H.M., Keng, Y.F., Zhang, Z.Y., Yim, M.B. and Chock, P.B. (1999) Regulation of PTP1B via glutathionylation of the active site cysteine 215. Biochemistry 38, 6699–6705.
[31] Teshima, R., Ikebuchi, H., Nakanishi, M. and Sawada, J. (1994) Stimulatory effect of pervanadate on calcium signals and histamine secretion of RBL-2H3 cells. Biochem. J. 302, 867–874.
[32] Heneberg, P., Dráberová, L., Bambousková, M., Pompach, P. and Dráber, P. (2010) Down-regulation of protein tyrosine phosphatases activates an immune receptor in the absence of its translocation into lipid rafts. J. Biol. Chem. 285, 12787–12802.
[33] Kimura, T., Zhang, J., Sagawa, K., Sakaguchi, K., Appella, E. and Siraganian, R.P. (1997) Syk-independent tyrosine phosphorylation and association of the protein tyrosine phosphatases SHP-1 and SHP-2 with the high affinity IgE receptor. J. Immunol. 159, 4426–4434.
[34] Swindle, E.J., Hunt, J.A. and Coleman, J.W. (2002) A comparison of reactive oxygen species generation by rat peritoneal macrophages and mast cells using the highly sensitive real-time chemiluminescent probe pholasin: inhibition of antigen-induced mast cell degranulation by macrophage-derived hydrogen peroxide. J. Immunol. 169, 5866–5873.
[35] Gil, D., Schamel, W.W., Montoya, M., Sánchez-Madrid, F. and Alarcón, B. (2002) Recruitment of Nck by CD3ε reveals a ligand-induced conformational change essential for T cell receptor signaling and synapse formation. Cell 109, 901–912.
[36] Tolar, P., Hanna, J., Krueger, P.D. and Pierce, S.K. (2009) The constant region of the membrane immunoglobulin mediates B cell-receptor clustering and signaling in response to membrane antigens. Immunity 30, 44–55.
[37] Lillemeier, B.F., Pfeiffer, J.R., Surviladze, Z., Wilson, B.S. and Davis, M.M. (2006) Plasma membrane-associated proteins are clustered into islands attached to the cytoskeleton. Proc. Natl. Acad. Sci USA 103, 18992–18997.
[38] Volná, P., Lebduška, P., Dráberová, L., Šímová, S., Heneberg, P., Boubelík, M., Bugajev, V., Malissen, B., Wilson, B.S., Hořejší, V., Malissen, M. and Dráber, P. (2004) Negative regulation of mast cell signaling and function by the adaptor LAB/NTAL. J. Exp. Med. 200, 1001–1013.
[39] Peirce, M. and Metzger, H. (2000) Detergent-resistant microdomains offer no refuge for proteins phosphorylated by the IgE receptor. J. Biol. Chem. 275, 34976–34982.
[40] Reth, M. (2002) Hydrogen peroxide as second messenger in lymphocyte activation. Nat. Immunol. 3, 1129–1134.

1.4 CROSS-TALK BETWEEN TETRASPANIN CD9 AND TRANSMEMBRANE ADAPTOR PROTEIN NON-T-CELL ACTIVATION LINKER (NTAL) IN MAST CELL ACTIVATION AND CHEMOTAXIS

J Biol Chem. 288(14):9801-14, 2013.

In attempts to identify new plasma membrane molecules affecting mast cell activation we generated new Ab recognizing mast cell surface Ag identified as CD9. We found that pretreatment of mast cells with CD9-specific Ab triggered activation events as phosphorylation of some key signaling proteins, calcium flux and dephosphorylation of ezrin, radexin, moesin (ERM) family proteins that is important step facilitating mast cell chemotaxis. After CD9 aggregation, NTAL but not LAT showed increased phosphorylation of tyrosine residues. Ultrasctructural analysis of CD9 topography in plasma membrane showed that upon activation, CD9 colocalized with NTAL but not LAT. The combined data helped to dentify different roles of LAT and NTAL in mast cell activation and chemotaxis.

THE JOURNAL OF BIOLOGICAL CHEMISTRY VOL. 288, NO. 14, pp. 9801–9814, April 5, 2013

Cross-talk between Tetraspanin CD9 and Transmembrane Adaptor Protein Non-T Cell Activation Linker (NTAL) in Mast Cell Activation and Chemotaxis*

Received for publication, December 27, 2012, and in revised form, February 21, 2013 Published, JBC Papers in Press, February 26, 2013, DOI 10.1074/jbc.M112.449231

Ivana Hálová, Lubica Dráberová, Monika Bambousková[1], Martin Machyna[2], Lucie Stegurová[1], Daniel Smrž[3], and Petr Dráber[4]

From the Department of Signal Transduction, Institute of Molecular Genetics, Academy of Sciences of the Czech Republic, CZ 14220 Prague, Czech Republic

Background: Chemotaxis is regulated by chemoattractants and poorly understood intrinsic regulators.
Results: Aggregation of tetraspanin CD9 leads to activation of mast cells and inhibition of their antigen-driven chemotaxis.
Conclusion: Chemotaxis toward antigen involves cross-talk between immunoreceptor, CD9, transmembrane adaptor proteins, and cytoskeleton-regulatory proteins.
Significance: Tetraspanin CD9 is defined as a novel regulator of mast cell chemotaxis.

Chemotaxis, a process leading to movement of cells toward increasing concentrations of chemoattractants, is essential, among others, for recruitment of mast cells within target tissues where they play an important role in innate and adaptive immunity. Chemotaxis is driven by chemoattractants, produced by various cell types, as well as by intrinsic cellular regulators, which are poorly understood. In this study we prepared a new mAb specific for the tetraspanin CD9. Binding of the antibody to bone marrow-derived mast cells triggered activation events that included cell degranulation, Ca^{2+} response, dephosphorylation of ezrin/radixin/moesin (ERM) family proteins, and potent tyrosine phosphorylation of the non-T cell activation linker (NTAL) but only weak phosphorylation of the linker for activation of T cells (LAT). Phosphorylation of the NTAL was observed with whole antibody but not with its $F(ab)_2$ or Fab fragments. This indicated involvement of the Fcγ receptors. As documented by electron microscopy of isolated plasma membrane sheets, CD9 colocalized with the high-affinity IgE receptor (FcεRI) and NTAL but not with LAT. Further tests showed that both anti-CD9 antibody and its $F(ab)_2$ fragment inhibited mast cell chemotaxis toward antigen. Experiments with bone marrow-derived mast cells deficient in NTAL and/or LAT revealed different roles of these two adaptors in antigen-driven chemotaxis. The combined data indicate that chemotaxis toward antigen is controlled in mast cells by a cross-talk among FcεRI, tetraspanin CD9, transmembrane adaptor proteins NTAL and LAT, and cytoskeleton-regulatory proteins of the ERM family.

Mast cells are derived from progenitors that are released from bone marrow into circulation, and subsequently migrate to peripheral tissues where they undergo differentiation and maturation (1). The process plays a vital role in innate and/or adaptive immune response and is controlled by a plethora of different chemoattractants, which require sophisticated mechanisms for their recognition and proper cellular responses (2–4). It is obvious that such mechanisms must involve efficient cross-talk between surface receptors, plasma membrane component organizers, such as tetraspanin, signal transducers, cytoskeletal effectors, and others. Signal transduction mediated by two important mast cell receptors, the high-affinity IgE receptor (FcεRI)[5] and the stem cell factor (SCF) receptor (KIT), is dependent on the presence of two transmembrane adaptor proteins (TRAPs), the linker for activated T cells (LAT) and the non-T cell activation linker (NTAL, also called LAB or LAT2) (5–8). Both adaptors are structurally similar and serve as plasma membrane docking sites for cytoplasmic signal transduction molecules. TRAPs are characterized by a short extracellular domain, a single transmembrane domain, and a cytoplasmic tail, which has no intrinsic enzymatic activity but possesses various tyrosine-containing motifs and domains. The properties of transmembrane domains and the presence of palmitoylation sites determine the solubility of LAT and NTAL in non-ionic detergents, distribution in the plasma membrane, and some other functional properties (9–11). Despite their

* This work was supported in part by the Projects 301/09/1826, P302/10/1759 and P302/12/G101, 204/09/H084 from Grant Agency of the Czech Republic, Action BM1007 from the European Cooperation in Science and Technology. Project LD12073 COST-CZ-MAST, Project TA01010436 of the Technology Agency of the Czech Republic, Project FR-TI3/067 of the Ministry of Industry and Trade of the Czech Republic, and Institutional Support Grant RVO 68378050.
[1] Supported in part by the Faculty of Science, Charles University, Prague, Czech Republic.
[2] Present address: Max Planck Institute of Molecular Cell Biology and Genetics, Dresden, Germany.
[3] Present address: Institute of Immunology, 2nd Medical School and University Hospital Motol, Charles University, V Úvalu 84, Prague, Czech Republic.
[4] To whom correspondence should be addressed: Laboratory of Signal Transduction, Institute of Molecular Genetics, Academy of Sciences of the Czech Republic, Vídeňská 1083, CZ-14220 Prague 4, Czech Republic. Tel.: 420-241062468; Fax: 420-241062214; E-mail: draberpe@img.cas.cz.

[5] The abbreviations used are: FcεRI, high-affinity IgE receptor; SCF, stem cell factor; TRAP, transmembrane adaptor protein; LAT, linker for activation of T cells; NTAL, non-T cell activation linker; KD, knockdown; BMMC, bone marrow-derived mast cell; Ag, antigen; ERM, ezrin/radixin/moesin; TNP, 2,4,6-trinitrophenol; 2KO, $Ntal^{-/-}/Lat^{-/-}$ double KO; BSS, buffered saline solution; BSSA, BSS supplemented with 0.1% BSA; $[Ca^{2+}]_i$, concentrations of intracellular Ca^{2+}; 2-PCCF, pair cross-correlation function; F-actin, filamentous actin.

structural similarity, NTAL and LAT were found in different microdomains in plasma membrane (5, 11). Studies with mast cells generated from NTAL or LAT KO mice (5, 6), human mast cells with NTAL knockdown (KD) (7), or rat basophilic leukemia cells with enhanced or reduced NTAL levels (12) showed that NTAL could act either as positive or negative regulator of FcεRI signaling, whereas LAT acts as positive regulator (4, 13). Although the role of these two adaptors in immunoreceptor signaling has been extensively studied, their function in mast cell migration is not fully understood. We have previously shown that NTAL serves as a negative regulator of bone marrow-derived mast cells (BMMCs) migration toward antigen (Ag) but has no apparent role in migration toward SCF (14). However, the role of LAT ablation either alone or together with NTAL on Ag-mediated chemotactic response is unknown.

Tetraspanins, similarly as TRAPs, have no enzymatic activity and regulate signaling events by cross-talk with other plasma membrane-associated protein molecules, including integrins (15–21), G-protein-coupled receptors (21–23), several immunoglobulin superfamily members (24, 25), and PKC (26). Although tetraspanins are involved in a variety of biological and pathological processes (27, 28), it is not clear whether tetraspanins interact with TRAPs and what are consequences of such interactions.

In this study we aggregated tetraspanin CD9 on the surface of mast cells and investigated signaling events elicited by such treatment. We also analyzed the effect of CD9 aggregation on cell activation events induced by Ag-mediated aggregation of the FcεRI, including degranulation, calcium response, phosphorylation of cytoskeleton-regulatory proteins of the ezrin/radixin/moesin (ERM) family, and chemotaxis. Using mast cells derived from NTAL- and/or LAT-deficient mice we studied a cross-talk of these adaptors with CD9 and its impact on mast cell chemotaxis. Finally, we investigated the role of CD9 in activation through the FcεRI and membrane topography of CD9 with respect to NTAL, LAT, and FcεRI. Our data indicate that chemotaxis toward Ag in mast cells is regulated by a cross-talk among CD9, FcεRI, TRAPs, and cytoskeleton-regulatory ERM family proteins.

EXPERIMENTAL PROCEDURES

Antibodies and Reagents—Anti-CD9 mAb (clone 2H9, IgG_1 type) was generated by immunizing a rat (Wistar strain) with BMMCs permeabilized with 0.1% saponin and washed. Hybridoma production and mAb selection was done as described previously (29) with the exception that rat spleen cells instead of mouse spleen cells were used. Specificity of the 2H9 antibody was verified by immunoprecipitation followed by mass spectrometry analysis as described (30) and by cross-immunoprecipitation using commercially available anti-CD9 antibody (KMC8.8, Santa Cruz Biotechnology, Inc.). Isotyping was performed with the IsoStrip Isotyping kit (Roche Diagnostics) following the manufacturer's protocol. $F(ab)_2$ and Fab fragments of the 2H9 antibody were generated using, respectively, $F(ab)_2$ and Fab Preparation Kits (Pierce) according to the manufacturer's protocol. Functionality of both types of the fragments was verified by FACS analysis and SDS-PAGE electrophoresis.

The following mAbs were used: 2,4,6-trinitrophenol (TNP)-specific IgE, clone IGEL b4 1 (31), anti-FcεRI β-subunit (JRK) (32), anti-NTAL (NAP-07) (33), anti-LAT (34), anti-Lyn (35), and anti-CD16/CD32 (2.4G2; directed against extracellular domains of mouse receptors FcγRIIB and FcγRIII; a gift from V. Horejsi). Polyclonal antibodies specific for LAT, NTAL, and IgE have been prepared in this laboratory after immunizing rabbits with the corresponding recombinant proteins or their fragments (36). Polyclonal antibodies specific for phospho-ERK (phospho-Y^{204}), phospho-Akt (phospho-S^{473}), phospho-c-Kit (phospho-$Y^{568/570}$), anti-integrin β1 (CD29), as well as HRP-conjugated goat anti-mouse IgG, and goat anti-rabbit IgG were obtained from Santa Cruz Biotechnology, Inc.; antibodies against phospho-p38 (Y^{182}/T^{180}; $pp38^{Y/T}$), phospho-Ezrin (T^{567})/Radixin (T^{564})/Moesin (T^{558}) ($pERM^{T}$), phospho-Syk (Y^{525}/Y^{526}; $pSyk^{Y}$), phospho-Akt (T^{308}; $pAkt^{T}$), and HRP-conjugated goat anti-rat IgG were obtained from Cell Signaling. Phospho-Tyr-specific mAb (PY-20) conjugated to HRP, anti-CD9 (KMC8), and anti-integrin β1 (HM β1–1) were purchased from BD Biosciences. Anti-mouse FcεRI-FITC conjugate and anti-mouse CD117 (KIT)-APC conjugate were obtained from eBioscience; anti-mouse integrin β1-FITC was from Millipore. Recombinant mouse IL-16 was obtained from Prospec. All other chemicals were obtained from Sigma.

Cells and Lentiviral Infection—BMMCs were derived from C57BL.6 mice of WT ($Ntal^{+/+}$ or $Lat^{+/+}$) or from $Ntal^{-/-}$, $Lat^{-/-}$ or $Ntal^{-/-}/Lat^{-/-}$ double KO (2KO) mice (5). In some experiments, Balb/c mice were also used as indicated in the text. All work with animals was conducted in accordance with institutional (33/2008) and national (2048/2004–1020) guidelines. Bone marrow cells were isolated and cultured as previously described (5). BMMCs deficient in Lyn ($Lyn^{-/-}$) and their WT controls ($Lyn^{+/+}$) were kindly provided by M. Hibbs (Ludwig Institute for Cancer Research, Melbourne, Australia) (37). HEK 293 T/17 packaging cells were purchased from American Type Culture Collection. The cells were grown as adherent monolayer culture in DMEM containing 10% FCS, 100 units/ml of penicillin, and 100 μg/ml of streptomycin. Cultures were passaged regularly every 4–5 days and kept at 37 °C in an atmosphere of 5% CO_2. The cells used for lentivirus production were at passage 4–15. Lentiviral infection was done as described previously (38). A set of murine CD9 shRNAs cloned into the pLKO.1 vector (TRCN0000066393, TRCN0000066394, TRCN0000066395, TRCN0000066396, and TRCN0000066397) were purchased from Open Biosystems. Stable selection was achieved by culturing the transfected cells for 2 weeks in the presence of puromycin (5 μg/ml). Cells were analyzed for CD9 expression by immunoblotting and FACS. Cells with the highest reduction of CD9 protein, obtained with TRCN0000066393 and TRCN0000066395, were selected for further experiments. Cells transfected with empty pLKO.1 vector were used as negative controls.

β-Glucuronidase Release, Ca^{2+} Response, Protein Phosphorylation, and Immunoprecipitation—BMMCs were sensitized in SCF- and IL-3-free culture medium supplemented with IGEL b4 1 mAb (1 μg/ml) for 16 h, unless stated otherwise. Then the cells were washed in buffered saline solution (BSS) supplemented with 0.1% BSA (BSSA), and activated with Ag (TNP-

BSA conjugate, 15–25 mol of TNP/mol of BSA; 100–500 ng/ml, depending on batch), SCF (20–100 ng/ml, depending on batch), or anti-CD9 (0.04–20 μg/ml) at concentrations and times giving maximum degranulation or protein phosphorylation, respectively. For inhibition experiments cells were pretreated with different concentrations of anti-CD9 mAb for 15 min. The extent of secretion was determined by determining the concentration of β-glucuronidase as described previously (39) except that the Infinite 200M (TECAN) plate reader instrument at excitation and emission wavelengths of 355 and 460 nm, respectively, was used. Cells used in calcium response assays were loaded with Fura-2AM as described previously (40) and changes in concentrations of intracellular Ca^{2+} ($[Ca^{2+}]_i$) were determined by spectrofluorometry as the changes in ratios of emissions at 510 nm when the cells were excited at 340 and 380 nm; selected cell activators were added automatically using the injector system (TECAN).

Protein phosphorylation was analyzed by immunoblotting of size-fractionated cell lysates. Cells were centrifuged and resuspended in sample buffer containing 10% SDS with or without 2-mercaptoethanol (2-ME) and then sonicated (3 × 10 s), resolved by SDS-PAGE, and immunoblotted with PY-20-HRP conjugate or with protein-specific antibodies followed by the corresponding secondary antibodies: HRP-conjugated anti-mouse, anti-rat, or anti-rabbit IgG. HRP signal was detected by the ECL reagent (Amersham Biosciences) and quantified by Luminescent Image Analyzer LAS 3000 (Fuji Photo Film Co.). Aida software (Raytest GmbH) was used for analysis.

For immunoprecipitation, postnuclear supernatants were prepared from 10–50 × 10^6 cells lysed in ice-cold lysis buffer (40) supplemented with 1% Nonidet P-40 and 1% *n*-dodecyl-β-D-maltoside (for LAT and NTAL immunoprecipitation), 1% CHAPS (for CD9 immunoprecipitation), or 0.2% Triton X-100 (for FcεRI immunoprecipitation). Target proteins were immunoprecipitated with appropriate antibodies attached to protein A/G PLUS-agarose (Santa Cruz) or Protein A UltraLink Resin (ThermoScientific).

Flow Cytometry Analysis—To quantify surface expression of CD9, BMMCs (3 × 10^5/ml) were exposed for 30 min on ice to 1–10 μg/ml of anti-CD9 followed by a 30-min incubation with FITC-conjugated anti-rat antibody. For detection of other membrane proteins, the cells were directly labeled with anti-mouse FcεRI-FITC, anti-mouse CD117-APC, or anti-mouse integrin β1-FITC conjugate. After a 30-min incubation on ice the cells were washed in ice-cold PBS and evaluated with LSRII flow cytometer (BD Biosciences). Median fluorescence intensities were determined in the FITC or APC channel and further processed using FlowJo software (Ashland, OR). For inhibition experiments, cells were pretreated with anti-CD9 mAb (10 μg/ml) for 15 min.

Chemotactic Response—Chemotactic responses were assayed using 24-well Transwell chambers (Corning) with 8-μm polycarbonate filters in the upper wells. Chemoattractants were added to the lower wells in 0.6 ml of chemotactic medium (RPMI 1640 supplemented with 1% BSA and 20 mM HEPES, pH 7.4). BMMCs (0.3 × 10^6 cells in 120 μl of chemotactic media) were added into each upper well. In experiments with Ag-mediated chemotaxis the cells were sensitized with IgE before the assay. Cells migrating into lower wells within the 8-h incubation period (37 °C, 5% CO_2 in air) were counted using Accuri C6 Flow Cytometer (BD Biosciences).

Electron Microscopy of Immunogold-labeled Membrane Sheets—Ultraclean glass coverslips (15 mm in diameter) were prepared as previously described (11). The coverslips in 24-well plates were coated by overnight incubation at 4 °C with fibronectin (50 μg/ml in PBS), followed by washing with distilled water, and used immediately. BMMCs (1.5 × 10^6) were washed twice with BSSA and then incubated on fibronectin-coated glass coverslips. After 1 h the cells were washed with BSSA and incubated with anti-CD9 antibody (15 μg/ml) in BSSA at room temperature. After 10 min the cells were washed 3 times in PBS and subsequently incubated with the secondary antibody conjugated with 12-nm gold particles. Alternatively, the cells were prefixed in 2% paraformaldehyde for 7 min, washed 3 times in PBS, and immersed in ice-cold HEPES buffer (25 mM HEPES, pH 7.0, 25 mM KCl, 2.5 mM magnesium acetate). Plasma membrane sheets were isolated and fixed in 2% paraformaldehyde in HEPES buffer for 10 min. After fixation, electron microscopy grids were transferred to PBS and target epitopes located on the cytoplasmic side of the plasma membrane were labeled with specific primary antibodies in 0.1% BSA in PBS (rabbit anti-NTAL, 1:200; rabbit anti-LAT, 1:200; mouse anti-FcεRI-β subunit mAb, clone JKR, 4 μg/ml) washed 4 times and subsequently labeled with goat anti-rabbit or anti-mouse secondary antibodies conjugated to gold nanoparticles. After extensive washing the membrane sheets were fixed in 2.5% glutaraldehyde in PBS for 10 min and the grids were transferred to PBS. After 10 min the membranes were stained with 1% OsO_4 in PBS, washed three times for 5 min in water, incubated for 10 min with 1% aqueous tannic acid, washed again in water, and stained for 10 min with 1% aqueous uranyl acetate. Finally, samples were washed twice with water for 5 min, air-dried, and observed with FEI Morgagni 268 electron microscope (FEI Czech Republic) operating at 80 kV. Typically, 10 micrographs covering 22.2 μm^2 of the cell surface were obtained from each grid; at least three independent experiments were made for each condition tested. The coordinates of gold particles were determined by ImageJ (National Institutes of Health). Statistical evaluation of colocalization of two types of particles was based on the program Gold using pair cross-correlation function (PCCF) (41).

Cell Adhesion and Spreading—IgE-sensitized BMMCs were loaded with Calcein-AM and incubated or not with anti-CD9 mAb (10 μg/ml) and/or anti-β1 integrin antibody (20 μg/ml) for 15 min before their transfer into fibronectin-coated wells. Cell adhesion was determined after a 30-min activation of the cells with Ag (50 ng/ml of TNP-BSA) using a TECAN fluorometer with excitation at 485 nm and emission at 538 nm. For cell spreading, wells of 96-well glass-bottom plates (InVitroSci) were coated with 50 μl of fibronectin in PBS (50 μg/ml). After 1 h at 22 °C the wells were washed with PBS, and 30 × 10^3 cells in BSSA were added into each well. Cells were allowed to attach for 30 min at 37 °C, gently washed, and then activated or not with Ag. After 20 min the cells were fixed for 30 min at room temperature with 3% paraformaldehyde in PBS. For filamentous (F)-actin staining, the cells were washed with 50 mM gly-

cine in PBS and then exposed to Alexa Fluor 488-phalloidin conjugate diluted 1:100 in PBS supplemented with L-α-lysophosphatidylcholine (120 μg/ml). After 1 h, the cells were washed in PBS, fixed, and kept in PBS supplemented with Hoechst 33258 stain. They were then examined with the Olympus Scan® system. Image processing and analysis were completed by means of CellProfiler software (Broad Institute, Boston, MA) (42).

Statistical Analysis—Unless specified otherwise, the significance of intergroup differences was evaluated by Student's *t* test.

RESULTS

Aggregation of CD9 Causes Activation of Mast Cells and Tyrosine Phosphorylation of NTAL but Not LAT—In an attempt to contribute to elucidating the role of membrane glycoproteins in mast cell signaling and chemotaxis we studied the properties of a new mAb prepared after immunization of a rat with cellular ghosts obtained after permeabilization of BMMCs with saponin. Previously we (30, 35, 40) and others (43, 44) showed that such ghosts are deprived of soluble cytoplasmic proteins, but possess plasma membrane proteins, cytoskeletal proteins, and nucleus. One of the mAbs prepared against such ghosts, the 2H9, was found to bind to the plasma membrane target (see below) and activate mast cells in a manner different from that known for other mast cell activators, the SCF and IgE-Ag complexes. When BMMCs were exposed to the 2H9 mAb, an increased degranulation (Fig. 1*A*) and calcium response (Fig. 1*B*) were noticed. The responses were comparable with those induced by SCF and lower than those observed in cells activated by Ag. The 2H9 mAb-induced tyrosine phosphorylation of several protein substrates in whole cell lysates was determined by immunoblotting with PY-20-HRP conjugate (Fig. 1*C*). The phosphorylation profile was, however, different from that induced by SCF or Ag (Fig. 1*C*). To identify the proteins that are phosphorylated in cells activated by 2H9 we analyzed several signaling targets using phosphospecific antibodies. For comparison we also quantified the extent of phosphorylation in cells activated by SCF and Ag. Data presented in Fig. 1*D* show that binding of 2H9 mAb had no effect on phosphorylation of Akt on Thr^{308} or Ser^{473}, and induced a weak phosphorylation of ERK and p38. Tyrosine phosphorylation profile of the whole cell lysate (Fig. 1*C*) suggested that NTAL (25–30 kDa) and LAT (36–38 kDa) could be among the proteins phosphorylated in 2H9-activated cells. To verify this, NTAL and LAT were immunoprecipitated from nonactivated or activated cells and tyrosine phosphorylation was determined using PY-20-HRP conjugate. Data in Fig. 1*E* show that tyrosine phosphorylation of NTAL in 2H9-activated cells was more pronounced than in SCF-activated cells but weaker than in Ag-activated cells. Similar analysis of LAT immunoprecipitates showed that 2H9 triggering caused only a weak LAT phosphorylation, comparable with that observed in SCF-activated cells. This was in sharp contrast to Ag-induced activation, which induced a strong phosphorylation of LAT.

Next, we attempted to identify which kinases are involved in NTAL phosphorylation in 2H9-activated cells. Previous studies showed that NTAL in Ag-activated mast cells is phosphory-

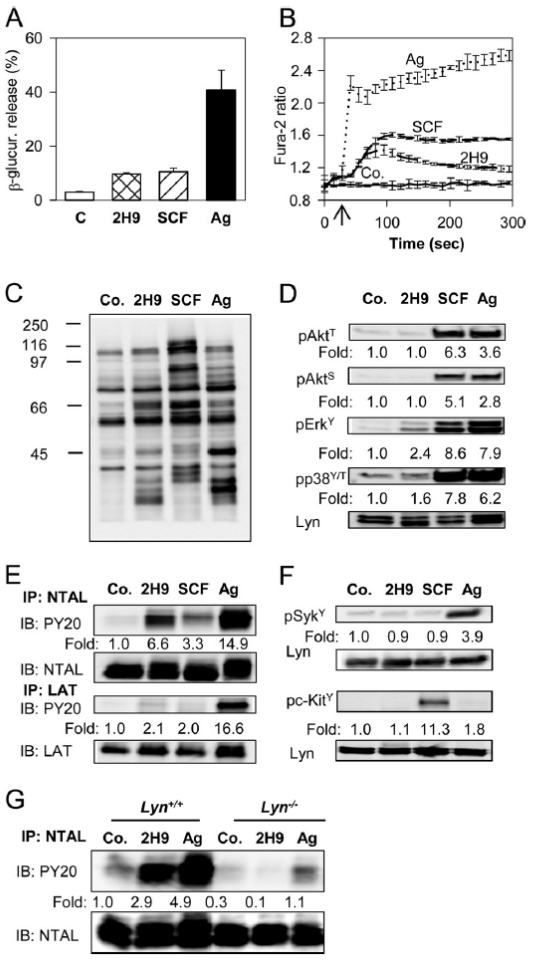

FIGURE 1. **Activation events in mast cells caused by 2H9 mAb.** BMMCs derived from WT C57BL.6 mice were sensitized overnight with TNP-specific IgE. *A*, the cells were exposed to BSSA (nonactivated control, *C*) or activated with 2H9 mAb (10 μg/ml), SCF (100 ng/ml), or Ag (500 ng/ml TNP-BSA) for 30 min. β-Glucuronidase released into supernatant was determined as described under "Experimental Procedures." Mean ± S.D. were calculated from 3 independent experiments performed in triplicates. *B*, IgE-sensitized BMMCs were loaded with Fura-2AM and exposed (*arrow*) to BSSA (*Co.*), 2H9 mAb (10 μg/ml), SCF (100 ng/ml), or Ag (500 ng/ml of TNP-BSA). Changes in $[Ca^{2+}]_i$ were determined by spectrofluorometry as the ratio of emissions at 510 nm when the cells were excited at 340 and 380 nm. *C*, *D*, and *F*, IgE-sensitized BMMCs were exposed to BSSA (*Co.*) or activated for 3 min with 2H9 mAb (1 μg/ml), SCF (100 ng/ml), or Ag (100 ng/ml TNP-BSA). Whole cell lysates were fractionated by SDS-PAGE and analyzed by immunoblotting with phosphotyrosine-specific mAb PY-20-HRP conjugate (*C*), antibodies specific for the indicated phosphotyrosines, pAkt-T^{308} ($pAkt^T$), pAkt-S^{473} ($pAkt^S$), pErk-Y^{204} ($pErk^Y$), and pp38-Y^{182}/T^{180} ($pp38^{Y/T}$) (*D*), or antibodies specific for pSyk-$Y^{525/526}$ ($pSyk^Y$), or pc-Kit-$Y^{568/570}$ ($pc\text{-}Kit^Y$) (*F*). In *D and F*, anti-Lyn mAb (*Lyn*) was used as a loading control. *E* and *G*, IgE-sensitized BMMCs derived from C57BL.6 mice (*E*) or $Lyn^{+/+}$ or $Lyn^{-/-}$ (*G*) were nonactivated (*Co.*) or activated with 2H9 mAb, SCF (*E* only), or Ag as above. The cells were solubilized in lysis buffer containing 1% Nonidet P-40 and 1% *n*-dodecyl-β-D-maltoside and postnuclear supernatants were immunoprecipitated (*IP*) with NTAL- or LAT-specific rabbit antibodies immobilized on protein A. The immunoprecipitates were analyzed by immunoblotting (*IB*) with phosphotyrosine-specific PY-20-HRP conjugate (PY20). Protein loading was determined by LAT- or NTAL-specific mAbs. In *D-G*, fold-increase in protein phosphorylation normalized to phosphorylation in nonactivated cells and protein loading is also shown. Typical results from at least 4 experiments performed are shown.

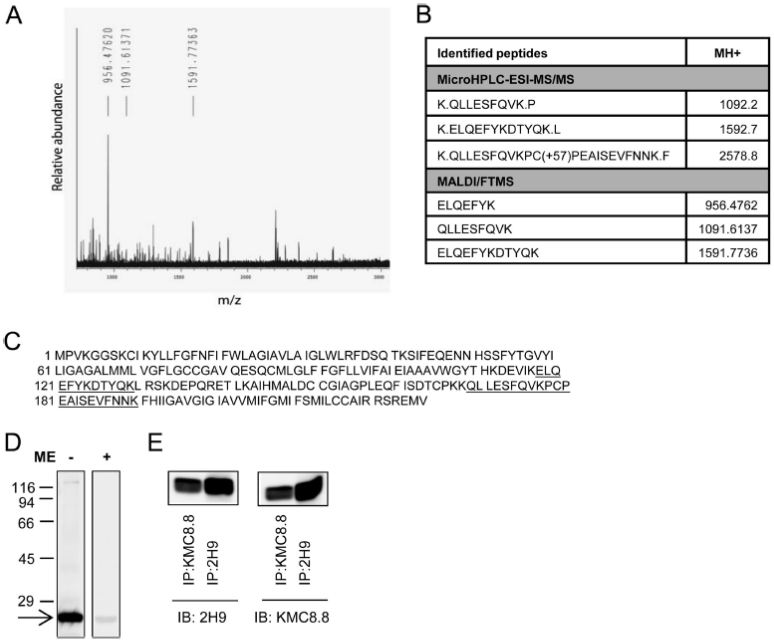

Identified peptides	MH+
MicroHPLC-ESI-MS/MS	
K.QLLESFQVK.P	1092.2
K.ELQEFYKDTYQK.L	1592.7
K.QLLESFQVKPC(+57)PEAISEVFNNK.F	2578.8
MALDI/FTMS	
ELQEFYK	956.4762
QLLESFQVK	1091.6137
ELQEFYKDTYQK	1591.7736

FIGURE 2. **Identification of CD9 as the target protein of 2H9 mAb.** 2H9 mAb covalently bound to protein G resin by dimethylpimelimidate was used to pulldown the target Ag from postnuclear supernatant of BMMCs lysed in a lysis buffer containing 1% Triton X-100. Bound material was eluted from the resin by SDS-PAGE sample buffer, size-fractionated on 12% SDS-PAGE, and stained with Coomassie Brilliant Blue. The major band was excised and analyzed with HPLC in combination with electrospray ionization tandem mass spectrometry (*microHPLC-ESI-MS/MS*) and MALDI-Fourier transform mass spectrometry (*MALDI/FTMS*). *A*, the chart represents the spectrum of detected peptides from trypsin-digested immunoprecipitated protein. Masses of identified peptides (*MH+*) and their corresponding peaks are indicated. *B*, table shows sequences identified by MS analysis with mass of their appropriate MH^+ ions. *C*, positions of the identified sequences (*underlined*) in the whole CD9 protein (NCBI Reference Sequence NP_031683.1). *D*, lysates from BMMCs were diluted with SDS-PAGE sample buffer supplemented with (+) or without (−) 2-mercaptoethanol (*ME*), size fractionated by SDS-PAGE, and analyzed by immunoblotting with 2H9 mAb followed by anti-rat IgG HRP conjugate. The *arrow* indicates the migration of the 2H9 target protein and *numbers on the left* represent the position of the molecular mass markers in kDa. *E*, BMMCs were lysed as in *A* and postnuclear supernatants were immunoprecipitated (*IP*) with 2H9 or KMC8.8 antibodies immobilized to protein G resin. Material released from the resin was fractionated on a 12% SDS-PAGE gel and analyzed by immunoblotting (*IB*) with 2H9 or KMC8.8 Abs. The data presented in *D* and *E* are typical results from at least 3 experiments performed.

lated by the Src family kinase Lyn, Syk kinase, and/or by KIT (45). Proper kinase activity of Syk and KIT is associated with their increased tyrosine phosphorylation (46, 47); we therefore first analyzed changes in phosphorylation of Syk and KIT. We found that these two kinases do not exhibit enhanced phosphorylation after 2H9 treatment (Fig. 1*F*). Control experiments showed, as expected, that Syk and KIT were phosphorylated in cells activated by Ag or SCF, respectively. To determine whether Lyn kinase is involved in 2H9-induced NTAL phosphorylation, NTAL was immunoprecipitated from BMMCs derived from $Lyn^{-/-}$ mice or WT ($Lyn^{+/+}$) mice. Data in Fig. 1*G* show that the absence of Lyn caused no increase in NTAL phosphorylation in 2H9-treated cells. The data suggest that Lyn is the kinase required for phosphorylation of NTAL after exposure of the cells to 2H9 mAb.

To identify the target recognized by the 2H9 mAb, we immunoprecipitated the target Ag from the lysate of resting BMMCs. The isolated material was digested with trypsin and analyzed by peptide mass mapping and peptide sequencing. Both analyses showed that 2H9 mAb binds to mouse CD9 (Fig. 2, *A-C*). The identity of the target was confirmed by decreased binding of the antibody to the cells with decreased expression of CD9 (see below). Furthermore, as determined by immunoblotting experiments, 2H9 mAb recognized a protein with a molecular mass of 22 kDa, corresponding to CD9; only unreduced samples were reactive (Fig. 2*D*). Finally, CD9 immunoprecipitated with commercially available CD9-specific antibody (KMC8.8) reacted by immunoblotting with 2H9 and vice versa (Fig. 2*E*). The combined data indicate that binding of anti-CD9 2H9 mAb induces mast cell signaling events that are different from those induced by Ag or SCF.

CD9 Colocalizes with NTAL—Previous studies showed that despite their similarity in structure and resistance to solubilization in nonionic detergents, NTAL and LAT occupy different membrane microdomains (5, 11). Tetraspanins are known to be present in both raft and nonraft regions of the plasma membrane and therefore it was of interest to determine whether CD9 colocalizes with NTAL and/or LAT. For co-localization experiments we used plasma membrane sheets isolated from BMMCs and probed them with immunogold labeling on the cytoplasmic (NTAL and LAT) or extracellular (CD9) side. Plasma membrane sheets isolated from BMMCs were fixed (i) before anti-CD9 (2H9) mAb exposure, (ii) 5 min after incubation with 2H9 mAb at 37 °C to induced CD9 dimerization, or (iii) after extensive aggregation of CD9–2H9 complexes with secondary anti-rat antibody (Fig. 3). As inferred from representative figures and PCCF analysis, NTAL exhibited some colocalization with CD9 in membranes obtained from cells

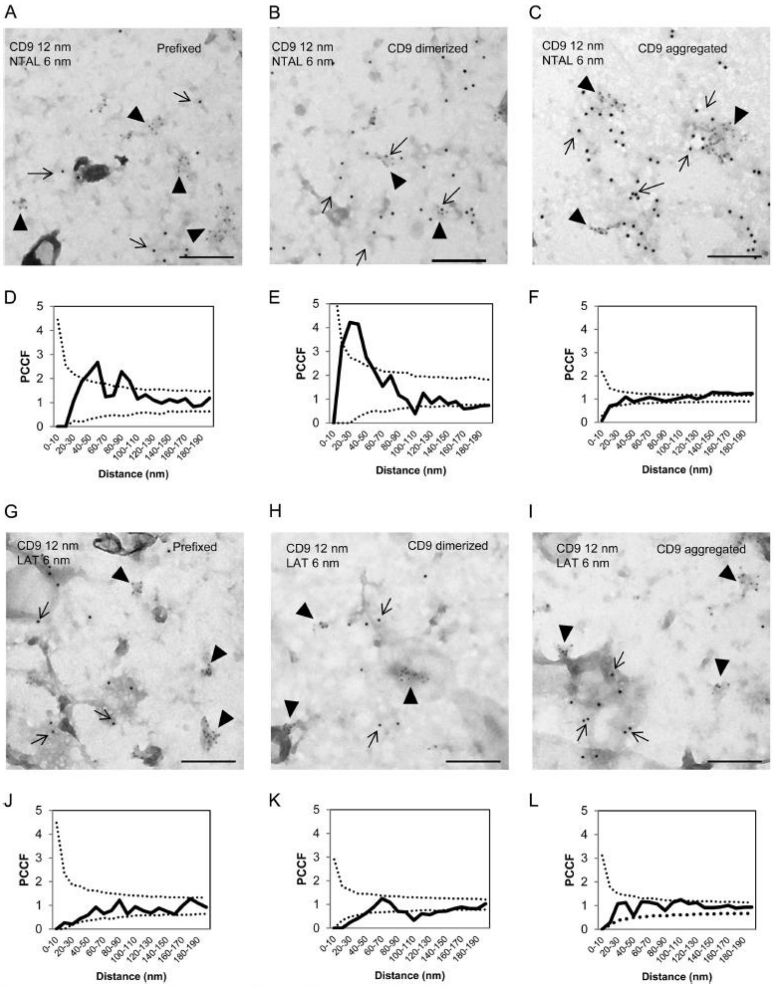

FIGURE 3. **Different colocalization of CD9 with NTAL or LAT.** BMMCs were prefixed in 2% paraformaldehyde and then stained with 2H9 mAb followed by secondary antibody conjugated to 12 nm of gold (*A, D, G,* and *J*). Alternatively, the cells were first treated with 2H9 mAb and then fixed and stained (*B, E, H,* and *K*) or the cells were first treated with 2H9 mAb followed by its aggregation with secondary antibody followed by fixation (*C, F, I,* and *L*). Plasma membrane sheets were then isolated and NTAL (*A-F*) or LAT (*G-L*) on the cytoplasmic side of the plasma membrane were labeled with primary antibodies followed by secondary antibodies conjugated to 6-nm gold particles. Topography of gold particles was evaluated by electron microscopy. Representatives from 3 independent experiments performed are shown (*A-C* and *G-I*). Evaluation of colocalization of 6- and 12-nm gold particles is represented as PCCF analysis for CD9/NTAL labeling (*D-F*) and CD9/LAT labeling (*J-L*). For calculation of PCCF, 20 μm^2 of the plasma membrane sheets was used in each experiment. PCCF indicates colocalization when experimental values (*solid line*) are higher than random distribution of particles presented by a *dotted line*. *Bars*, 200 nm.

fixed before labeling (Fig. 3, *A* and *D*). Antibody-mediated dimerization of CD9 before fixation promoted this colocalization (Fig. 3, *B* and *E*) and extensive CD9 aggregation with secondary antibody led to localization of both CD9 and NTAL in large separated clusters (Fig. 3, *C* and *F*). In contrast, LAT showed no significant colocalization with CD9 at any condition tested (Fig. 3, *G-L*). These data suggest that NTAL (unlike LAT) is located together with CD9 in membrane microdomains; this could form a mechanistical basis for their functional cross-talk.

Inhibitory Effect of Anti-CD9 on Ag-mediated Chemotaxis—Previous studies showed that tetraspanins are involved in regulation of chemotaxis in several cell types, including mast cells (48, 49). In further experiments we therefore tested the effect of the 2H9 anti-CD9 mAb on chemotaxis driven by Ag. We found that pretreatment of IgE-sensitized BMMCs with anti-CD9 mAb inhibited migration toward Ag even at low concentrations of the mAb (Fig. 4*A*). Visual microscopic inspection showed that exposure of the cells to all concentrations of the 2H9 mAb tested in the chemotaxis assays did not induce aggregation of BMMCs (not shown), which could be responsible to the observed inhibitory effect. When commercially available CD9-specific mAb, KMC8, was used, the binding to BMMCs was comparable with 2H9, but no inhibition of Ag-driven chemotaxis was observed (not shown). This suggests unique binding properties of 2H9 mAb. Previous studies showed that mast cells use tetraspanin CD9 as an alternate IL-16 receptor (48). Next we therefore examined whether anti-CD9 antibodies will interfere with IL-16-driven chemotaxis. Data presented in Fig.

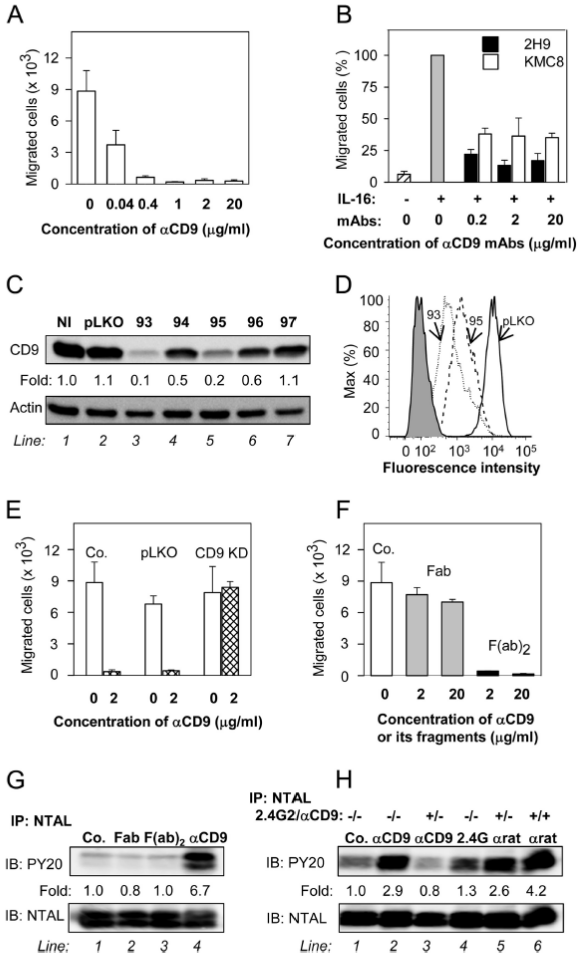

FIGURE 4. **Anti-CD9 mAb inhibits chemotaxis toward Ag and induces tyrosine phosphorylation of NTAL by different mechanism.** *A,* IgE-sensitized BMMCs were pretreated with the indicated concentrations of anti-CD9 mAb 2H9 for 15 min and their chemotactic response toward Ag (250 ng/ml of TNP-BSA in the lower chamber) was determined in the Transwell system. *B,* BMMCs were pretreated or not with the indicated concentrations of anti-CD9 antibodies (2H9 or KMC8) for 15 min and their chemotactic response toward IL-16 (50 ng/ml) was determined as above. Data were normalized toward the maximum response attained in the absence of antibody pretreatment. Migration in the absence of IL-16 is also shown. *C* and *D,* a set of murine CD9 shRNAs cloned into the pLKO.1 vector (TRCN0000066393 (*93*), TRCN0000066394 (*94*), TRCN0000066395 (*95*), TRCN0000066396 (*96*), TRCN0000066397 (*97*)) was used for lentiviral infection of BMMCs. After selection in puromycin, the cellular proteins were size fractionated by SDS-PAGE and analyzed by immunoblotting (*IB*) with anti-CD9 mAb 2H9. Actin was used as a loading control. Immunoblots were evaluated by densitometry and data were normalized to noninfected controls (*NI*) and actin amount. Similar results were obtained in at least three independent experiments. *D,* flow cytometry analysis of surface expression of CD9 in clones selected for further studies, 93 (*dotted line*) and 95 (*dashed line*). *Gray filled region* represents control cells exposed to secondary anti-rat Alexa 488 antibody alone. *Thick line* indicates cells infected with empty vector (pLKO). *E,* BMMCs were deprived of CD9 after infection with CD9 shRNA-containing vector (*CD9 KD*), uninfected cells (*Co.*), or cells infected with empty vector (*pLKO*) served as controls. Ag-mediated chemotaxis in the cells was measured as in *A*. *F,* BMMCs were not exposed (*Co.*) or exposed for 15 min to 2H9 mAb Fab or $F(ab)_2$ fragments, each at a concentration 2 or 20 μg/ml. Their chemotaxis was determined as in *A*. *G,* BMMCs were exposed to BSSA (negative control, Co., *line 1*), 2H9 mAb Fab fragment (*line 2*), 2H9 mAb $F(ab)_2$ fragment (*line 3*), or 2H9 whole molecule (αCD9; *line 4*); each at a concentration of 10 μg/ml. After 5 min the cells were solubilized in lysis buffer containing 1% Nonidet P-40 and 1% *n*-dodecyl-β-D-maltoside and postnuclear supernatants were immunoprecipitated (*IP*) with rabbit anti-NTAL antibody. The immunoprecipitates were analyzed by immunoblotting (*IB*) with phosphotyrosine-specific antibody PY-20-HRP conjugate (*PY20*) or NTAL-specific antibody as a loading control. Fold-increase in protein tyrosine phosphorylation, normalized to phosphorylation in nonactivated cells and NTAL amount is also indicated. A typical experiment from 4 performed is shown. *H,* BMMCs were pretreated or not with anti-CD16/CD32 (2.4G2; 1:50 diluted supernatant) and/or anti-CD9 mAb 2H9 (1 μg/ml, αCD9) for 15 min and then exposed to control BSSA (*Co.*, line *1*), anti-CD9 (1 μg/ml, *lines 2* and *3*), 2.4G2 antibody (1:50 diluted supernatant, *line 4*), or anti-rat IgG (1 μg/ml, *lines 5* and *6*). After 3 min the cells were lysed and NTAL was immunoprecipitated and analyzed as in *G*. Typical results from at least 3 experiments performed are shown. Mean ± S.D. in *A*, *B*, *E*, and *F* were calculated from 3 to 5 independent experiments.

4*B* indicate that both 2H9 and KMC8 inhibited chemotaxis toward IL-16; 2H9 was more potent than KMC8 at all concentrations tested.

To find out whether binding of 2H9 mAb to CD9 is indeed involved in chemotaxis inhibition, we prepared BMMCs with CD9 KD after infection of the cells with lentiviral vectors containing CD9 shRNA. From the 5 vectors used, two of them (TRCN0000066393 (*93*) and TRCN0000066395 (*95*)) strongly inhibited CD9 expression as detected by immunoblotting (Fig. 4*C*) and flow cytometry analysis (Fig. 4*D*) and were used in further experiments. Both vectors gave comparable results and therefore experimental data were pooled for presentation. Data shown in Fig. 4*E* indicate that chemotaxis toward Ag was not reduced by anti-CD9 in cells with CD9 KD, but was inhibited in control cells with empty pLKO vector. Interestingly, cells with reduced expression of CD9 showed normal migration toward Ag. These data indicate that reduced expression of CD9 is compatible with chemotaxis but not with the inhibitory effect of anti-CD9.

In macrophages (50) and platelets (51–53) anti-CD9 induced changes in signaling pathways that were caused by co-cross-linking of CD9 with FcγRs. Next we therefore studied the role of FcγRs in anti-CD9 mAb-mediated inhibition of chemotaxis. We prepared Fab and $F(ab)_2$ fragments of 2H9 mAb and compared their effects on Ag-driven chemotaxis. Pretreatment of BMMCs with anti-CD9 $F(ab)_2$ fragments had a similar inhibitory effect on chemotaxis toward Ag as caused by the whole IgG (compare Fig. 4, *A* and *F*). However, when Fab fragments were used only minimal effects were observed (Fig. 4*F*). These findings suggest that inhibition of chemotaxis is caused by aggregation of CD9 and does not require co-cross-linking of CD9 with FcγR. It should be noted that the binding capacity of the whole 2H9 IgG or its $F(ab)_2$ and Fab fragments to BMMCs was comparable as determined by flow cytometry (not shown).

CD9, Fcγ Receptors, and NTAL Phosphorylation—As shown in Fig. 1, *E* and *G*, NTAL becomes tyrosine phosphorylated after exposure of the cells to anti-CD9 mAb 2H9. The logical next step was therefore to find out whether FcγRs are involved in the process. Whereas intact 2H9 mAb induced strong tyrosine phosphorylation of NTAL (Fig. 4*G*, *line 4*), $F(ab)_2$ as well as Fab fragments of the mAb were without any effect (Fig. 4*G*, *lines 2* and *3*). In this context it should be mentioned that phosphorylation of NTAL was observed when $F(ab)_2$ or Fab fragments of the 2H9 mAb were aggregated by anti-rat IgG antibodies (not shown). These data together with the finding that 2H9 $F(ab)_2$

fragments inhibit Ag-directed chemotaxis indicate that there is no simple connection between 2H9-induced chemotaxis inhibition and NTAL tyrosine phosphorylation. It should be also mentioned that 2H9 mAb was able to induce a weak tyrosine phosphorylation of NTAL in CD9 KD cells (not shown). This indicates that aggregation of residual CD9 on cells with CD9 KD (Fig. 4*D*) is still capable to induce NTAL phosphorylation, but is no longer capable of inhibiting chemotaxis (Fig. 4*E*).

To confirm the role of Fcγ receptors in NTAL phosphorylation induced by 2H9 mAb we used rat 2.4G2 antibody, which is specific for mouse FcγRIIB/FcγRIII. BMMCs pretreated or not with a saturating concentration of 2.4G2 mAb and/or anti-CD9 mAb (1st step) was followed by exposure to anti-CD9 mAb, 2.4G2 mAb, or anti-rat IgG antibody (2nd step). The results show that the 2.4G2 antibody alone caused weak phosphorylation of NTAL (Fig. 4*H*, compare *line 1* with *line 4*). Phosphorylation of NTAL was enhanced when 2.4G2 mAb was aggregated in the 2nd step by anti-rat IgG (Fig. 4*H*, *line 5*). Pretreatment of the cells with 2.4G2 mAb followed by exposure to anti-CD9 mAb resulted in lower phosphorylation of NTAL (Fig. 4*H*, *line 3*) than after exposure of the cells to anti-CD9 alone (Fig. 4*H*, *line 2*). Maximum NTAL phosphorylation was observed when both FcγR and CD9 were extensively aggregated with the first and second layer of antibodies (Fig. 4*H*, *line 6*).

CD9 Aggregation Does Not Interfere with Early FcεRI-mediated Signaling Events—Because 2H9 binding inhibited chemotaxis toward Ag, we were curious to know whether other Ag-induced signaling pathways are affected and whether CD9 colocalizes with FcεRI. Our data show that FcεRI exhibited colocalization with CD9 after CD9 dimerization or a more extensive aggregation (Fig. 5, *A-F*). Furthermore, we could demonstrate that Ag-induced degranulation (Fig. 5*G*), Ca^{2+} release (Fig. 5*H*), and tyrosine phosphorylation of Akt, ERK, and pp38 (Fig. 5*I*) were not affected by anti-CD9 mAb binding. We also found that phosphorylation of the FcεRI-β subunit was not changed (Fig. 5*J*). These data thus indicate that signaling pathways leading to degranulation after FcεRI triggering were not affected by anti-CD9. The experiments presented in Fig. 5 were performed with BMMCs from Balb/c mice, but similar results were obtained with BMMCs derived from C57BL/6 mice (not shown).

Different Roles of LAT and NTAL in Mast Cell Chemotaxis and Cross-talk with CD9—Data presented above show that anti-CD9 inhibits chemotaxis toward Ag and induces disparate phosphorylation of NTAL and LAT. Next we investigated the role of NTAL and LAT in mast cell chemotaxis and their sensitivity to the inhibitory effect of anti-CD9. For such experiments, BMMCs were obtained by growing progenitors from bone marrow of $Ntal^{-/-}$, $Lat^{-/-}$, 2KO mice, and corresponding controls. The cells were sensitized with TNP-specific IgE overnight and their migration toward Ag was investigated. Surprisingly, LAT-deficient cells ($Lat^{-/-}$) showed similar Ag-mediated chemotaxis as WT ($Lat^{+/+}$) cells (Fig. 6*A*). In accordance with our previous findings (14), BMMCs derived from $Ntal^{-/-}$ mice exhibited significantly higher migration toward Ag than the corresponding WT ($Ntal^{+/+}$) cells (Fig. 6*A*). These data confirm that NTAL is a negative regulator of Ag-driven chemotaxis. Interestingly, 2KO cells exhibited higher migration toward Ag than WT ($Ntal^{+/+}$ or $Lat^{+/+}$) cells or $Lat^{-/-}$ cells, but lower migration than $Ntal^{-/-}$ cells. This suggests that in the absence of NTAL even LAT negatively regulates chemotaxis. To verify that LAT and NTAL had the anticipated regulatory roles in Ag-induced degranulation, we also tested the release of β-glucuronidase after activation of the cells with Ag. Data shown in Fig. 6*B* indicate, as expected, decreased degranulation in $Lat^{-/-}$ and even more in 2KO cells and an enhanced response in $Ntal^{-/-}$ cells, when compared with the corresponding WT ($Ntal^{+/+}$ or $Lat^{+/+}$) controls.

To examine a functional regulatory cross-talk between NTAL and CD9 in chemotaxis, we compared the effect of anti-CD9 on Ag-driven chemotaxis of $Ntal^{-/-}$ and WT $Ntal^{+/+}$ cells. Data presented in Fig. 6*C* show that treatment with anti-CD9 mAb inhibited chemotaxis toward Ag in both $Ntal^{+/+}$ cells and $Ntal^{-/-}$ cells. However, $Ntal^{-/-}$ cells were more perceptive to the inhibitory effect of anti-CD9 than $Ntal^{+/+}$ cells.

CD9 Forms Complex with β1-Integrin but Anti-CD9 Does Not Interfere with β1-Integrin Function—The most prominent partners of tetraspanins are integrins (15–17, 20, 21). Next, we therefore investigated the effect of anti-CD9 mAb on integrin-mediated signaling pathways. Pretreatment of BMMCs with anti-CD9 mAb inhibited the binding of β1-integrin antibody to the cells (Fig. 7, *A* and *D*). The inhibitory effect was not affected by pretreatment with F-actin disrupting drugs, latrunculin B (0.4 μM, 30 min) or cytochalasin D (1 μM, 30 min; data not shown). This suggests that F-actin-dependent events, such as internalization, are not responsible for the observed inhibitory effect. On the other hand, pretreatment of the cells with anti-CD9 mAb had no effect on the binding of antibodies against FcεRI and KIT (Fig. 7, *B-D*); these data support the concept that integrin is in close proximity to CD9. Immunoprecipitation data indicated that CD9 and β1-integrin are physically associated in complexes after solubilization of the cells in lysis buffer containing 1% CHAPS (Fig. 7*E*). To investigate the functional cross-talk between CD9 and β1-integrin, we tested the effect of anti-CD9 on Ag-induced adhesion of mast cells to fibronectin. It is remarkable that although anti-CD9 mAb blocked the binding of anti-β1 integrin antibody to the cells, no significant inhibition of anti-CD9 on adhesion to fibronectin was observed. As a control we used antibody against β1-integrin and found that it significantly inhibited adhesion of BMMCs to the fibronectin (Fig. 7*F*). We also tested the effect of anti-CD9 on Ag-induced spreading of mast cell on surfaces coated with fibronectin. Data presented in Fig. 7, *G* and *H*, indicate that binding of anti-CD9 at saturation concentrations to BMMCs had no significant effect on Ag-induced spreading of the cells to fibronectin. The combined data indicate that although CD9 forms complexes with β1-integrin, binding of anti-CD9 mAb does not interfere with the studied β1-integrin functions.

Cross-talk between CD9 and Cytoskeleton-regulatory Proteins of the ERM Family—An important feature of cell activation and chemotaxis is a rapid and extensive communication between plasma membrane components and cellular cytoskeleton. This process is regulated by conformational changes in ERM family proteins caused by transient dephosphorylation of their regulatory threonines. Although such changes have been documented in immunoreceptor-activated B cells, T cells, and

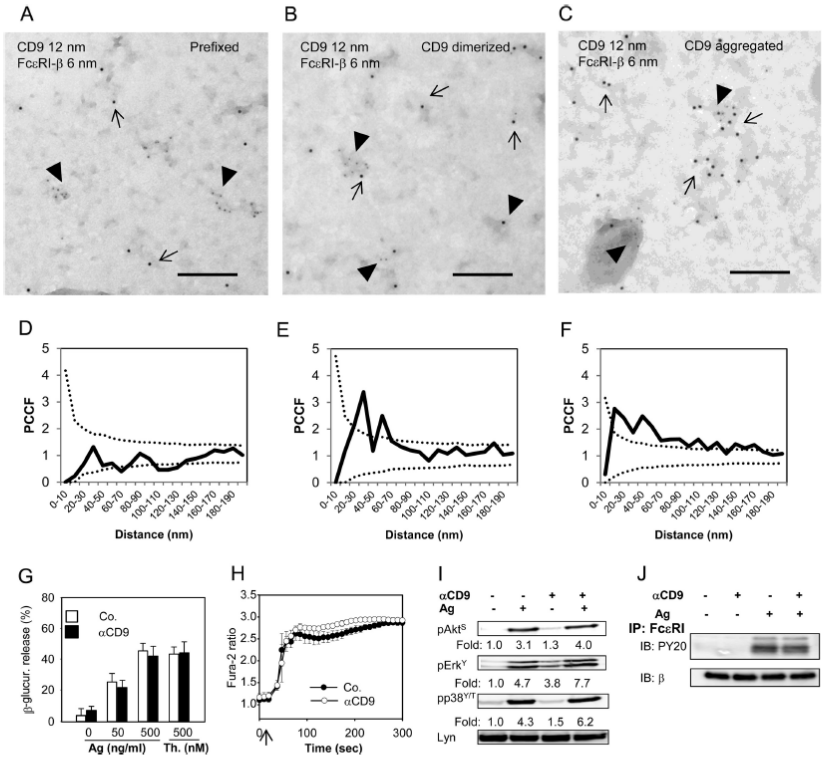

FIGURE 5. **CD9 colocalizes with FcεRI on the plasma membrane but CD9 aggregation does not interfere with early Ag-induced activation events.** *A* and *D*, BMMCs derived from Balb/c mice were prefixed with paraformaldehyde and then labeled with anti-CD9 mAb 2H9 followed by secondary anti-rat antibody-12 nm gold conjugate. Plasma membrane sheets were then isolated and the FcεRI-*β* subunit was labeled on the cytoplasmic side of the membrane with JRK mAb followed by secondary anti-mouse antibody-6 nm gold conjugate. Colocalization of CD9 (12 nm gold particles) and FcεRI-*β* (6-nm gold particles) was analyzed by electron microscopy (*A*) and evaluated by PCCF (*D*) as described in the legend to Fig. 3. *B* and *E*, BMMCs were exposed to 2H9 mAb (CD9 dimerized) before fixation and labeling for CD9; other procedures and evaluations were as in *A* and *D*. *C* and *F*, the cells were exposed to 2H9 mAb followed by the secondary anti-mouse antibody (CD9 aggregation) and then fixed and further processed as in *A* and *D*. In *A-C* representatives from 3 independent experiments are shown. *Bars*, 200 nm. *G-J*, IgE-sensitized BMMCs derived from Balb/c mice were pretreated (αCD9) or not (*Co.*; −) with anti-CD9 mAb 2H9 (10 μg/ml) for 15 min before activation. *G*, the cells were exposed to various concentrations of Ag (0–500 ng/ml TNP-BSA) or 500 nM thapsigargin (*Th.*) and 30 min later amounts of *β*-glucuronidase released into the cell supernatants were determined. Mean ± S.D. were calculated from at least 3 independent experiments performed in triplicates. *H*, the cells were loaded with Fura-2AM at the time of exposure to anti-CD9 and stimulated (*arrow*) with Ag (500 ng/ml of TNP-BSA). $[Ca^{2+}]_i$ was measured as described in the legend to Fig. 1*B*. Mean ± S.D. were calculated from 3 independent experiments performed in triplicates. *I*, IgE-sensitized BMMCs were exposed (+) or not (−) to anti-CD9 mAb 2H9 and then activated (+) or not (−) with Ag (100 ng/ml of TNP-BSA) for 3 min. Whole cell lysates were prepared and analyzed by immunoblotting with antibodies specific for pAkt-S^{473} (pAkt^S), pErk-Y^{204} (pErk^Y) or pp38-Y^{182}/T^{180} (pp38$^{Y/T}$); anti-Lyn mAb (*Lyn*) was used as a loading control. Fold-increase in protein phosphorylation, normalized to phosphorylation in nonactivated cells and protein loading is also shown. Typical results from at least 4 experiments performed are shown. *J*, IgE-sensitized BMMCs were exposed (+) or not (−) to anti-CD9 mAb and then activated by Ag (+; 250 ng/ml of TNP-BSA) or not (−). After 5 min the cells (15×10^6 per sample) were solubilized in lysis buffer containing 0.2% Triton X-100 and FcεRI was immunoprecipitated from postnuclear supernatants by anti-IgE antibody immobilized to Protein A beads. Tyrosine phosphorylation of the receptor subunits was evaluated with PY-20-HRP conjugate (PY-20). The amount of immunoprecipitated receptor was estimated by immunoblotting (after stripping of the membrane) with JRK mAb recognizing FcεRI *β* subunit. A typical experiment from 3 performed is shown.

mast cells (54–58), whether aggregation of CD9 could also induce such dephosphorylations is unknown. We have examined the phosphorylation status of the regulatory threonine after exposure of BMMCs to anti-CD9 mAb 2H9, SCF, or Ag and found that all 3 activators significantly reduced phosphorylation of the regulatory threonine (Fig. 7, *I* and *J*).

DISCUSSION

Migration of mast cell progenitors from bone marrow to connective tissues and subsequent movement of mature mast cells to the sites of inflammation is crucial for proper functioning of innate and adaptive immunity. Mast cell migration is directed by chemoattractants, which are produced by a variety of cells localized in different target tissues, as well as by intrinsic mast cell regulators that are still poorly understood (2). This study was initiated by functional screening of mAbs prepared after immunization of rats with cellular ghosts obtained by treatment of BMMCs with saponin. One of the antibodies, 2H9, recognizing tetraspanin CD9, was found capable to induce cell activation and inhibit Ag-driven mast cell chemotaxis. Several lines of evidence presented in this study indicate that 2H9-mediated CD9 aggregation triggers signaling pathways, which are different from those activated through FcεRI or KIT, and have impact on mast cell chemotaxis.

First, exposure of BMMCs to CD9-specific mAb 2H9 resulted in phosphorylation of several signal transduction proteins. Importantly, the phosphorylation profile of the target proteins differed from that produced by SCF- or Ag-mediated

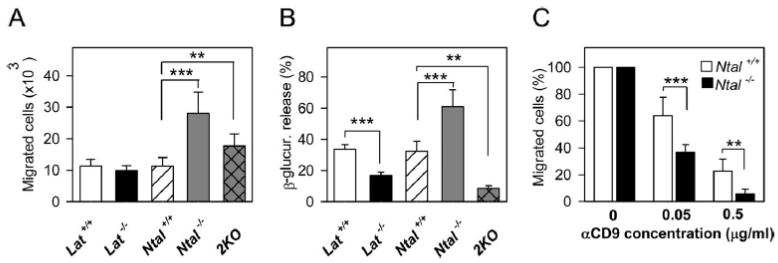

FIGURE 6. **Different roles of LAT and NTAL in mast cell chemotaxis and cross-talk with CD9.** *A*, BMMCs derived from *Lat*$^{-/-}$, *Ntal*$^{-/-}$, 2KO, and corresponding littermate (*Lat*$^{+/+}$, *Ntal*$^{+/+}$) control mice were sensitized overnight with TNP-specific IgE and their migration toward Ag (250 ng/ml of TNP-BSA) was tested in the Transwell system. *B*, the same IgE-sensitized BMMCs as in *A* were activated with Ag (250 ng/ml TNP-BSA) for 30 min and β-glucuronidase released into the supernatant was determined as described under "Experimental Procedures." *C*, BMMCs from *Ntal*$^{+/+}$ and *Ntal*$^{-/-}$ mice were sensitized with IgE and treated with the indicated concentrations of anti-CD9 mAb 2H9. Chemotaxis toward Ag was determined as in *A*. Numbers of cells migrating toward Ag were normalized to controls, 2H9 nontreated cells. Mean ± S.D. were calculated from 3 to 5 independent experiments performed in duplicates. **, $p < 0.01$; ***, $p < 0.001$.

activation (Table 1). Specifically, 2H9 mAb induced stronger phosphorylation of NTAL than activation through KIT but weaker than activation via FcεRI. On the other hand, several proteins, which were phosphorylated in KIT- and FcεRI-activated cells, were either not at all or only weakly phosphorylated after CD9 triggering (Akt, Erk, and p38). Other proteins, which were strongly phosphorylated after Ag-induced activation (Syk and LAT), showed no or only weak tyrosine phosphorylation after CD9 triggering. Enhanced phosphorylation of NTAL in anti-CD9-treated cells was only observed when whole IgG was used; Fab and $F(ab)_2$ fragments had no effect. This suggested that co-cross-linking of CD9 and Fcγ receptor(s) is required for tyrosine phosphorylation of NTAL and other targets. This conclusion was corroborated by experiments where antibody specific for FcγRIIB/FcγRIII induced tyrosine phosphorylation of NTAL, on the one hand, and, on the other, partially inhibited NTAL phosphorylation after exposure to anti-CD9. Involvement of Fcγ receptors in CD9 signaling was also described in CD9-dependent activation of platelets (53, 59) and macrophages (50).

Second, binding of anti-CD9 to target structures on the surface of mast cells resulted in weak calcium and degranulation responses, comparable with those observed in SCF-activated cells (Table 1). However, because tyrosine phosphorylation of LAT was lower in cells activated through CD9 than through KIT and because phosphorylated NTAL is unable to bind phospholipase γ and thus substitute for phosphorylated LAT in calcium metabolism (5, 6), it is evident that activation through CD9 or KIT is initiated by different activation pathways. In this connection it should be noted that pretreatment with anti-CD9 had no significant effect on subsequent binding of IgE to FcεRI and on Ag-induced degranulation, Ca^{2+} responses, and tyrosine phosphorylation of numerous substrates. In this respect, CD9 seems to differ from CD81, another tetraspanin, whose Ab-mediated aggregation inhibited Ag-induced degranulation in rat basophilic leukemia cells without affecting the Ca^{2+} response or protein tyrosine phosphorylation (60).

Third, electron microscopy studies on isolated plasma membrane sheets disclosed colocalization of CD9 with NTAL, but not with LAT, in quiescent cells. After CD9 dimerization the colocalization of CD9 with NTAL became even more prominent. This finding and the potent phosphorylation of NTAL after CD9 triggering suggest that these two molecules are physically and functionally coupled. This could explain our previous findings that although NTAL and LAT are very similar TRAPs, they, nevertheless, occupy different membrane domains (5). CD9 also colocalized with FcεRI. However, this colocalization was clearly seen only after Ab-mediated dimerization or extensive aggregation of CD9.

Fourth, pretreatment of BMMCs with anti-CD9 mAb abolished chemotaxis toward Ag. The inhibitory effect was observed not only with intact mAb but also with the corresponding $F(ab)_2$ fragment. These data suggest that the inhibitory effect is caused by CD9 aggregation and is not dependent on signals derived from cross-linking of CD9 with FcγR. This conclusion is further supported by findings that chemotaxis was not affected by Fab fragments of the anti-CD9 mAb. When another CD9-specific mAb, KMC8, was tested, no inhibition of chemotaxis was observed. This finding could be related to different epitopes recognized by 2H9 and KMC8 antibodies and/or other differences between the antibodies, such as configurational constraints (61). On the other hand, both antibodies inhibited IL-16-mediated chemotaxis by a mechanism, which seems to involve blocking binding of IL-16 to its alternate receptor, CD9 (48). We have also noticed that chemotaxis toward Ag was not affected in BMMCs with CD9 KD. This suggests that CD9 is dispensable for Ag-driven chemotaxis or that the remaining CD9 is sufficient for signal processing. Alternatively, it is possible that antibody-mediated aggregation of CD9 and CD9-bound proteins leads to uncoupling of key elements important for chemotaxis (see below).

The molecular mechanism of the inhibitory effect of anti-CD9 on Ag-induced chemotaxis seems to be complex and involves TRAPs. We found that anti-CD9 mAb was more potent in inhibiting Ag-induced chemotaxis in NTAL-deficient cells than in WT cells. This could be related to the multiple regulatory roles of NTAL and its cross-talk with CD9 and LAT (Fig. 8).

Fifth, extensive communication between plasma membrane components and the cellular cytoskeleton is crucial for immunoreceptor activation and chemotaxis. This process is regulated by conformational changes in ERM family proteins reflecting the phosphorylation status of their regulatory threonine. Our finding of increased dephosphorylation of ERM pro-

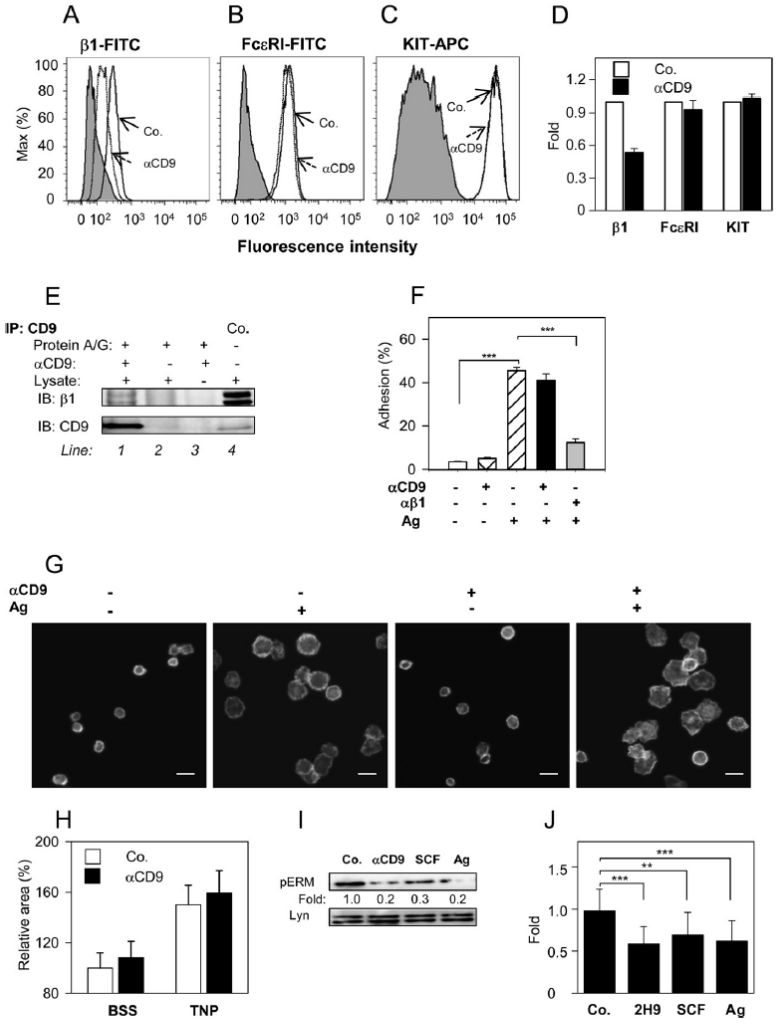

FIGURE 7. **CD9 aggregation does not interfere with β1-integrin function, but induces dephosphorylation of ERM proteins.** *A-D*, BMMCs were pretreated or not with anti-CD9 mAb 2H9 (1 μg/ml) for 15 min and the binding anti-integrin-β1-FITC conjugate (*A*), anti-FcεRI-FITC conjugate (*B*), and anti-c-Kit-APC conjugate (*C*) were estimated by flow cytometry. *Gray filled regions* represent control cells not exposed to antibodies; *dashed* and *thick lines* indicate antibody binding to anti-CD9 treated (*dashed*; αCD9) or nontreated cells (*thick*; *Co.*). *D*, data obtained as in *A-C* were normalized to maximal values obtained in the absence of anti-CD9; mean ± S.D. were determined from at least 3 independent experiments. *E*, BMMCs (10^7 per sample) were solubilized in lysis buffer supplemented with 1% CHAPS. CD9 was immunoprecipitated from postnuclear supernatants by 2H9 mAb immobilized on protein A/G beads (*line 1*). Material bound to protein A/G beads without 2H9 mAb (*line 2*) or 2H9 mAb armed protein A/G beads without cell lysate (*line 3*) served as negative controls. Whole lysates from 2.5×10^5 cells were used as positive controls (*Co.*; *line 4*). Immunoprecipitated material and controls were recovered in SDS-PAGE sample buffer with or without 2-mrecaptoethanol. Reduced and unreduced samples were immunoblotted with anti-β1 integrin (β1) or anti-CD9 (CD9), respectively. *F*, cell adhesion to fibronectin. IgE-sensitized and Calcein-loaded BMMCs were incubated with (+) or without (−) anti-CD9 mAb 2H9 and/or anti-β1 integrin antibody for 15 min before their transfer into fibronectin-coated wells. Adherence to fibronectin was determined by fluorometry after a 30-min exposure of the cells to Ag (+) or BSSA alone (−). Fluorescence was evaluated before (100%) and after washing out the non-adherent cells and percentages of adherent cells were calculated. *G*, cell spreading on fibronectin. IgE-sensitized BMMCs were pretreated (+) or not (−) with anti-CD9 mAb 2H9 and allowed to attach to fibronectin immobilized on glass surface. Then the cells were exposed (+) or not (−) to Ag for 20 min, fixed, permeabilized, and stained for actin with Alexa Fluor 488-phalloidin conjugate. Examples of the cells are shown. *Bars*, 20 μm. *H*, average areas of the cells processed as in *G* were calculated using automated CellProfiller software. Mean ± S.D. from three independent experiments, each involving ~500 cells, are shown. *I*, IgE-sensitized BMMCs were nonactivated (*Co.*) or activated with 2H9 mAb (*αCD9*), SCF, or Ag for 3 min. Whole cell lysates were prepared and analyzed by immunoblotting with *p*-ERM^T-specific Ab; anti-Lyn was used as a loading control. *Numbers* correspond to the fold-increase in phosphorylation after normalization to the total amount of protein and phosphorylation in nonactivated cells. Typical results are shown. *J*, mean ± S.D. were calculated from 10 to 18 independent experiments performed as in *I*. **, $p < 0.01$; ***, $p < 0.001$.

teins in cells exposed to anti-CD9 suggested that anti-CD9 interferes with the process of phosphorylation/dephosphorylation of ERM family members, and in this way could interfere with chemotaxis. The molecular mechanism of the cross-talk between CD9 and ERM family members is unknown. Recent studies imply an important role of the phosphorylation state of threonine in actin-binding domains of ERM proteins in cell chemotaxis (54–57). The proteins exist in an open (active) conformation with regulatory threonine phosphorylated, or closed (inactive) conformation with the regulatory threonine dephos-

TABLE 1
Comparison of anti-CD9 mAb, SCF, and Ag in their ability to induce signaling events in mast cells

Parameter[a]	Anti-CD9	SCF	Ag
Protein phosphorylation			
Akt-S^{473}	–[b]	+++	+++
Akt-T^{308}	–	+++	+++
Erk-Y^{204}	+	+++	+++
p38-T^{180}/Y^{182}	+	+++	+++
Syk	–	–	+++
NTAL	++	+	+++
LAT	–/+	–	+++
Protein dephosphorylation			
ERM-$T^{567/564/558}$	++	++	++
Degranulation (β-glucuronidase)	+	+	+++
Ca^{2+} mobilization	+	+	+++
Adhesion	–	++[c]	++
Spreading	–	+++[c]	+++
Chemotaxis	–	+++[c]	++

[a] Specific protein phosphorylation or dephosphorylation, degranulation, Ca^{2+} mobilization, adhesion, and chemotactic potential of CD9-specific mAb 2H9, SCF and Ag were measured using appropriate methods as indicated under "Experimental Procedures" and "Results."
[b] –, No signal; +, weak signal; ++, medium signal; +++, strong signal.
[c] See Ref. 14.

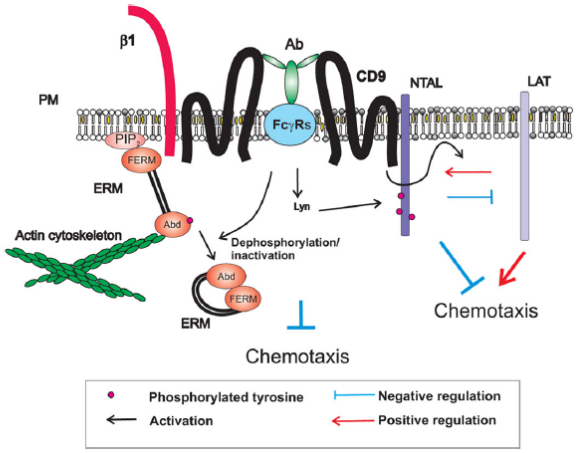

FIGURE 8. **A model of chemotaxis regulators involving CD9 and NTAL-LAT cross-talk.** Tetraspanin CD9 resides in the plasma membrane (*PM*) in close proximity to β1-integrin (β1) and NTAL. CD9-specific antibody 2H9 (*Ab*) binds to CD9 and FcγR through its Ag-binding site and Fc region, respectively. This leads to tyrosine phosphorylation of NTAL and other proteins. CD9 cross-linking also results in dephosphorylation of the regulatory threonine of ERM family proteins leading to changes in their conformation and subsequent disconnection from binding to phosphatidylinositol 4,5-bisphosphate (*PIP2*) and/or other membrane components (throughout N-terminal FERM domain) and actin cytoskeleton (through actin-binding domain, *Abd*). These and other events under certain conditions inhibit mast cell chemotaxis. Chemotaxis is also regulated by cross-talk between NTAL, LAT, and CD9. LAT and NTAL seem to be, respectively, predominantly positive and negative regulators of chemotaxis. Binding of the anti-CD9 mAb 2H9 interferes with NTAL-LAT cross-talk.

phorylated (62, 63). In the case of ezrin, the open conformation enables its binding through the actin-binding domain to F-actin and through the FERM domain to phosphatidylinositol 4,5-biphosphate on the plasma membrane, to adapter proteins or directly to cytoplasmic portions of the transmembrane molecules (59, 64). Transient dephosphorylation of the regulatory threonine disrupts this binding and has been shown to be crucial for migration of lymphocytes (54–57). A recent study with mast cells showed that dephosphorylation of the regulatory tyrosine is mediated by activity of the protein phosphatase 2A after interaction with the p21-activated kinase 1 (58). Based on our own findings and published data we propose that aggregation of CD9 leads to dephosphorylation of ERM proteins leading to their dissociation from the membrane and restrictions in communication of membrane proteins with actin cytoskeleton. This in combination with some other events involving NTAL and/or LAT contributes to inhibition of Ag-driven chemotaxis (Fig. 8). As shown in experiments with $F(ab)_2$ fragments, tyrosine phosphorylation of NTAL is not required for the inhibitory effect of anti-CD9 mAb. Nevertheless, it is possible that NTAL functions in chemotaxis even in the absence of its phosphorylation, similarly to its role in phospholipase Cγ-independent calcium uptake (12).

The combined data support the view that chemotaxis and early activation events leading to degranulation and cytokine production are processes that use different signaling pathways. The differences could be important for switching between the migratory and secretory phases depending on the concentrations of Ag and/or other chemoattractant mast cell encounters (65). At low concentrations of the Ag, mast cells migrate toward its higher concentrations. When regions of higher concentrations of the Ag are attained, the cells stop moving and activate the signaling pathways leading to secretion of the preformed allergy mediators and production and release of cytokines, leukotrienes, and other inflammatory mediators that then act as chemoattractants for other cells and/or orchestrate local immune responses. Tetraspanin CD9 and NTAL are important regulators of these events. CD9 could regulate chemotaxis through direct or indirect interactions with FcεRI, other plasma membrane receptors, and cytoskeletal components. On the other hand NTAL, which acts as a negative regulator of chemotaxis, could contribute to fine tuning of chemotaxis by competing with LAT, as suggested for its negative role in mast cell degranulation (5).

REFERENCES

1. Okayama, Y., and Kawakami, T. (2006) Development, migration, and survival of mast cells. *Immunol. Res.* **34,** 97–115
2. Halova, I., Draberova, L., and Draber, P. (2012) Mast cell chemotaxis-chemoattractants and signaling pathways. *Front Immunol.* **3,** 119
3. Wedemeyer, J., and Galli, S. J. (2000) Mast cells and basophils in acquired immunity. *Br. Med. Bull.* **56,** 936–955
4. Saitoh, S., Arudchandran, R., Manetz, T. S., Zhang, W., Sommers, C. L., Love, P. E., Rivera, J., and Samelson, L. E. (2000) LAT is essential for FcεRI-mediated mast cell activation. *Immunity* **12,** 525–535
5. Volná, P., Lebduška, P., Dráberová, L., Šímová, Š., Heneberg, P., Boubelík, M., Bugajev, V., Malissen, B., Wilson, B. S., Hořejší, V., Malissen, M., and Dráber, P. (2004) Negative regulation of mast cell signaling and function by the adaptor LAB/NTAL. *J. Exp. Med.* **200,** 1001–1013
6. Zhu, M., Liu, Y., Koonpaew, S., Granillo, O., and Zhang, W. (2004) Positive and negative regulation of FcεRI-mediated signaling by the adaptor protein LAB/NTAL. *J. Exp. Med.* **200,** 991–1000
7. Tkaczyk, C., Horejsi, V., Iwaki, S., Draber, P., Samelson, L. E., Satterthwaite, A. B., Nahm, D. H., Metcalfe, D. D., and Gilfillan, A. M. (2004) NTAL phosphorylation is a pivotal link between the signaling cascades leading to human mast cell degranulation following Kit activation and FcεRI aggregation. *Blood* **104,** 207–214
8. Draber, P., Halova, I., Levi-Schaffer, F., and Draberova, L. (2011) Transmembrane adaptor proteins in the high-affinity IgE receptor signaling. *Front. Immunol.* **2,** 95
9. Rivera, J. (2005) NTAL/LAB and LAT. A balancing act in mast-cell acti-

vation and function. *Trends Immunol.* **26,** 119–122
10. Simeoni, L., Lindquist, J. A., Smida, M., Witte, V., Arndt, B., and Schraven, B. (2008) Control of lymphocyte development and activation by negative regulatory transmembrane adapter proteins. *Immunol. Rev.* **224,** 215–228
11. Lebduška, P., Korb, J., Tůmová, M., Heneberg, P., and Dráber, P. (2007) Topography of signaling molecules as detected by electron microscopy on plasma membrane sheets isolated from non-adherent mast cells. *J. Immunol. Methods* **328,** 139–151
12. Dráberová, L., Shaik, G. M., Volná, P., Heneberg, P., Tůmová, M., Lebduska, P., Korb, J., and Dráber, P. (2007) Regulation of Ca^{2+} signaling in mast cells by tyrosine-phosphorylated and unphosphorylated non-T cell activation linker. *J. Immunol.* **179,** 5169–5180
13. Kimura, T., Hisano, M., Inoue, Y., and Adachi, M. (2001) Tyrosine phosphorylation of the linker for activator of T cells in mast cells by stimulation with the high affinity IgE receptor. *Immunol. Lett.* **75,** 123–129
14. Tůmová, M., Koffer, A., Šimíček, M., Dráberová, L., and Dráber, P. (2010) The transmembrane adaptor protein NTAL signals to mast cell cytoskeleton via the small GTPase Rho. *Eur. J. Immunol.* **40,** 3235–3245
15. Charrin, S., Le Naour, F., Oualid, M., Billard, M., Faure, G., Hanash, S. M., Boucheix, C., and Rubinstein, E. (2001) The major CD9 and CD81 molecular partner. Identification and characterization of the complexes. *J. Biol. Chem.* **276,** 14329–14337
16. Kotha, J., Longhurst, C., Appling, W., and Jennings, L. K. (2008) Tetraspanin CD9 regulates β_1 integrin activation and enhances cell motility to fibronectin via a PI-3 kinase-dependent pathway. *Exp. Cell Res.* **314,** 1811–1822
17. Levy, S., and Shoham, T. (2005) Protein-protein interactions in the tetraspanin web. *Physiology* **20,** 218–224
18. Hemler, M. E., Mannion, B. A., and Berditchevski, F. (1996) Association of TM4SF proteins with integrins. Relevance to cancer. *Biochim. Biophys. Acta* **1287,** 67–71
19. Xu, D., Sharma, C., and Hemler, M. E. (2009) Tetraspanin12 regulates ADAM10-dependent cleavage of amyloid precursor protein. *FASEB J.* **23,** 3674–3681
20. Berditchevski, F., and Odintsova, E. (1999) Characterization of integrin-tetraspanin adhesion complexes. Role of tetraspanins in integrin signaling. *J. Cell Biol.* **146,** 477–492
21. Berditchevski, F. (2001) Complexes of tetraspanins with integrins. More than meets the eye. *J. Cell Sci.* **114,** 4143–4151
22. Little, K. D., Hemler, M. E., and Stipp, C. S. (2004) Dynamic regulation of a GPCR-tetraspanin-G protein complex on intact cells: central role of CD81 in facilitating GPR56-$G\alpha_{q/11}$ association. *Mol. Biol. Cell* **15,** 2375–2387
23. Murayama, Y., Shinomura, Y., Oritani, K., Miyagawa, J., Yoshida, H., Nishida, M., Katsube, F., Shiraga, M., Miyazaki, T., Nakamoto, T., Tsutsui, S., Tamura, S., Higashiyama, S., Shimomura, I., and Hayashi, N. (2008) The tetraspanin CD9 modulates epidermal growth factor receptor signaling in cancer cells. *J. Cell Physiol.* **216,** 135–143
24. Sala-Valdés, M., Ursa, A., Charrin, S., Rubinstein, E., Hemler, M. E., Sánchez-Madrid, F., and Yáñez-Mó, M. (2006) EWI-2 and EWI-F link the tetraspanin web to the actin cytoskeleton through their direct association with ezrin-radixin-moesin proteins. *J. Biol. Chem.* **281,** 19665–19675
25. Stipp, C. S., Kolesnikova, T. V., and Hemler, M. E. (2001) EWI-2 is a major CD9 and CD81 partner and member of a novel Ig protein subfamily. *J. Biol. Chem.* **276,** 40545–40554
26. Zhang, X. A., Bontrager, A. L., and Hemler, M. E. (2001) Transmembrane-4 superfamily proteins associate with activated protein kinase C (PKC) and link PKC to specific β_1-integrins. *J. Biol. Chem.* **276,** 25005–25013
27. Hemler, M. E. (2005) Tetraspanin functions and associated microdomains. *Nat. Rev. Mol. Cell Biol.* **6,** 801–811
28. Rubinstein, E. (2011) The complexity of tetraspanins. *Biochem. Soc. Trans.* **39,** 501–505
29. Dráber, P., Zikán, J., and Vojtíšková, M. (1980) Establishment and characterization of permanent murine hybridomas secreting monoclonal anti-thy-1 antibodies. *J. Immunogenet.* **7,** 455–474
30. Smrž, D., Lebduška, P., Dráberová, L., Korb, J., and Dráber, P. (2008) Engagement of phospholipid scramblase 1 in activated cells. Implication for phosphatidylserine externalization and exocytosis. *J. Biol. Chem.* **283,** 10904–10918
31. Rudolph, A. K., Burrows, P. D., and Wabl, M. R. (1981) Thirteen hybridomas secreting hapten-specific immunoglobulin E from mice with Iga or Igb heavy chain haplotype. *Eur. J. Immunol.* **11,** 527–529
32. Rivera, J., Kinet, J. P., Kim, J., Pucillo, C., and Metzger, H. (1988) Studies with a monoclonal antibody to the β subunit of the receptor with high affinity for immunoglobulin E. *Mol. Immunol.* **25,** 647–661
33. Brdička, T., Imrich, M., Angelisová, P., Brdičková, N., Horváth, O., Špička, J., Hilgert, I., Lusková, P., Dráber, P., Novák, P., Engels, N., Wienands, J., Simeoni, L., Osterreicher, J., Aguado, E., Malissen, M., Schraven, B., and Hořejší, V. (2002) Non-T cell activation linker (NTAL). A transmembrane adaptor protein involved in immunoreceptor signaling. *J. Exp. Med.* **196,** 1617–1626
34. Tolar, P., Tůmová, M., and Dráber, P. (2001) *Folia Biol.* **47,** 215–217
35. Dráberová, L., Amoui, M., and Dráber, P. (1996) Thy-1-mediated activation of rat mast cells. The role of Thy-1 membrane microdomains. *Immunology* **87,** 141–148
36. Kovářová, M., Tolar, P., Arudchandran, R., Dráberová, L., Rivera, J., and Dráber, P. (2001) Structure-function analysis of Lyn kinase association with lipid rafts and initiation of early signaling events after Fcϵ receptor I aggregation. *Mol. Cell Biol.* **21,** 8318–8328
37. Hibbs, M. L., Tarlinton, D. M., Armes, J., Grail, D., Hodgson, G., Maglitto, R., Stacker, S. A., and Dunn, A. R. (1995) Multiple defects in the immune system of Lyn-deficient mice, culminating in autoimmune disease. *Cell* **83,** 301–311
38. Hájková, Z., Bugajev, V., Dráberová, E., Vinopal, S., Dráberová, L., Janáček, J., Dráber, P., and Dráber, P. (2011) STIM1-directed reorganization of microtubules in activated mast cells. *J. Immunol.* **186,** 913–923
39. Surviladze, Z., Dráberová, L., Kovářová, M., Boubelík, M., and Dráber, P. (2001) Differential sensitivity to acute cholesterol lowering of activation mediated via the high-affinity IgE receptor and Thy-1 glycoprotein. *Eur. J. Immunol.* **31,** 1–10
40. Hálová, I., Dráberová, L., and Dráber, P. (2002) A novel lipid raft-associated glycoprotein, TEC-21, activates rat basophilic leukemia cells independently of the type 1 Fcϵ receptor. *Int. Immunol.* **14,** 213–223
41. Philimonenko, A. A., Janáček, J., and Hozák, P. (2000) Statistical evaluation of colocalization patterns in immunogold labeling experiments. *J. Struct. Biol.* **132,** 201–210
42. Carpenter, A. E., Jones, T. R., Lamprecht, M. R., Clarke, C., Kang, I. H., Friman, O., Guertin, D. A., Chang, J. H., Lindquist, R. A., Moffat, J., Golland, P., and Sabatini, D. M. (2006) CellProfiler. Image analysis software for identifying and quantifying cell phenotypes. *Genome Biol.* **7,** R100
43. Fiskum, G., Craig, S. W., Decker, G. L., and Lehninger, A. L. (1980) The cytoskeleton of digitonin-treated rat hepatocytes. *Proc. Natl. Acad. Sci. U.S.A.* **77,** 3430–3434
44. Bangham, A. D., Horne, R. W., Glauert, A. M., Dingle, J. T., and Lucy, J. A. (1962) Action of saponin on biological cell membranes. *Nature* **196,** 952–955
45. Iwaki, S., Spicka, J., Tkaczyk, C., Jensen, B. M., Furumoto, Y., Charles, N., Kovarova, M., Rivera, J., Horejsi, V., Metcalfe, D. D., and Gilfillan, A. M. (2008) Kit- and FcεRI-induced differential phosphorylation of the transmembrane adaptor molecule NTAL/LAB/LAT2 allows flexibility in its scaffolding function in mast cells. *Cell Signal* **20,** 195–205
46. Zhang, J., Billingsley, M. L., Kincaid, R. L., and Siraganian, R. P. (2000) Phosphorylation of Syk activation loop tyrosines is essential for Syk function. An *in vivo* study using a specific anti-Syk activation loop phosphotyrosine antibody. *J. Biol. Chem.* **275,** 35442–35447
47. Linnekin, D. (1999) Early signaling pathways activated by c-Kit in hematopoietic cells. *Int. J. Biochem. Cell Biol.* **31,** 1053–1074
48. Qi, J. C., Wang, J., Mandadi, S., Tanaka, K., Roufogalis, B. D., Madigan, M. C., Lai, K., Yan, F., Chong, B. H., Stevens, R. L., and Krilis, S. A. (2006) Human and mouse mast cells use the tetraspanin CD9 as an alternate interleukin-16 receptor. *Blood* **107,** 135–142
49. Krämer, B., Schulte, D., Körner, C., Zwank, C., Hartmann, A., Michalk, M., Söhne, J., Langhans, B., Nischalke, H. D., Coenen, M., Möhl, C., Vogt, A., Hennenberg, M., Sauerbruch, T., Spengler, U., and Nattermann, J. (2009) Regulation of NK cell trafficking by CD81. *Eur. J. Immunol.* **39,** 3447–3458

50. Kaji, K., Takeshita, S., Miyake, K., Takai, T., and Kudo, A. (2001) Functional association of CD9 with the Fcγ receptors in macrophages. *J. Immunol.* **166,** 3256–3265
51. Kuroda, K., Ozaki, Y., Qi, R., Asazuma, N., Yatomi, Y., Satoh, K., Nomura, S., Suzuki, M., and Kume, S. (1995) FcγII receptor-mediated platelet activation induced by anti-CD9 monoclonal antibody opens Ca^{2+} channels which are distinct from those associated with Ca^{2+} store depletion. *J. Immunol.* **155,** 4427–4436
52. Qi, R., Ozaki, Y., Kuroda, K., Asazuma, N., Yatomi, Y., Satoh, K., Nomura, S., and Kume, S. (1996) Differential activation of human platelets induced by Fcγ receptor II cross-linking and by anti-CD9 monoclonal antibody. *J. Immunol.* **157,** 5638–5645
53. Worthington, R. E., Carroll, R. C., and Boucheix, C. (1990) Platelet activation by CD9 monoclonal antibodies is mediated by the Fcγ II receptor. *Br. J. Haematol.* **74,** 216–222
54. Gupta, N., Wollscheid, B., Watts, J. D., Scheer, B., Aebersold, R., and DeFranco, A. L. (2006) Quantitative proteomic analysis of B cell lipid rafts reveals that ezrin regulates antigen receptor-mediated lipid raft dynamics. *Nat. Immunol.* **7,** 625–633
55. Liu, Y., Belkina, N. V., Park, C., Nambiar, R., Loughhead, S. M., Patino-Lopez, G., Ben-Aissa, K., Hao, J. J., Kruhlak, M. J., Qi, H., von Andrian, U. H., Kehrl, J. H., Tyska, M. J., and Shaw, S. (2012) Constitutively active ezrin increases membrane tension, slows migration, and impedes endothelial transmigration of lymphocytes *in vivo* in mice. *Blood* **119,** 445–453
56. Parameswaran, N., Matsui, K., and Gupta, N. (2011) Conformational switching in ezrin regulates morphological and cytoskeletal changes required for B cell chemotaxis. *J. Immunol.* **186,** 4088–4097
57. Treanor, B., Depoil, D., Bruckbauer, A., and Batista, F. D. (2011) Dynamic cortical actin remodeling by ERM proteins controls BCR microcluster organization and integrity. *J. Exp. Med.* **208,** 1055–1068
58. Staser, K., Shew, M. A., Michels, E. G., Mwanthi, M. M., Yang, F. C., Clapp, D. W., and Park, S. J. (2013) A Pak1-PP2A-ERM signaling axis mediates F-actin rearrangement and degranulation in mast cells. *Exp. Hematol.* **41,** 56–66
59. Yonemura, S., Hirao, M., Doi, Y., Takahashi, N., Kondo, T., Tsukita, S., and Tsukita, S. (1998) Ezrin/radixin/moesin (ERM) proteins bind to a positively charged amino acid cluster in the juxta-membrane cytoplasmic domain of CD44, CD43, and ICAM-2. *J. Cell Biol.* **140,** 885–895
60. Fleming, T. J., Donnadieu, E., Song, C. H., Laethem, F. V., Galli, S. J., and Kinet, J. P. (1997) Negative regulation of FcεRI-mediated degranulation by CD81. *J. Exp. Med.* **186,** 1307–1314
61. Ortega, E., Schweitzer-Stenner, R., and Pecht, I. (1988) Possible orientational constraints determine secretory signals induced by aggregation of IgE receptors on mast cells. *EMBO J.* **7,** 4101–4109
62. Gary, R., and Bretscher, A. (1995) Ezrin self-association involves binding of an N-terminal domain to a normally masked C-terminal domain that includes the F-actin binding site. *Mol. Biol. Cell* **6,** 1061–1075
63. Reczek, D., and Bretscher, A. (1998) The carboxyl-terminal region of EBP50 binds to a site in the amino-terminal domain of ezrin that is masked in the dormant molecule. *J. Biol. Chem.* **273,** 18452–18458
64. Hirao, M., Sato, N., Kondo, T., Yonemura, S., Monden, M., Sasaki, T., Takai, Y., Tsukita, S., and Tsukita, S. (1996) Regulation mechanism of ERM (ezrin/radixin/moesin) protein/plasma membrane association. Possible involvement of phosphatidylinositol turnover and Rho-dependent signaling pathway. *J. Cell Biol.* **135,** 37–51
65. Gonzalez-Espinosa, C., Odom, S., Olivera, A., Hobson, J. P., Martinez, M. E., Oliveira-Dos-Santos, A., Barra, L., Spiegel, S., Penninger, J. M., and Rivera, J. (2003) Preferential signaling and induction of allergy-promoting lymphokines upon weak stimulation of the high affinity IgE receptor on mast cells. *J. Exp. Med.* **197,** 1453–1465

1.5 TRANSMEMBRANE ADAPTOR PROTEIN PAG/CBP IS INVOLVED IN BOTH POSITIVE AND NEGATIVE REGULATION OF MAST CELL SIGNALING

Mol Cell Biol. 34(23):4285-300, 2014.

Previous studies in the laboratory investigated the role of TRAPs LAT and NTAL in mast cell signaling. Here we focused on deciphering the role of other TRAP, PAG, that has shown variable functions in immunoreceptor signaling across the literature. We used BMMCs derived from PAG KO mice and prepared also BMMCs with PAG KD. BMMCs with decreased expression of PAG showed impaired Ag-mediated activation but increased activation when stimulated via KIT receptor. Observed increased activity of SFKs in resting PAG deficient cells indicate that PAG regulates the basal activity of SFKs and increased SFK activity in PAG KO cells is involved in negative regulatory loop controlling FcεRI signaling.

MCB
Journals.ASM.org

Transmembrane Adaptor Protein PAG/CBP Is Involved in both Positive and Negative Regulation of Mast Cell Signaling

Lubica Draberova,[a] Viktor Bugajev,[a] Lucie Potuckova,[a] Ivana Halova,[a] Monika Bambouskova,[a] Iva Polakovicova,[a] Ramnik J. Xavier,[b,c] Brian Seed,[b] Petr Draber[a]

Department of Signal Transduction, Institute of Molecular Genetics, Academy of Sciences of the Czech Republic, Prague, Czech Republic[a]; Center for Computational and Integrative Biology, Massachusetts General Hospital, Harvard Medical School, Boston, Massachusetts, USA[b]; Broad Institute of Harvard University and Massachusetts Institute of Technology, Cambridge, Massachusetts, USA[c]

The transmembrane adaptor protein PAG/CBP (here, PAG) is expressed in multiple cell types. Tyrosine-phosphorylated PAG serves as an anchor for C-terminal SRC kinase, an inhibitor of SRC-family kinases. The role of PAG as a negative regulator of immunoreceptor signaling has been examined in several model systems, but no functions *in vivo* have been determined. Here, we examined the activation of bone marrow-derived mast cells (BMMCs) with PAG knockout and PAG knockdown and the corresponding controls. Our data show that PAG-deficient BMMCs exhibit impaired antigen-induced degranulation, extracellular calcium uptake, tyrosine phosphorylation of several key signaling proteins (including the high-affinity IgE receptor subunits, spleen tyrosine kinase, and phospholipase C), production of several cytokines and chemokines, and chemotaxis. The enzymatic activities of the LYN and FYN kinases were increased in nonactivated cells, suggesting the involvement of a LYN- and/or a FYN-dependent negative regulatory loop. When BMMCs from PAG-knockout mice were activated via the KIT receptor, enhanced degranulation and tyrosine phosphorylation of the receptor were observed. *In vivo* experiments showed that PAG is a positive regulator of passive systemic anaphylaxis. The combined data indicate that PAG can function as both a positive and a negative regulator of mast cell signaling, depending upon the signaling pathway involved.

Mast cells are widely distributed in the body, where they play important roles in innate as well as adaptive immune responses (1). To fulfill their role in adaptive immune responses, the cells express the high-affinity IgE receptor FcεRI on their plasma membranes. Aggregation of this tetrameric immunoreceptor, αβγ2, induces cell signaling events leading to the release of preformed inflammatory mediators and the *de novo* synthesis and release of leukotrienes, cytokines, and chemokines. The first well-defined biochemical step after FcεRI triggering is tyrosine phosphorylation of the immunoreceptor tyrosine-based activation motifs in the cytoplasmic tail of the FcεRI β and γ subunits by the SRC family protein tyrosine kinase (PTK) LYN (2, 3). The phosphorylated β and γ subunits then serve as binding and activation sites for LYN kinase and spleen tyrosine kinase (SYK), respectively. These two enzymes, together with FYN and other kinases, then phosphorylate various adaptor proteins and enzymes with a variety of functions in signal transduction pathways. The exact molecular events preceding LYN-mediated tyrosine phosphorylation of the FcεRI β subunit are not clear, and several models have been proposed, including the transphosphorylation model (4), the lipid raft model (5), and the PTK-protein tyrosine phosphatase (PTP) interplay model (6).

Our previous study with murine bone marrow-derived mast cells (BMMCs) showed that FcεRI triggering induced transient hyperphosphorylation of LYN kinase on its C-terminal regulatory tyrosine (Tyr 487), leading to the formation of a closed inactive conformation where the SRC homology 2 (SH2) domain interacts with phospho-Tyr 487 and transiently decreases LYN enzymatic activity (7). This finding was surprising because in T cells the corresponding SRC family kinase (SFK), LCK, showed decreased tyrosine phosphorylation of the C-terminal regulatory tyrosine and enhanced enzymatic activity after activation through T cell immunoreceptors (8, 9). Phosphorylation of the C-terminal inhibitory tyrosine in SFKs is catalyzed by the C-terminal SRC kinase (CSK) (10), a cytoplasmic PTK that can be anchored through its SH2 domain to PAG (11), also termed CBP (12). PAG/CBP (here, PAG) is a ubiquitously expressed transmembrane adaptor protein containing a short extracellular domain, a transmembrane domain, and a long cytoplasmic tail with multiple tyrosine-based motifs. Phosphorylated Tyr 314 in mouse PAG has been shown to be essential for CSK binding. PAG also possesses two proline-rich sequences that serve as binding sites for proteins with SH3 domains and a C-terminal VTRL motif for interaction with the PDZ domain of the cytoskeletal linker ezrin/radixin/moesin-binding protein of 50 kDa (13). Similar to some other transmembrane adaptor proteins, such as the non-T cell activation linker and linker for activation of T cells (LAT), PAG has two conserved cysteine residues, located in the vicinity of the transmembrane domain, which are the subject of posttranslational palmitoylation and which contribute to the poor solubility of the proteins in nonionic detergents and their presumed localization in membrane microdomains called lipid rafts (14, 15).

PAG in resting T cells associates with FYN kinase, which constitutively phosphorylates PAG on Tyr 314 to create a docking site for the CSK SH2 domain. This binding brings CSK to the vicinity of its substrate, SFK LCK, and enhances CSK catalytic activity, leading to phosphorylation of the LCK-inhibitory C-terminal tyrosine. Upon T cell receptor activation, PAG is rapidly dephospho-

Received 25 July 2014 **Accepted** 13 September 2014
Published ahead of print 22 September 2014
Address correspondence to Petr Draber, draberpe@img.cas.cz.

doi:10.1128/MCB.00983-14

rylated, CSK is released from PAG, and LCK is dephosphorylated on its C-terminal tyrosine. This modification increases the activity of LCK, leading to increased tyrosine phosphorylation of T cell receptor subunits and other substrates. A negative regulatory role of PAG in T cell signaling was confirmed in experiments with PAG knockdowns (KDs) (16) but not with PAG knockouts (KOs) (17, 18), suggesting that developmental compensatory mechanisms are involved.

In mast cells, PAG is phosphorylated by LYN kinase instead of FYN kinase, and following FcεRI triggering, the decrease in PAG phosphorylation is replaced by an increase (19, 20). Overexpression of PAG has been reported to inhibit FcεRI-mediated degranulation in rat basophilic leukemia (RBL) cells (21). Further experiments showed that FcεRI activation of BMMCs from LYN-deficient mice resulted in enhanced degranulation, whereas FYN-deficient cells showed the opposite effect (22–24). This finding supports the concept that SFKs are tightly regulated in the course of mast cell activation and important differences exist between early regulatory events induced by engagement of the T cell receptors and FcεRI. The exact role of PAG in mast cell activation remains to be determined.

Herein we present data on FcεRI-mediated activation events in BMMCs derived from mice deficient in PAG (PAG-KO mice) and from the corresponding wild-type (WT) mice (PAG-WT mice). We also attempted to determine whether any differences in activation are detectable between BMMCs in which PAG is downregulated by RNA interference and the corresponding control cells. Furthermore, we examined the role of PAG in cells activated through another important mast cell surface receptor, KIT. The combined data indicate that PAG functions as a positive or negative regulator of mast cell signaling and that the specific effect depends on the particular signaling pathway. We also show that PAG-deficient mice have a distinct phenotype *in vivo*, as assessed by induction of a passive systemic anaphylaxis response.

MATERIALS AND METHODS

Mice and cells. Mice deficient in PAG were generated by use of a modified bacterial artificial chromosome technology as previously described (25, 26). Briefly, the bacterial artificial chromosome clones were electroporated into strain 129Sv/J embryonic stem cells. Targeting in clone 7 was confirmed by fluorescence *in situ* hybridization. PAG-KO mice derived from clone 7 were born in the expected Mendelian frequency and were healthy. Transgenic founders were backcrossed to C57BL/6 mice for more than eight generations. For experiments, PAG-KO mice were mated with C57BL/6 mice, and their F1 descendants were genotyped by PCR using the following primers: PAG 1 F (5′-GAC AGC ACA GGA AAG GCC AAG-3′), PAG 2 R (5′-GTG TCC ACC GGT CCC TTC TG-3′), and PAG ZEO R (5′-CCA GGG TGT TGT CCG GCA C-3′), giving PCR products of 498 and 390 bp for the WT and PAG-KO alleles, respectively. Bone marrow cells were isolated from the femurs and tibias of 6- to 8-week-old PAG-KO mice or their WT littermates (PAG-WT mice). All animal studies were performed in compliance with the *Guide for the Care and Use of Laboratory Animals* (27) and were approved by the Animal Care and Usage Committee of the Institute of Molecular Genetics. Cells were cultured in RPMI 1640 medium supplemented with 100 U/ml penicillin, 100 μg/ml streptomycin, 71 μM 2-mercaptoethanol, minimum essential medium (MEM) nonessential amino acids, 0.7 mM sodium pyruvate, 2.5 mM L-glutamine, 12 mM D-glucose, recombinant mouse stem cell factor (SCF; 20 ng/ml; PeproTech EC), mouse recombinant interleukin-3 (IL-3; 20 ng/ml; PeproTech EC), and 10% fetal calf serum (FCS).

Antibodies and reagents. The following monoclonal antibodies (MAbs) were used: anti-LAT (28), anti-LYN (29), anti-FcεRI β chain (30), trinitrophenol (TNP)-specific immunoglobulin E (IgE) (IGEL b4.1) (31), and anti-hypoxanthine guanine phosphoribosyltransferase (anti-HPRT; Santa Cruz Biotechnology Inc.). Antipaxillin was obtained from BD Transduction Laboratories. Polyclonal antibodies specific for LYN and LAT were prepared in the Department of Signal Transduction, Prague, Czech Republic, by immunization of rabbits with the corresponding recombinant proteins or their fragments (32). Rabbit anti-IgE was prepared by immunization with whole IGEL b4.1. Polyclonal antibodies specific for FYN, actin, phospholipase C γ1 (PLCγ1), PLCγ2, GRB2, CSK, KIT, STAT5, SHIP1, phospho-KIT (Y568/570), and phospho-focal adhesion kinase (phospho-FAK; Y925), as well as horseradish peroxidase (HRP)-conjugated donkey anti-goat IgG, goat anti-mouse IgG, and goat anti-rabbit IgG, were obtained from Santa Cruz Biotechnology Inc. Antibodies specific for phospho-SYK (Y525/Y526), phospho-STAT5 (Y694), phospho-SH2-containing inositol 5′-phosphatase 1 (SHIP1; Y1020), and the Myc tag were obtained from Cell Signaling. PAG-specific rabbit polyclonal antibody was from Exbio. HRP-conjugated antiphosphotyrosine MAb (PY-20) was obtained from BD Biosciences. Antibodies specific for tumor necrosis factor alpha (TNF-α), IL-6, and IL-13 were purchased from PeproTech EC. Anti-mouse FcεRI labeled with fluorescein isothiocyanate (FITC) and anti-mouse KIT–allophycocyanin (APC) conjugates were obtained from eBiosciences. ^{45}Ca (specific activity, 773 MBq/mg Ca^{2+}) and [γ-^{32}P]ATP (specific activity, 222 TBq/mmol) were purchased from the Institute of Isotopes Co., Ltd. (Budapest, Hungary). A donkey anti-rabbit IgG–Alexa Fluor 488 conjugate and thapsigargin were obtained from Invitrogen. Mowiol 4-88 mounting solution was from Merck. Colloidal gold nanoparticles (Au-NPs; diameter, 30 nm), consisting of approximately 2×10^{11} Au-NPs/ml, were obtained from BBInternational. All other reagents were from Sigma-Aldrich.

Lentivirus shRNA constructs and cell transduction. A set of four murine Pag1 (Swiss-Prot accession number Q3U1F9) short hairpin (shRNA) constructs based on the pLKO.1 vector (TRCN0000124814 [shRNA14], TRCN0000124815 [shRNA15], TRCN0000124816 [shRNA16], and TRCN0000124817 [shRNA17]) were obtained from Open Biosystems. Each of the Pag1 shRNA constructs (14 μg) was mixed with Opti-MEM (1 ml; Invitrogen), 21 μl of ViraPower lentiviral packaging mix (Invitrogen), and 82 μl of Lipofectamine 2000 (Invitrogen). The mixture was homogenized by vortexing for 10 s and then incubated at room temperature for 20 min before it was added to semiconfluent (70%) HEK-293FT packaging cells growing in 20 ml of freshly added Dulbecco's medium supplemented with antibiotic and 10% FCS in 150-cm^2 tissue culture flasks. Three days later, the viruses in the culture supernatant were concentrated by centrifugation at 25,000 rpm for 2 h using a JA-25.50 rotor (Beckman Coulter). The pellets were resuspended in 1 ml of culture medium and added to 29 ml of culture medium containing 5×10^7 BMMCs. After 2 days, the medium was changed to virus-free medium and the cells were cultured for an additional 2 days (recovery period). Stable selection was achieved by culturing the transduced cells for 1 week in the presence of puromycin (5 μg/ml). Cells were pooled and analyzed for PAG expression by immunoblotting. Cells with the highest reduction in the amount of PAG, obtained with shRNA14 and shRNA15, were used for further experiments. Cells transfected with empty pLKO.1 vector were used as negative controls. For rescue experiments, mouse Pag1 cDNA (RefSeq accession number BC145761; catalog number 40131064; Open Biosystems) was amplified using forward primer 5′-AAAGAATTCGCCG CCACCATGGGCCCTGCAGGAAGCGT-3′ (the EcoRI restriction site is underlined, the coding sequence is in bold) and reverse primer 5′-TTTG TCGACGAGCCTGGTGACATCTCTGC-3′ (the SalI restriction site is underlined, the coding sequence is in bold). The amplified DNA was cloned via the EcoRI and SalI restriction sites (upstream of Myc) into the pFLAG-CMV-5a expression vector (Sigma-Aldrich) modified to express the Myc tag (kindly provided by V. Korinek). The cassette encoding the Myc-tagged Pag1 sequence was then amplified with the same forward primer described above and reverse primer 5′-TTTGCGGCCGCTTACA GGTCCTCCTCTGAGA-3′ (the NotI restriction site is underlined, the

coding sequence is in bold) and recloned via EcoRI and NotI restriction sites into the pCDH-CMV-MCS-EF1-Puro expression lentivector (pCDH; catalog number CD510B-1; System Biosciences). The construct was verified by DNA sequencing. Viruses with pCDH-Pag-myc or empty pCDH were produced as described above. Medium with virus (30 ml) was filtered through a 0.22-μm-pore-size filter and divided into two aliquots. The first aliquot was used to transduce the WT or PAG-KO BMMCs at day 0. The second aliquot was preserved at 4°C and used for the second transduction of the same cells at day 3. Stable selection was achieved by culturing the cells for 7 days in the presence of puromycin (2 μg/ml), added 5 days after the first transduction.

Flow cytometry. To determine the surface expression of FcεRI, cells were exposed to FITC-conjugated anti-FcεRI (1 μg/ml). The samples were evaluated by flow cytofluorometry using a FACSCalibur instrument (BD Biosciences). For rescue experiments, cells were sensitized with TNP-specific IgE for 20 h of incubation in culture medium without IL-3 and SCF. Then they were washed and activated by antigen (TNP-bovine serum albumin [BSA] conjugate; 15 to 25 mol of TNP/mol of BSA; 100 ng/ml) for 90 min and fixed in 4% paraformaldehyde for 10 min at 37°C. The cells were washed once in phosphate-buffered saline (PBS), and free binding sites were blocked with 5% normal donkey serum (Jackson ImmunoResearch Laboratories) in PBS. After washing, the cells were incubated for 45 min with anti-TNF antibody diluted 1:100 in PBS with 0.5% BSA. After repeated washing, the cells were incubated for 30 min with a secondary donkey anti-rabbit IgG–Alexa Fluor 488 antibody conjugate, washed, and analyzed by flow cytometry using an LSR II flow cytometer (Becton Dickinson). For analysis of peritoneal mast cells, mice were sacrificed and injected intraperitoneally with 5 ml of PBS supplemented with 1% FCS. The peritoneal cavity was gently massaged for 30 s, and the injected PBS with free peritoneal fluid cells was withdrawn. One milliliter of PBS with peritoneal cells was spun down (400 × *g*, 5 min), and the cells were washed in cold PBS and stained for FcεRI (as described above) or KIT using the anti-mouse KIT–APC conjugate.

Cell activation. Before the experiments, BMMCs were cultured for 48 h in medium without SCF, followed by incubation for 12 to 16 h in SCF- and IL-3-free medium supplemented with IgE (1 μg/ml). Sensitized cells were washed in buffered salt solution (BSS; 20 mM HEPES, pH 7.4, 135 mM NaCl, 5 mM KCl, 1.8 mM $CaCl_2$, 5.6 mM glucose, 1 mM $MgCl_2$, 0.1% BSA). To quantify degranulation, the cells (0.15×10^6) in 30-μl aliquots were transferred into the wells of a 96-well plate and challenged with 30 μl of antigen (TNP-BSA conjugate), thapsigargin, or SCF at the concentrations indicated in Results. The degree of degranulation was determined as the amount of β-glucuronidase released into the supernatant, as described previously (33). Briefly, 40-μl aliquots of the cell supernatants were mixed in white wells of a 96-well plate (Nunc) with 40 μl of β-glucuronidase substrate (40 μM 4-methylumbelliferyl-β-D-glucuronide hydrate). After incubation for 60 min at 37°C, the reaction was stopped by adding 200 μl of ice-cold 0.2 M glycine buffer, pH 10.0, and fluorescence was determined in an Infinite M200 microtiter plate reader (Tecan) with 355-nm excitation and 460-nm emission filters. The total content of the enzyme in the cells was evaluated by measuring the levels of enzyme in the supernatant from cells lysed in 1% Triton X-100.

Extracellular calcium uptake. Calcium uptake was determined by a modification of a previously described procedure (34). Briefly, IgE-sensitized BMMCs (2×10^6) were resuspended in 100 μl BSS-BSA with 1 mM Ca^{2+}, mixed with 100 μl of BSS-BSA supplemented with $^{45}Ca^{2+}$ and various concentrations of antigen or thapsigargin, and incubated for selected time intervals at 37°C. The reactions were terminated by placing the tubes on ice and then suspending 100-μl aliquots on the walls of microtest tubes to make them separated by air space from the 12% BSA in PBS (300 μl) at the bottoms. Cells with bound $^{45}Ca^{2+}$ were separated from free $^{45}Ca^{2+}$ by centrifugation through 12% BSA at 3,220 × *g* for 15 min at 4°C. The cell pellets were recovered by freezing the tubes and slicing off the tube bottoms, and the cell pellets were solubilized with 1 ml of 1% Triton X-100. The radioactivity was counted in 10 ml scintillation liquid (EcoLite; ICN Biomedicals) in a scintillation counter with QuantaSmart software (PerkinElmer).

Immunoprecipitation and immunoblotting. Cells were pelleted and solubilized in ice-cold lysis buffer for immunoprecipitation (25 mM Tris-HCl, pH 8.0, 140 mM NaCl, 1 mM Na_3VO_4, 2 mM EDTA, 1 μg/ml aprotinin, 1 μg/ml leupeptin, 1 mM phenylmethylsulfonyl fluoride) supplemented with 1% *n*-dodecyl-β-D-maltoside and 1% Nonidet P-40 (for most experiments), 0.2% Triton X-100 (for FcεRI immunoprecipitation), or 1% Brij 96 (for kinase assays). After incubation (30 min on ice), the lysates were spun down (16,000 × *g* for 5 min at 4°C) and postnuclear supernatants were immunoprecipitated with the corresponding antibodies prebound to UltraLink-immobilized protein A or G (Pierce, Thermo Scientific). The immunoprecipitates were size fractionated by sodium dodecyl sulfate-polyacrylamide gel electrophoresis (SDS-PAGE) and immunoblotted with phosphotyrosine-specific PY-20–HRP conjugate or with protein-specific antibodies, followed by HRP-conjugated anti-mouse or anti-rabbit IgG antibody. Some phosphorylated proteins were determined by direct immunoblotting with phosphoprotein-specific antibodies, followed by immunoblotting with the corresponding secondary HRP-conjugated anti-mouse or anti-rabbit IgG. The HRP signal was detected by chemiluminescence. Immunoblots were quantified by use of a luminescent image analyzer (LAS-3000; Fuji Photo Film Co., Tokyo, Japan) and further analyzed by Aida image analyzer software (Raytest). The amount of phosphorylated proteins was normalized to the amount of immunoprecipitated proteins after stripping off the membranes, followed by development with the corresponding antibodies. In some experiments, parallel immunoblots instead of stripped membranes were used.

Sucrose density gradient fractionation. Sucrose density gradient separations were performed as previously described (35), with some modifications. Briefly, BMMCs (30×10^6) were lysed with 0.8 ml ice-cold lysis buffer (20 mM Tris-HCl, pH 8.0, 100 mM NaCl, 10 mM EDTA, 1 mM Na_3VO_4, 10 mM glycerophosphate, 1 mM phenylmethylsulfonyl fluoride, 100× diluted protease inhibitor cocktail, 5 mM iodoacetamide) supplemented with 1% Brij 96. The lysates were homogenized by passing them 10 times through a 27-gauge needle and adjusted to 40% (wt/vol) using 80% stock sucrose in 25 mM Tris-HCl, pH 7.5, 125 mM NaCl, and 2 mM EDTA. The gradient was prepared by adding 0.5 ml 80% sucrose at the bottom of a polyallomer tube (11 by 60 mm; Beckman Instruments), followed by 1.5 ml of 40% sucrose containing the cell lysate, 2 ml of 30% sucrose, and 1 ml of 10% sucrose. The gradient was ultracentrifuged at 210,000 × *g* for 4 h at 4°C using an SW55 Ti rotor (Beckman Instruments), and 0.5-ml fractions were collected from the top.

Immunocomplex kinase assay. The *in vitro* kinase assays were performed as previously described (36), with some modifications. FcεRI, LYN, and FYN were immunoprecipitated from nonactivated or antigen-activated cells lysed in lysis buffer for immunoprecipitation. Proteins immobilized to antibody-armed protein A beads were washed with kinase buffer (25 mM HEPES–NaOH, pH 7.2, 3 mM $MnCl_2$, 0.1% Nonidet P-40, 100 mM Na_3VO_4, 20 mM $MgCl_2$) and then resuspended in 25 μl kinase buffer supplemented with 2.5 μCi (92.5 kBq) of [γ-^{32}P]ATP, 100 μM ATP, and 0.5 μg/μl of acid-denatured enolase as the exogenous substrate. After incubation for 30 min at 37°C, the immunoprecipitates were eluted from the beads with reducing 2×-concentrated SDS-PAGE sample buffer and boiled for 7 min. The ^{32}P-labeled proteins were size fractionated by SDS-PAGE, transferred to a nitrocellulose membrane, and visualized by autoradiography. Films were quantified with Aida image analyzer software.

Cytokine and chemokine detection. IgE-sensitized BMMCs were activated with different concentrations of antigen. One hour later, mRNA was extracted using a TurboCapture 96 mRNA kit (Qiagen). Single-stranded cDNA was synthesized with Moloney murine leukemia virus reverse transcriptase (Invitrogen) according to the manufacturer's instructions. Real-time PCR amplifications of cDNAs were performed in 10-μl reaction volumes of a quantitative PCR (qPCR) mix containing 1 M 1,2-propanediol, 0.2 M trehalose, and SYBR green 1 (37) in 384-well

plates sealed with LightCycler 480 sealing foil (Roche Diagnostics) and analyzed in a LightCycler 480 apparatus (Roche Diagnostics). The following primer sets (sense/antisense) were used for amplification of the different cDNA fragments (the sizes of the amplified fragments are indicated in parentheses): actin, 5′-GATCTGGCACCACACCTTCT-3′/5′-GGGGTG TTGAAGGTCTCAAA-3′ (138 bp); glyceraldehyde-3-phosphate dehydrogenase (GAPDH), 5′-AACTTTGGCATTGTGGAAGG-3′/5′-ATCCA CAGTCTTCTGGGTGG-3′ (69 bp); ubiquitin, 5′-ATGTGAAGGCCAA GATCCAG-3′/5′-TAATAGCCACCCCTCAGACG-3′ (160 bp); TNF-α, 5′-CCCTCACACTCAGATCATCTTCT-3′/5′-GCTACGACGTGGGCT ACAG-3′ (61 bp); IL-6, 5′-GAGGATACCACTCCCAACAGACC-3′/5′-AAGTGCATCATCGTTGTTCATACA-3′ (141 bp); IL-13, 5′-AGACCA GACTCCCCTGTGCA-3′/5′-TGGGTCCTGTAGATGGCATTG-3′ (123 bp); CCL3, 5′-CATCGTTGACTATTTTGAAACCAG-3′/5′-GCCGGTT TCTCTTAGTCAGGAA-3′ (72 bp); and CCL4, 5′-CTTGGAGTTGAAC TGAGCAGC-3′/5-AGAGGGGCAGGAAATCTGAA-3′ (126 bp). The following cycling conditions were used: 3 min at 95°C, followed by 50 cycles of 10 s at 95°C, 20 s at 60°C, and 20 s at 72°C. Threshold cycle (C_T) values were determined by automated threshold analysis of the cycler. The specificity of the PCR was evaluated by examining melting curves. The genes for actin, GAPDH, and ubiquitin were used as reference genes, and the expression levels of all mRNAs were normalized to the geometric mean level of expression of these genes. The relative increase in the expression level of a cytokine was normalized to the level of expression by nonactivated WT cells in each experiment.

For detection of cytokines, an immuno-PCR method was used as described previously (38). Briefly, anti-TNF-α (1 μg/ml), anti-IL-6 (2 μg/ml), or anti-IL-13 (1 μg/ml) in 100 mM borate buffer (pH 9.5) was dispensed in 50-μl aliquots into the wells of a real-time 96-well plate (Eppendorf). After overnight incubation at 4°C, each well was washed four times with 200 μl of Tris-buffered saline (10 mM Tris-HCl, pH 7.4, 150 mM NaCl) containing 0.05% Tween 20 (TBST), and the remaining binding sites were blocked by 2 h of incubation at 37°C with TBST supplemented with 2% BSA. After washing, 50 μl of serial dilutions (0.1 to 100 ng/ml) of recombinant TNF-α, IL-6, or IL-13 (all from PeproTech EC) or the tested samples diluted in PBS–1% BSA was added. The samples were incubated for 1 h at 37°C, and after washing with TBST, 50 μl of Au-NPs armed with thiolated DNA oligonucleotide template (5′-thiol modifier C6 S-S/18-atom hexa-ethyleneglycol spacer-CCTTGAACCT GTGCCATTTGAATATATTAAGACTATACGCGGGAACA-3′] and with the corresponding cytokine-specific antibody was applied into each well. The wells were incubated for 1 h at 37°C and washed with TBST and deionized water. Fifty-microliter aliquots of qPCR master mix solution (see above) supplemented with 60 nM oligonucleotide primers 5′-CCTTGAACCTGTGCC ATTTG-3′ and 5′-GTCCCTCCATCTTCCTACTGTTCCACATGTTC CCGCGTATAGTCTT-3′ were then dispensed into each well. The plates were sealed, and the amount of template DNA bound to antigen-anchored functionalized Au-NPs was evaluated by real-time PCR using a Realplex4 Mastercycler apparatus (Eppendorf) with the following cycling conditions: 2 min at 94°C, followed by 40 cycles of 20 s at 94°C, 20 s at 53°C, and 20 s at 72°C. For the calculation of TNF-α, IL-6, and IL-13 concentrations, the corresponding C_T values were substituted into the regression equations obtained from the calibration curves constructed from the concentration series of appropriate recombinant proteins.

Chemotaxis assay. Chemotaxis responses were assayed in 24-well Transwell chambers (Corning) with 8-μm-pore-size polycarbonate filters in the upper wells. Chemoattractants (antigen or SCF) in 0.6 ml chemotaxis medium (RPMI 1640 supplemented with 1% BSA and 20 mM HEPES, pH 7.4) were added to the lower wells. IgE-sensitized BMMCs (0.3×10^6 in 120 μl chemotactic medium) were added to the upper wells. Cells migrating into the lower wells during the 8 h of incubation (37°C, 5% CO_2) were counted using an Accuri C6 flow cytometer (BD Biosciences).

Confocal microscopy. BMMCs (3×10^5) were attached to fibronectin-coated multitest slides (MP Biomedicals). Cells were fixed with 4% paraformaldehyde for 15 min at room temperature and permeabilized in 0.3% Triton X-100 for 20 min. Free binding sites were blocked with 5% normal donkey serum, and the cells were stained with rabbit anti-Myc tag antibody, followed by labeling with secondary antibody (donkey anti-rabbit IgG–Alexa Fluor 488 conjugate). After 60 min, the cells were washed and mounted in Mowiol 4-88 mounting solution supplemented with Hoechst 33258 nucleic acid stain (1 μg/ml; Molecular Probes) to label the nuclei. Samples were examined with a confocal laser scanning microscope (Leica TCS SP5) equipped with a ×63 (numerical aperture, 1.4) oil immersion objective.

Passive systemic anaphylaxis. The systemic anaphylactic reaction is accompanied by the release of histamine from activated mast cells, leading to a decreased body temperature (39). The body temperature was measured with an accuracy of ±0.1°C using a VitalView data acquisition system with ER-4000 energizer receivers, G2 E-mitter transponders, and VitalView software (Mini Mitter). G2 probes were implanted intra-abdominally into mice while they were under systemic anesthesia with isoflurane (Abbott Laboratories). Monitoring of body temperature was initiated 9 days after the surgery. Mice aged 11 to 18 weeks were sensitized by tail vein injection of TNP-specific IgE (3 μg in 100 μl PBS per mouse), and 24 h later, anaphylaxis was induced by intravenous administration of antigen (500 μg in 100 μl PBS per mouse). The body temperature was recorded at 1-min intervals for at least 3 h after antigen challenge.

Serum IgE quantification. Ninety-six-well enzyme-linked immunosorbent assay plates (Nunc) were coated for 16 h at 4°C with rat antibody specific for mouse IgE (1 μg/ml in PBS; 50 μl/well; BD Biosciences). Wells were washed (four times with TBST) and blocked by incubation at 22°C with TBST–2% BSA. After 2 h, the plates were washed and incubated for 1 h at 22°C with various concentrations of mouse IgE standard (1.95 to 125 ng/ml in PBS–1% BSA; BD Biosciences) or mouse serum samples (diluted 1:5 in PBS–1% BSA). Then, the wells were washed and the captured IgE was detected with biotinylated rat anti-mouse IgE antibody (2 μg/ml in PBS–1% BSA; BD Bioscience), washed, and incubated for 30 min with streptavidin-HRP conjugate (diluted 1:1,000 in PBS–1% BSA; BD Biosciences). Peroxidase substrate solution (0.5 mg/ml *o*-phenylenediamine and 0.015% H_2O_2 in 0.1 M NaH_2PO_4, pH 6.0) was used for colorimetric reaction. The reaction was stopped by adding 50 μl of 4 M H_2SO_4, and the absorbance at 492 nm was determined using an Infinite M200 plate reader (Tecan).

Statistical analysis. The significance of intergroup differences was evaluated by Student's *t* test.

RESULTS

Positive regulatory role of PAG on antigen-induced degranulation. To examine the role of PAG in mast cell signaling, we isolated bone marrow cells from homozygous F1-descendant PAG-KO and PAG-WT mice and cultured them in the presence of IL-3 and SCF to obtain BMMCs. Cells with or without PAG exhibited comparable growth parameters under *in vitro* conditions (not shown), suggesting that PAG had no effect on the growth response of mast cells to IL-3 and SCF. The same PAG-WT BMMCs were used for the production of PAG-KD cells after transduction with lentiviral vectors containing PAG shRNA constructs based on a pLKO vector (shRNA14 to shRNA17), followed by selection in puromycin. PAG-WT BMMCs infected with empty lentiviral vector were used as a negative control (pLKO). PAG-KO and PAG-WT cells expressed comparable amounts of surface FcεRI, as detected by flow cytometry (Fig. 1A). Similarly, no difference in surface FcεRI was observed among various PAG-KD cells and controls (not shown). As expected, we found no detectable PAG in PAG-KO cells using immunoblotting with PAG-specific antibody (Fig. 1B). The amount of PAG in PAG-KD cells was substantially reduced compared to that in control (pLKO) cells. The strongest inhibition was observed in the cells infected with the shRNA14 and shRNA15

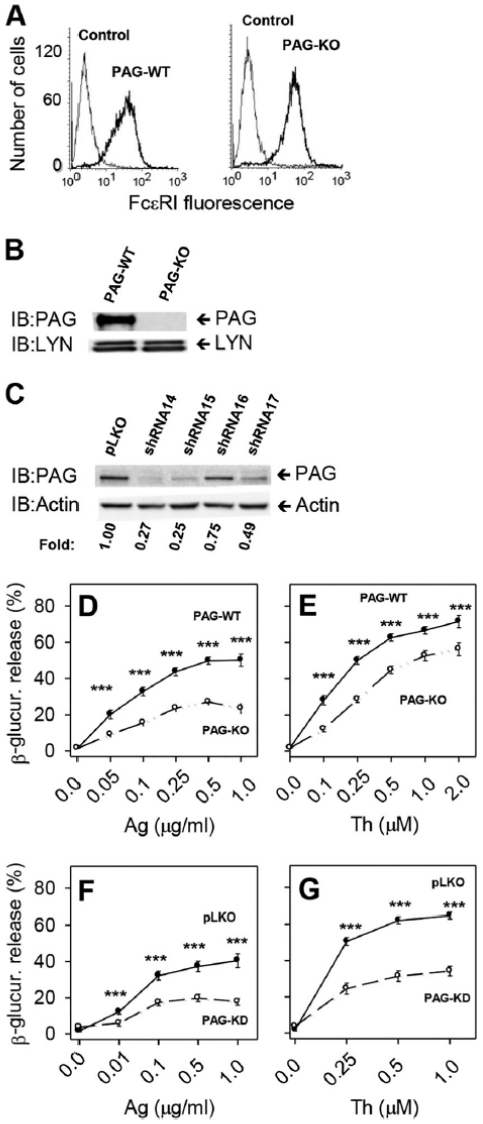

FIG 1 Positive regulatory role of PAG in antigen- or thapsigargin-induced degranulation. (A) BMMCs derived from WT mice (PAG-WT) or PAG-deficient mice (PAG-KO) were stained for surface FcεRI by use of an anti-FcεRI-FITC conjugate. Unstained WT cells were used as negative controls. Samples were analyzed by flow cytometry. (B, C) The presence of PAG in lysates from PAG-WT and PAG-KO BMMCs (B) or WT BMMCs infected with empty pLKO lentiviral vector (pLKO) or lentiviral vectors shRNA14 to shRNA17 (C) was determined by immunoblotting (IB). As loading controls, the membranes were also developed for LYN (B) or actin (C). The amount of PAG normalized to its amount in cells infected with the empty pLKO vector and actin loading control (fold) is also shown (C). For each panel, the results of one representative experiment out of a minimum of three performed are shown. (D, E) PAG-WT or PAG-KO BMMCs were sensitized (D) or not (E) with TNP-specific IgE (1 μg/ml) and then stimulated for 30 min with various concentrations of antigen (Ag) (D) or thapsigargin (Th) (E). (F, G) PAG-WT BMMCs were infected with empty pLKO lentiviral vector (pLKO) or with PAG shRNA14 and shRNA15 vectors (PAG-KD), and stable transfectants were activated with antigen (F) or thapsigargin (G), as described above. The amount of β-glucuronidase (β-glucur.) released from the cells was determined 30 min after triggering. Data represent means ± SEs calculated from 11 independent experiments performed in duplicate or triplicate in panels D and E and from 6 to 8 independent experiments performed in duplicate or triplicate in panels F and G. The statistical significance of differences between PAG-WT and PAG-KO cells or pLKO and PAG-KD cells is shown: ***, $P < 0.001$.

constructs, which reduced PAG expression by 73% and 75%, respectively (Fig. 1C). Infection with constructs containing shRNA16 and shRNA17 reduced PAG expression by 25% and 51%, respectively. Guided by these data, we used viruses containing shRNA14 and shRNA15 for further experiments with BMMCs. Because of the similar knockdown characteristics of these constructs, data from BMMCs infected with these shRNAs were combined and are presented under the common heading of PAG-KDs.

Using BMMCs with PAG-KO and PAG-KD and the corresponding controls, we first investigated whether PAG deficiency has any effect on mast cell degranulation after FcεRI triggering. Degranulation was estimated from the amount of β-glucuronidase released from activated cells. BMMCs were sensitized with TNP-specific IgE and then exposed to various concentrations of antigen. After 30 min, PAG-KO cells exhibited significantly lower levels of degranulation than WT cells at all concentrations of the antigen tested (0.05 to 1.0 μg/ml; Fig. 1D); the total amount of β-glucuronidase released from both cell types by Triton X-100 was similar (data not shown). These data indicate that the absence of PAG reduces antigen-induced degranulation but does not interfere with the production of β-glucuronidase in secretory vesicles. Significant inhibition of degranulation was also observed in PAG-KO cells activated with various concentrations of thapsigargin (0.1 to 2.0 μM; Fig. 1E). Thapsigargin induces the release of Ca^{2+} from intracellular stores by inhibiting the endoplasmic reticulum (ER) ATPase (40). The combined data suggest that PAG not only is involved in the CSK-mediated FcεRI-proximal regulation of SFKs but also could still have other functions distal to FcεRI regulation.

To test whether compensatory developmental alterations could be responsible for the unexpected properties of PAG-KO BMMCs, we examined antigen- and thapsigargin-induced degranulation in cells with PAG-KD and the corresponding controls. The data shown in Fig. 1F and G demonstrate that stimulation of PAG-KD cells with antigen or thapsigargin decreased the level of degranulation compared to that in the pLKO controls, supporting previous findings that PAG is a positive regulator of mast cell degranulation.

Positive regulatory role of PAG on Ca^{2+} response. Early events in mast cell signaling involve the release of Ca^{2+} from intracellular stores followed by the influx of extracellular Ca^{2+} through store-operated Ca^{2+} (SOC) channels in the plasma membrane (41). To determine whether PAG has a role in this process, we quantified Ca^{2+} uptake in PAG-deficient and control BMMCs. The data presented in Fig. 2A show that stimulation with antigen causes significantly lower levels of uptake of extracellular $^{45}Ca^{2+}$ in PAG-KO cells than in PAG-WT cells, reaching a peak at approximately 5 min after triggering in both cell types. Inhibition of Ca^{2+} uptake in PAG-KO cells was observed 5 min after triggering at all concentrations of the antigen tested (Fig. 2B). Significant inhibition of Ca^{2+} uptake in PAG-KO cells was also seen after stimulation for various time intervals (Fig. 2C) or with various

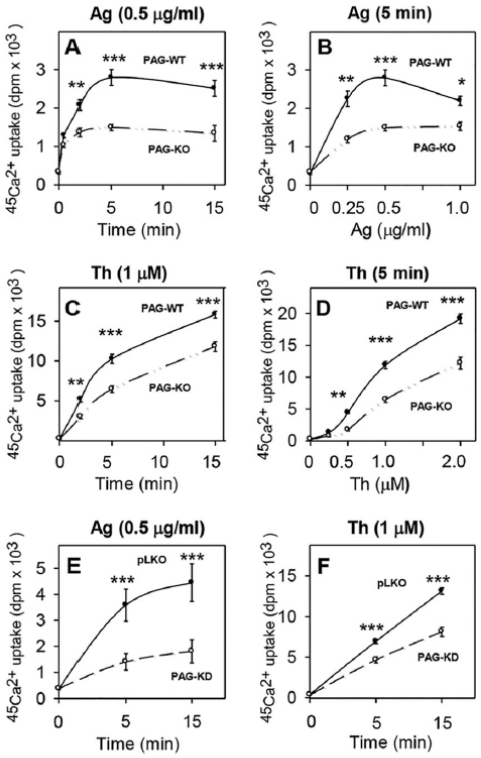

FIG 2 Positive regulatory role of PAG on antigen- or thapsigargin-induced calcium uptake. (A, B) PAG-WT and PAG-KO BMMCs were sensitized with IgE and then stimulated for various time intervals with antigen (0.5 μg/ml) (A) or with various concentrations of antigen for 5 min (B) in the presence of 1 mM extracellular $^{45}Ca^{2+}$. The reactions were terminated by centrifugation of the cells through a BSA gradient, and cell-bound radioactivity (in the sediment) was determined. (C, D) PAG-WT and PAG-KO BMMCs were activated for various time intervals with 1 μM thapsigargin (C) or with various concentrations of thapsigargin for 5 min (D), and the uptake of $^{45}Ca^{2+}$ was determined as described above. (E, F) PAG-WT BMMCs were infected with empty pLKO lentiviral vector (pLKO) or with PAG shRNA vectors (PAG-KD), and stable transfectants were activated with antigen (E) or thapsigargin (F) and analyzed as described above. Data represent means ± SEs from three to six independent experiments performed in duplicate or triplicate. *, $P < 0.05$; **, $P < 0.01$; ***, $P < 0.001$.

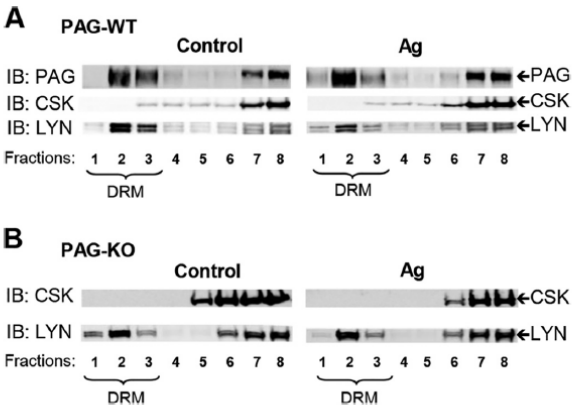

FIG 3 Localization of CSK in lipid rafts depends on PAG. IgE-sensitized PAG-WT BMMCs (A) or PAG-KO BMMCs (B) were nonactivated (Control) or activated for 5 min with antigen (250 ng/ml). After solubilization in lysis buffer containing 1% Brij 96, the whole-cell lysates were fractionated by sucrose density gradient ultracentrifugation as described in Materials and Methods. Individual fractions were collected and analyzed by immunoblotting for the presence of PAG, CSK, and LYN. Fractions containing DRMs are indicated. Representative data from three independent experiments are shown.

concentrations of thapsigargin (Fig. 2D). A positive regulatory role of PAG in calcium uptake after antigen (Fig. 2E) or thapsigargin (Fig. 2F) activation was also evident when PAG-KD cells were compared to the corresponding PAG-expressing (pLKO) controls. These data imply that the observed inhibition of degranulation in PAG-deficient cells could be at least in part attributable to decreased calcium mobilization.

Localization of CSK in lipid rafts depends on PAG. Previous studies localized PAG almost exclusively to lipid rafts, where it could interact with CSK and through this interaction negatively regulate lipid raft-associated SFKs (15). This conclusion was based on data evaluating the distribution of PAG in fractions after sucrose density gradient ultracentrifugation of lysates from cells disintegrated in nonionic detergents (11, 12) or 0.5 M $NaHCO_3$ (21). However, there are inconsistencies regarding the role of PAG in the localization of CSK in lipid rafts. One study found that the level of lipid raft-associated CSK in thymocytes was greatly reduced in the absence of PAG (18), whereas another concluded that PAG is dispensable for the localization of CSK in lipid rafts (17). To determine whether PAG contributes to the localization of CSK in lipid rafts in BMMCs, nonactivated or antigen-activated PAG-WT and PAG-KO BMMCs were solubilized in a buffer supplemented with 1% Brij 96 and fractionated by sucrose density gradient ultracentrifugation, and their presence in individual fractions was analyzed by immunoblotting. The distribution of LYN kinase, a well-known lipid raft marker in BMMCs, was also examined. In accordance with previous data (42), most of the LYN (88%) in nonactivated cells was associated with detergent-resistant membranes (DRM; fractions 1 to 3). Five minutes after activation with antigen, this amount was reduced by approximately half (Fig. 3A). In the same gradient fractions, less PAG was found in DRMs (55%), and no significant changes were observed after stimulation with antigen. Only a small fraction of CSK was found in DRM fractions (4%), and no significant changes were observed after activation with antigen. When lysates from PAG-KO BMMCs were analyzed, no CSK was found in DRM fractions from activated and nonactivated cells even after a longer exposure (Fig. 3B), suggesting that PAG is involved in the localization of CSK in DRMs.

PAG and tyrosine phosphorylation of signal transduction proteins. The first biochemically defined step after FcεRI triggering is tyrosine phosphorylation of the FcεRI subunits by SFK LYN, followed by engagement of other kinases and phosphorylation of a number of signal transduction proteins. To specify the role of PAG in these processes, we examined tyrosine phosphorylation of FcεRI and several selected proteins involved in early stages of antigen-induced mast cell signaling (SYK, LAT, extracellular signal-regulated kinase [ERK]) (43), as well as proteins involved in cell movement (FAK and paxillin) (44). In initial experiments, we looked for proteins phosphorylated on tyrosine in total cellular

lysates. We found that PAG-WT cells differed from PAG-KO cells in several tyrosine-phosphorylated proteins not only after antigen stimulation but also in the nonactivated state (Fig. 4A). Further analysis showed that FcεRI triggering caused an increase in tyrosine phosphorylation of FcεRI β and γ chains in WT cells and that this process was significantly reduced in PAG-KO cells (Fig. 4B). Tyrosine phosphorylation of SYK (Fig. 4C) and its substrates, LAT (Fig. 4D) and ERK (Fig. 4E), was also impaired in PAG-deficient cells. In contrast, FAK (Fig. 4F) and the focal adhesion-associated adaptor protein paxillin (Fig. 4G) showed elevated basal levels of tyrosine phosphorylation in PAG-KO cells; this difference was maintained after FcεRI triggering (Fig. 4F and G).

The observed decrease in tyrosine phosphorylation of FcεRI β and γ subunits in antigen-activated PAG-KO cells suggested an imbalance between PTKs and PTPs in the vicinity of the receptor. To examine FcεRI-associated PTK activity toward its endogenous substrate, FcεRI was immunoprecipitated from nonactivated and antigen-activated PAG-WT and PAG-KO cells, and the immunocomplexes were analyzed by *in vitro* kinase assays with [γ-^{32}P]ATP. Using PAG-WT cells, we observed a significant increase in radioactivity bound to FcεRI β and γ receptor subunits after activation with antigen (Fig. 5A and B). Surprisingly, when the receptor was precipitated from PAG-KO cells, strong phosphorylation of the receptor β and γ subunits was observed in nonactivated cells and was decreased after FcεRI triggering. These data, together with the results of immunoblotting experiments showing weak and comparable tyrosine phosphorylation of the β and γ subunits of FcεRI isolated from nonactivated PAG-WT and PAG-KO cells, suggest that the activity of PTKs bound to FcεRI isolated from PAG-KO cells is enhanced.

To determine the enzymatic activities of total LYN and FYN, the kinases were immunoprecipitated and their activities were assessed by an *in vitro* kinase assay. To overcome the problem with possible variation in the extent of nonphosphorylated residues in the target proteins, we used acid-denatured enolase as the exogenous substrate in immunocomplex kinase assays. The data in Fig. 5C to F show low but significantly higher levels of autophosphorylation of the LYN and FYN kinases immunoprecipitated from PAG-KO cells than of those immunoprecipitated from PAG-WT cells. Importantly, enolase phosphorylation was also enhanced in LYN and FYN immunoprecipitates obtained from PAG-KO cells. In contrast to the findings of previous studies (3, 19), we did not observe any increase in the activity of the kinases after FcεRI triggering, which is probably due to the different culture condition used (45).

LYN is a positive regulator of PTPs (46, 47), which could be responsible for the decreased tyrosine phosphorylation of several substrates, as shown in Fig. 4A to E. One of the phosphatases involved in the regulation of mast cell degranulation and calcium responses is SHIP1. LYN kinase phosphorylates SHIP1 and thus enhances its enzymatic activity and downregulates degranulation (47, 48). In further experiments, we therefore examined tyrosine phosphorylation of SHIP1 in BMMCs from PAG-WT and PAG-KO mice. In nonactivated WT cells, SHIP1 showed baseline phosphorylation which was enhanced after FcεRI triggering (Fig. 5G and H). Compared to PAG-WT cells, nonactivated PAG-KO cells exhibited significantly higher levels of SHIP1 tyrosine phosphorylation. After activation with antigen, the difference between PAG-WT and PAG-KO cells became insignificant.

Different regulatory roles of PAG in SCF signaling. An important surface receptor of mast cells is KIT, which binds SCF and thereby triggers mast cell activation and enhances activation induced by FcεRI (49). However, no data on the involvement of PAG in SCF-induced activation are available. To determine a possible role of PAG in KIT-mediated activation, PAG-WT and PAG-KO BMMCs were activated with different concentrations of SCF and degranulation was examined. PAG-WT cells released increasing amounts of β-glucuronidase when activated with 25 to 200 ng/ml SCF. The extent of SCF-induced degranulation was higher than that described in previous studies (50, 51) and was apparently related to the growth of bone marrow cells in the presence of both IL-3 and SCF. When BMMCs were derived from cultures containing IL-3 alone, their SCF-induced degranulation was low (45). PAG-KO cells released significantly more β-glucuronidase than PAG-WT cells at all concentrations of SCF tested (Fig. 6A). This effect was associated with higher levels of KIT tyrosine phosphorylation in PAG-KO cells (Fig. 6B and C). However, an opposite effect of PAG on FcεRI- and KIT-mediated signaling events was absent when tyrosine phosphorylation of PLCγ1 was examined. Stimulation of PAG-WT cells with antigen as well as with SCF resulted in tyrosine phosphorylation of PLCγ1, even though it was slower in SCF-activated cells. Similar findings have been previously described (50) and indicate that FcεRI-activated PTKs are more potent for the phosphorylation of PLCγ1 than that of KIT. In PAG-KO cells, the extent of PLCγ1 tyrosine phosphorylation was significantly inhibited in both antigen- and SCF-triggered cells (Fig. 6D and E). A similar effect was observed when PLCγ2 was examined (data not shown). No significant effect of PAG was observed when the tyrosine phosphorylation of several other signaling molecules (SYK, LAT, FAK, paxillin) was examined in PAG-WT and PAG-KO cells. Furthermore, no effect of PAG on the calcium response was observed in SCF-activated BMMCs (not shown).

An important aspect of mast cell physiology is chemotaxis directed by various ligands (52). Here we compared chemotaxis toward antigen or SCF in cells differing in PAG expression. In transwell migration assays, PAG-WT BMMCs exhibited faster migration toward the antigen than PAG-KO cells. The difference was almost 2-fold and was significant (Fig. 6F). When SCF was used as a chemoattractant, both cell types migrated faster and no significant difference between them was evident. To exclude possible compensatory developmental alterations in PAG-KO cells, we also compared the chemotaxis of BMMCs with PAG-KD and their corresponding controls (pLKO cells). We found significantly lower levels of migration of PAG-KD cells than of pLKO cells after exposure to antigen. Again, no significant difference between the two cell types was observed when SCF was used as a chemoattractant (Fig. 6G).

Positive regulatory role of PAG in cytokine and chemokine production. Previous studies showed that activation of mast cells resulted in the rapid tyrosine phosphorylation of several transcription factors. We selected STAT5, which has been extensively studied in FcεRI- or KIT-activated cells (53, 54), as the transcription factor. To elucidate the role of PAG in this process, we examined tyrosine phosphorylation of STAT5 in nonactivated and antigen- or SCF-activated PAG-WT and PAG-KO cells (Fig. 7A and B). Antigen-induced tyrosine phosphorylation of STAT5 was positively regulated by PAG. A significantly lower level of phosphorylation of STAT5 in PAG-KO cells was observable even without activation, but activation intensified the difference. Phosphorylation of STAT5 was also observed in cells stimulated with SCF

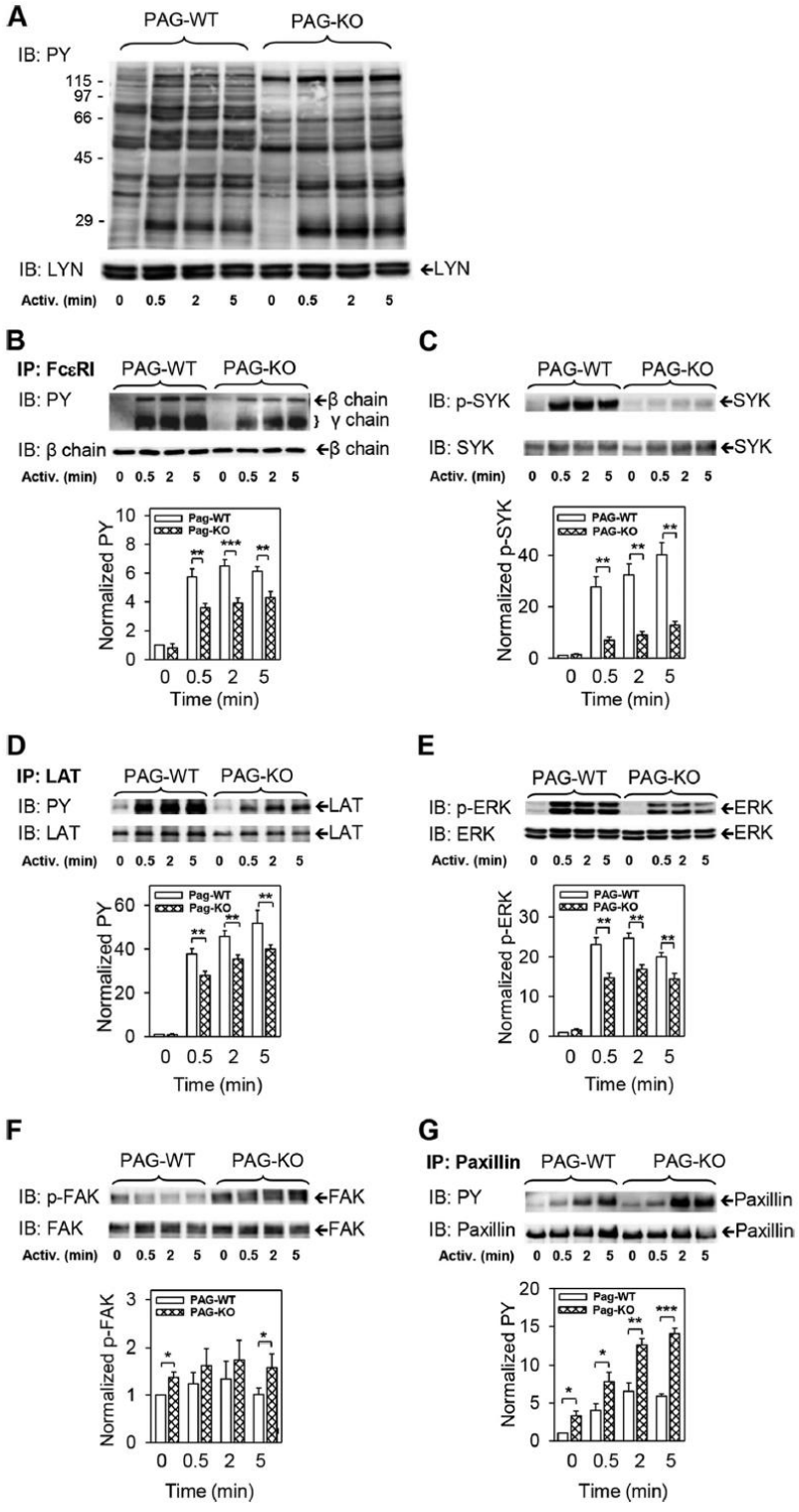
A
PAG-WT
PAG-KO
IB: PY
115 -
97 -
66 -
45 -
29 -
IB: LYN
←LYN
Activ. (min) 0 0.5 2 5 0 0.5 2 5
B
IP: FcεRI
PAG-WT
PAG-KO
IB: PY
←β chain
γ chain
IB: β chain
←β chain
Activ. (min) 0 0.5 2 5 0 0.5 2 5
Pag-WT
Pag-KO
Normalized PY
Time (min)
C
PAG-WT
PAG-KO
IB: p-SYK
←SYK
IB: SYK
←SYK
Activ. (min) 0 0.5 2 5 0 0.5 2 5
PAG-WT
PAG-KO
Normalized p-SYK
Time (min)
D
IP: LAT
PAG-WT
PAG-KO
IB: PY
←LAT
IB: LAT
←LAT
Activ. (min) 0 0.5 2 5 0 0.5 2 5
Pag-WT
Pag-KO
Normalized PY
Time (min)
E
PAG-WT
PAG-KO
IB: p-ERK
←ERK
IB: ERK
←ERK
Activ. (min) 0 0.5 2 5 0 0.5 2 5
PAG-WT
PAG-KO
Normalized p-ERK
Time (min)
F
PAG-WT
PAG-KO
IB: p-FAK
←FAK
IB: FAK
←FAK
Activ. (min) 0 0.5 2 5 0 0.5 2 5
PAG-WT
PAG-KO
Normalized p-FAK
Time (min)
G
IP: Paxillin
PAG-WT
PAG-KO
IB: PY
←Paxillin
IB: Paxillin
←Paxillin
Activ. (min) 0 0.5 2 5 0 0.5 2 5
Pag-WT
Pag-KO
Normalized PY
Time (min)

(Fig. 7A and B). However, no significant difference between PAG-WT and PAG-KO cells was observed.

The decreased phosphorylation of STAT5 in antigen-stimulated PAG-KO cells suggested the reduced production of cytokines and chemokines in such cells (55). Detailed analysis at the protein and mRNA levels showed that, indeed, the levels of three selected cytokines, TNF-α, IL-6, and IL-13, were significantly reduced in antigen-stimulated PAG-KO cells compared with their levels in PAG-WT cells at both the protein and mRNA levels (Fig. 7C). Antigen-activated PAG-KO BMMCs also exhibited significant inhibition of transcription of two chemokines, CCL3 and CCL4 (Fig. 7D).

Phenotype rescue of PAG-KO cells. Next, we attempted to confirm the role of PAG as a positive regulator of cytokine production. We prepared a PAG-myc construct in the pCDH vector and transfected it into PAG-KO BMMCs. Control cells were transfected with the empty pCDH vector, and puromycin-resistant cells were further analyzed. Staining for myc after cell permeabilization and confocal microscopy showed the association of the PAG-myc with the plasma membrane (Fig. 8A). No signal was observed in cells transduced with empty pCDH (Fig. 8B). Furthermore, immunoblotting analysis with Myc tag-specific antibody confirmed the expression of PAG-myc in cells transduced with the pCDH-PAG-myc vector but not the pCDH empty vector (Fig. 8C). These data suggest that PAG-myc was expressed as expected. Next, we examined the production of TNF-α in antigen-activated PAG-WT and PAG-KO cells transfected with empty pCDH and PAG-KO cells transfected with pCDH-PAG-myc. For this analysis we selected flow cytometry, which allowed us to evaluate TNF-α-positive cells, after gating out the cellular debris detected in forward and side scatter plots. This eliminated the problem associated with the presence of different proportions of living cells and debris in various transduction experiments. Data presented in Fig. 8D indicate that the level of production of TNF-α in cells transfected with the empty pCDH vector was significantly lower in PAG-KO cells than in PAG-WT cells. PAG-KO cells transfected with pCDH-PAG-myc produced significantly more TNF-α than pCDH transfectants. These data confirm the phenotype rescue in PAG-KO cells.

Impaired passive systemic anaphylaxis in PAG-KO mice. Finally, we examined degranulation in antigen-activated mast cells under *in vivo* conditions. We induced passive systemic anaphylaxis in PAG-KO and PAG-WT mice by sensitizing them with TNP-specific IgE MAb and subsequent challenge with antigen. In control mice, the decrease in body temperature was observable within the first 60 min and was followed by slow recovery for more than 180 min after antigen injection (Fig. 9A). In PAG-KO mice, the decrease in body temperature was less pronounced and recovery was faster, being complete 150 min after antigen administration. The difference in body temperature between PAG-WT and PAG-KO mice was significant in the interval ranging from 45 to 170 min after antigen administration. The observed decrease in systemic anaphylaxis was not likely attributable to decreased numbers of mast cells in PAG-KO mice, as inferred from comparable mast cell (KIT and FcεRI positive) counts in the peritoneal lavage fluid of PAG-WT and PAG-KO cells (Fig. 9B). Furthermore, we found no significant difference in serum IgE levels between PAG-WT and PAG-KO mice (Fig. 9C). This finding indicates that the production of IgE is not affected by the absence of PAG and that the decreased anaphylactic response in PAG-KO mice is not caused by enhanced production of IgE, which might preclude sensitization with antigen-specific IgE.

DISCUSSION

In this study, we used BMMCs derived from PAG-KO and PAG-WT mice to understand the role of PAG in FcεRI and SCF signaling. To minimize the possible effect of compensatory developmental alterations in PAG-KO cells, we also used BMMCs with PAG-KD and corresponding controls. Several lines of evidence indicate that PAG has positive as well as negative regulatory roles in FcεRI- or KIT-mediated signaling, depending on the receptor triggered and the signaling pathway involved.

First, when stimulated with antigen, mast cells derived from PAG-KO mice exhibited decreased degranulation. In view of previous results obtained with other immunoreceptors (17, 18, 26), this was an unexpected finding because phosphorylated PAG was regarded as a plasma membrane anchor of CSK, a negative regulator of SFKs. Furthermore, overexpression of PAG reportedly resulted in decreased degranulation in RBL-2H3 cells (21). The positive regulatory role of PAG in FcεRI-mediated signaling described here was not the consequence of developmental changes caused by the absence of PAG, since a similar phenotype was also observed in PAG-KD BMMCs where PAG expression was downregulated by RNA interference, nor was the decreased degranulation caused by the reduced production of β-glucuronidase or the reduced expression of FcεRI in PAG-KO and PAG-KD cells. Interestingly, a defect in degranulation was also observed in PAG-deficient cells activated by thapsigargin, a noncompetitive inhibitor of ER Ca^{2+} ATPase.

Second, antigen-activated PAG-KO cells exhibited decreased tyrosine phosphorylation of FcεRI β and γ subunits. This change implies that the reduced degranulation in PAG-deficient cells is caused at least in part by inhibition of the earliest stages of mast cell signaling, starting from reduced phosphorylation of the FcεRI β and γ subunits, followed by impaired membrane anchoring, phosphorylation, and activation of SYK. The exact molecular mechanism of the impaired phosphorylation of FcεRI in PAG-

FIG 4 Antigen-induced tyrosine phosphorylation of signal transduction proteins is dependent on PAG. (A to G) IgE-sensitized PAG-WT and PAG-KO cells were activated (Activ.) for the indicated time intervals with antigen (250 ng/ml). The cells were lysed, and total cellular lysates were analyzed by immunoblotting with the tyrosine-specific MAb PY-20–HRP conjugate (PY). Alternatively, FcεRI (B), LAT (D), and paxillin (G) were immunoprecipitated (IP) from the lysates and examined by immunoblotting with tyrosine-specific MAb as in the experiment whose results are shown in panel A. For SYK (C), ERK (E), and FAK (F), size-fractionated proteins in cell lysates were directly analyzed by immunoblotting with the corresponding phosphoprotein-specific antibodies. For loading controls, the membranes were analyzed by immunoblotting for LYN kinase (A), the FcεRI β chain (B), SYK (C), LAT (D), ERK (E), FAK (F), and paxillin (G). Panel A and the tops of panels B to G show representative immunoblots from at least three experiments. The bottoms of panels B to G show the results of densitometry analysis of the corresponding immunoblots in which signals from tyrosine-phosphorylated proteins in activated cells were normalized to the signals in nonactivated cells and loading control proteins. Means ± SEs were calculated from a minimum of four independent experiments. The statistical significance of the differences between PAG-WT and PAG-KO cells is also shown: *, $P < 0.05$; **, $P < 0.01$; ***, $P < 0.001$. p-SYK, p-ERK, and p-FAK, phosphorylated SYK, ERK, and FAK, respectively.

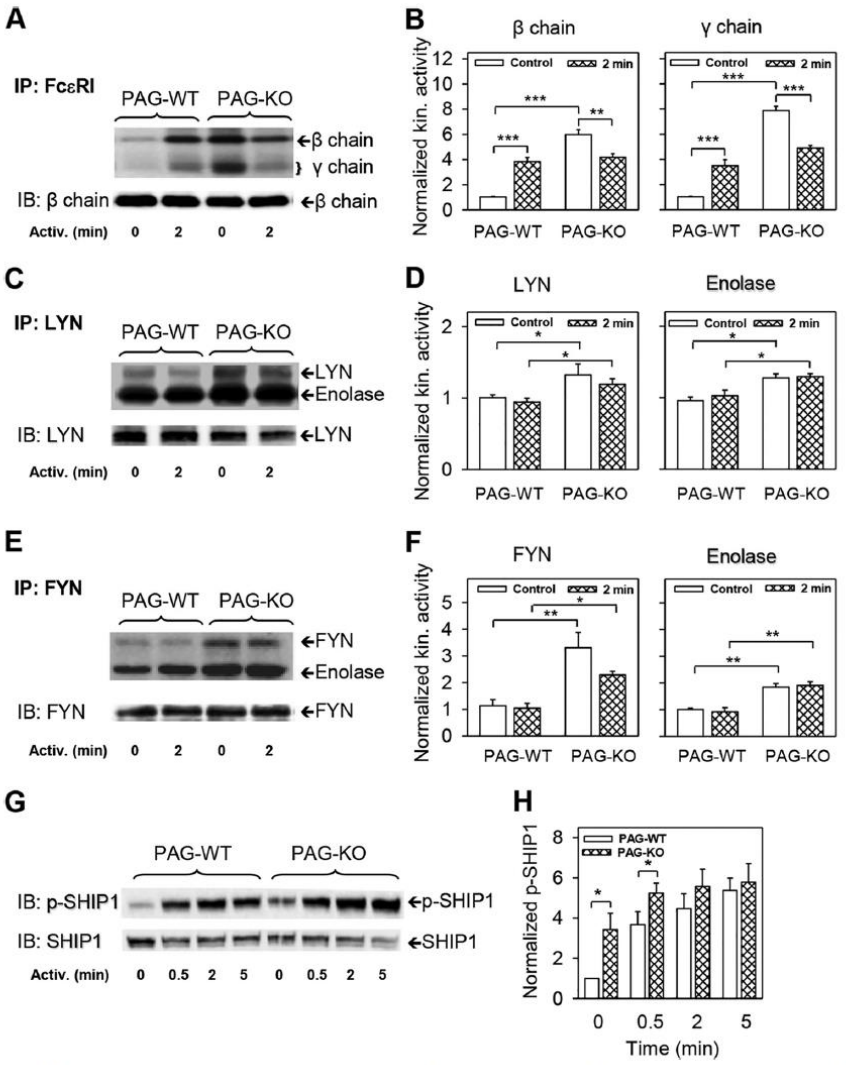

FIG 5 PAG-dependent regulation of LYN and FYN kinase (kin.) activities and SHIP1 tyrosine phosphorylation. (A) IgE-sensitized PAG-WT and PAG-KO BMMCs were activated or not for 2 min with antigen (250 ng/ml) and then solubilized with lysis buffer containing 1% Brij 96. FcεRI-IgE complexes were immunoprecipitated and incubated in a kinase buffer containing [γ-^{32}P]ATP. After the kinase assay, ^{32}P-labeled proteins were size fractionated, transferred to nitrocellulose membranes, and examined by autoradiography. The relative amounts of the FcεRI β chain were determined by immunoblotting. The positions of FcεRI β and γ chains are indicated. (B) Autoradiograms obtained as described in the legend to panel A were quantified, and the signals corresponding to the FcεRI β and γ chains were normalized to the signals in nonactivated PAG-WT cells and the amount of FcεRI β chain immunoprecipitated. (C to F) The cells were activated and solubilized as described in the legend to panel A. LYN (C and D) and FYN (E and F) were immunoprecipitated and incubated in kinase buffer supplemented with [γ-^{32}P]ATP and acid-denatured enolase, used as an exogenous substrate. Kinase assays and further analyses were performed as described in the legend to panel A. Autoradiograms were quantified, and the signals corresponding to LYN, FYN, and enolase were normalized to the signals in nonactivated PAG-WT cells and the amount of immunoprecipitated LYN (D) or FYN (F). (G and H) IgE-sensitized PAG-WT and PAG-KO BMMCs were activated for the indicated time intervals with antigen as described in the legend to panel A. The cells were lysed and analyzed by immunoblotting with phosphorylated-SHIP1 (p-SHIP1)-specific antibody. The amount of SHIP1 was used as a loading control. (H) Densitometry analysis of the immunoblots in which the signal for phospho-SHIP1 was normalized to the signal in nonactivated PAG-WT cells and the amount of SHIP1. The results of representative experiments are shown in panels A, C, E, and G. The means ± SEs in panels B, D, F, and H were calculated from three to five independent experiments. The statistical significance of intergroup differences is indicated: *, $P < 0.05$; **, $P < 0.01$; ***, $P < 0.001$.

deficient cells is unknown and is likely connected to local changes in the activity and/or the topography of SFKs and PTPs within the FcεRI signalosome. Our finding that FcεRI immunocomplexes isolated from nonionic detergent-solubilized nonactivated PAG-KO cells show kinase activity higher than those isolated from PAG-WT cells would be compatible with this hypothesis, provided that PTKs are more stably associated with isolated FcεRI immunocomplexes than PTPs. Furthermore, we found that ty-

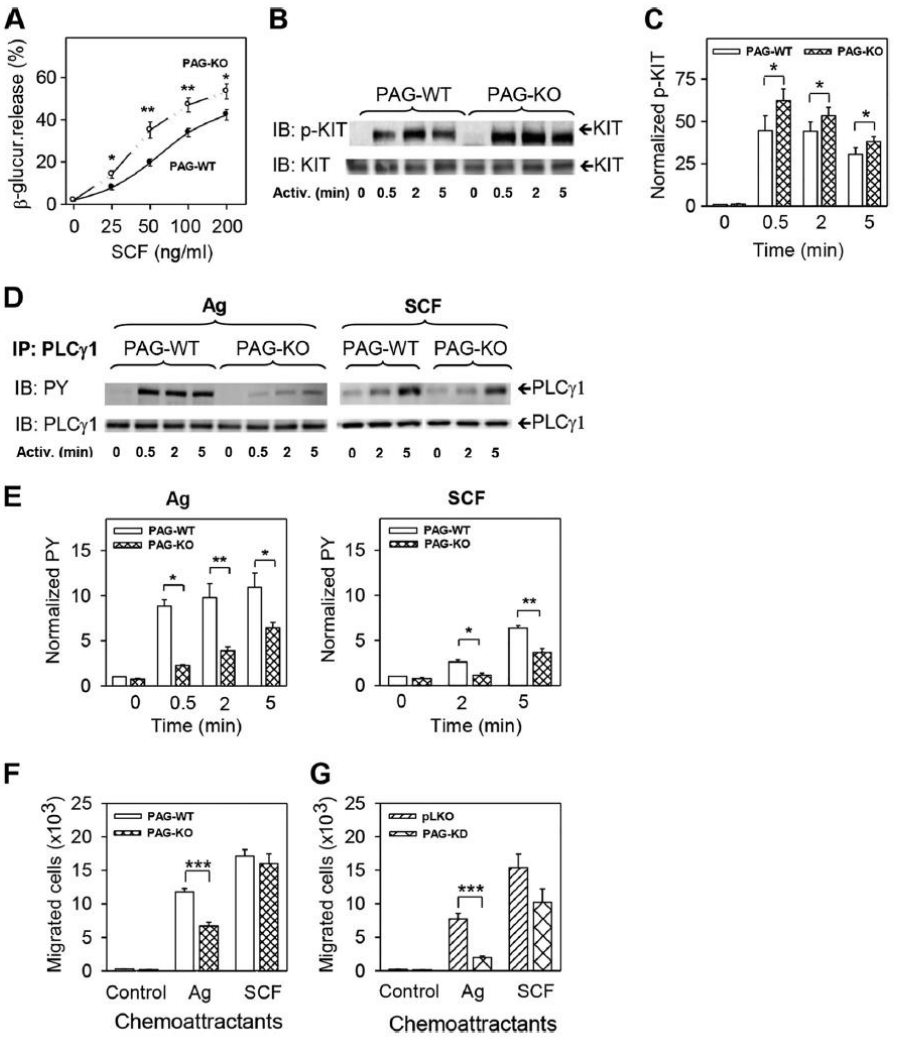

FIG 6 Different regulatory roles of PAG in KIT and FcεRI signaling. (A) PAG-WT and PAG-KO BMMCs were stimulated for 30 min with various concentrations of SCF, and the amount of β-glucuronidase released into the supernatant was determined. (B) PAG-WT and PAG-KO cells were exposed to SCF (50 ng/ml) for different time intervals and lysed, and tyrosine phosphorylation of KIT was analyzed by immunoblotting with phosphorylated-KIT (p-KIT)-specific antibody. Immunoblotting with KIT-specific antibody served as a loading control. The results of one representative experiment out of three performed are shown. (C) The immunoblots obtained as described in the legend to panel B were analyzed by densitometry, and the amounts of tyrosine-phosphorylated KIT were normalized to the amounts of tyrosine-phosphorylated KIT in nonactivated PAG-WT cells and loading controls. (D and E) PAG-WT and PAG-KO BMMCs were activated for different time intervals with antigen (250 ng/ml) or SCF (50 ng/ml) and lysed, and PLCγ1 was immunoprecipitated. The immunoprecipitates were analyzed by immunoblotting with tyrosine-specific MAb PY-20–HRP conjugate (PY) (D). As loading controls, the membranes were also analyzed by immunoblotting for PLCγ1. Representative immunoblots out of three performed are shown. The immunoblots obtained were analyzed by densitometry, and the relative amounts of tyrosine-phosphorylated proteins were normalized to the amounts of the proteins immunoprecipitated and to the amounts of tyrosine-phosphorylated proteins in nonactivated PAG-WT cells (E). (F) IgE-sensitized PAG-WT or PAG-KO BMMCs were analyzed in a chemotactic assay with chemotaxis medium alone (Control) or with chemotaxis medium supplemented with antigen (250 ng/ml) or SCF (100 ng/ml) in the lower wells. The numbers of cells migrating into the lower wells were determined after 8 h. (G) The experiments were performed as described in the legend to panel F, except that cells with PAG-KD and the corresponding controls (pLKO) were used. Means ± SEs were calculated from a minimum of nine independent experiments performed in triplicate (A), three independent experiments (C, E, and G), or six independent experiments (F). The statistical significance of differences between PAG-WT/PAG-KO cells (A, C, E, and F) and pLKO/PAG-KD cells (G) is shown: *, $P < 0.05$; **, $P < 0.01$; ***, $P < 0.001$.

rosine phosphorylation of SHIP1, a negative regulator of mast cell activation (48, 56), is increased in nonactivated PAG-KO cells. This could be caused by the enhanced enzymatic activity of LYN, which phosphorylates and activates SHIP1 (47), and in this manner could contribute to decreased calcium and degranulation responses (48, 56).

In contrast to FcεRI and several other signaling proteins involved in the calcium response (SYK, LAT, and PLCγ), FAK and at

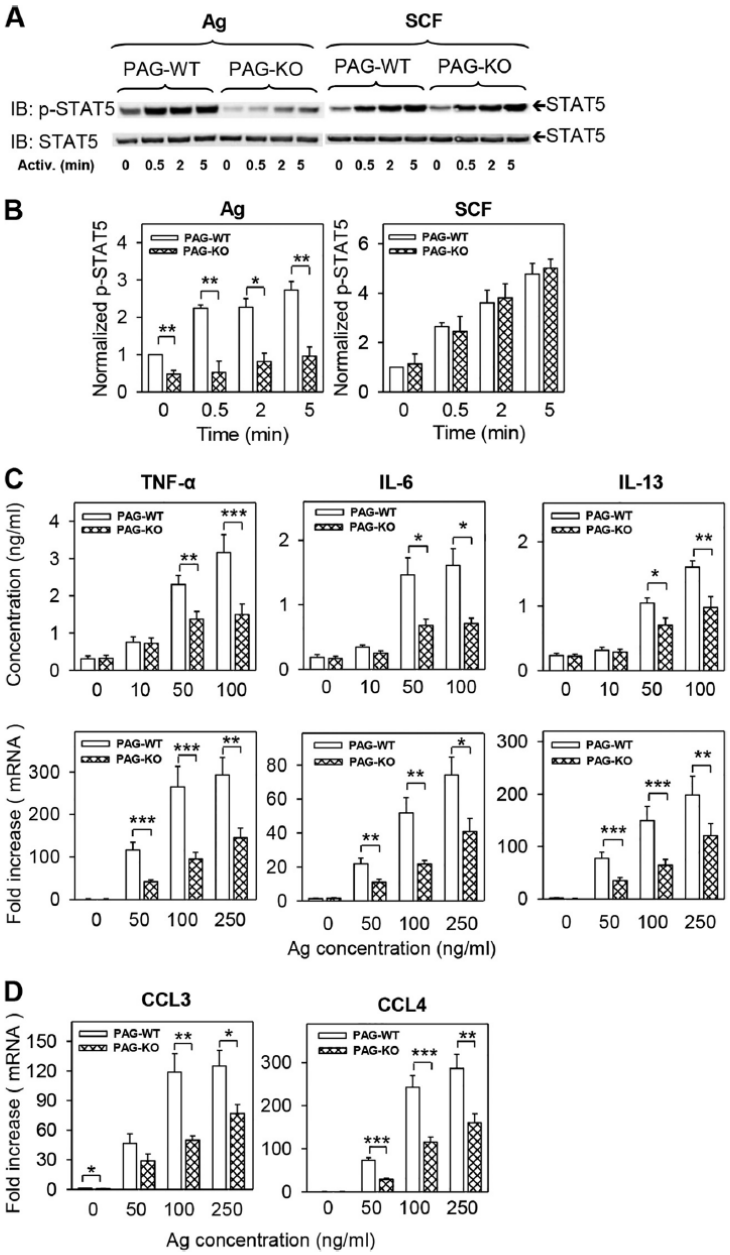

FIG 7 Decreased tyrosine phosphorylation of STAT5 and production of cytokines and chemokines in antigen-activated PAG-KO BMMCs. (A) Cells were activated for different time intervals with antigen (250 ng/ml) or SCF (50 ng/ml), lysed, and analyzed for STAT5 tyrosine 694 phosphorylation by immunoblotting. As loading controls, the membranes were also immunoblotted with STAT5-specific antibody. Representative immunoblots are shown. (B) The immunoblots were analyzed by densitometry, and the relative amount of tyrosine-phosphorylated STAT5 (p-STAT5) was normalized to its amount in nonactivated cells and the corresponding loading control. (C, D) The levels of production of cytokines (TNF-α, IL-6, and IL-13) at the protein level (C, top) and mRNA level (C, bottom) and chemokines (CCL3 and CCL4) (D) were evaluated at the mRNA level in PAG-WT and PAG-KO BMMCs activated with various concentrations of antigen for 1 h (mRNA) or 6 h (protein). Specific proteins and mRNAs were quantified by immuno-PCR and qPCR, respectively. Means ± SEs were calculated from 4 to 12 independent experiments. The statistical significance of differences between PAG-WT and PAG-KO cells is shown: *, $P < 0.05$; **, $P < 0.01$; ***, $P < 0.001$.

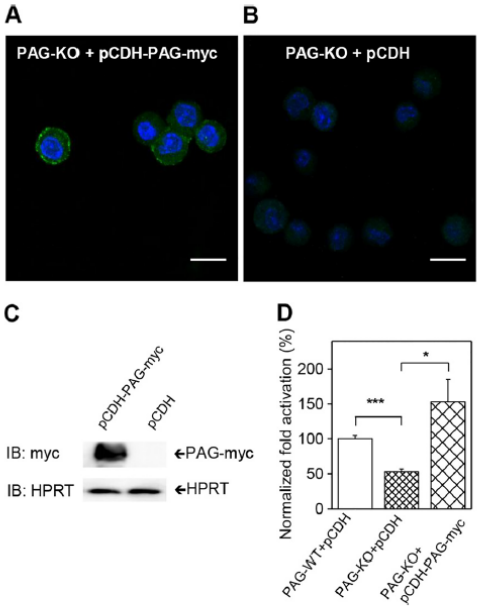

FIG 8 Phenotype rescue of PAG-KO BMMCs. (A, B) PAG-KO BMMCs were transfected with the pCDH-PAG-myc vector (A) or the control empty vector (pCDH) (B). Puromycin-resistant transfectants were isolated and attached to fibronectin-coated slides. Then, the cells were fixed, permeabilized, and labeled for PAG-myc with an anti-Myc tag/anti-IgG–Alexa Fluor 488 conjugate (green) and Hoechst 33258 (blue). Bars, 10 μm. (C) Puromycin-resistant pCDH-PAG-myc- or empty pCDH vector-transfected cells were solubilized, and the presence of PAG-myc was determined by immunoblotting with anti-Myc tag antibody. As loading controls, the membranes were developed for HPRT. (D) PAG-WT or PAG-KO BMMCs stably transfected with the pCDH vector (PAG-WT+pCDH and PAG-KO+pCDH, respectively) or PAG-KO BMMCs transfected with pCDH-PAG-myc (PAG-KO+pCDH-PAG-myc) were sensitized overnight with IgE and then activated with antigen (100 ng/ml). After 90 min the cells were fixed and stained with TNF-α specific rabbit antibody, followed by anti-rabbit IgG–Alexa Fluor 488 conjugate. The cells were analyzed by flow cytometry, and the ratios of the mean fluorescence intensity between activated and nonactivated cells were normalized to those for the pCDH-transfected PAG-WT controls. Data show means ± SEs calculated from three independent experiments. The statistical significance of the differences is indicated: *, $P < 0.05$; ***, $P < 0.001$.

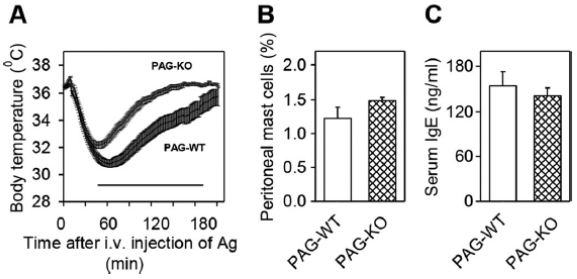

FIG 9 Decreased passive systemic anaphylaxis in PAG-KO mice. (A) PAG-WT ($n = 17$) and PAG-KO mice ($n = 16$) were passively sensitized with TNP-specific IgE (3 μg/mouse) and 24 h later were challenged with antigen (500 μg per mouse) to induce systemic anaphylaxis. Body temperature responses at various time intervals after antigen administration were recorded. Means ± SEs are shown. Statistically significant differences ($P < 0.05$) between PAG-WT and PAG-KO mice are indicated by the black line below the curves. i.v., intravenous. (B) Percentage of mast cells (KIT and FcεRI positive) in peritoneal lavage fluid of PAG-WT and PAG-KO mice. (C) Serum IgE levels in PAG-WT and PAG-KO mice. Data are means ± SEs calculated for three (B) or four (C) animals in each group.

least one of its substrates, the multidomain scaffolding adaptor protein paxillin, showed enhanced tyrosine phosphorylation in PAG-KO cells. The molecular mechanism of enhanced phosphorylation of FAK and paxillin in PAG-KO cells remains to be determined but apparently reflects changes in the activity of SFKs and PTPs which use FAK and paxillin as a substrate (57, 58).

Third, PAG-deficient BMMCs showed reduced calcium uptake after activation with antigen. This could be attributed to the reduced tyrosine phosphorylation and activity of PLCγ, which cleaves the plasma membrane-bound phosphatidylinositol 4,5-bisphosphate into diacylglycerol and inositol 1,4,5-trisphosphate; the latter binds to its receptors and regulates the release of calcium from intracellular organelles. Increases in cytoplasmic calcium lead to the influx of extracellular calcium into the cytoplasm through SOC channels. Reduced calcium uptake in PAG-KO cells was observed not only after exposure to antigen but also after activation with thapsigargin. This could be related to previous findings documenting that PLCγ is involved in thapsigargin-induced Ca^{2+} entry (59–61) and reduced phosphorylation of PLCγ in PAG-deficient cells. Furthermore, it has been shown that STIM1, which is indispensable for opening SOC channels in mast cells (62, 63), needs for its function expression and phosphorylation of SYK and LYN kinases (64). Enhanced tyrosine phosphorylation of SHIP1 and, presumably, its increased enzymatic activity (45, 46) could also contribute to decreased calcium mobilization in activated PAG-KO cells.

Fourth, PAG-KO cells exhibited higher degranulation when activated by SCF. SCF binds to KIT, a type III plasma membrane receptor tyrosine kinase. After SCF binding, the receptor forms a dimer that stimulates its intrinsic tyrosine kinase activity, creating phosphotyrosine binding sites for FYN (65) and LYN (66) kinases and many other signaling molecules, including SHIP1 and PLCγ (67). These molecules are apparently integrated into signaling circuits regulated by PAG.

Fifth, it has previously been shown that activation through FcεRI as well as KIT rapidly stimulates STAT5 tyrosine phosphorylation and that STAT5 deficiency greatly reduces early and late mast cell responses (68). PAG-KO cells exhibited lower tyrosine phosphorylation of STAT5 when activated via FcεRI but not when activated via KIT. This difference could be explained by the different kinases involved in STAT5 phosphorylation. In SCF-activated cells, KIT activates STAT5 partly through the tyrosine kinase JAK2 (69). In contrast, JAK2 is dispensable in IgE-activated cells, which use FYN for STAT5 phosphorylation (53). Phosphorylated STAT5 serves as a transcription factor for a number of inflammatory genes (55). The reduced transcription of genes for cytokines (TNF-α, IL-6, and IL-13) and chemokines (CCL3 and CCL4) and the reduced production of TNF-α, IL-6, and IL-13 in antigen-activated PAG-KO cells could be a direct consequence of impaired STAT5 tyrosine phosphorylation.

Sixth, IgE-sensitized PAG-KO cells exhibited decreased chemotaxis toward antigen. Mast cell chemotaxis is a complex process dependent on numerous signaling molecules and cell signaling pathways (52). The observed inhibition of tyrosine phosphorylation of the FcεRI β and γ subunits, SYK, and LAT in an-

18. Xu S, Huo J, Tan JE, Lam KP. 2005. Cbp deficiency alters Csk localization in lipid rafts but does not affect T-cell development. Mol. Cell. Biol. 25:8486–8495. http://dx.doi.org/10.1128/MCB.25.19.8486-8495.2005.
19. Odom S, Gomez G, Kovarova M, Furumoto Y, Ryan JJ, Wright HV, Gonzalez-Espinosa C, Hibbs ML, Harder KW, Rivera J. 2004. Negative regulation of immunoglobulin E-dependent allergic responses by Lyn kinase. J. Exp. Med. 199:1491–1502. http://dx.doi.org/10.1084/jem.20040382.
20. Kitaura J, Kawakami Y, Maeda-Yamamoto M, Horejsi V, Kawakami T. 2007. Dysregulation of Src family kinases in mast cells from epilepsy-resistant ASK versus epilepsy-prone EL mice. J. Immunol. 178:455–462. http://dx.doi.org/10.4049/jimmunol.178.1.455.
21. Ohtake H, Ichikawa N, Okada M, Yamashita T. 2002. Cutting edge: transmembrane phosphoprotein Csk-binding protein/phosphoprotein associated with glycosphingolipid-enriched microdomains as a negative feedback regulator of mast cell signaling through the FcεRI. J. Immunol. 168:2087–2090. http://dx.doi.org/10.4049/jimmunol.168.5.2087.
22. Nishizumi H, Horikawa K, Mlinaric-Rascan I, Yamamoto T. 1998. A double-edged kinase Lyn: a positive and negative regulator for antigen receptor-mediated signals. J. Exp. Med. 187:1343–1348. http://dx.doi.org/10.1084/jem.187.8.1343.
23. Kawakami Y, Kitaura J, Satterthwaite AB, Kato RM, Asai K, Hartman SE, Maeda-Yamamoto M, Lowell CA, Rawlings DJ, Witte ON, Kawakami T. 2000. Redundant and opposing functions of two tyrosine kinases, Btk and Lyn, in mast cell activation. J. Immunol. 165:1210–1219. http://dx.doi.org/10.4049/jimmunol.165.3.1210.
24. Parravicini V, Gadina M, Kovarova M, Odom S, Gonzalez-Espinosa C, Furumoto Y, Saitoh S, Samelson LE, O'Shea JJ, Rivera J. 2002. Fyn kinase initiates complementary signals required for IgE-dependent mast cell degranulation. Nat. Immunol. 3:741–748. http://dx.doi.org/10.1038/ni817.
25. Yang Y, Seed B. 2003. Site-specific gene targeting in mouse embryonic stem cells with intact bacterial artificial chromosomes. Nat. Biotechnol. 21:447–451. http://dx.doi.org/10.1038/nbt803.
26. Lindquist S, Karitkina D, Langnaese K, Posevitz-Fejfar A, Schraven B, Xavier R, Seed B, Lindquist JA. 2011. Phosphoprotein associated with glycosphingolipid-enriched microdomains differentially modulates SRC kinase activity in brain maturation. PLoS One 6:e23978. http://dx.doi.org/10.1371/journal.pone.0023978.
27. National Research Council. 2011. Guide for the care and use of laboratory animals, 8th ed. National Academies Press, Washington, DC.
28. Tolar P, Tůmová M, Dráber P. 2001. New monoclonal antibodies recognizing the adaptor protein LAT. Folia Biol. (Praha) 47:215–217.
29. Dráberová L, Amoui M, Dráber P. 1996. Thy-1-mediated activation of rat mast cells: the role of Thy-1 membrane microdomains. Immunology 87:141–148.
30. Rivera J, Kinet J-P, Kim J, Pucillo C, Metzger H. 1988. Studies with a monoclonal antibody to the β subunit of the receptor with high affinity for immunoglobulin E. Mol. Immunol. 25:647–661. http://dx.doi.org/10.1016/0161-5890(88)90100-9.
31. Rudolph AK, Burrows PD, Wabl MR. 1981. Thirteen hybridomas secreting hapten-specific immunoglobulin E from mice with Ig^a or Ig^b heavy chain haplotype. Eur. J. Immunol. 11:527–529. http://dx.doi.org/10.1002/eji.1830110617.
32. Kovářová M, Tolar P, Arudchandran R, Dráberová L, Rivera J, Dráber P. 2001. Structure-function analysis of Lyn kinase association with lipid rafts and initiation of early signaling events after Fcε receptor I aggregation. Mol. Cell. Biol. 21:8318–8328. http://dx.doi.org/10.1128/MCB.21.24.8318-8328.2001.
33. Surviladze Z, Dráberová L, Kovářová M, Boubelík M, Dráber P. 2001. Differential sensitivity to acute cholesterol lowering of activation mediated via the high-affinity IgE receptor and Thy-1 glycoprotein. Eur. J. Immunol. 31:1–10. http://dx.doi.org/10.1002/1521-4141(200101)31:1<1::AID-IMMU1>3.0.CO;2-W.
34. Dráberová L. 1990. Cyclosporin A inhibits rat mast cell activation. Eur. J. Immunol. 20:1469–1473. http://dx.doi.org/10.1002/eji.1830200710.
35. Surviladze Z, Dráberová L, Kubínová L, Dráber P. 1998. Functional heterogeneity of Thy-1 membrane microdomains in rat basophilic leukemia cells. Eur. J. Immunol. 28:1847–1858. http://dx.doi.org/10.1002/(SICI)1521-4141(199806)28:06<1847::AID-IMMU1847>3.0.CO;2-O.
36. Amoui M, Dráber P, Dráberová L. 1997. Src family-selective tyrosine kinase inhibitor, PP1, inhibits both FcεRI- and Thy-1-mediated activation of rat basophilic leukemia cells. Eur. J. Immunol. 27:1881–1886. http://dx.doi.org/10.1002/eji.1830270810.
37. Horáková H, Polakovičová I, Shaik GM, Eitler J, Bugajev V, Dráberová L, Dráber P. 2011. 1,2-Propanediol-trehalose mixture as a potent quantitative real-time PCR enhancer. BMC Biotechnol. 11:41. http://dx.doi.org/10.1186/1472-6750-11-41.
38. Potůčková L, Franko F, Bambousková M, Dráber P. 2011. Rapid and sensitive detection of cytokines using functionalized gold nanoparticle-based immuno-PCR, comparison with immuno-PCR and ELISA. J. Immunol. Methods 371:38–47. http://dx.doi.org/10.1016/j.jim.2011.06.012.
39. Makabe-Kobayashi Y, Hori Y, Adachi T, Ishigaki-Suzuki S, Kikuchi Y, Kagaya Y, Shirato K, Nagy A, Ujike A, Takai T, Watanabe T, Ohtsu H. 2002. The control effect of histamine on body temperature and respiratory function in IgE-dependent systemic anaphylaxis. J. Allergy Clin. Immunol. 110:298–303. http://dx.doi.org/10.1067/mai.2002.125977.
40. Thastrup O, Dawson AP, Scharff O, Foder B, Cullen PJ, Drobak BK, Bjerrum PJ, Christensen SB, Hanley MR. 1989. Thapsigargin, a novel molecular probe for studying intracellular calcium release and storage. Agents Actions 27:17–23. http://dx.doi.org/10.1007/BF02222186.
41. Putney JW, Jr. 2005. Capacitative calcium entry: sensing the calcium stores. J. Cell Biol. 169:381–382. http://dx.doi.org/10.1083/jcb.200503161.
42. Volná P, Lebduška P, Dráberová L, Šímová S, Heneberg P, Boubelík M, Bugajev V, Malissen B, Wilson BS, Hořejší V, Malissen M, Dráber P. 2004. Negative regulation of mast cell signaling and function by the adaptor LAB/NTAL. J. Exp. Med. 200:1001–1013. http://dx.doi.org/10.1084/jem.20041213.
43. Gilfillan AM, Rivera J. 2009. The tyrosine kinase network regulating mast cell activation. Immunol. Rev. 228:149–169. http://dx.doi.org/10.1111/j.1600-065X.2008.00742.x.
44. Huang C, Jacobson K, Schaller MD. 2004. MAP kinases and cell migration. J. Cell Sci. 117:4619–4628. http://dx.doi.org/10.1242/jcs.01481.
45. Nocka KH, Levine BA, Ko JL, Burch PM, Landgraf BE, Segal R, Lobell R. 1997. Increased growth promoting but not mast cell degranulation potential of a covalent dimer of c-Kit ligand. Blood 90:3874–3883.
46. Heneberg P, Dráber P. 2002. Nonreceptor protein tyrosine and lipid phosphatases in type I Fcε receptor-mediated activation of mast cells and basophils. Int. Arch. Allergy Immunol. 128:253–263. http://dx.doi.org/10.1159/000063864.
47. Hernandez-Hansen V, Smith AJ, Surviladze Z, Chigaev A, Mazel T, Kalesnikoff J, Lowell CA, Krystal G, Sklar LA, Wilson BS, Oliver JM. 2004. Dysregulated FcεRI signaling and altered Fyn and SHIP activities in Lyn-deficient mast cells. J. Immunol. 173:100–112. http://dx.doi.org/10.4049/jimmunol.173.1.100.
48. Huber M, Helgason CD, Damen JE, Liu L, Humphries RK, Krystal G. 1998. The src homology 2-containing inositol phosphatase (SHIP) is the gatekeeper of mast cell degranulation. Proc. Natl. Acad. Sci. U. S. A. 95:11330–11335. http://dx.doi.org/10.1073/pnas.95.19.11330.
49. Gilfillan AM, Tkaczyk C. 2006. Integrated signalling pathways for mast-cell activation. Nat. Rev. Immunol. 6:218–230. http://dx.doi.org/10.1038/nri1782.
50. Iwaki S, Tkaczyk C, Satterthwaite AB, Halcomb K, Beaven MA, Metcalfe DD, Gilfillan AM. 2005. Btk plays a crucial role in the amplification of FcεRI-mediated mast cell activation by kit. J. Biol. Chem. 280:40261–40270. http://dx.doi.org/10.1074/jbc.M506063200.
51. Iwaki S, Spicka J, Tkaczyk C, Jensen BM, Furumoto Y, Charles N, Kovarova M, Rivera J, Horejsi V, Metcalfe DD, Gilfillan AM. 2008. Kit- and FcεRI-induced differential phosphorylation of the transmembrane adaptor molecule NTAL/LAB/LAT2 allows flexibility in its scaffolding function in mast cells. Cell. Signal. 20:195–205. http://dx.doi.org/10.1016/j.cellsig.2007.10.013.
52. Halova I, Draberova L, Draber P. 2012. Mast cell chemotaxis—chemoattractants and signaling pathways. Front. Immunol. 3:119. http://dx.doi.org/10.3389/fimmu.2012.00119.
53. Pullen NA, Barnstein BO, Falanga YT, Wang Z, Suzuki R, Tamang TD, Khurana MC, Harry EA, Draber P, Bunting KD, Mizuno K, Wilson BS, Ryan JJ. 2012. Novel mechanism for FcεRI-mediated signal transducer and activator of transcription 5 (STAT5) tyrosine phosphorylation and the selective influence of STAT5B over mast cell cytokine production. J. Biol. Chem. 287:2045–2054. http://dx.doi.org/10.1074/jbc.M111.311142.
54. Grange M, Verdeil G, Arnoux F, Griffon A, Spicuglia S, Maurizio J, Buferne M, Schmitt-Verhulst AM, Auphan-Anezin N. 2013. Active STAT5 regulates T-bet and eomesodermin expression in CD8 T cells and imprints a T-bet-dependent Tc1 program with repressed IL-6/TGF-beta1 signaling. J. Immunol. 191:3712–3724. http://dx.doi.org/10.4049/jimmunol.1300319.
55. Pullen NA, Falanga YT, Morales JK, Ryan JJ. 2012. The Fyn-STAT5

pathway: a new frontier in IgE- and IgG-mediated mast cell signaling. Front. Immunol. 3:117. http://dx.doi.org/10.3389/fimmu.2012.00117.
56. Huber M, Helgason CD, Scheid MP, Duronio V, Humphries RK, Krystal G. 1998. Targeted disruption of SHIP leads to Steel factor-induced degranulation of mast cells. EMBO J. 17:7311–7319. http://dx.doi.org/10.1093/emboj/17.24.7311.
57. Deakin NO, Turner CE. 2008. Paxillin comes of age. J. Cell Sci. 121:2435–2444. http://dx.doi.org/10.1242/jcs.018044.
58. Fang X, Lang Y, Wang Y, Mo W, Wei H, Xie J, Yu M. 2012. Shp2 activates Fyn and Ras to regulate RBL-2H3 mast cell activation following FcεRI aggregation. PLoS One 7:e40566. http://dx.doi.org/10.1371/journal.pone.0040566.
59. Broad LM, Braun FJ, Lievremont JP, Bird GS, Kurosaki T, Putney JW, Jr. 2001. Role of the phospholipase C-inositol 1,4,5-trisphosphate pathway in calcium release-activated calcium current and capacitative calcium entry. J. Biol. Chem. 276:15945–15952. http://dx.doi.org/10.1074/jbc.M011571200.
60. Litjens T, Nguyen T, Castro J, Aromataris EC, Jones L, Barritt GJ, Rychkov GY. 2007. Phospholipase C-γ1 is required for the activation of store-operated Ca^{2+} channels in liver cells. Biochem. J. 405:269–276. http://dx.doi.org/10.1042/BJ20061762.
61. Antigny F, Jousset H, Konig S, Frieden M. 2011. Thapsigargin activates Ca^{2+} entry both by store-dependent, STIM1/Orai1-mediated, and store-independent, TRPC3/PLC/PKC-mediated pathways in human endothelial cells. Cell Calcium 49:115–127. http://dx.doi.org/10.1016/j.ceca.2010.12.001.
62. Baba Y, Nishida K, Fujii Y, Hirano T, Hikida M, Kurosaki T. 2008. Essential function for the calcium sensor STIM1 in mast cell activation and anaphylactic responses. Nat. Immunol. 9:81–88. http://dx.doi.org/10.1038/ni1546.
63. Hájková Z, Bugajev V, Dráberová E, Vinopal S, Dráberová L, Janáček J, Dráber P, Dráber P. 2011. STIM1-directed reorganization of microtubules in activated mast cells. J. Immunol. 186:913–923. http://dx.doi.org/10.4049/jimmunol.1002074.
64. Chung SC, Limnander A, Kurosaki T, Weiss A, Korenbrot JI. 2007. Coupling Ca^{2+} store release to Icrac channel activation in B lymphocytes requires the activity of Lyn and Syk kinases. J. Cell Biol. 177:317–328. http://dx.doi.org/10.1083/jcb.200702050.
65. Timokhina I, Kissel H, Stella G, Besmer P. 1998. Kit signaling through PI 3-kinase and Src kinase pathways: an essential role for Rac1 and JNK activation in mast cell proliferation. EMBO J. 17:6250–6262. http://dx.doi.org/10.1093/emboj/17.21.6250.
66. Linnekin D, DeBerry CS, Mou S. 1997. Lyn associates with the juxtamembrane region of c-Kit and is activated by stem cell factor in hematopoietic cell lines and normal progenitor cells. J. Biol. Chem. 272:27450–27455. http://dx.doi.org/10.1074/jbc.272.43.27450.
67. Lennartsson J, Ronnstrand L. 2012. Stem cell factor receptor/c-Kit: from basic science to clinical implications. Physiol. Rev. 92:1619–1649. http://dx.doi.org/10.1152/physrev.00046.2011.
68. Barnstein BO, Li G, Wang Z, Kennedy S, Chalfant C, Nakajima H, Bunting KD, Ryan JJ. 2006. Stat5 expression is required for IgE-mediated mast cell function. J. Immunol. 177:3421–3426. http://dx.doi.org/10.4049/jimmunol.177.5.3421.
69. Morales JK, Falanga YT, Depcrynski A, Fernando J, Ryan JJ. 2010. Mast cell homeostasis and the JAK-STAT pathway. Genes Immun. 11:599–608. http://dx.doi.org/10.1038/gene.2010.35.
70. Hálová I, Dráberová L, Bambousková M, Machyna M, Stegurová L, Smrž D, Dráber P. 2013. Crosstalk between tetraspanin CD9 and transmembrane adaptor protein non-T cell activation linker (NTAL) in mast cell activation and chemotaxis. J. Biol. Chem. 288:9801–9814. http://dx.doi.org/10.1074/jbc.M112.449231.
71. Samayawardhena LA, Hu J, Stein PL, Craig AW. 2006. Fyn kinase acts upstream of Shp2 and p38 mitogen-activated protein kinase to promote chemotaxis of mast cells towards stem cell factor. Cell. Signal. 18:1447–1454. http://dx.doi.org/10.1016/j.cellsig.2005.11.005.
72. Samayawardhena LA, Kapur R, Craig AW. 2007. Involvement of Fyn kinase in Kit and integrin-mediated Rac activation, cytoskeletal reorganization, and chemotaxis of mast cells. Blood 109:3679–3686. http://dx.doi.org/10.1182/blood-2006-11-057315.
73. Metcalfe DD, Baram D, Mekori YA. 1997. Mast cells. Physiol. Rev. 77:1033–1079.
74. Williams CM, Galli SJ. 2000. The diverse potential effector and immunoregulatory roles of mast cells in allergic disease. J. Allergy Clin. Immunol. 105:847–859. http://dx.doi.org/10.1067/mai.2000.106485.
75. Schuck S, Honsho M, Ekroos K, Shevchenko A, Simons K. 2003. Resistance of cell membranes to different detergents. Proc. Natl. Acad. Sci. U. S. A. 100:5795–5800. http://dx.doi.org/10.1073/pnas.0631579100.
76. Garner AE, Smith DA, Hooper NM. 2008. Visualization of detergent solubilization of membranes: implications for the isolation of rafts. Biophys. J. 94:1326–1340. http://dx.doi.org/10.1529/biophysj.107.114108.

1.6 NEGATIVE REGULATORY ROLES OF ORMDL3 IN THE FcεRI-TRIGGERED EXPRESSION OF PROINFLAMMATORY MEDIATORS AND CHEMOTACTIC RESPONSE IN MURINE MAST CELLS

Cell Mol Life Sci. 73(6):1265-85, 2016.

In this study we provide evidence that downregulation of ORMDL3 expression in mast cells enhances AKT and NF-κB-directed signaling pathways and chemotaxis and contributes to the development of mast cell-mediated local inflammation *in vivo*.

Cell. Mol. Life Sci. (2016) 73:1265–1285
DOI 10.1007/s00018-015-2047-3

Cellular and Molecular Life Sciences

ORIGINAL ARTICLE

Negative regulatory roles of ORMDL3 in the FcεRI-triggered expression of proinflammatory mediators and chemotactic response in murine mast cells

Viktor Bugajev[1] · Ivana Halova[1] · Lubica Draberova[1] · Monika Bambouskova[1] · Lucie Potuckova[1] · Helena Draberova[1] · Tomas Paulenda[1] · Sergi Junyent[1] · Petr Draber[1]

Received: 16 April 2015 / Revised: 19 August 2015 / Accepted: 17 September 2015 / Published online: 25 September 2015

Abstract Single-nucleotide polymorphism studies have linked the chromosome 17q12-q21 region, where the human orosomucoid-like (*ORMDL*)*3* gene is localized, to the risk of asthma and several other inflammatory diseases. Although mast cells are involved in the development of these diseases, the contribution of ORMDL3 to the mast cell physiology is unknown. In this study, we examined the role of ORMDL3 in antigen-induced activation of murine mast cells with reduced or enhanced ORMDL3 expression. Our data show that in antigen-activated mast cells, reduced expression of the ORMDL3 protein had no effect on degranulation and calcium response, but significantly enhanced phosphorylation of AKT kinase at Ser 473 followed by enhanced phosphorylation and degradation of IκBα and translocation of the NF-κB p65 subunit into the nucleus. These events were associated with an increased expression of proinflammatory cytokines (TNF-α, IL-6, and IL-13), chemokines (CCL3 and CCL4), and cyclooxygenase-2 dependent synthesis of prostaglandin D2. Antigen-mediated chemotaxis was also enhanced in ORMDL3-deficient cells, whereas spreading on fibronectin was decreased. On the other hand, increased expression of ORMDL3 had no significant effect on the studied signaling events, except for reduced antigen-mediated chemotaxis. These data were corroborated by increased IgE-antigen-dependent passive cutaneous anaphylaxis in mice with locally silenced ORMDL3 using short interfering RNAs. Our data also show that antigen triggers suppression of ORMDL3 expression in the mast cells. In summary, we provide evidence that downregulation of ORMDL3 expression in mast cells enhances AKT and NF-κB-directed signaling pathways and chemotaxis and contributes to the development of mast cell-mediated local inflammation in vivo.

Keywords Mast cell · RNA interference · ORMDL3 knockdown · Prostaglandin D2 · Degranulation · Chemotaxis · Proinflammatory cytokines

Abbreviations

Ag	Antigen
BMMC	Bone marrow-derived mast cell
BSS	Buffered saline solution
Bp	Base pairs
$[Ca^{2+}]_i$	Concentrations of free intracellular Ca^{2+}
COX	Cyclooxygenase
Ct	Threshold cycle
NT	Nontarget
O3_KD	ORMDL3 knockdown
O3_OE	ORMDL3 overexpression
ORM	Orosomucoid
ORMDL	Orosomucoid-like
PCA	Passive cutaneous anaphylaxis
pCDH	pCDH-CMV-MCS-EF1-Puro
PG	Prostaglandin
SERCA	Sarco/endoplasmic reticulum Ca^{2+} ATPase
sh	Short hairpin
siRNA	Short interfering RNA
SNP	Single-nucleotide polymorphisms
TNP	2,4,6-Trinitrophenol

Electronic supplementary material The online version of this article (doi:10.1007/s00018-015-2047-3) contains supplementary material, which is available to authorized users.

✉ Petr Draber
draberpe@img.cas.cz

[1] Department of Signal Transduction, Institute of Molecular Genetics, Academy of Sciences of the Czech Republic, v.v.i., Videnska 1083, 142 20 Prague 4, Czech Republic

WT Wild type

Introduction

Orosomucoid-like (ORMDL)3 protein has attracted increased attention since the discovery of single-nucleotide polymorphisms (SNPs) in the chromosome 17q12-q21 region that were associated with onset of asthma in childhood [1]. Further studies confirmed these data in ethnically diverse populations [2, 3]. Interestingly, SNPs associated with 17q12-q21 were also linked to chronic obstructive pulmonary disease [4], ulcerative colitis [5], primary biliary cirrhosis [6], type 1 diabetes [6], Crohn disease [6, 7] and rheumatoid arthritis [8]. It has been suggested that the risk alleles for asthma mapped in the 17q12-q21 region are linked to increased levels of the *ORMDL3* gene transcript [1, 6], but the risk alleles implicated in the predisposition to primary biliary cirrhosis, type 1 diabetes and Crohn disease are associated with decreased ORMDL3 mRNA levels [6]. Since *ORMDL3* is only one of several genes in the chromosome 17q12-q21 region, the observed data underline the complexity of inflammatory diseases [6, 9].

Human and mouse *ORMDL3* genes encode 153 aa proteins belonging to the conserved ORMDL family consisting of three members. All three members of this family (ORMDL1–3) are embedded in the endoplasmic reticulum membrane [10]. Pivotal studies of ORMDL3 yeast homologs, orosomucoid (ORM)1 and ORM2, showed that ORM proteins are negative regulators of sphingolipid synthesis [11, 12] and that knockdown of all three ORMDL isoforms resulted in increased ceramide production in distinct mammalian cell lines [11, 13, 14]. Further experiments showed that disruption of sphingolipid homeostasis in the mouse model increased bronchial reactivity in the absence of inflammatory stimulus [15]. ORMDL3 has also been found to play a role as a regulator of Ca^{2+} homeostasis in the endoplasmic reticulum [16, 17] and as a trigger of unfolded protein response [16, 18, 19].

Several studies attempted to explain the physiological role of ORMDL3 in cells and tissues relevant to asthma. Mice challenged with allergen exhibited enhanced expression of ORMDL3 in macrophages, eosinophils and lung epithelial cells [18]. Furthermore, a lung epithelial cell line transfected with ORMDL3 cDNA showed increased transcription of genes encoding metalloproteases, chemokines and oligoadenylate synthetases [18]. In addition, bone marrow-derived eosinophils transduced with ORMDL3 cDNA showed enhanced rolling and nuclear localization of the phosphorylated NF-κB p65 subunit [20]. Transgenic mice overexpressing human ORMDL3 exhibited increased levels of serum IgE and showed spontaneous development of enhanced airway responsiveness. This correlated with increased numbers of $CD4^+$ cells, macrophages, eosinophils and neutrophils, and enhanced Th2 cytokine levels in the lungs of transgenic mice [19]. Although mast cells are crucial effector cells in IgE-dependent allergic disorders [21, 22] and are critical for promoting the severity of collagen-induced arthritis, which is an autoimmune inflammatory disease [23], the involvement of ORMDL3 in FcεRI-dependent activation and mast cell-mediated inflammation has not yet been determined.

In this study, we decided to test the hypothesis that changes in the expression levels of ORMDL3 could modulate mast cell proinflammatory responses. Bone marrow-derived mast cells (BMMCs) with enhanced or reduced expression of ORMDL3 were produced and examined. We focused on the NF-κB signaling axis, which is an important player in the transcription of proinflammatory cytokines and immunoregulatory proteins [24] and is involved in the promotion of inflammation [25–27]. We found that ORMDL3-deficient cells exhibited significantly increased translocation of the NF-κB p65 subunit into the nucleus. These events were accompanied by enhanced expression of genes encoding proinflammatory cytokines, chemokines, and cyclooxygenase (COX)-2, an inducible enzyme involved in prostaglandin (PG)D2 synthesis [28]. In an attempt to identify the signaling pathway that precedes activation of NF-κB, we found that AKT kinase exhibited increased phosphorylation. We also studied the roles of ORMDL3 in the migration of mast cells toward antigen (Ag) and changes in ORMDL3 expression after high-affinity IgE receptor (FcεRI) triggering. Altogether, our data provide evidence that in mast cells, ORMDL3 functions predominantly as a negative regulator of FcεRI-mediated signaling events leading to the expression of proinflammatory mediators and chemotaxis. These data were corroborated by the finding of enhanced passive cutaneous anaphylaxis (PCA) in mice with locally silenced ORMDL3.

Materials and methods

Cells and lentiviral infection

BMMCs were derived from femurs and tibias of 8- to 10-week-old BALB/c mice bred, maintained, and used in accordance with the Institute of Molecular Genetics guidelines (Permit number 12135/2010-17210) and national guidelines (2048/2004-1020). The cells were cultured in RPMI-1640 medium supplemented with 100 U/ml penicillin, 100 μg/ml streptomycin, 71 μM 2-mercaptoethanol, MEM non-essential amino acids, 0.7 mM

SulfoLink™ Immobilization Kit for Peptides (Pierce) according to the manufacturer's instructions. Fura-2, AM was obtained from Life Technologies. All other reagents were obtained from Sigma-Aldrich.

β-Glucuronidase release and Ca^{2+} response

BMMCs were sensitized with TNP-specific IgE (IGEL b4 1 mAb, 1 μg/ml) in stem cell factor- and IL-3-free culture medium for 16 h, unless stated otherwise. Then the cells were washed in buffered saline solution (BSS; 135 mM NaCl, 5 mM KCl, 1.8 mM CaCl2, 5.6 mM glucose, 20 mM HEPES, pH 7.4) supplemented with 0.1 % BSA and activated with Ag (TNP–BSA conjugate, 15–25 mol TNP/mol BSA). The extent of degranulation was evaluated by determining β-glucuronidase concentrations as described previously [33] except that an Infinite 200 M (TECAN) plate reader was used at 355 nm excitation and 460 nm emission wavelengths. Calcium mobilization was determined using Fura-2 acetoxymethyl ester (Fura-2 AM; Life Technologies) as a reporter. Cells were incubated with Fura-2 AM (1 ng/ml) and probenecid (2.5 mM) in BSS supplemented with 0.1 % BSA and incubated in the shaker for 30 min at 37 °C. Fura-2 AM-loaded cells were washed twice with 2.5 mM probenecid in BSS-0.1 % BSA and then transferred to BSS-0.1 % BSA supplemented with 2.5 mM probenecid and incubated in Thermomixer (Eppendorf; 15 min, 37 °C, 500 rpm). Cells were pelleted by centrifugation at 500×*g* for 3 min, resuspended in BSS-0.1 % BSA and transferred to white polysorp 96 well plate (NUNC, Thermo Scientific). After 1 min, BSS-0.1 % BSA supplemented with Ag (final concentration 100 ng/ml) was added using the TECAN injector system. Measurement continued up to 200 s. Levels of Ca^{2+} were determined by spectrofluorometry using the Infinite 200 M plate reader with excitation wavelengths at 340 and 380 nm and with a constant emission at 510 nm. To determine basal concentrations of free intracellular Ca^{2+} ($[Ca^{2+}]_i$) in various cell types, Triton X-100 (0.1 % final concentration) was added to the Fura-2-loaded cells and Fura-2 fluorescence was determined. Then, EGTA (16 mM final concentration) was added and Fura-2 fluorescence was again determined. Calcium concentrations were then calculated using the formula: $[Ca^{2+}]_i = K_d \times S_{f2}/S_{b2} \times (R - R_{min})/(R_{max} - R)$, where K_d represents the dissociation constant for Fura-2 (224 nM), S_{f2} the average fluorescence obtained at 380 nm after EGTA addition, S_{b2} the average fluorescence obtained at 380 nm after addition of Triton X-100, R_{min} the mean ratio calculated from the data acquired after EGTA addition, R_{max} the mean of ratio calculated from data acquired after addition of Triton X-100, and R the ratio of fluorescence obtained at 340/380.

Detection of ORMDL, cytokines, and chemokines at the mRNA level

IgE-sensitized BMMCs were activated with different concentrations of Ag. One hour later, mRNA was extracted using a TurboCapture 96 mRNA kit or RNeasy miniKit (Qiagen). Single-stranded cDNA was synthesized with M-MLV reverse transcriptase (Invitrogen) according to the manufacturer's instructions. Real-time PCR amplifications of cDNAs were performed in 10 μl reaction volumes of qPCR mix containing 1 M 1,2-propanediol, 0.2 M trehalose and SYBR green 1 [34] in 384-well plates sealed with LightCycler 480 sealing foil and analyzed by LightCycler 480 (Roche Diagnostics). The following cycling conditions were used: 3 min at 95 °C, followed by 50 cycles of 10 s at 95 °C, 20 s at 60 °C and 20 s at 72 °C. Threshold cycle (Ct) values were determined by automated threshold analysis of the cycler. Specificity of the PCR was evaluated by examining the melting curves. For data presented in Fig. 2a, actin, *GAPDH*, ubiquitin, *TBP*, *SDHA*, and *HPRT* were used as reference genes and the expression levels of ORMDL3 mRNA were normalized to the geometric mean of the reference genes in nonactivated control cells. In all other experiments, actin, *GAPDH*, and ubiquitin were used as the reference genes. The relative changes in the mRNA expression levels were normalized to the ones of the corresponding controls. The following primer sets were used for amplification of different cDNA fragments (sense/antisense; numbers in square brackets are sizes of the fragments in bps): actin, 5′-GATCTGGCACCACACCTTCT-3′/5′-GGGGTGTTGAAGGTCTCAAA-3′ [138]; GAPDH, 5′-AACTTTGGCATTGTGGAAGG-3′/5′-ATCCACAGTCTTCTGGGTGG-3′ [69]; ubiquitin, 5′-ATGTGAAGGCCAAGATCCAG-3′/5′-TAATAGCCACCCCTCAGACG-3′ [160]; HPRT, 5′-CTGGTGAAAAGGACCTCTCGAA-3′/5′-CTGAAGTACTCATTATAGTCAAGGGCAT-3′ [109]; TBP, 5′-GAAGAACAATCCAGACTAGCAGCA-3′/5′-CCTTATAGGGAACTTCACATCACAG-3′ [128]; SDHA, 5′-AAGGCAAATGCTGGAGAAGA-3′/5′-TGGTTCTGCATCGACTTCTG-3′ [112]; ORMDL3, 5′- CCAACCTTATCCACAACCTGG-3′/5′-GACCCCGTAGTCCATCTGC-3′ [124]; ORMDL2, 5′-CACAGCGAAGTAAACCCCAAC-3′/5′-AGGGTCCAGACAACAGGAATG-3′ [134]; ORMDL1, 5′-ACAGTGAGGTAAACCCCAATACT-3′/5′-GCAAAAACACATACATCCCCAGA-3′ [174]; TNF-α, 5′-CCCTCACACTCAGATCATCTTCT-3′/5′-GCTACGACGTGGGCTACAG-3′ [61]; IL-6, 5′-GAGGATACCACTCCCAACAGACC-3′/5′-AAGTGCATCATCGTTGTTCATACA-3′ [141]; IL-13, 5′-AGACCAGACTCCCCTGTGCA-3′/5′-TGGGTCCTGTAGATGGATTG-3′ [123]; CCL3, 5′-CATCGTTGACTATTTTGAAACCAG-3′/5′-GCCGGTTTCTCTTAGTCAGGAA-3′ [72]; CCL4, 5′-CTTGGAGTTGAACTGAGCA

GC-3′/5′-AGAGGGGCAGGAAATCTGAA-3′ [126]; SERCA2b, 5′-GAGAACGCTCACACAAAGACC-3′/5′-CAATTCGTTGGAGCCCCAT-3′ [120]; COX-2, 5′-TGAGCAACTATTCCAAACCAGC-3′/5′-GCACGTAGTCTTCGATCACTATC-3′ [74].

For detection of cytokine secretion, the nano-iPCR method was used as described [35]. Briefly, anti-TNF-α, anti-IL-13 (each at 1 μg/ml), or anti-IL-6 (2 μg/ml) in 100 mM borate buffer (pH 9.5) was dispensed in 50 μl aliquots into wells of a real-time 96-well plate (Eppendorf). After overnight incubation at 4 °C, each well was washed four times with 200 μl of TBST (10 mM Tris–HCl, pH 7.4, 150 mM NaCl, and 0.05 % Tween 20) and the remaining binding sites were blocked by 2 h incubation at 37 °C with TBST supplemented with 2 % BSA. After washing, 50 μl of serial dilutions (0.1–100 ng/ml) of recombinant TNF-α, IL-13 or IL-6, or the tested samples diluted in PBS-1 % BSA were added. The samples were incubated 1 h at 37 °C and after washing with TBST, 50 μl of gold nanoparticles armed with thiolated DNA oligonucleotide template were added and further processed as described [35]. For calculation of the cytokine concentrations, the obtained Ct values were compared with those from the corresponding calibration curves.

PGD2 measurements

IgE-sensitized mast cells were seeded at 2×10^5 cells per well in 100 μl of BSS–BSA buffer in a 96-well culture plate. Cells were stimulated by adding 100 μl of Ag to a final concentration of 100 ng/ml for 5 h. Cell-free supernatants were collected and assessed for PGD2 using competitive enzyme immunoassay based on measurement of PGD2-methoxylamine hydrochloride derivate according to the manufacturer's conditions (Cayman Chemicals). For detection, the Infinite 200 M plate reader was used. Supernatants of nonactivated and activated cells were diluted 1/10 and 1/40, respectively, to be read within the range of the respective standard curve.

Gel electrophoresis and immunoblotting

Whole-cell extracts were prepared by washing the cells in cold PBS, solubilizing them in hot SDS-sample buffer [36], sonicating, and boiling for 5 min. Proteins were size fractionated on 10 or 12.5 % SDS-PAGE gels, electrophoretically transferred onto nitrocellulose membrane, and analyzed by immunoblotting with protein- or phosphoprotein-specific Abs. Bound primary Abs were detected with HRP-conjugated secondary Abs. The HRP signal was detected with chemiluminescence reagent [37] and quantified by a Luminescent Image Analyzer LAS 3000 (Fuji Photo Film Co.). Aida software (Raytest GmbH) was used for signal quantification. Protein levels were normalized to the corresponding controls.

Flow cytometry analysis

To quantify the surface expression of FcεRI and KIT, BMMCs (3×10^5/ml) were exposed simultaneously to anti-mouse FcεRI-FITC and anti-mouse KIT-allophycocyanin for 30 min on ice. Then, the cells were washed with ice-cold PBS and evaluated using an Accuri C6 flow cytometer (BD Biosciences).

Cell adhesion and spreading

IgE-sensitized BMMCs were loaded with calcein-AM and transferred into a 96-well plate (Thermo Scientific) coated with fibronectin (10 ng/ml) diluted in PBS [38]. Cells activated for 30 min with 100 ng/ml of Ag were examined for adhesion assay using the Infinite 200 M plate reader with excitation and emission filters at 485 nm and 538 nm, respectively. For cell spreading, wells in 96-well glass-bottom plates (InVitroSci) were coated with fibronectin (50 μl; 50 μg/ml) diluted in PBS. Wells were then washed with PBS, and 30×10^3 cells in BSS-0.1 % BSA were added per well. Cells were allowed to attach for 30 min at 37 °C, washed, and activated or not with Ag. After 30 min, cells were fixed with 3 % paraformaldehyde in PBS for 30 min at room temperature. For filamentous (F)-actin staining, cells were exposed to Alexa Fluor 488-phalloidin conjugate (Invitrogen, #A12379), diluted 1:100 in PBS supplemented with L-α-lysophosphatidylcholine (80 μg/ml). After 1 h, cells were washed and kept in PBS supplemented with Hoechst 33258 stain (1 μg/ml) until measurement. Cells were then examined with the Scan^R system (Olympus).

Chemotactic response

Ag-Mediated chemotactic responses were evaluated using 24-well Transwell chambers (Corning) with 8 μm polycarbonate filters as described previously [38]. Cells migrating into lower compartments within the 8-h incubation period were counted using an Accuri C6 Flow Cytometer (Becton–Dickinson).

F-actin assay

The total amount of F-actin in nonactivated and Ag-activated cells was determined by flow cytometry. BMMCs in a 96-well plate (5×10^4 cells per well) were exposed to various stimuli at 37 °C, fixed with 3 % paraformaldehyde in phosphate-buffered saline, and then permeabilized and stained in a single step by a mixture of lysophosphatidylcholine (200 mg/ml)

and 1000× diluted Alexa Fluor 488-phalloidin (Molecular Probes) in phosphate-buffered saline. The fluorescence intensity was measured using LSRII flow cytometer (Becton–Dickinson). The acquired data were analyzed using FlowJo software (Tree Star Inc).

Confocal microscopy

IgE-sensitized BMMCs (3×10^5) were attached (60 min at 37 °C) to a fibronectin-coated multitest slide (MP Biomedicals) and then activated by Ag. After 30 min, the cells were fixed with 4 % paraformaldehyde for 15 min at room temperature and permeabilized with 0.3 % Triton X-100 for 20 min. Free binding sites were blocked with 5 % donkey serum (Jackson ImmunoResearch Laboratories) in PBS and the cells were stained with a mixture of rabbit Abs against p65 subunit of NF-κB diluted 1:400 (#8242) and 1:200 (#sc-372), followed by labeling with secondary antibody, donkey anti-rabbit-Alexa Fluor 488 conjugate, and diluted 1:200 in PBS containing 1 % BSA. ORMDL was labeled with rabbit polyclonal serum (described in Antibodies and reagents) followed by labeling with donkey anti-rabbit-Alexa Fluor 568 (1:100). After 60 min incubation, the cells were washed and mounted in Mowiol 4-88, supplemented with 1 μg/ml Hoechst 33258 to label nuclei. Samples were examined with a confocal laser scanning microscope Leica TCS SP5 equipped with an X63/1.4.N.A. oil-immersion objective. STIM1-YFP (kind gift of Dr. T. Meyer, Stanford University Medical School) was used as an endoplasmic reticulum marker. Golgi marker (YFP-GT) was from Clontech Laboratories. ORMDL3-YFP was cloned into the N1-YFP plasmid (Clontech) using forward primer 5′-AAACTCGAGGCCGCCACCATGAATGTG GGCACAGCAC-3′ and reverse complementary primer 5′-AAAGAATTCGGTACTTATTGATTCCAAAG-3′, introducing *XhoI* and *EcoRI* restriction endonuclease sites (underlined), respectively. Amaxa Nucleofector II (Lonza Cologne AG, Cologne, Germany) was used to nucleofect mast cells using a Mouse Macrophage Kit and program Y-001.

Image analysis

Image processing and analysis were performed using CellProfiler software (Broad Institute, Boston, MA) [39]. For cell spreading, areas corresponding to individual cells were identified by F-actin staining with Alexa Fluor 488-phalloidin and the mean values were calculated from 200 to 400 cells in each sample. The fraction of NF-κB p65 subunit in the nucleus was determined as the difference between NF-κB mean fluorescence in the nucleus (stained with Hoechst 332578) and NF-κB mean fluorescence in the cytoplasm as described [40]. Fifty to hundred cells were evaluated per sample and the values obtained for each cell were plotted in GraphPad Prism (San Diego, CA, USA). Other charts were done in SigmaPlot 8.0 (San Jose, CA, USA).

Short interfering RNA (siRNA)-mediated inhibition of ORMDL3 expression and measurements of PCA

To silence ORMDL3 in the mouse ear, we followed the experimental procedure described by Kanada et al. [41] with some modifications. The specificity of ORMDL3 siRNAs was first confirmed by immunoblotting analysis of lysates from BMMCs nucleofected by Amaxa Nucleofector II 48 h earlier with 1 μg of ORMDL3 siRNA pool (Accell Mouse Ormdl3 siRNA; E-049023-00-0005; Dharmacon) or 1 μg control siRNAs ORMDL3 (O3_siRNA; Accell Non-targeting Pool; D-001910-10-05; Dharmacon) using a Mouse Macrophage Kit and program Y-001 as recommended by the manufacturer (Lonza). For PCA, 20 μL of PBS containing 4 μg/ml of anti-TNP-specific IgE and 2.5 μg of ORMDL3 siRNAs pool was injected into the right ear. As a control, 20 μL of anti-TNP-specific IgE (4 μg/ml) and 2.5 μg of control siRNA was injected intradermally into the left ear. After 48 h, the mice were challenged with an intravenously injected PBS (200 μl) containing Ag (100 μg TNP–BSA) and 1 mg of Evans blue. Two hours later, the mice were killed and the ears removed for measurement of the amount of extravasated dye. Formamide (0.75 ml) was then added to each ear, which was then homogenized with the T-25 ULTRA-TURRAX Digital High-Speed Homogenizer Systems (IKA) and incubated at 80^{O}C for 2 h. The samples were centrifuged at 14,000×*g* for 15 min and supernatants were used for measurement of absorbance at 620 nm.

Statistical analyses

Unless stated otherwise, the significance of intergroup differences was evaluated by Student's *t* test; *, $P < 0.05$; **, $P < 0.01$; ***, $P < 0.001$. Microsoft Excel 2010 or GraphPad Prism was used for statistical analysis evaluation.

Results

Properties of BMMCs with reduced or enhanced expression of ORMDL3

Although ORMDL3 expression was described in various cells of the immune system [1, 18], its presence in mast cells has not yet been determined. Here, we used RT-PCR to show the expression of ORMDL3 in BMMCs. We found

that ORMDL3 as well as ORMDL1 and ORMDL2 are expressed in BMMCs (Fig. 1a). We did not observe any variations in the expression of ORMDL3 during BMMC cultivation in medium supplemented with IL-3 and SCF (data not shown). Using BMMCs transduced with markers of endoplasmic reticulum or Golgi apparatus, we confirmed previous findings [16, 18] that endogenous ORMDL proteins detected by the NVG antibody recognizing all three ORMDLs (Fig. S1a, c, d) are associated with the endoplasmic reticulum and perinuclear membrane, but not with the Golgi apparatus (Fig. 1b). Next, we examined whether the changes in ORMDL3 expression influence mast cell effector functions. To induce ORMDL3 knockdown (O3_KD), BMMCs were transduced using the pLKO.1 lentiviral vector with ORMDL3 shRNAs (200, 201, 202, and 203, Fig. 1c). As controls, BMMCs were transduced with the empty pLKO.1 vector. Quantification of ORMDL3 mRNA expression by RT-qPCR showed its 30–80 % decrease after transduction of ORMDL3 shRNAs (Fig. 1c). To find out whether silencing of ORMDL3 is accompanied by changes in expression of other ORMDL family members, we assessed the expression of all members of the ORMDL family in BMMCs with O3_KD. Data in Fig. 1d indicate that silencing with the O3_KD vector (shRNA 200) led to a significant reduction of ORMDL3 mRNA without any effect on the expression of ORMDL1 and ORMDL2 mRNA. For production of cells with enhanced expression of ORMDL3, we used pCDH vectors containing ORMDL3 cDNA tagged with myc at the N terminus (myc-O3) or C terminus (O3-myc). Cells transduced with ORMDL3 cDNAs exhibited an 8- to 12-fold increase in ORMDL3 mRNA when compared with cells transduced with the empty pCDH vector, but expression of ORMDL1 and ORMDL2 mRNAs was not significantly changed (Fig. 1e). It should be noted that orientation of the tag attached to ORMDL3 influenced the mobility of the proteins in the gel ([11]; Fig. 1f). However, because in functional assays we did not see any significant differences between cells transduced with the two constructs, the data obtained with both of them were pooled and are presented as cells with ORMDL3 overexpressors (O3_OE). The observed downregulation or upregulation of ORMDL3 mRNA in cells with O3_KD or O3_OE, respectively, resulted in the expected changes in the intensity of the band corresponding to the ORMDL family proteins as detected by immunoblotting with polyclonal serum. The amount of the band corresponding to the ORMDL proteins was reduced by 60–80 % depending on the shRNA used (Fig. 1f). The characteristics of the rabbit serum used for immunoblotting (TPF) are shown in Fig. S1b, c. Both sera (NVG and TPF) recognize other members of the ORMDL family, as determined by their reactivity with cells expressing cDNAs encoding ORMDL1 and ORMDL2 (Fig. S1c). Therefore, we refer to the corresponding band of 17 kDa as ORMDL. In BMMCs transfected with myc-O3 or O3-myc vectors, ORMDL3 protein was enhanced approximately three to fourfold (Fig. 1f), although the increase of ORMDL3 expression at the mRNA level was more prominent (Fig. 1e). BMMCs with both O3_KD (all four shRNAs) and O3_OE (myc-O3 or O3-myc vectors) had preserved expression of FcεRI and KIT receptors on the plasma membrane (Fig. S2), but statistical evaluation revealed that shRNAs 201 and 202 exhibited significant changes in the expression of c-Kit ($P < 0.05$) and shRNA 201 as well as in FcεRI expression (Fig. 1g; $P < 0.05$). Based on these results, we excluded shRNAs 201 and 202 from further work. All experiments with O3_KD are based on shRNA 200. Cells transduced with shRNA 203 exhibited similar properties to those with shRNA 200. Based on these findings, experimental data were pooled and all data are presented as O3_KD. Alcian blue staining of cytospin slides showed that the morphology of O3_KD and O3_OE mast cells was not different from that of cells transduced with appropriate controls (see examples in Fig. 1h).

Ag activation of BMMCs induces downregulation of ORMDL3

A previous study showed that challenge with allergen induced expression of ORMDL3 in mouse bronchial epithelial cells, lung macrophages, or BM-derived eosinophils, but not in peripheral blood neutrophils [18]. Moreover, increased ORMDL3 expression in bronchial airway epithelial cells was stimulated with IL-4 and IL-13 [18] and in eosinophils triggered with IL-3 and eotaxin-1 [20]. In further experiments, we therefore examined whether FcεRI activation of BMMCs would also lead to changes in ORMDL3 expression. Interestingly, in IgE-sensitized cells, activation with Ag resulted in a significant decrease of ORMDL3 mRNA expression 1, 4, and 6 h after FcεRI triggering, but ORMDL1 and ORMDL2 mRNA expression was not significantly affected (Fig. 2a). At the protein level, for detection we used polyclonal antibodies recognizing all members of the ORMDL family (Fig. S1a–c). Data presented in Fig. 2b and c indicate that there is a slight, but significant decrease in ORMDL family member expression in cells activated for 8–24 h with Ag. Attenuation of ORMDL3 transcription in activated cells was also observed in cells with O3_KD, in which the residual amount of ORMDL3 mRNA was further lowered (Fig. 2d). Thus, FcεRI-activated mast cells exhibit downregulation of ORMDL3 and in this regard differ from activated eosinophils, lung macrophages, and bronchial airway epithelial cells.

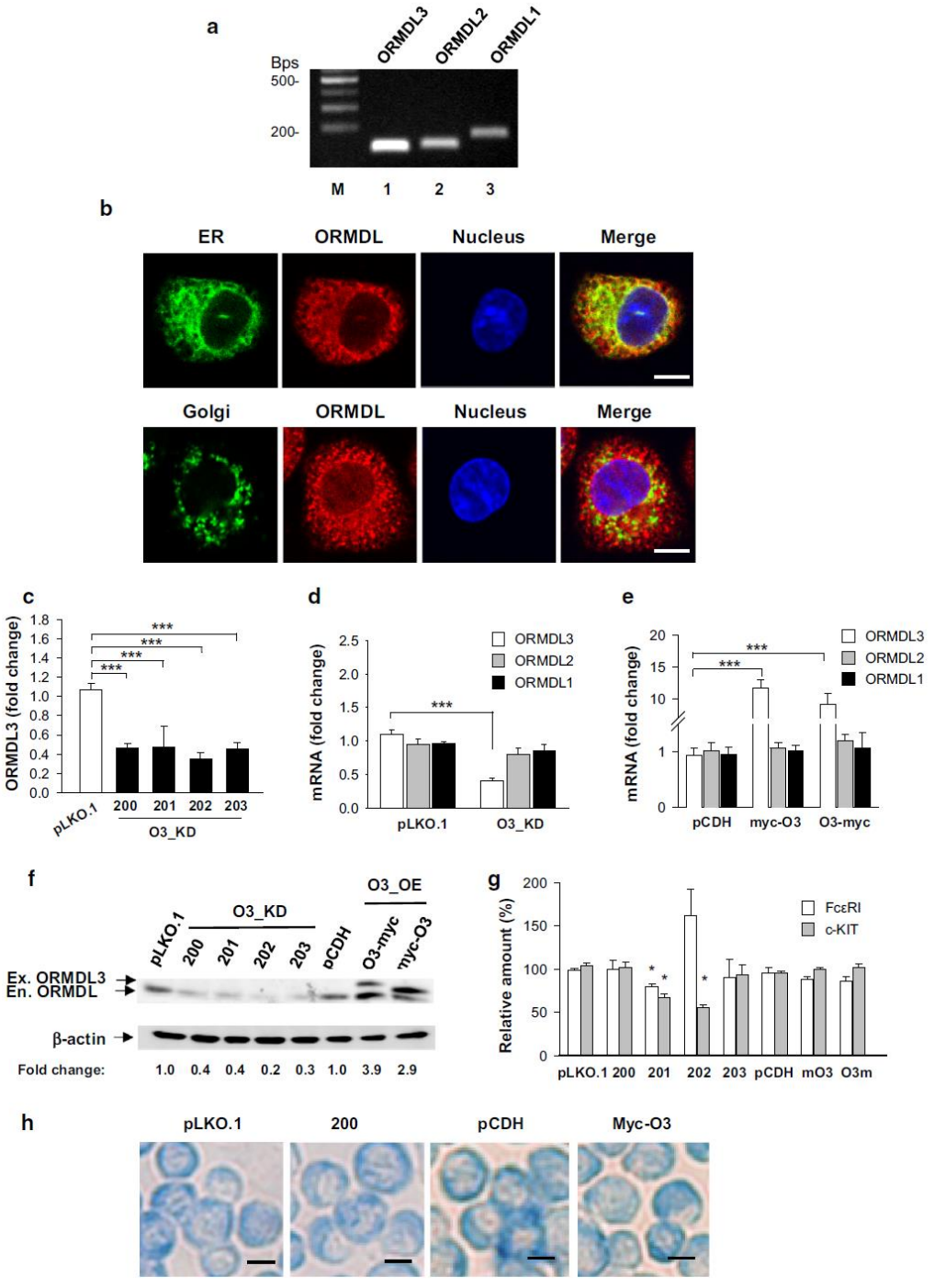
a
ORMDL3
ORMDL2
ORMDL1
Bps
500-
200-
M 1 2 3
b
ER
ORMDL
Nucleus
Merge
Golgi
ORMDL
Nucleus
Merge
c
ORMDL3 (fold change)
pLKO.1
200 201 202 203
O3_KD
d
mRNA (fold change)
ORMDL3
ORMDL2
ORMDL1
pLKO.1
O3_KD
e
mRNA (fold change)
ORMDL3
ORMDL2
ORMDL1
pCDH
myc-O3
O3-myc
f
O3_OE
pLKO.1
O3_KD
200 201 202 203
pCDH
O3-myc
myc-O3
Ex. ORMDL3
En. ORMDL
β-actin
Fold change: 1.0 0.4 0.4 0.2 0.3 1.0 3.9 2.9
g
Relative amount (%)
FcεRI
c-KIT
pLKO.1 200 201 202 203 pCDH mO3 O3m
h
pLKO.1
200
pCDH
Myc-O3

◀**Fig. 1** Properties of BMMCs with reduced or enhanced ORMDL3 expression. **a** Expression of ORMDL1-3 mRNAs in BMMCs as determined by RT-PCR followed by agarose gel electrophoresis and staining with ethidium bromide. DNA marker in bps is shown in *line M*. **b** Colocalization of endogenous ORMDL proteins (shown in *red pseudocolor*) with STIM1-YFP, a marker of endoplasmic reticulum (ER *upper panel*; green pseudocolor), but not with GT-YFP, a marker of Golgi (*lower panel* green pseudocolor) is shown. Nuclei were stained with Hoechst 33258 (shown in blue pseudocolor); *bars* 5 μm. **c** BMMCs with O3_KD were obtained after transduction with lentiviruses containing four shRNAs denoted 200, 201, 202, and 203. Control cells were transduced with empty pLKO.1 vector. ORMDL3 mRNAs were quantified by RT-qPCR. **d** RT-qPCR quantification of individual ORMDL family members in cells with O3_KD or in control cells transduced with empty pLKO.1 vector. **e** BMMCs with O3_OE were obtained after transduction with lentiviruses containing ORMDL3 cDNAs terminally tagged with myc at the N-(myc-O3) or C-(O3-myc) end. Control cells were transduced with empty pCDH vector. The levels of ORMDL1 and ORMDL2 mRNAs are shown. RT-qPCR data in **c**–**e** were normalized as described in "Materials and methods" and represent the means and SEMs calculated from three to seven independent experiments. **f** Quantification of ORMDL proteins (serum not specific for ORMDL3) by immunoblotting in whole-cell lysates after transduction of the cells as in **c** and **e**. *Numbers* under the immunoblots indicate the amounts of ORMDL proteins normalized to control cells transfected with pLKO.1 vector (for O3_KD) or pCDH vector (for O3_OE) and to the amount of β-actin used as a loading control (fold change). The positions of endogenous (En.) and exogenous (Ex.) ORMDL3 and β-actin are indicated by *arrows*. **g** Statistical evaluation of FcεRI and c-Kit expression in the transduced BMMCs. **h** Alcian blue staining of cytospin preparations of BMMCs transduced as above; *bars* 10 μm

BMMCs with reduced or enhanced expression of ORMDL3 do not exhibit changes in SYK tyrosine phosphorylation, degranulation, and Ca^{2+} response after FcεRI triggering

FcεRI-mediated signaling events are initiated by tyrosine phosphorylation of the FcεRI β and γ subunits by Src family kinase LYN, followed by propagation of the signal through activity of the Src family kinases and SYK kinase [22]. To examine a possible role of ORMDL3 in FcεRI signaling, we first examined phosphorylation of SYK in Ag-activated BMMCs with reduced or enhanced ORMDL3 expression. Our data indicate that cells with O3_KD (Fig. 3a) or O3_OE (Fig. 3b) show similar SYK phosphorylation as the corresponding controls.

Next, we examined Ag-induced degranulation estimated by the release of β-glucuronidase from preformed secretory lysosomes. We found that BMMCs with O3_KD (Fig. 3c) or O3_OE (Fig. 3d) exhibited similar degranulation as the control cells. We also compared cells transduced with pLKO.1 and nontransduced wild-type (WT) cells to show that mast cell degranulation is not changed by lentivirus transduction (Fig. S3a).

Previous studies have shown that ORMDL3 affects Ca^{2+} mobilization in lymphocytes and eosinophils [16, 17, 20] and regulates the expression of sarco/endoplasmic reticulum Ca^{2+} ATPase (SERCA)2b [19]. Interestingly, BMMCs with O3_KD (Fig. 3e) or O3_OE (Fig. 3f) exhibited similar Ca^{2+} mobilization to cells transduced with empty pLKO.1 or pCDH vectors. We also compared cells transduced with pLKO.1 and WT cells to show that calcium mobilization in mast cells is not changed by lentivirus transduction (Fig. S3b). We also found that expression of mRNA for SERCA2b was not significantly changed in activated and nonactivated mast cells with O3_KD (Fig. 3g) or O3_OE (Fig. 3h) when compared with the corresponding controls. The mRNA levels of SERCA2b in cells transduced with pLKO.1 were comparable to those in WT cells (Fig. S3c). In line with the SERCA2b expression, the basal levels of $[Ca^{2+}]_i$ were not changed in O3_KD (Fig. S4a) or O3_OE (Fig. S4b) when compared with the corresponding controls. We conclude that early FcεRI-induced activation events, including SYK tyrosine phosphorylation, degranulation, and calcium responses in mast cells, are not affected by enhanced or reduced expression of ORMDL3. Furthermore, we show that changes in ORMDL3 protein levels have no significant effect on SERCA2b expression.

Negative regulatory role of ORMDL3 in the expression of cytokines and chemokines

Mast cells are potent producers of various cytokines and chemokines involved in both asthma and autoimmune diseases [22, 23, 42, 43]. In further experiments, we therefore quantified the levels of mRNA encoding cytokines (TNF-α, IL-6, and IL-13; Fig. 4a) and chemokines (CCL3 and CCL4; Fig. 4b) in BMMCs with O3_KD. Using RT-qPCR, we found that all the studied transcripts for cytokines and chemokines were significantly increased in cells with O3_KD when compared with control cells transduced with empty pLKO.1 vector in both nonactivated and Ag-activated cells (Fig. 4a, b). The observed increase in cytokine mRNA levels corresponded to enhanced secretion of the cytokines TNF-α, IL-6 and IL-13 from Ag-activated BMMCs with O3_KD (Fig. 4c). In contrast, no significant changes in the transcription of TNF-α, IL-6, and IL-13 at the RNA (not shown) or protein (Fig. 4d) level were observed when BMMCs with O3_OE were compared with the corresponding controls. These data indicate that ORMDL3 in mast cells is a negative regulator of the production of proinflammatory cytokines such as TNF-α, IL-6, and IL-13 and chemokines CCL3 and CCL4.

ORMDL3 functions as a negative regulator of Ag-mediated chemotaxis

The observed changes in the expression of genes for cytokines and chemokines depending on the expression of

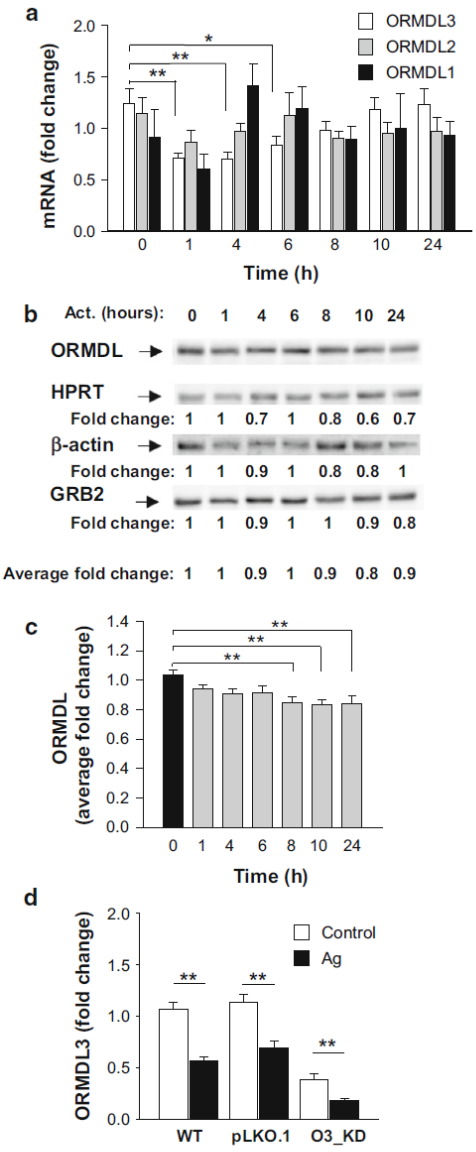

Fig. 2 Changes in ORMDL3 expression in Ag-activated BMMCs. ► **a** BMMCs were sensitized for 16 h with IgE and then activated with Ag (100 ng/ml) or not (0 h) for the indicated time intervals. ORMDL3, ORMDL2, and ORMDL1 mRNAs were quantified by RT-qPCR and normalized as described in "Materials and methods". The means and SEMs were calculated from three independent experiments performed in duplicate. **b** Immunoblot quantification of ORMDL proteins at various time intervals after activation of IgE-sensitized BMMCs with Ag (100 ng/ml). *Numbers* under the immunoblots indicate the relative amounts of ORMDL3 normalized to its amount in nonactivated cells and the amounts of HPRT, β-actin, and GRB2 were used as loading controls (Average fold change). A representative immunoblot from seven independent experiments with similar results is shown. **c** Statistical evaluation of ORMDL proteins expression is shown. ORMDL3 was normalized to its amount in nonactivated cells and the amount of the average fold change of three loading controls mentioned above. **d** RT-qPCR quantification of ORMDL3 in nonactivated (control) or Ag-activated (100 ng/ml; 1 h) BMMCs with the empty vector (pLKO.1) or O3_KD. Data are normalized as in **a**. The means and SEMs were calculated from six independent experiments performed in duplicate

ORMDL3 led us to examine the capability of IgE-sensitized cells to migrate toward Ag and to adhere and spread on fibronectin-coated substrates. BMMCs with O3_KD exhibited a significantly stronger chemotactic response to all tested concentrations of Ag when compared with control cells transfected with empty pLKO.1 vector (Fig. 5a). In contrast, BMMCs with O3_OE showed a less efficient chemotactic response than the corresponding control cells (Fig. 5b). We also compared cells transduced with pLKO.1 and WT cells to show that mast cell migration is not changed by lentivirus transduction (Fig. S3d). When adhesion to fibronectin was measured, cells with O3_KD (Fig. S5a) or O3_OE (Fig. S5b) exhibited adhesion similar to the corresponding control cells. In contrast, spreading on fibronectin-coated surfaces after exposure to Ag was reduced in cells with O3_KD (Fig. 5c, d). When compared to control cells, cells with O3_OE exhibited no significant difference in Ag-induced spreading (Fig. 5e, f). We also compared cells transduced with pLKO.1 and WT cells and showed that Ag-induced mast cells adhesion to and spreading on fibronectin was not changed by lentivirus transduction (Fig. S3e, f). Finally, we examined the depolymerization of F-actin in Ag-activated cells with O3_KD (Fig. S5c) or O3_OE (Fig. S5d) and corresponding controls and found that F-actin content was independent of ORMDL3 expression levels.

Upregulation of NF-κB signaling axis in mast cells with O3_KD

Previous studies with eosinophils showed that increased expression of ORMDL3 enhanced translocation of NF-κB into the nucleus and its activation [20]. Based on our findings that reduced expression of ORMDL3 upregulated the expression of cytokine and chemokine genes (Fig. 4a–d) and that these mediators were directed by transcription factor NF-κB [44–48], we decided to analyze the NF-κB signaling axis in BMMCs with enhanced or decreased ORMDL3 protein levels. First, we examined the phosphorylation of IκBα, a negative regulator of NF-κB signaling. We found that 5 min after Ag activation, BMMCs with O3_KD exhibited higher phosphorylation of IκBα than control pLKO.1 cells. Interestingly, we found that IκBα in activated BMMCs with O3_KD is more degraded than in control cells (Fig. 6a). This is in accord with the previously described observation that phosphorylation of IκBα triggers its degradation [49]. Densitometry evaluation of the data and normalization of pIκBα to LYN

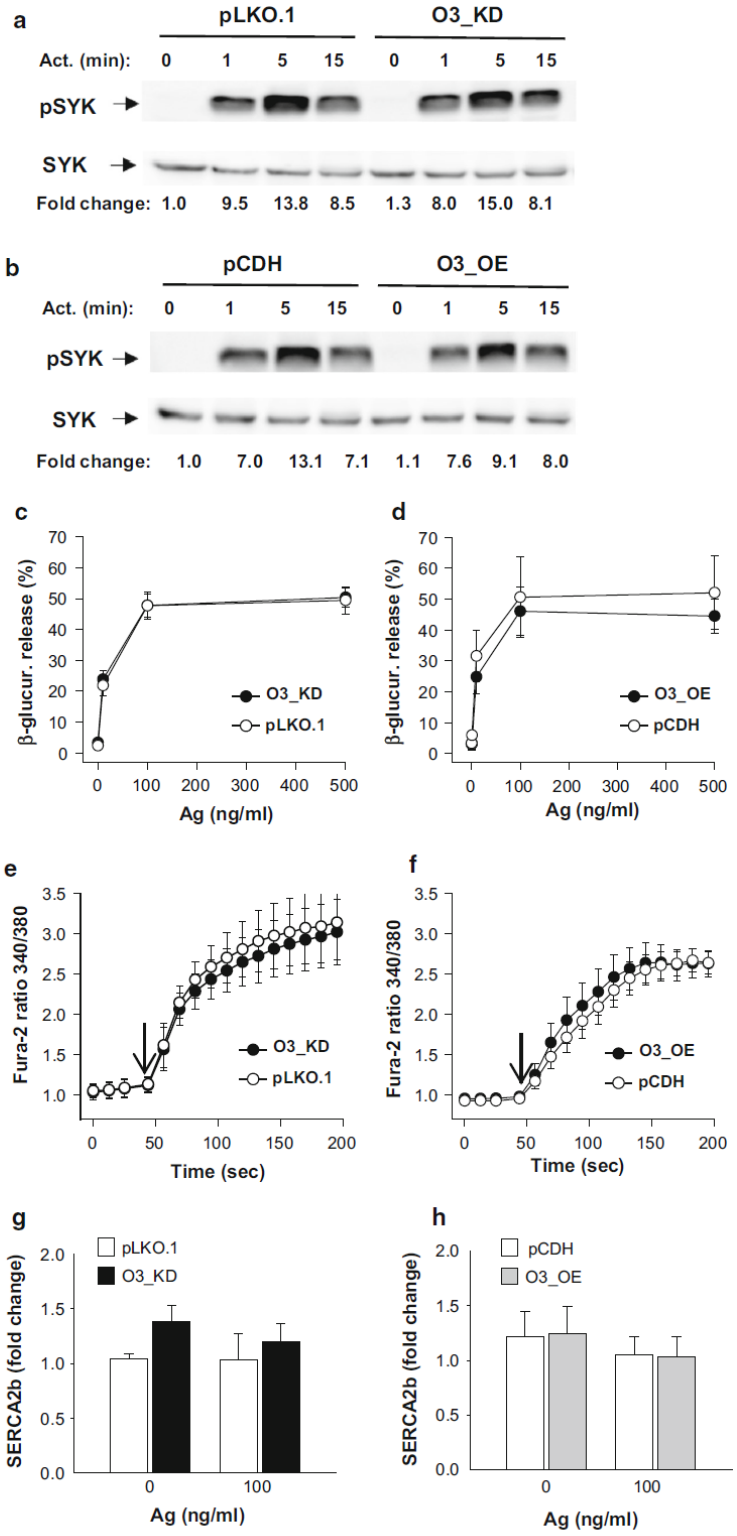

Fig. 3 Early activation events in BMMCs with enhanced or reduced ORMDL3 expression. **a** Ag-induced tyrosine phosphorylation of SYK as determined by immunoblotting of whole-cell lysates from BMMCs with O3_KD or control cells transfected with empty pLKO.1. IgE-sensitized cells were activated for various time intervals with Ag (100 ng/ml). The positions of pSYK and SYK, used as loading controls, are indicated by *arrows*. **b** Phosphorylation of SYK was examined as in **a**, except that the lysates were from cells with O3_OE or control cells transfected with empty pCDH. Representative immunoblots from at least three performed in each group are shown in **a** and **b**. Numbers under the immunoblots indicate the relative amounts of pSYK normalized to its amounts in nonactivated cells transduced with empty vectors and total amounts of SYK in individual samples (fold change). **c**, **d** β-Glucuronidase release in IgE-sensitized BMMCs. The cells were activated with various concentrations of Ag and after 30 min β-glucuronidase released into the supernatant was determined. Data presented are means and SEMs for cells with O3_KD (**c**, $n = 19$), pLKO.1 controls (**c**, $n = 19$), O3_OE (**d**, $n = 8$), and pCDH control cells (**d**, $n = 5$). **e**, **f** Calcium response in IgE-sensitized BMMCs activated with Ag (100 ng/ml) for various time intervals. *Arrows* show the time points when Ag was added. Means and SEMs were calculated for cells with O3_KD (**e**, $n = 16$), pLKO.1 controls (**e**, $n = 8$), O3_OE (**f**, $n = 3$), and pCDH controls (**f**, $n = 5$). **g**, **h** RT-qPCR quantification of SERCA2b mRNA in resting and activated BMMCs with O3_KD (**g**, $n = 4$) pLKO.1 controls (**g**, $n = 4$), O3_OE (**h**, $n = 4$) and pCDH controls (**h**, $n = 4$). Data for SERCA2b mRNA were normalized as described in "Materials and methods"

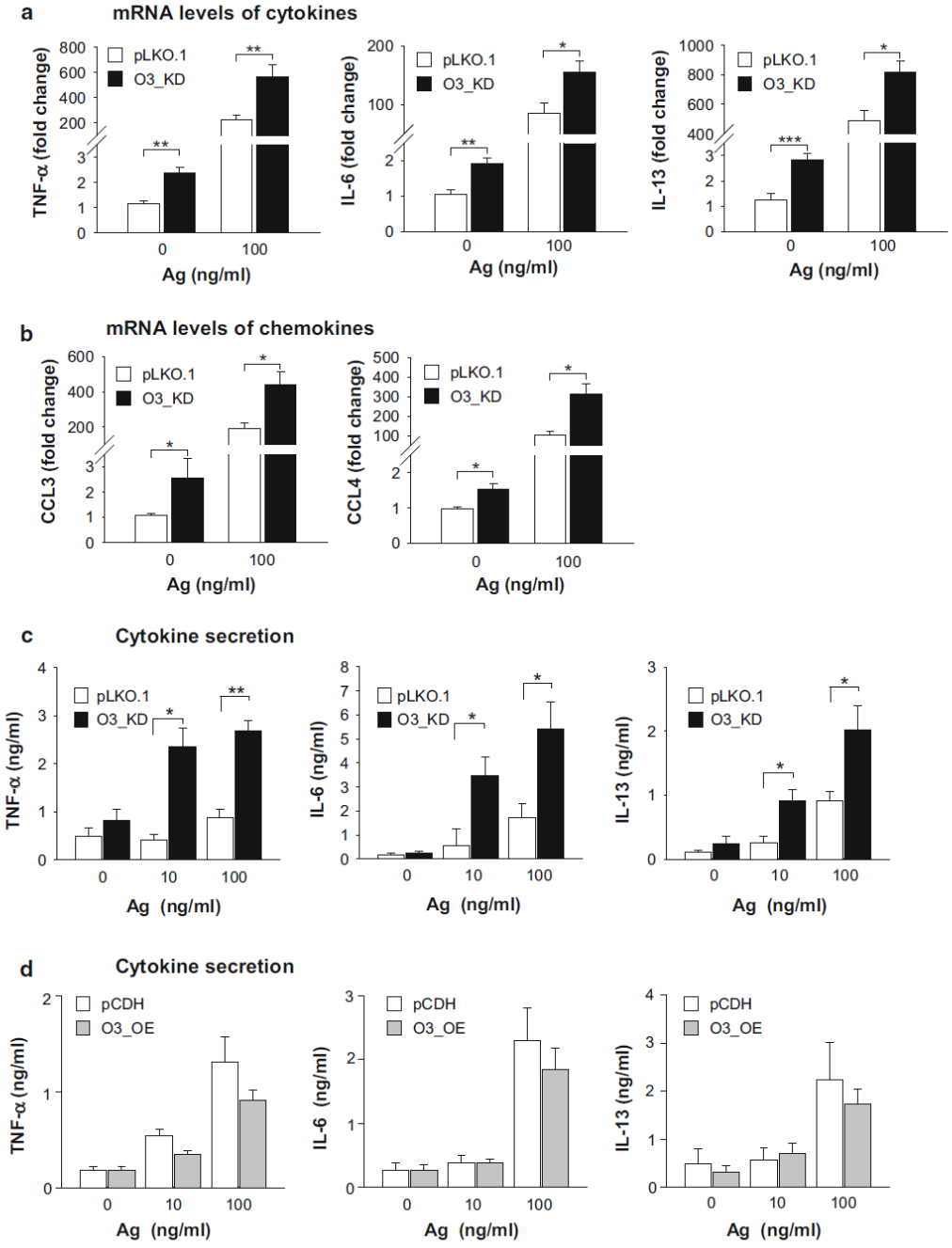

Fig. 4 Expression of cytokine and chemokine genes and production of cytokines in BMMCs with O3_KD and O3_OE. **a** RT-qPCR quantification of mRNAs encoding TNF-α, IL-6, and IL-13 in nonactivated or Ag-activated (100 ng/ml; 1 h) BMMCs with O3_KD and the corresponding control cells, pLKO.1. Means and SEMs were calculated from 13 to 16 independent experiments. **b** RT-qPCR quantification of mRNA for CCL3 and CCL4 chemokines from cells as in **a**. The means and SEMs were calculated from six to eight experiments. Data in **a** and **b** were normalized as described in "Materials and methods". **c**, **d** Quantification of cytokines TNF-α, IL-6, and IL-13 secreted into the supernatants of nonactivated or Ag-activated (100 ng/ml; 6 h) BMMCs with O3_KD or pLKO.1 control (**c**) and O3_OE or pCDH control (**d**) as determined by nano-iPCR. The means and SEMs were calculated from four to five independent experiments

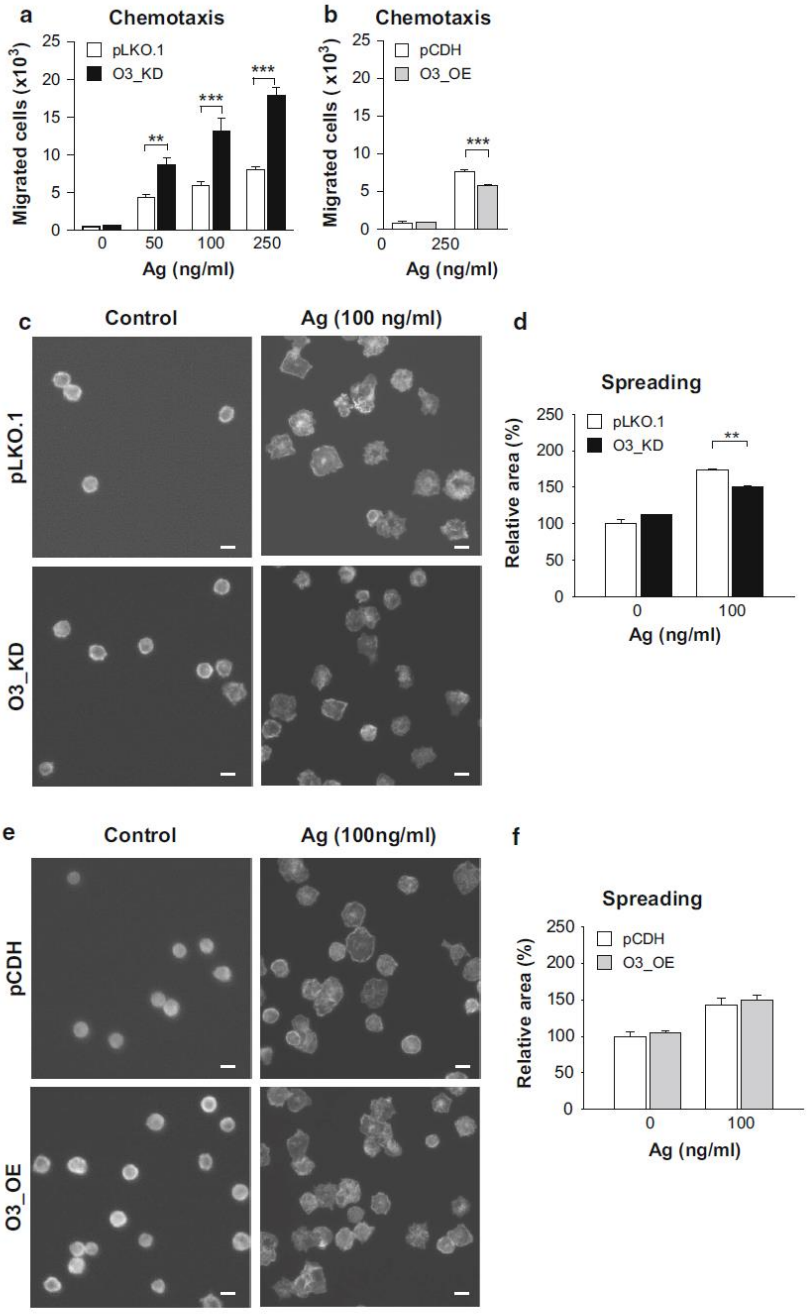

Fig. 5 Negative regulatory role of ORMDL3 in Ag-mediated chemotaxis, but not cell spreading on fibronectin. **a**, **b** Migration of BMMCs toward various concentrations of Ag was determined in IgE-sensitized BMMCs with O3_KD (**a**) or O3_OE (**b**) and the corresponding controls. The means and SEMs were calculated from four to eight independent experiments performed in duplicate. **c**–**f** Spreading of BMMCs with O3_KD (**c**, **d**), O3_OE (**e**, **f**), and the corresponding controls. The cells were attached to fibronectin-coated slides and activated with Ag (100 ng/ml) for 30 min. Representative fluorescent images are shown in **c** and **e**; *bars* 10 μm. Quantification and statistical evaluation of data obtained as in **c** and **e** are shown in **d** and **f**, respectively. The means and SEMs were calculated from five independent experiments

kinase, used as a loading control, showed significantly higher IκBα phosphorylation in O3_KD cells than control pLKO.1 cells (Fig. 6b). BMMCs with O3_OE showed a small, but nonsignificant decrease of IκBα phosphorylation (not shown). Based on these data, we next examined the consequences of reduced ORMDL3 levels on translocation of the NF-κB p65 subunit into the nucleus in BMMCs. We found that Ag-induced translocation of the p65 subunit into the nucleus was higher in BMMCs with O3_KD than in control cells (Fig. 6c). The difference was statistically significant (Fig. 6d). Interestingly, resting BMMCs with O3_KD also exhibited increased p65 nuclear localization

when compared with resting control pLKO.1 cells. These data are consistent with the findings that basal levels of mRNAs for cytokines (Fig. 4a) and chemokines (Fig. 4b) were higher in cells with O3_KD than in control cells. We also compared cells transduced with pLKO.1 and WT cells and found that p65 nuclear localization after activation was not changed by lentivirus transduction (Fig. S3g).

To determine which signaling pathways are involved in enhanced IκBα phosphorylation we examined phosphorylation of ERK kinase, which is involved in IκBα phosphorylation [50]. We found that mast cells with decreased expression of ORMDL3 exhibited similar ERK phosphorylation as pLKO.1 control cells (Fig. 6e, f). Next, we therefore tested phosphorylation of AKT kinase, which is a positive regulator of NF-κB signaling [51]. Interestingly, BMMCs with O3_KD exhibited significantly enhanced phosphorylation of AKT at Ser 473 at all examined time points, but phosphorylation of AKT at Thr 308 was not significantly affected (Fig. 6g–i). To exclude the possibility that the observed immunological responses are not specifically activated by siRNA [52], we compared the phosphorylation of IκBα and AKT (at Ser 473) in WT cells, BMMCs transduced with empty pLKO.1, or cells transduced with NT shRNA (Fig. S6a). We found that cells with O3_KD showed enhanced responses when compared with all controls. We also used the same controls in experiments with cytokines to demonstrate that lentiviral transduction had no impact on cytokine production and that cytokines were specifically increased by O3_KD (Fig. S6b–d). Collectively, these data demonstrate that decreased expression of ORMDL3 is accompanied in Ag-activated cells by enhanced phosphorylation of AKT, increased translocation of the p65 subunit into the nucleus, and enhanced production of cytokines.

ORMDL3 is a negative regulator of COX-2 expression and PGD2 synthesis

We also examined the expression of an inducible enzyme, COX-2, which is regulated by NF-κB [53, 54]. COX-2 converts arachidonic acid to PGH2, a precursor of PGD2 and PGE2 [28]. When compared with control cells (pLKO.1), BMMCs with O3_KD exhibited significantly higher levels of COX-2 mRNA than both resting and Ag-activated control cells (Fig. 7a), while cells with O3_OE showed decreased COX-2 mRNA expression when compared with the control cells (pCDH); however, the difference was not significant (Fig. 7b). These data were corroborated by studies of the COX-2 protein in Ag-activated BMMCs. After 5 h stimulation with Ag, we observed a higher increase of COX-2 levels in cells with O3_KD than in control cells (Fig. 7c); this difference was significant ($P < 0.05$; $n = 3$). On the other hand, Ag-activated cells with O3_OE showed lower COX-2 levels than the corresponding control cells (Fig. 7d); however, this difference was not significant ($P > 0.05$; $n = 3$). The stronger band of exogenous ORMDL3-myc after 5 h of activation in Fig. 7d was reproducibly observed. Ag-induced activation apparently induces enhanced transcription from the CMV promoter. We found that this enhancement was not ORMDL3 specific, rather it depended on the CMV promoter, as several other ORMDL family nonrelated proteins cloned into the same pCDH vector exhibited a similar increase (data not shown).

Supernatants collected from the experiments as depicted in Fig. 7 c, d were assessed for PGD2 levels. We found that Ag-activated mast cells with O3_KD released significantly higher amounts of PGD2 than appropriate controls (Fig. 7e). Furthermore, PGD2 expression was not significantly changed in mast cells with O3_OE (Fig. 7f). To show that COX-2 expression is independent of immunological responses toward dsRNAs, we compared COX-2 production in cells with O3_KD and controls (NT and WT). We found that in O3_KD cells activated with Ag, the levels of COX2 were more elevated than in control cells (Fig. S6e). These data support the negative regulatory role of ORMDL3 in the activation of the NF-κB signaling axis.

Fig. 6 Negative regulatory role of ORMDL3 in AKT and NF-κB signaling axis in Ag-activated BMMCs. **a** Phosphorylation of IκBα and its amount was determined by immunoblotting of whole-cell lysates from BMMCs with O3_KD and control cells (pLKO.1) with the corresponding antibodies. Representative immunoblots from four independent experiments areshown. Numbers under the immunoblots indicate the relative amounts of pIκBα and IκBα normalized to their amounts in nonactivated pLKO.1 control cells and the amount of Lyn used as a loading control (Fold change). **b** Quantification and statistical evaluation of pIκBα in pLKO.1 control cells and O3_KD cells activated with Ag for 5 min as in **a**. Means and SEMs were calculated from four independent experiments. **c** Representative confocal microscopy pictures of NF-κB p65 subunit (p65) localization in the nuclei (stained with Hoechst 33258) and cytoplasm in nonactivated or Ag-activated (100 ng/ml; 30 min) BMMCs with O3_KD or pLKO.1 control; *bars* 10 μm. **d** Quantification of NF-κB p65 subunit localization in the nucleus of nonactivated or Ag-activated (100 ng/ml, 30 min) O3_KD and pLKO.1 control cells. *Values* from two independent experiments as in **c** (50–100 cells per experiment) were plotted; each *symbol* represents one cell, *red horizontal lines* indicate means. **e–i** Phosphorylation of ERK at Tyr 204 (**e**, **f**), AKT at Ser 473 (**g**, **h**), and AKT at Thr 308 (**g**, **i**) was assessed by immunoblotting with the corresponding antibodies of the whole-cell lysates from BMMCs with O3_KD or pLKO.1 controls. Representative immunoblots from at least three in each group are shown in **e** and **g**. Numbers under the immunoblots indicate the relative amounts of pERK (**e**) or pAKT (**g**) normalized to their amounts in nonactivated pLKO.1 control cells and the amount of ERK or AKT used as loading controls (fold changes). Quantification and statistical analyses of differences in fold changes between cells with O3_KD and pLKO.1 controls in $pERK^{Y204}$ (**f**), $pAKT^{S473}$ (**h**), and $pAKT^{T308}$ (**i**) are also shown. Means and SEMs were calculated from three experiments in each group

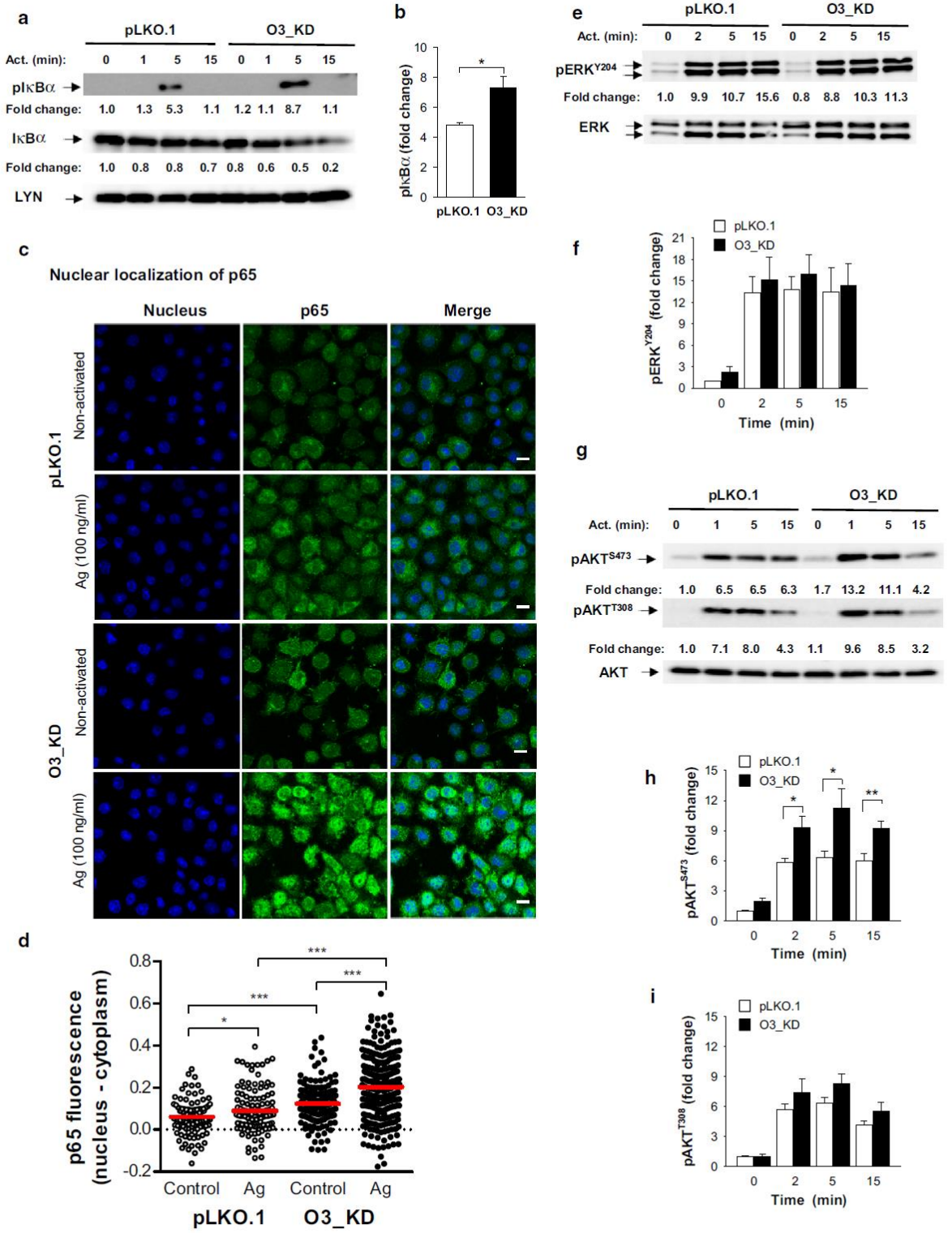
a
pLKO.1
O3_KD
Act. (min): 0 1 5 15 0 1 5 15
pIκBα
Fold change: 1.0 1.3 5.3 1.1 1.2 1.1 8.7 1.1
IκBα
Fold change: 1.0 0.8 0.8 0.7 0.8 0.6 0.5 0.2
LYN
b
pIκBα (fold change)
pLKO.1 O3_KD
c
Nuclear localization of p65
Nucleus
p65
Merge
pLKO.1
Non-activated
Ag (100 ng/ml)
O3_KD
Non-activated
Ag (100 ng/ml)
d
p65 fluorescence (nucleus - cytoplasm)
Control Ag Control Ag
pLKO.1 O3_KD
e
pLKO.1
O3_KD
Act. (min): 0 2 5 15 0 2 5 15
pERK^Y204
Fold change: 1.0 9.9 10.7 15.6 0.8 8.8 10.3 11.3
ERK
f
pLKO.1
O3_KD
pERK^Y204 (fold change)
Time (min)
g
pLKO.1
O3_KD
Act. (min): 0 1 5 15 0 1 5 15
pAKT^S473
Fold change: 1.0 6.5 6.5 6.3 1.7 13.2 11.1 4.2
pAKT^T308
Fold change: 1.0 7.1 8.0 4.3 1.1 9.6 8.5 3.2
AKT
h
pLKO.1
O3_KD
pAKT^S473 (fold change)
Time (min)
i
pLKO.1
O3_KD
pAKT^T308 (fold change)
Time (min)

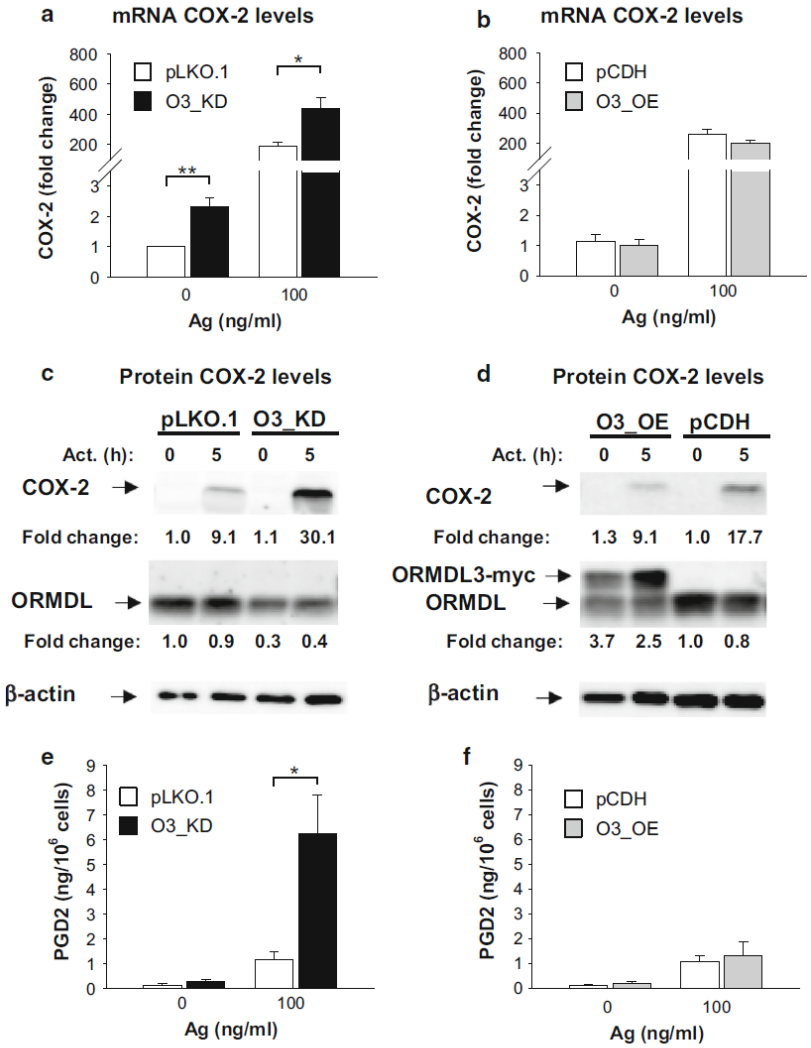

Fig. 7 Increased COX-2 expression and PGD2 synthesis in nonactivated or Ag-activated BMMCs with O3_KD. **a, b** RT-qPCR quantification of COX-2 mRNAs in nonactivated or Ag-activated (100 ng/ml; 1 h) BMMCs with O3_KD (**a**), O3_OE (**b**), and the corresponding controls, pLKO.1 (**a**) and pCDH (**b**). The means and SEMs were calculated from five independent experiments. **c, d** Amount of COX-2 protein in nonactivated or Ag-activated (100 ng/ml; 5 h) BMMCs with O3_KD (**c**), O3_OE (**d**), and the corresponding controls, pLKO.1 (**c**) and pCDH (**d**). Numbers under the COX-2 immunoblots indicate the relative amount of COX-2 normalized to its levels in nonactivated control cells and to the amount of β-actin, used as a loading control, in individual samples (fold change). Levels of ORMDL3 normalized as above are also shown. Representative immunoblots from three independent experiments are shown. **e, f** Levels of PGD2 released into supernatants of nonactivated or Ag-activated (100 ng/ml; 5 h) BMMCs with O3_KD (**e**), O3_OE (**f**), and the corresponding controls, pLKO.1 (**e**) and pCDH (**f**). The means and SEMs were calculated from three independent experiments

Silencing of ORMDL3 enhances mast cell-dependent PCA

To evaluate whether ORMDL3 has a function in mast cells in vivo, we silenced ORMDL3 locally by intradermal injection of the ORMDL3 siRNA pool. First, we examined the efficiency of ORMDL3 siRNA in vitro. When compared with BMMCs exposed to nontargeting control siRNA pool, the ORMDL3 siRNA pool reduced ORMDL expression by approximately 60 % as determined by immunoblotting (Fig. 8a, b; serum specific for all members of murine ORMDL family). For FcεRI-mediated PCA reactions, mice were intradermally injected with ORMDL3 siRNAs together with TNP-specific IgE into the right ears and control siRNAs together with TNP-specific IgE into the left ears. After 48 h, mice were challenged intravenously with Ag (TNP–BSA) and Evans blue dye and 2 h later Evans blue in both ears was quantified. Data presented in Fig. 8c show that ears injected with ORMDL3 siRNA displayed significantly higher amounts of Evans blue than ears injected with control siRNA. These data corroborate previous results obtained with BMMCs in vitro. Based on these results, we conclude that silencing of ORMDL3 in vivo leads to enhanced local inflammation triggered by mast cells.

Discussion

In this study, we examined the role of ORMDL3 protein in Ag-mediated mast cell signaling. Although enhanced or reduced expression of ORMDL3 had no effect on Ag-

induced degranulation and calcium responses, several lines of evidence presented in this study indicate that ORMDL3 is a negative regulator of proinflammatory activities of mast cells (Table 1). Increased expression of cytokines, chemokines, and COX-2 in O3_KD cells could be explained by our observation that BMMCs with O3_KD exhibited enhanced phosphorylation of IκBα, which is a regulator of transcription factor NF-κB [24]. Indeed, localization of the NF-κB p65 subunit was increased in the nuclei of Ag-activated ORMDL3-deficient mast cells. It is known that enhanced nuclear localization of the NF-κB p65 subunit leads to increased transcription of NF-κB-regulated genes encoding various cytokines, including TNF-α, IL-6 and IL-13, chemokines, CCL3 and CCL4, and COX-2 enzyme [44–48, 53–55]. Moreover, improperly regulated NF-κB causes a broad variety of inflammatory diseases [25–27]. Our findings regarding the regulatory roles of ORMDL3 are different from those obtained with other cell types, demonstrating a positive regulatory role of ORMDL3 in cell signaling. For example, eosinophils overexpressing ORMDL3 exhibited enhanced localization of the phosphorylated NF-κB p65 subunit in the nucleus [20]. Furthermore, transfection of ORMDL3 into lung epithelial cell line A549 increased the expression of several genes, including those for metalloproteases, ADAM-8 and MMP-9, chemokines CXCL-10, CXCL-11, IL-8, CCL-20, and oligoadenylate synthetases [18]. It has also been shown that the expression of several genes, including TGF-β1, ADAM8, MMP9, and CXCL-10, is enhanced in the bronchial epithelium of transgenic mice overexpressing ORMDL3 [19]. Recent studies showed that in eosinophils with O3_OE, ERK kinase played a role in regulating NF-κB signaling [20]. However, mast cells with O3_KD or O3_OE (not shown) exhibited similar ERK^{Y204} phosphorylation when compared with control cells. Although we did not exclude the possibility that phosphorylation of other targets in ERK could be affected by changing ORMDL3 levels, we focused on another potent activator of the NF-κB pathway, AKT kinase. We found that AKT kinase is more phosphorylated at the Ser 473 (but not at the Thr 308) in BMMCs with O3_KD than control cells. These data suggested a regulatory role of AKT in NF-κB signaling in mast cells with O3_KD. However, the exact molecular mechanism by which ORMDL3 activates AKT kinase remains unclear. To exclude the possibility that immunological responses toward dsRNAs could non-specifically activate IκBα/AKT phosphorylation, COX-2 expression, and cytokine production, we included cells transduced with pLKO.1 containing NT shRNA as a control. It should be mentioned that BMMCs poorly expressed toll-like receptors recognizing dsRNA, and their activation by specific ligands had little impact on TNF-α, IL-6, and IL-13 expression [56].

It has been shown that silencing of all three members of the ORMDL family potentiates de novo synthesis of sphingolipids [11]. In our study, we used shRNA to decrease the expression of ORMDL3 and found that expression of the other two members, ORMDL1 and ORMDL2, remained unchanged. Thus, we propose that in mast cells, a decrease in ORMDL3 expression alone is capable of promoting inflammation without the coordinate silencing of the ORMDL family genes. It should be noted that the NF-κB transcription factor is activated by multiple stimuli and that the multiprotein NF-kB signaling complex is subjected to extensive regulation [24]. TNF-α is known to be involved in the phosphorylation of IκBα [57, 58], and autocrine activation of NF-κB by TNF-α was observed in human mast cells [59]. Collectively, our data suggest a unique role of ORMDL3 in mast cells in the negative regulation of proinflammatory mediator synthesis. Interestingly, mast cells with O3_OE exhibited no significant inhibition of IκBα/AKT signaling and no suppression of proinflammatory mediator production. This could be explained at least in part by a recently published study, which showed that the expression levels of ORMDL3 were crucial for regulation of cell signaling in lipopolysaccharide-mediated activation of RAW264.7 macrophage cell line and A549 lung epithelial cells [60]. Thus, the relatively low overexpression of ORMDL3 in BMMCs could be under the threshold to regulate signaling pathways leading to the changes in cytokine expression. Our attempt to increase the exogenous expression of ORMDL3 in BMMCs failed because of enhanced mortality of BMMCs.

As already mentioned, no significant changes in calcium mobilization were found in Ag-activated BMMCs with O3_KD or O3_OE. These findings are different from those obtained with ORMDL3-deficient BM-derived eosinophils which, when compared with wild-type cells, showed reduced Ca^{2+} response after activation with eotaxin-1 [20]. On the other hand, Jurkat T cells with an siRNA-mediated O3_KD exhibited elevated mobilization of Ca^{2+} when activated via CD3, while a decreased Ca^{2+} response was observed in Jurkat cells with O3_OE [17]. Recent data showed that transgenic mice with elevated expression of ORMDL3 exhibited enhanced lung expression of SERCA2b, a known regulator of cytosolic calcium concentrations [19]. In contrast, our data with BMMCs showed that the expression of SERCA2b was not affected by changes in the ORMDL3 levels. These data are in line with our finding that BMMCs with decreased or enhanced expression of ORMDL3 exhibited similar levels of basal $[Ca^{2+}]_i$, and Ag-induced calcium mobilization when compared with corresponding control cells.

ORMDL3 has been described as an inducible gene upon *Alternaria* allergen challenge of mouse lung epithelial cells,

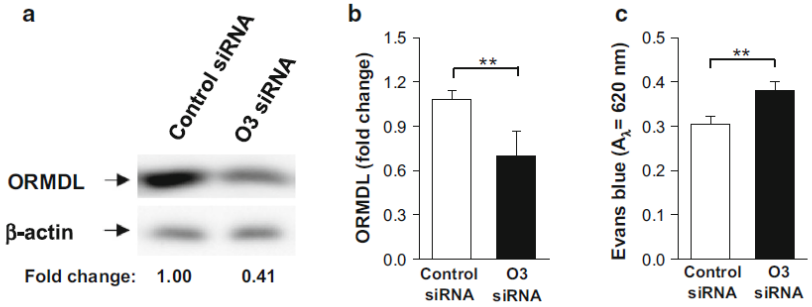

Fig. 8 Enhanced PCA in mice pretreated with ORMDL3 siRNA (O3 siRNA). **a** Specificity of the O3 siRNA. BMMCs were exposed to O3 siRNA pool or non-targeting control siRNA. 48 h later, the cells were lysed and analyzed for ORMDL3 and β-actin by immunoblotting. The position of ORMDL3 and β-actin, used as a loading control, is indicated by an *arrow*. Numbers under immunoblots indicate the relative amount of ORMDL3 normalized to its level in cells nucleofected with control siRNA and the amount of β-actin. **b** Quantification of ORMDL3 from data as in **a**. Means ± SEMs are shown ($n = 5$). **c** Role of ORMDL3 in PCA. TNP-specific IgE and O3 siRNA were injected intradermally into the right ears and TNP-specific IgE and control siRNA into the left ears. After 48 h, TNP–BSA was administered intravenously together with Evans blue dye and mice were killed 2 h later. Extravasation of Evans blue in both ears was determined. Means ± SEMs are shown ($n = 7$)

Table 1 Summary of Ag-induced responses of BMMCs with O3_KD or O3_OE when compared with control cells

Parameter	BMMCs with	
	O3_KD	O3_OE
Degranulation	–	–
Ca^{2+} response	–	–
SERCA2b (mRNA)	–	–
Chemotaxis toward Ag	↑	↓
Adhesion to fibronectin	–	–
Spreading on fibronectin	↓	–
F-actin content	–	–
Phosphorylation of IκBα (Ser 32/36)	↑	–
Phosphorylation of AKT (Ser 473)	↑	–
Phosphorylation of AKT (Thr 308)	–	–
Phosphorylation of ERK (Tyr 204)	–	–
Nuclear p65 subunit of NF-κB	↑	–
Production of cytokines (mRNA and protein)		
TNF-α	↑	–
IL-6	↑	–
IL-13	↑	–
Production of chemokines (mRNA)		
CCL3	↑	–
CCL4	↑	–
Expression of COX-2 (mRNA and protein)	↑	–
PGD2 synthesis	↑	–

BMMCs with O3_KD or O3_OE exhibited unchanged (–), decreased (↓) or increased (↑) responses when compared to control cells transduced with the corresponding empty vectors (pLKO.1 or pCDH)

lung eosinophils, and lung macrophages, but not lung neutrophils [18]. Moreover, IL-4 and IL-13 were capable of inducing ORMDL3 expression in lung epithelial cells [18]. These data were extended to mouse BM-derived eosinophils, which exhibited IL-3- and eotaxin-1-dependent induction of ORMDL3 expression [20]. In contrast to these data, our studies with mouse mast cells showed that expression of the *ORMDL3* gene was downregulated after FcεRI triggering. Interestingly, a similar decrease was observed in our previous study in which gene expression was analyzed in nonactivated and Ag-activated BMMCs (Gene Expression Omnibus repository dataset GSE40731 [61]). The data show that 2 h after FcεRI triggering, ORMDL3 was decreased to 0.6 in WT and to 0.43 in pLKO.1-transduced cells ($n = 3$ for each group, adj. P value <0.006). There were no significant changes between ORMDL1 and ORMDL2. The amounts of all ORMDL family members were not significantly changed between WT and pLKO.1 BMMCs. These data suggest a distinct regulation of *ORMDL3* gene expression in Ag-activated mast cells when compared with activated eosinophils, macrophages, and lung epithelial cells [18, 20]. Recently, it has been shown that lipopolysaccharide activation of macrophage cell line RAW267.4 induces coordinated transient suppression of expression of genes encoding the ORMDL family and in this way regulates sphingolipids homeostasis [14]. Chemotaxis is another example of distinct ORMDL3 regulatory roles in mast cells and eosinophils. ORMDL3-deficient eosinophils exhibited decreased chemotaxis toward eotaxin-1 [20], while we showed that BMMCs with O3_KD increasingly migrate toward Ag. Moreover, O3_KD exhibited decreased Ag-induced spreading on fibronectin. These data are consistent with previous observations of indirect relationship between mast cell migration and cell spreading [62]. The observed difference between mast cells and eosinophils could be caused by distinct chemoattractants and different methods

used and/or different involvement of ORMDL3 in chemotaxis of BMMCs and bone marrow-derived eosinophils.

Dysregulation of ORMDL3 expression is linked to various inflammatory diseases [1, 4–7]. It has been shown that upregulation of ORMDL3 stimulates the release of proinflammatory mediators [18, 20] and that ORMDL3 transgenic mice exhibit the proinflammatory phenotype [19]. On the other hand, decreased expression of all members of the ORMDL family led to activation of sphingolipid synthesis [11]. In this study, we showed for the first time that O3_KD alone is able to enhance the inflammatory response of mast cells. In BMMCs with O3_KD, we described a complex phenotype based on the enhanced AKT–NF-κB signaling axis, followed by increased secretion of TNF-α, IL-6, and IL-13 and enhanced expression of COX-2 associated with increased PGD2 synthesis. In addition, the chemotactic response of IgE-sensitized BMMCs to Ag was increased in cells with O3_KD and decreased in O3_OE. Moreover, we have found that ORMDL3 mRNA levels are decreased after challenge of IgE-sensitized BMMCs with Ag. These data were corroborated by an in vivo study, which showed that decreased ORMDL3 expression in mast cells was capable of inducing Ag-dependent inflammation. The opposite results obtained in mast cells versus other cell types described in the literature could be explained by formation of different functional complexes of ORMDL3 with other molecules in various cell types. Clarification of this issue and ORMDL3 properties in human mast cells requires further studies.

Collectively, our data show that ORMDL3 is predominantly a negative regulator of proinflammatory responses in Ag-activated murine mast cells, both in vitro and in vivo.

Acknowledgments This work was supported by projects P305-14-00703S, P302/12/G101, and P302-14-09807S from the Grant Agency of the Czech Republic and Institutional project RVO 68378050 from the Academy of Sciences of the Czech Republic. L.P., H.D., M.B., and T.P. were supported in part by the Faculty of Science, Charles University, Prague. We thank J. Eitler for preparation of ORMDL3-myc plasmid, H. Mrazova, and R. Budovicova for technical assistance, and Pavel Draber, Peter Draber, and S. Takacova for critical reading of the manuscript.

References

1. Moffatt MF, Kabesch M, Liang L, Dixon AL, Strachan D, Heath S, Depner M et al (2007) Genetic variants regulating ORMDL3 expression contribute to the risk of childhood asthma. Nature 448:470–473
2. Galanter J, Choudhry S, Eng C, Nazario S, Rodriguez-Santana JR, Casal J, Torres-Palacios A et al (2008) ORMDL3 gene is associated with asthma in three ethnically diverse populations. Am J Respir Crit Care Med 177:1194–1200
3. Hirota T, Harada M, Sakashita M, Doi S, Miyatake A, Fujita K, Enomoto T et al (2008) Genetic polymorphism regulating ORM1-like 3 (*Saccharomyces cerevisiae*) expression is associated with childhood atopic asthma in a Japanese population. J Allergy Clin Immunol 121:769–770
4. Balantic M, Rijavec M, Flezar M, Camlek T, Hudoklin I, Kosnik M, Korosec P, Suskovic S (2013) A polymorphism in ORMDL3 is associated not only with asthma without rhinitis but also with chronic obstructive pulmonary disease. J Investig Allergol Clin Immunol 23:256–261
5. McGovern DP, Gardet A, Torkvist L, Goyette P, Essers J, Taylor KD, Neale BM et al (2010) Genome-wide association identifies multiple ulcerative colitis susceptibility loci. Nat Genet 42:332–337
6. Verlaan DJ, Berlivet S, Hunninghake GM, Madore AM, Lariviere M, Moussette S, Grundberg E et al (2009) Allele-specific chromatin remodeling in the ZPBP2/GSDMB/ORMDL3 locus associated with the risk of asthma and autoimmune disease. Am J Hum Genet 85:377–393
7. Barrett JC, Hansoul S, Nicolae DL, Cho JH, Duerr RH, Rioux JD, Brant SR et al (2008) Genome-wide association defines more than 30 distinct susceptibility loci for Crohn's disease. Nat Genet 40:955–962
8. Kurreeman FA, Stahl EA, Okada Y, Liao K, Diogo D, Raychaudhuri S, Freudenberg J et al (2012) Use of a multiethnic approach to identify rheumatoid- arthritis-susceptibility loci, 1p36 and 17q12. Am J Hum Genet 90:524–532
9. Li X, Ampleford EJ, Howard TD, Moore WC, Torgerson DG, Li H, Busse WW et al (2012) Genome-wide association studies of asthma indicate opposite immunopathogenesis direction from autoimmune diseases. J Allergy Clin Immunol 130:861–868
10. Hjelmqvist L, Tuson M, Marfany G, Herrero E, Balcells S, Gonzalez-Duarte R (2002) ORMDL proteins are a conserved new family of endoplasmic reticulum membrane proteins. Genome Biol 3:RESEARCH0027-1-16
11. Breslow DK, Collins SR, Bodenmiller B, Aebersold R, Simons K, Shevchenko A, Ejsing CS, Weissman JS (2010) Orm family proteins mediate sphingolipid homeostasis. Nature 463:1048–1053
12. Roelants FM, Breslow DK, Muir A, Weissman JS, Thorner J (2011) Protein kinase Ypk1 phosphorylates regulatory proteins Orm1 and Orm2 to control sphingolipid homeostasis in Saccharomyces cerevisiae. Proc Natl Acad Sci USA 108:19222–19227
13. Siow DL, Wattenberg BW (2012) Mammalian ORMDL proteins mediate the feedback response in ceramide biosynthesis. J Biol Chem 287:40198–40204
14. Kiefer K, Carreras-Sureda A, Garcia-Lopez R, Rubio-Moscardo F, Casas J, Fabrias G, Vicente R (2015) Coordinated regulation of the orosomucoid-like gene family expression controls de novo ceramide synthesis in mammalian cells. J Biol Chem 290:2822–2830
15. Worgall TS, Veerappan A, Sung B, Kim BI, Weiner E, Bholah R, Silver RB, Jiang XC, Worgall S (2013) Impaired sphingolipid synthesis in the respiratory tract induces airway hyperreactivity. Sci Transl Med 5:186ra67
16. Cantero-Recasens G, Fandos C, Rubio-Moscardo F, Valverde MA, Vicente R (2010) The asthma-associated ORMDL3 gene product regulates endoplasmic reticulum-mediated calcium signaling and cellular stress. Hum Mol Genet 19:111–121
17. Carreras-Sureda A, Cantero-Recasens G, Rubio-Moscardo F, Kiefer K, Peinelt C, Niemeyer BA, Valverde MA, Vicente R (2013) ORMDL3 modulates store-operated calcium entry and lymphocyte activation. Hum Mol Genet 22:519–530
18. Miller M, Tam AB, Cho JY, Doherty TA, Pham A, Khorram N, Rosenthal P et al (2012) ORMDL3 is an inducible lung epithelial

gene regulating metalloproteases, chemokines, OAS, and ATF6. Proc Natl Acad Sci USA 109:16648–16653
19. Miller M, Rosenthal P, Beppu A, Mueller JL, Hoffman HM, Tam AB, Doherty TA et al (2014) ORMDL3 transgenic mice have increased airway remodeling and airway responsiveness characteristic of asthma. J Immunol 192:3475–3487
20. Ha SG, Ge XN, Bahaie NS, Kang BN, Rao A, Rao SP, Sriramarao P (2013) ORMDL3 promotes eosinophil trafficking and activation via regulation of integrins and CD48. Nat Commun 4:2479
21. Galli SJ (2000) Mast cells and basophils. Curr Opin Hematol 7:32–39
22. Galli SJ, Tsai M, Piliponsky AM (2008) The development of allergic inflammation. Nature 454:445–454
23. Schubert N, Dudeck J, Liu P, Karutz A, Speier S, Maurer M, Tuckermann J, Dudeck A (2015) Mast cell promotion of T cell-driven antigen-induced arthritis despite being dispensable for antibody-induced arthritis in which T cells are bypassed. Arthritis Rheumatol 67:903–913
24. Oeckinghaus A, Ghosh S (2009) The NF-κB family of transcription factors and its regulation. Cold Spring Harb Perspect Biol 1:a000034
25. Bollrath J, Greten FR (2009) IKK/NF-κB and STAT3 pathways: central signalling hubs in inflammation-mediated tumour promotion and metastasis. EMBO Rep 10:1314–1319
26. Sheller JR, Polosukhin VV, Mitchell D, Cheng DS, Peebles RS, Blackwell TS (2009) Nuclear factor κB induction in airway epithelium increases lung inflammation in allergen-challenged mice. Exp Lung Res 35:883–895
27. Wullaert A, Bonnet MC, Pasparakis M (2011) NF-κB in the regulation of epithelial homeostasis and inflammation. Cell Res 21:146–158
28. Ricciotti E, FitzGerald GA (2011) Prostaglandins and inflammation. Arterioscler Thromb Vasc Biol 31:986–1000
29. Hájková Z, Bugajev V, Dráberová E, Vinopal S, Dráberov L, Janáček J, Dráber P, Dráber P (2011) STIM1-directed reorganization of microtubules in activated mast cells. J Immunol 186:913–923
30. Rudolph AK, Burrows PD, Wabl MR (1981) Thirteen hybridomas secreting hapten-specific immunoglobulin E from mice with Ig^a or Ig^b heavy chain haplotype. Eur J Immunol 11:527–529
31. Tolar P, Dráberová L, Dráber P (1997) Protein tyrosine kinase Syk is involved in Thy-1 signaling in rat basophilic leukemia cells. Eur J Immunol 27:3389–3397
32. Dráberová L, Amoui M, Dráber P (1996) Thy-1-mediated activation of rat mast cells: the role of Thy-1 membrane microdomains. Immunology 87:141–148
33. Draberova L, Bugajev V, Potuckova L, Halova I, Bambouskova M, Polakovicova I, Xavier RJ, Seed B, Draber P (2014) Transmembrane adaptor protein PAG/CBP is involved in both positive and negative regulation of mast cell signaling. Mol Cell Biol 34:4285–4300
34. Horáková H, Polakovičová I, Shaik GM, Eitler J, Bugajev V, Dráberová L, Dráber P (2011) 1,2-propanediol-trehalose mixture as a potent quantitative real-time PCR enhancer. BMC Biotechnol 11:41
35. Potůčková L, Franko F, Bambousková M, Dráber P (2011) Rapid and sensitive detection of cytokines using functionalized gold nanoparticle-based immuno-PCR, comparison with immuno-PCR and ELISA. J Immunol Methods 371:38–47
36. Laemmli UK (1970) Cleavage of structural proteins during the assembly of the head of bacteriophage T4. Nature 227:680–685
37. Haan C, Behrmann I (2007) A cost effective non-commercial ECL-solution for Western blot detections yielding strong signals and low background. J Immunol Methods 318:11–19
38. Hálová I, Dráberová L, Bambousková M, Machyna M, Stegurová L, Smrž D, Dráber P (2013) Crosstalk between tetraspanin CD9 and transmembrane adaptor protein non-T cell activation linker (NTAL) in mast cell activation and chemotaxis. J Biol Chem 288:9801–9814
39. Carpenter AE, Jones TR, Lamprecht MR, Clarke C, Kang IH, Friman O, Guertin DA et al (2006) Cell Profiler: image analysis software for identifying and quantifying cell phenotypes. Genome Biol 7:R100
40. Ding GJ, Fischer PA, Boltz RC, Schmidt JA, Colaianne JJ, Gough A, Rubin RA, Miller DK (1998) Characterization and quantitation of NF-κB nuclear translocation induced by interleukin-1 and tumor necrosis factor-α. Development and use of a high capacity fluorescence cytometric system. J Biol Chem 273:28897–28905
41. Kanada S, Nishiyama C, Nakano N, Suzuki R, Maeda K, Hara M, Kitamura N, Ogawa H, Okumura K (2011) Critical role of transcription factor PU.1 in the expression of CD80 and CD86 on dendritic cells. Blood 117:2211–2222
42. Bradding P (2007) Mast cell regulation of airway smooth muscle function in asthma. Eur Respir J 29:827–830
43. Walker ME, Hatfield JK, Brown MA (2012) New insights into the role of mast cells in autoimmunity: evidence for a common mechanism of action? Biochim Biophys Acta 1822:57–65
44. Hinz M, Lemke P, Anagnostopoulos I, Hacker C, Krappmann D, Mathas S, Dorken B, Zenke M, Stein H, Scheidereit C (2002) Nuclear factor κB-dependent gene expression profiling of Hodgkin's disease tumor cells, pathogenetic significance, and link to constitutive signal transducer and activator of transcription 5a activity. J Exp Med 196:605–617
45. Klemm S, Gutermuth J, Hultner L, Sparwasser T, Behrendt H, Peschel C, Mak TW, Jakob T, Ruland J (2006) The Bcl10-Malt1 complex segregates FcεRI-mediated nuclear factor κB activation and cytokine production from mast cell degranulation. J Exp Med 203:337–347
46. Marquardt DL, Walker LL (2000) Dependence of mast cell IgE-mediated cytokine production on nuclear factor-κB activity. J Allergy Clin Immunol 105:500–505
47. Peng Y, Power MR, Li B, Lin TJ (2005) Inhibition of IKK down-regulates antigen + IgE-induced TNF production by mast cells: a role for the IKK-IκB-NF-κB pathway in IgE-dependent mast cell activation. J Leukoc Biol 77:975–983
48. Widmer U, Manogue KR, Cerami A, Sherry B (1993) Genomic cloning and promoter analysis of macrophage inflammatory protein (MIP)-2, MIP-1 α, and MIP-1 β, members of the chemokine superfamily of proinflammatory cytokines. J Immunol 150:4996–5012
49. Baba Y, Nishida K, Fujii Y, Hirano T, Hikida M, Kurosaki T (2008) Essential function for the calcium sensor STIM1 in mast cell activation and anaphylactic responses. Nat Immunol 9:81–88
50. Lee FS, Hagler J, Chen ZJ, Maniatis T (1997) Activation of the IκBα kinase complex by MEKK1, a kinase of the JNK pathway. Cell 88:213–222
51. Dan HC, Cooper MJ, Cogswell PC, Duncan JA, Ting JP, Baldwin AS (2008) Akt-dependent regulation of NF-κB is controlled by mTOR and Raptor in association with IKK. Genes Dev 22:1490–1500
52. Marques JT, Williams BR (2005) Activation of the mammalian immune system by siRNAs. Nat Biotechnol 23:1399–1405
53. Kaltschmidt B, Linker RA, Deng J, Kaltschmidt C (2002) Cyclooxygenase-2 is a neuronal target gene of NF-κB. BMC Mol Biol 3:16
54. Mortaz E, Redegeld FA, Nijkamp FP, Engels F (2005) Dual effects of acetylsalicylic acid on mast cell degranulation, expression of cyclooxygenase-2 and release of pro-inflammatory cytokines. Biochem Pharmacol 69:1049–1057

55. Kurumbail RG, Kiefer JR, Marnett LJ (2001) Cyclooxygenase enzymes: catalysis and inhibition. Curr Opin Struct Biol 11:752–760
56. Matsushima H, Yamada N, Matsue H, Shimada S (2004) TLR3-, TLR7-, and TLR9-mediated production of proinflammatory cytokines and chemokines from murine connective tissue type skin-derived mast cells but not from bone marrow-derived mast cells. J Immunol 173:531–541
57. Lin WJ, Yeh WC (2005) Implication of Toll-like receptor and tumor necrosis factor α signaling in septic shock. Shock 24:206–209
58. Aggarwal BB (2004) Nuclear factor-κB: the enemy within. Cancer Cell 6:203–208
59. Coward WR, Okayama Y, Sagara H, Wilson SJ, Holgate ST, Church MK (2002) NF-κB and TNF-α: a positive autocrine loop in human lung mast cells? J Immunol 169:5287–5293
60. Oyeniran C, Sturgill JL, Hait NC, Huang WC, Avni D, Maceyka M, Newton J et al (2015) Aberrant ORM (yeast)-like protein isoform 3 (ORMDL3) expression dysregulates ceramide homeostasis in cells and ceramide exacerbates allergic asthma in mice. J Allergy Clin Immunol. doi:10.1016/j.jaci.2015.02.031
61. Polakovicova I, Draberova L, Simicek M, Draber P (2014) Multiple Regulatory Roles of the Mouse Transmembrane Adaptor Protein NTAL in Gene Transcription and Mast Cell Physiology. PLoS ONE 9:e105539
62. Tůmová M, Koffer A, Šimíček M, Dráberová L, Dráber P (2010) The transmembrane adaptor protein NTAL signals to mast cell cytoskeleton via the small GTPase Rho. Eur J Immunol 40:3235–3245

1.7 ETHANOL INHIBITS HIGH-AFFINITY IMMUNOGLOBULIN E RECEPTOR (FcεRI) SIGNALING IN MAST CELLS BY SUPPRESSING THE FUNCTION OF FcεRI-CHOLESTEROL SIGNALOSOMES

PLoS One. 10(12):e0144596, 2015.

In this study we show that short-term exposure of BMMCs to nontoxic concentrations of ethanol inhibits FcεRI-mediated degranulation, calcium response, and production of several cytokines (TNF-α, IL-6, and IL-13) in a dose-dependent manner. We found that ethanol interferes with the function of FcεRI-cholesterol signalosomes and support the lipid-centric theory of ethanol action in this system at the early stages of cell activation.

PLOS | ONE

RESEARCH ARTICLE

Ethanol Inhibits High-Affinity Immunoglobulin E Receptor (FcεRI) Signaling in Mast Cells by Suppressing the Function of FcεRI-Cholesterol Signalosome

Lubica Draberova*, Tomas Paulenda, Ivana Halova, Lucie Potuckova, Viktor Bugajev, Monika Bambouskova, Magda Tumova, Petr Draber*

Laboratory of Signal Transduction, Institute of Molecular Genetics, Academy of Sciences of the Czech Republic, Prague, Czech Republic

* draberovalu@img.cas.cz (LD); draberpe@img.cas.cz (PD)

Citation: Draberova L, Paulenda T, Halova I, Potuckova L, Bugajev V, Bambouskova M, et al. (2015) Ethanol Inhibits High-Affinity Immunoglobulin E Receptor (FcεRI) Signaling in Mast Cells by Suppressing the Function of FcεRI-Cholesterol Signalosome. PLoS ONE 10(12): e0144596. doi:10.1371/journal.pone.0144596

Editor: David Holowka, Cornell University, UNITED STATES

Received: July 25, 2015

Accepted: November 21, 2015

Published: December 14, 2015

Data Availability Statement: All relevant data are within the manuscript.

Funding: This work was supported by Project P302/12/G101 from the Grant Agency of the Czech Republic and Project LD12073 COST-CZ-MAST from the Ministry of Education Youth and Sports of the Czech Republic. The funders had no role in study design, data collection and analysis, decision to publish, or preparation of the manuscript.

Abstract

Ethanol has multiple effects on biochemical events in a variety of cell types, including the high-affinity immunoglobulin E receptor (FcεRI) signaling in antigen-activated mast cells. However, the underlying molecular mechanism remains unknown. To get better understanding of the effect of ethanol on FcεRI-mediated signaling we examined the effect of short-term treatment with non-toxic concentrations of ethanol on FcεRI signaling events in mouse bone marrow-derived mast cells. We found that 15 min exposure to ethanol inhibited antigen-induced degranulation, calcium mobilization, expression of proinflammatory cytokine genes (tumor necrosis factor-α, interleukin-6, and interleukin-13), and formation of reactive oxygen species in a dose-dependent manner. Removal of cellular cholesterol with methyl-β-cyclodextrin had a similar effect and potentiated some of the inhibitory effects of ethanol. In contrast, exposure of the cells to cholesterol-saturated methyl-β-cyclodextrin abolished in part the inhibitory effect of ethanol on calcium response and production of reactive oxygen species, supporting lipid-centric theories of ethanol action on the earliest stages of mast cell signaling. Further studies showed that exposure to ethanol and/or removal of cholesterol inhibited early FcεRI activation events, including tyrosine phosphorylation of the FcεRI β and γ subunits, SYK kinases, LAT adaptor protein, phospholipase Cγ, STAT5, and AKT and internalization of aggregated FcεRI. Interestingly, ethanol alone, and particularly in combination with methyl-β-cyclodextrin, enhanced phosphorylation of negative regulatory tyrosine 507 of LYN kinase. Finally, we found that ethanol reduced passive cutaneous anaphylactic reaction in mice, suggesting that ethanol also inhibits FcεRI signaling under *in vivo* conditions. The combined data indicate that ethanol interferes with early antigen-induced signaling events in mast cells by suppressing the function of FcεRI-cholesterol signalosomes at the plasma membrane.

Competing Interests: The authors have declared that no competing interests exist.

Introduction

Although it is known that ethanol has multiple effects on a variety of cells types, the molecular mechanisms of its action are far from understood. There are two basic theories of ethanol action on the cells, lipid-centric and protein-centric [1]. The lipid theory of ethanol action postulates that ethanol, similarly to anesthetics [2,3], dissolves in cellular lipids and acts by non-specific mechanisms. This theory was supported by experiments showing that alcohols and anesthetics induce changes in properties of cellular membranes, including fluidity [4], lateral mobility of lipid molecules [5], phase transition temperature [6,7], and membrane permeability [8]. The protein theory of alcohol and anesthetics action proposes that the drugs interact specifically with certain proteins and in this way affect their properties [9]. This theory was mostly based on experiments suggesting that binding of alcohols and anesthetics induces conformational changes that diminish or abolish the function of some proteins, such as those forming neurotransmitter-gated ion channels [10–13]. However, concentrations of ethanol required to cause significant changes in the receptor functions were often greater than those attainable *in vivo*, and effects mediated by lower concentrations have not always been replicated [14].

Previous studies showed that alcohol modulates various components of the immune system [15–17]. Acute exposure to ethanol resulted in reduced monocyte/macrophage phagocytosis [18,19], T-cell receptor signaling [20], Toll-like receptor-mediated activation of macrophages [21,22], and reduced neutrophil migration [23]. It has also been reported that *in vitro* exposure of mast cells to ethanol for 1 hour or longer inhibited the high-affinity immunoglobulin E (IgE) receptor (FcεRI)-induced degranulation and production of tumor necrosis factor (TNF)-α and interleukin (IL)-8 [24,25]. Although these data suggested that ethanol inhibits signal transduction from the immunoreceptors, molecular mechanisms of the inhibitory action of ethanol on early steps of immunoreceptor signaling remained enigmatic.

In this study we used primary mouse bone marrow-derived mast cells (BMMCs) and examined sensitivity to ethanol of the earliest signaling events after FcεRI triggering. We also examined effect of ethanol on FcεRI activation in cells with reduced levels of cholesterol and on passive cutaneous anaphylaxis (PCA) in mice. Our data indicate that ethanol inhibits tyrosine phosphorylation of the FcεRI β and γ subunits, the first biochemically defined event after antigen-mediated aggregation of FcεRI, and support lipid-centric theory of ethanol action in mast cells.

Materials and Methods

Mice and cells

Mice were bred and maintained in specific pathogen free facility of the Institute of Molecular Genetics and used in compliance with the Institute guidelines. All protocols, including killing mice by decapitation, was approved by the Animal Care and Use Committee of the Institute of Molecular Genetics (Permit number 12135/2010-17210) and was in compliance with the EU Directive 2010/63/EU for animal experiments. All efforts were made to minimize suffering of the mice.

Bone marrow mast cells were isolated from femurs and tibias of C57BL/6 mice (females, 6–8 weeks old). The cells were cultured in RPMI-1640 medium supplemented with 100 U/ml penicillin, 100 μg/ml streptomycin, 71 μM 2-mercaptoethanol, minimum essential medium non-essential amino acids, 0.7 mM sodium pyruvate, 2.5 mM L-glutamine, 12 mM D-glucose, recombinant mouse stem cell factor (SCF; 20 ng/ml, ProSpec), mouse recombinant IL-3 (20 ng/ml, ProSpec) and 10% fetal calf serum (FCS). For PCA experiments, BALB/c male mice aged 8–12 weeks were used.

Antibodies and reagents

The following monoclonal antibodies (mAbs) were used: anti-FcεRI β chain [26], trinitrophenol (TNP)-specific IgE mAb (IGEL b4 1) [27], anti-LAT [28], anti-LYN [29], and anti-NTAL [30]. Polyclonal antibodies specific for LYN and LAT were prepared by immunization of rabbits with the corresponding recombinant proteins or their fragments [31]. Rabbit anti-IgE was prepared by immunization with whole IGEL b4.1. Polyclonal antibodies specific for phospholipase C (PLC)γ1, phospho(p)PLCγ1 (Tyr 783), STAT5, ERK, pERK (Tyr 783), AKT, pAKT (Ser 473) as well as horseradish peroxidase (HRP)-conjugated goat anti-mouse IgG, and goat anti-rabbit IgG, were obtained from Santa Cruz Biotechnology Inc. Antibodies specific for pSYK (Tyr 525/Tyr 526), pSTAT5 (Tyr 694), pLYN (Tyr 507), and pLYN (Tyr 416) were obtained from Cell Signaling. Antibody specific for pLAT (Tyr 191) cross-reacting with pNTAL was obtained from Merc-Millipore. PAG-specific rabbit polyclonal antibody was from Exbio. V450-conjugated rat anti-mouse CD107a (LAMP1) and HRP-conjugated anti- phosphotyrosine mAb (PY-20) were obtained from BD Biosciences. Anti-mouse FcεRI labeled with fluorescein isothiocyanate (FITC) and anti-mouse KIT-allophycocyanin conjugates were obtained from eBiosciences. Donkey anti-mouse Ig-Alexa Fluor 568 conjugate was obtained from Invitrogen. All other reagents were from Sigma-Aldrich.

Flow cytometry

For flow cytometry measurements, BMMCs (10^5/sample) were used. To analyze the surface levels of FcεRI and Kit receptor, the labeling proceeded as described previously [32]. For analysis of surface CD107a (LAMP1), BMMCs were activated with various concentrations of antigen for 10 min at 37°C. Activation was stopped by pelleting the cells at 4°C. Cells were then resuspended in 50 μl of phosphate-buffered saline (PBS) containing 1% bovine serum albumin (BSA) and 1:200 diluted V450-conjugated rat anti-mouse CD107a (LAMP1). After 30 min on ice, the cells were washed with ice-cold PBS and analyzed by an LSRII flow cytometer (BD Biosciences). Median fluorescence intensities were determined and further processed using FlowJo software (Ashland).

Cell activation

BMMCs were cultured for 48 hours in medium without SCF, followed by incubation in SCF- and IL-3-free medium supplemented with TNP-specific IgE (1 μg/ml). After 14 hours the cells were washed in buffered salt solution (BSS; 20 mM HEPES, pH 7.4, 135 mM NaCl, 5 mM KCl, 1.8 mM $CaCl_2$, 5.6 mM glucose, 1 mM $MgCl_2$) supplemented with 0.1% BSA and incubated with or without ethanol and/or other drugs. After 15 min, antigen was added and the cells were activated in the presence or absence of the drugs. The degree of degranulation was determined as the amount of β-glucuronidase released into the supernatant as described [32].

Measurement of free intracellular calcium

Changes in concentrations of free intracellular calcium were determined using cell permeant Fura-2 acetoxymetyl ester (Fura-2 AM; Life Technologies) as a reporter. IgE-sensitized cells were harvested, washed in BSS-0.1% BSA and transferred to BSS-0.1% BSA supplemented with Fura-2 AM (1 ng/ml) and probenecid (2.5 mM) used to prevent dye leakage [33], and incubated in the shaker for 30 min at 37°C, 500 rpm. Fura-2 loaded cells were washed twice with 2.5 mM probenecid in BSS-0.1% BSA and then transferred to BSS-0.1% BSA supplemented with 2.5 mM probenecid and various drugs as specified in the Results. Cells were then incubated in Thermomixer (Eppendorf; 10 min, 37°C, 500 rpm). For measurement in the presence

of extracellular calcium, cells were pelleted by centrifugation 500 x g for 3 min, resuspended in BSS-0.1% BSA and transferred to white polysorp 96 well plate (NUNC, Thermo Scientific). To determine free intracellular Ca^{2+} levels in the absence of extracellular Ca^{2+}, cells were pelleted by centrifugation, washed in Ca^{2+}-free BSS-0.1% BSA and transferred to the plate. Free intracellular Ca^{2+} was measured on INFINITE M200 (Tecan) as Fura-2 emission at 510 nm after excitation with 340 nm and 380 nm. Basal level of calcium was usually measured in the first 60 sec, followed by addition of antigen (TNP-BSA, final concentration 100 ng/ml) in BSS-0.1% BSA. Measurement continued up to 350 s. In the absence of extracellular calcium the cells were activated with antigen for 5 min followed by addition of $CaCl_2$ to final concentration 1 mM and measurement continued up to 600 s.

Immunoprecipitation and immunoblotting

Activated or nonactivated cells were solubilized in ice-cold lysis buffer (25 mM Tris-HCl, pH 8.0, 140 mM NaCl, 1 mM Na_3VO_4, 2 mM EDTA, 1 μg/ml aprotinin, 1 μg/ml leupeptin, 1 mM phenylmethylsulfonyl fluoride) supplemented with 0.2% Triton X-100 (for FcεRI immunoprecipitation). After incubation on ice for 30 min, the lysates were centrifuged (16,000 x g for 5 min at 4°C) and postnuclear supernatants were immunoprecipitated with rabbit anti-IgE antibody prebound to UltraLink-immobilized protein A (Pierce, Thermo Scientific). The immunoprecipitated proteins were size-fractionated by sodium dodecyl sulfate-polyacrylamide gel electrophoresis (SDS-PAGE), transferred to nitrocellulose membrane and immunoblotted with PY-20-HRP conjugate or with FcεRI-β chain-specific antibody followed by HRP-conjugated anti-mouse IgG. For immunoblotting analysis of other proteins, the cells were solubilized in lysis buffer supplemented with 1% n-dodecyl β-D-maltoside and 1% Nonidet P-40 and postnuclear supernatants were directly analyzed by SDS-PAGE followed by immunoblotting with phospho-protein-specific or the corresponding protein-specific antibodies and HRP-conjugated secondary antibodies. The HRP signals were detected by chemiluminescence, quantified by luminescent image analyzer LAS-3000 (Fuji Photo Film Co), and further analyzed by Aida image analyzer software (Raytest). The amount of phosphorylated proteins was normalized to the loading controls, run in parallel experiments [32]. We found that this approach gave more reliable data than normalization towards specific proteins after stripping of the membranes.

Sucrose density gradient fractionation and expression of cytokine genes

Sucrose density gradient separations were performed as previously described [32] and individual fractions were analyzed by SDS-PAGE followed by immunoblotting with PY-20-HRP and protein-specific antibodies. Expression of cytokine genes was examined by quantitative polymerase chain reaction (qPCR) as described [32].

Confocal microscopy

The wells of microscopy slides (CN Biomedicals) were coated with CellTak (BD Biosciences; 8 μl in 1 ml PBS). IgE-sensitized cells were left to attach to the coated wells for 15 min in BSS-0.1% BSA and then activated or not with Ag. After 15 min, the cells were fixed for 30 min with 3% paraformaldehyde in PBS and then permeabilized with 0.1% Triton X-100 in PBS for 30 min. After washing with PBS, the samples were blocked in PBS-1% BSA, and subsequently IgE was detected with Alexa Fluor 568-labeled donkey anti-mouse Ig. After labeling, the cells were washed and mounted in glycerol mounting solution supplemented with Hoechst 33258 stain to label nuclei. Samples were examined with a confocal laser scanning microscope Leica TCS SP5 equipped with an X63/1.4.N.A. oil-immersion objective. The image analysis was performed using a pipeline generated in CellProfiler software (Broad Institute, Boston) [34].

ROS measurements

Reactive oxygen species (ROS) were examined with cell-permeant 2',7'-dichlorodihydrofluorescein diacetate (H_2DCFDA; Life Technologies) as a reporter. Cells were sensitized for 16 hours with anti-TNP IgE (1 μg/ml) at 37°C in culture medium supplemented with 10% FCS, but devoid of SCF and IL-3. Then, the cells were washed and loaded into the wells of a 96-well plate (0.25 x 10^6 cells/well) in 100 μl of the same medium supplemented with H_2DCFDA (5 μg/ml) in the presence of probenecid (2.5 mM) and various concentrations of ethanol. After 15 min, the cells were centrifuged and resuspended in 50 μl BSS-BSA. Activation was triggered by adding 50 μl of 500 ng/ml TNP-BSA (final concentration 250 ng/ml) in the absence or presence of different concentrations of ethanol. Alternatively, in the experiment with methyl-β-cyclodextrin (Mβ) and cholesterol-saturated Mβ (sMβ), the cells were stained with H_2DCFDA as above, washed and incubated 15 min in BSS-BSA supplemented or not with 0.5% (v/v) ethanol, 2 mM Mβ, and/or 2 mM sMβ. The activation was triggered by antigen (TNP-BSA; 250 ng/ml final concentrations) in the presence of the drugs; sMβ was prepared as previously described [35]. After 10 min, changes in fluorescence intensity were monitored in an LSRII flow cytometer (BD Biosciences; Ex/Em 488/505-535 nm).

PCA

Mice were anesthetized by intraperitoneal injection of a cocktail containing ketamine (Narketan 10; 40 mg/kg, final concentration), xylazine (Xylapan; 10 mg/kg), and atropine (Atropin Biotika; 0.1 mg/kg) and then sensitized by intradermal injection of 20 μl of anti-TNP-specific IgE (50 μg/ml) in PBS into the left ear; the right ear was injected with 20 μl of PBS alone. Twenty-four hours later, 5% (v/v), 10% or 20% absolute ethanol in PBS was injected intraperitoneally (0.5 ml per mouse weighing 20 g). Mice injected with 0.5 ml of 10% or 20% ethanol exhibited reduced motoric activity, which lasted for 30 min or 90 min, respectively. Mice challenged with 0.5 ml of 5% ethanol were without any clinical signs. One hour after ethanol in PBS or PBS alone injection, each mouse was challenged with an intravenous injection of antigen (TNP-BSA, 100 μg) in 200 μl of PBS containing 1% Evans blue. The mice were killed 30 min later and their ears were removed for measurement of the amount of the Evans blue extravasated. The dye was extracted by adding 1 ml of formamide to each ear, followed by homogenization with the IKA T-25 ULTRA-TURRAX digital high-speed homogenizer systems (IKA) and incubation at 80°C. After 2 h, the formamide solution was centrifuged for 15 min at 13.000 x g and absorbance at 620 nm was determined in the supernatants.

Statistical analysis

Statistical significance of intergroup differences was determined by one-way ANOVA with Tukey's post-test using the Prism version 5.04 graphics and statistics software package (GraphPad); *, $P<0.05$; **, $P<0.01$, ***, $P<0.001$.

Results

Short-term exposure to ethanol inhibits FcεRI-induced degranulation and calcium response

To examine the inhibitory effect of ethanol on antigen-induced activation of mast cells, we isolated bone marrow cells from C57BL/6 mice and cultured them for 6–12 weeks in culture media supplemented with SCF and IL-3. More than 98% of the cells were mast cells as deduced from expression of both FcεRI and KIT receptors (see below). Exposure of BMMCs for 15 min– 2 hours with ethanol at concentrations up to 2% had no toxic effect, as determined by

trypan blue dye exclusion test (not shown). Pretreatment of IgE-sensitized BMMCs for 15 min with ethanol at concentrations 0.2–1%, inhibited degranulation induced by multivalent antigen in a dose-dependent way. Significant inhibition was observed at all concentrations of ethanol tested when the cells were activated with antigen (50 ng/ml or 100 ng/ml) for 5 min or 15 min, except for cells treated with 0.2% ethanol and stimulated with antigen (50 ng/ml) for 5 min (Fig 1A and 1B).

Ethanol at all concentrations used also inhibited, in a dose-dependent way, the calcium response after stimulation of IgE-sensitized cells with antigen in the presence of extracellular calcium (Fig 1C). When the cells were stimulated with antigen in the absence of extracellular calcium, the calcium response was significantly inhibited by 0.5% and 1% ethanol. Addition of extracellular calcium resulted in increased calcium response, which was significantly lower in cells exposed to 0.2%, 0.5% or 1% ethanol (Fig 1D). These data suggested that ethanol could act on early signaling events leading to the release of calcium from internal stores as well as on calcium channels directing influx of calcium from the extracellular space. When the cells were pretreated with 4-methylpyrazole (4-MP; 0.1 or 1 mM), a known inhibitor of alcohol dehydrogenase [36], the inhibitory effect of ethanol was not affected (Fig 2), suggesting that ethanol itself, rather than its metabolite product, is responsible for the inhibitory effect.

Involvement of cholesterol in the inhibitory effect of ethanol on FcεRI-mediated activation

Recently, Setiawan and Blanchard showed that ethanol interferes with the size and distribution of cholesterol domains in planar lipid bilayer structures [37]. To determine whether plasma membrane cholesterol could be involved in the inhibitory effect of ethanol, we evaluated the effect of Mβ alone or together with ethanol on FcεRI-mediated degranulation. Mβ is a water-soluble cyclic heptasaccharide that binds cholesterol and can extract cholesterol from the exoplasmic leaflet of the plasma membrane by harboring cholesterol in a hydrophobic cavity [35,38,39]. Exposure of cells for 15 min to 2 mM Mβ alone or in combination with 0.5% ethanol had no significant effect on spontaneous release of β-glucuronidase (Fig 3A–3C). In cells activated with antigen at a concentration 50 ng/ml or 100 ng/ml for 5 (Fig 3A) or 15 min (Fig 3B), degranulation was significantly reduced by both Mβ and ethanol. When ethanol and Mβ were used together, the inhibition of degranulation was higher than in cells treated with ethanol or Mβ alone. Mβ is not specific for cholesterol, but has pleiotropic effects on the level and distribution of various membrane components [40]. Next, we therefore evaluated antigen-induced degranulation in cells pretreated with cholesterol-saturated Mβ (sMβ), which increases plasma membrane cholesterol [35]. We found that sMβ, in contrast to Mβ, had no significant inhibitory effect on degranulation (Fig 3C). Interestingly, sMβ-treatment did not protect the cells from the inhibitory effect of ethanol (Fig 3B and 3C). We also found that exposure of cells to 2 mM Mβ or sMβ with or without ethanol for 15 min had no effect on the FcεRI expression as determined by flow cytometry (not shown).

Degranulation is accompanied by enhanced surface expression of CD107a (LAMP1), a secretory granule/lysosomal marker detectable by flow cytometry [41]. In agreement with antigen-induced β-glucuronidase release, 2 mM Mβ and 0.5% ethanol alone inhibited CD107a (LAMP1) surface expression, even though ethanol was less potent. An additive effect of the drugs was observed when the cells were activated with antigen at optimal (100 ng/ml) and supra-optimal (500 ng/ml) concentrations (Fig 3D).

We also analyzed the combined effect of Mβ and/or ethanol pretreatment on antigen-induced calcium response. The data indicate that pretreatment with Mβ did not intensify the inhibitory effect of ethanol (Fig 4A). When the cells were activated in the absence of extracellular calcium,

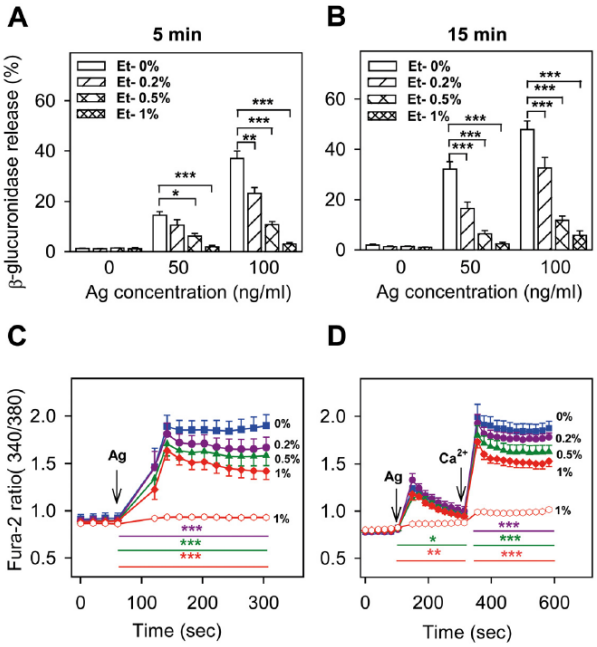

Fig 1. Short-term exposure to ethanol inhibits antigen-induced degranulation and calcium response in BMMCs. IgE-sensitized cells were preincubated for 15 min with various concentrations of ethanol (0–1%), which was also present during antigen-mediated activation. (A, B) Degranulation (release of β-glucuronidase) was measured 5 min (A) or 15 min (B) after exposure of the cells to the indicated concentrations of antigen. (C, D) Calcium response after addition of antigen (arrow, Ag, 100 ng/ml) was measured in the presence of 1 mM extracellular calcium (C), or in its absence (D), followed by addition of 1 mM calcium (arrow, Ca^{2+} in D). Calcium levels in the absence of antigen activation but in the presence of 1% ethanol is also shown in C and D (empty circles). Data are means ± SEs (n = 6–8). Statistical significance of intergroup differences is shown in A and B. In C and D, statistical significance of differences between control cells (0% ethanol) and cells exposed to 0.2% ethanol (violet line), 0.5% ethanol (green line) or 1% ethanol (red line) calculated for the corresponding time intervals (coloured lines) are also indicated.

doi:10.1371/journal.pone.0144596.g001

the inhibitory effect of ethanol was abrogated by Mβ. After addition of calcium, both ethanol and ethanol+Mβ showed comparable responses (Fig 4B). Cells pretreated with sMβ showed increased calcium response and were more resistant to the inhibitory effect of ethanol (Fig 4C). When the difference between sMβ + ethanol and ethanol was calculated, it was lower than the difference between sMβ and controls (Fig 4D). The data suggest that manipulation with the cellular cholesterol modulates sensitivity of antigen-induced calcium response to ethanol, and thus support the lipid-centric hypothesis of ethanol action in this system.

Ethanol exposure or cholesterol removal inhibit expression of cytokine genes in antigen-activated BMMCs

Next we examined the effect of short-term pretreatment of BMMCs with various concentrations of ethanol (0–1%) on antigen-induced expression of cytokines. Data presented in Fig 5A indicate dose-dependent inhibition of antigen-induced mRNA production of TNF-α, IL-6 and IL-13, as determined by qPCR. Transcriptional inhibition of cytokines was also observed in cells with reduced levels of cholesterol after pretreatment with Mβ. When the cells were

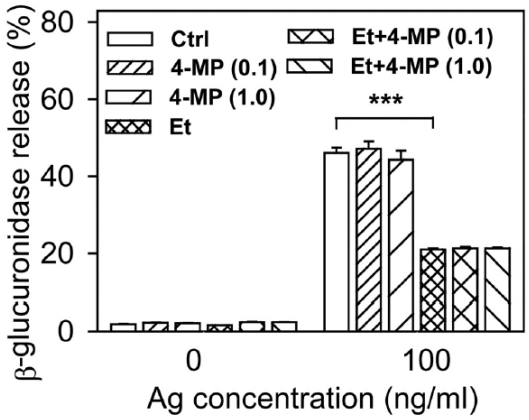

Fig 2. The inhibitory effect of ethanol on antigen-induced degranulation is not affected by blocking alcohol dehydrogenase. IgE-sensitized cells were pretreated or not (Ctrl) for 15 min with ethanol (0.5%) and/or 4-MP (0.1 or 1.0 mM). The cells were non-activated or activated with antigen (100 ng/ml) in the presence of ethanol and/or 4-MP for 15 min and degranulation was determined. Data are means ± SEs (n = 6). Statistical significance of differences between antigen-activated control cells and ethanol-treated cells is also shown. 4-

doi:10.1371/journal.pone.0144596.g002

pretreated simultaneously with both Mβ and ethanol, less-than-additive effects were observed (Fig 5B). These data suggest that both drugs could inhibit a similar signaling pathway.

Protective effect of cholesterol against ethanol-mediated inhibition of ROS in antigen-activated BMMCs

Recent studies indicated that exposure of macrophages to ethanol promoted generation of ROS [42–44]. To determine whether ROS could also be generated by ethanol in BMMCs, we first measured ROS production in cells exposed to various concentrations of ethanol. Our data show that short-term exposure to ethanol had no effect on production of ROS in non-activated cells (Fig 6A). In cells activated with antigen, in accord with previous studies [45,46], ROSs were increased. Pretreatment with ethanol resulted in a dose-dependent decrease of ROS after activation with antigen (Fig 6A). Next we examined whether cholesterol could be involved in ROS production (Fig 6B). IgE-sensitized cells were pretreated or not with ethanol, Mβ, and/or sMβ. In non-activated cells, ethanol had no significant effect on ROS, but pretreatment with Mβ reduced baseline ROS production. sMβ had a lower inhibitory effect on ROS levels than Mβ. In antigen-activated cells, ROS production was more inhibited by Mβ than by ethanol. In contrast, pretreatment with sMβ followed by antigen activation resulted in higher ROS production than in control cells. When ethanol was combined with Mβ, strong inhibition of antigen-induced ROS production was observed, whereas ethanol had no inhibitory effect in cells exposed to sMβ. These data suggest that cholesterol has a dramatic effect on ROS production and its sensitivity to ethanol.

Inhibitory effect of ethanol on tyrosine phosphorylation of FcεRI-related signal transduction proteins

The first biochemically well-defined step in FcεRI signaling is tyrosine phosphorylation of the receptor subunits, followed by formation of the FcεRI signalosome and phosphorylation of

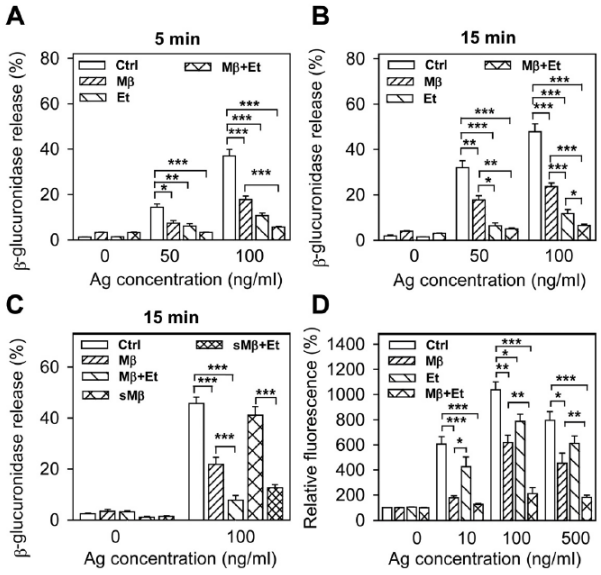

Fig 3. Involvement of cholesterol in the inhibitory effect of ethanol on FcεRI-mediated degranulation. (A, B) IgE-sensitized BMMCs were preincubated for 15 min without (Ctrl) or with Mβ (2 mM), and/or ethanol (0.5%), followed by exposure to the indicated concentrations of antigen in the presence of the drugs. Degranulation was measured 5 min (A) or 15 min (B) after triggering. (C) IgE-sensitized cells were preincubated for 15 min without (Ctrl) or with Mβ (2 mM), sMβ (2 mM), and/or ethanol (0.5%) and then activated (Ag; 100 ng/ml) or not in the presence of the drugs. Degranulation was determined 15 min after triggering. (D) IgE-sensitized cells were preincubated with various drugs as above, then exposed to various concentrations of antigen and cell activation, measured by CD107a (LAMP1) expression, was determined by flow cytometry. Data are means ± SEs (n = 4–12). Statistical significance of the intergroup differences is also shown.

doi:10.1371/journal.pone.0144596.g003

other substrates [47]. Next, we therefore investigated global tyrosine phosphorylation of proteins in non-activated or antigen-activated cells pretreated or not with various concentrations of ethanol. To determine whether there are any changes in association of the tyrosine phosphorylated proteins with membrane domains, the cells were solubilized in solubilization buffer containing 1% Brij-96 and fractionated on sucrose density gradient to separate cellular components according to their solubility in detergents and density. Data presented in Fig 7A indicate distribution of tyrosine phosphorylated proteins in non-activated control cells, not exposed to ethanol. In low-density detergent-resistant membranes (DRM, fractions 1–3), the key tyrosine phosphorylated proteins were transmembrane adaptor proteins PAG and NTAL and SRC family kinase LYN, as determined by immunoblotting with protein-specific antibodies. A number of other tyrosine phosphorylated proteins were observed in detergent-soluble fractions (fractions 6–9). In cells pretreated with various concentrations of ethanol (Fig 7B–7D), there were dose-dependent changes in the distribution of some tyrosine phosphorylated proteins in the low-density and high-density fractions. Densitometry analysis of the immunoblots showed a significant increase in the percentage of tyrosine phosphorylated PAG (Fig 7G) and LYN (Fig 7H) in DRMs from cells exposed to low concentrations of ethanol (0.2%). However, when ethanol was used at a higher concentration (1%), percentage of tyrosine phosphorylated LYN (Fig 7H) and NTAL (Fig 7I) in DRMs was significantly reduced (Fig 7D). In antigen-activated cells, some proteins were more tyrosine phosphorylated in both low- and high-density fractions

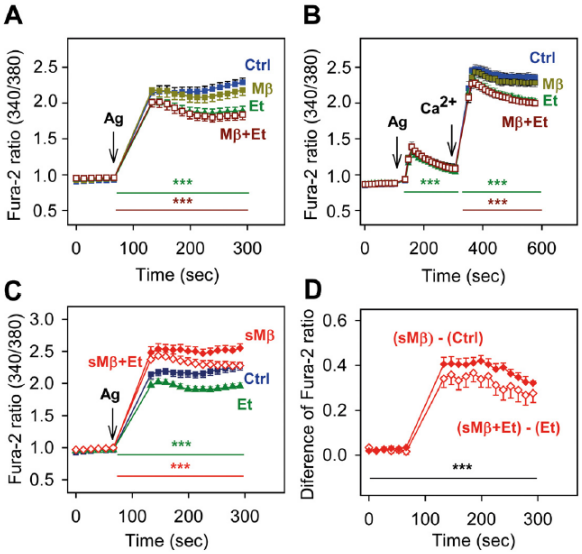

Fig 4. Involvement of cholesterol in the inhibitory effect of ethanol on FcεRI-mediated calcium response. (A, B) IgE-sensitized BMMCs were incubated for 15 min without (Ctrl) or with ethanol (Et, 0.5%) and/or Mβ (2 mM). Calcium response after adding antigen (arrow, Ag; 100 ng/ml) was measured in the presence of the drugs as indicated. The cells were activated in the presence of extracellular calcium (A) or in its absence, followed by addition of 1 mM calcium (B, Ca^{2+}, arrow). (C) IgE-sensitized cells were incubated for 15 min in medium alone (Ctrl) or medium supplemented with ethanol (Et; 0.5%), Mβ saturated with cholesterol (sMβ; 2 mM), or sMβ (2mM) and ethanol (0.5%). The cells were activated in the presence of the drugs with antigen (arrow, Ag; 100 ng/ml) and calcium response was determined. (D) Data from Fig 4C were used to calculate the difference between calcium response in cells exposed to sMβ or Ctrl and sMβ+Et or Et. Data are means ± SEs (n = 6–12). Statistical significance of differences in A and B [Ctrl versus Et-treated cells (green line) and Ctrl versus Mβ+Et-treated cells (brown line)], C [sMβ versus Ctrl (green line) and sMβ+Et versus Et (red line)], and D [sMβ—Ctrl versus sMβ+Et—Et (black line)] calculated for the corresponding time intervals (coloured lines) are also indicated.

doi:10.1371/journal.pone.0144596.g004

(compare Fig 7A and 7E). After activation, the percentage of tyrosine phosphorylated LYN in DRMs was increased by ethanol (Fig 7H). When PAG-, LYN-, or NTAL-specific antibodies were used, no significant differences in the distribution of proteins in DRMs from control and ethanol-pretreated cells were observed (Fig 7G–7H). These data suggest that ethanol at the concentrations used caused fine changes in the cross-talk between signaling molecules rather than global changes in the detergent solubility of plasma membrane proteins.

To determine changes in tyrosine phosphorylation of FcεRI, the receptor was immunoprecipitated and analyzed by immunoblotting with phosphotyrosine-specific antibody, PY-20-HRP conjugate. In non-activated cells, the receptor β and γ subunits exhibited weak tyrosine phosphorylation, and ethanol (0.5%) with or without Mβ had no significant effect on their phosphorylation (Fig 8A). In cells exposed to Mβ alone, a significant increase in tyrosine phosphorylation of FcεRI β and γ subunits was observed, which is in line with our previous studies indicating that cholesterol removal enhances phosphorylation of various substrates in mast cells [48]. Tyrosine phosphorylation of FcεRI β and γ subunits was increased after FcεRI triggering, as expected [47], and pretreatment with Mβ, ethanol, and especially Mβ+ethanol, significantly reduced this phosphorylation (Fig 7A).

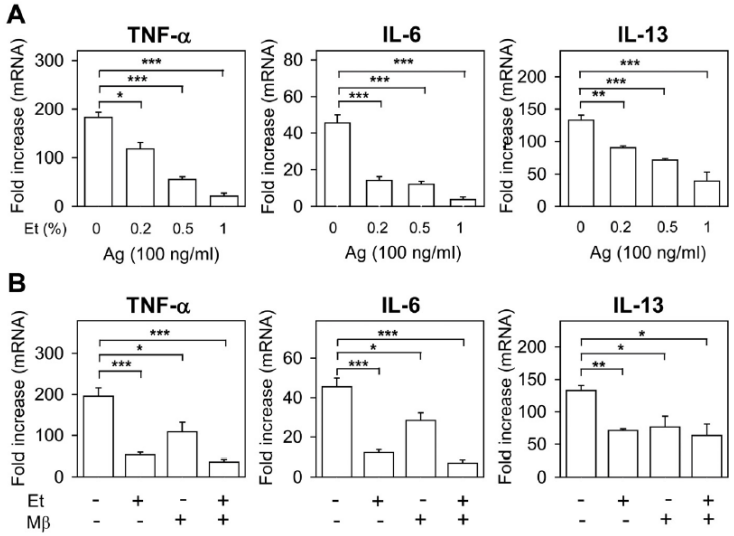

Fig 5. Ethanol or cholesterol removal inhibit expression of cytokine genes in antigen-activated BMMCs. (A) IgE-sensitized cells were preincubated for 15 min with the indicated concentrations of ethanol, which were also present during activation with antigen (100 ng/ml). mRNAs for TNF-α, IL-6, and IL-13 were isolated one hour after triggering and quantified by qPCR. (B) The cells were exposed to medium alone (-), ethanol (0.5%) and/or Mβ (2 mM) and mRNAs for TNF-α, IL-6, and IL-13 were quantified as above. Data are means ± SEs (n = 6–8). The statistical significance of the intergroup differences is also shown.

doi:10.1371/journal.pone.0144596.g005

Tyrosine phosphorylation of several other proteins involved in FcεRI signaling was examined by direct immunoblotting of size-fractionated cell lysates with phosphotyrosine protein-specific antibodies. For these experiments we used IgE-sensitized cells pretreated or not with Mβ and/or ethanol (Fig 8B and 8C). The cells were either non-activated or activated with

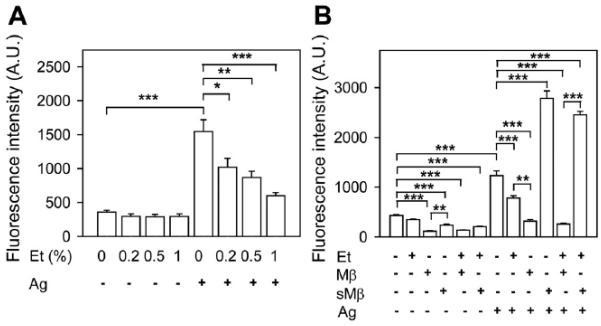

Fig 6. Protective effect of cholesterol against ethanol-mediated inhibition of ROS production in antigen-activated BMMCs. (A) IgE-sensitized cells were incubated for 15 min with the indicated concentrations of ethanol, which was also present during the activation. Then the cells were activated or not with antigen (250 ng/ml) and ROSs were determined using H_2DCFDA as a substrate. The values on y-axes indicate fluorescence intensities observed 10 min after triggering. (B) The cells were exposed to BSS-BSA supplemented or not with ethanol (0.5%), Mβ (2 mM) and/or sMβ (2 mM), and after 20 min activated or not with antigen (250 ng/ml). ROSs were determined as above. Data are means ± SEs (n = 6–8). The statistical significance of the intergroup differences is also shown.

doi:10.1371/journal.pone.0144596.g006

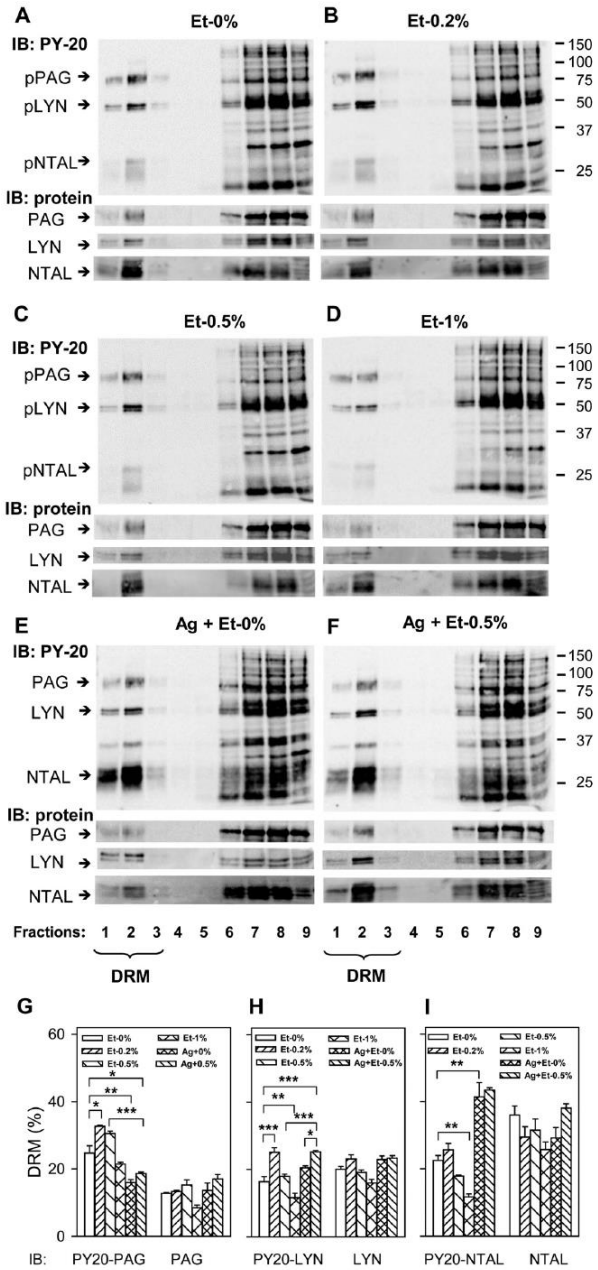

Fig 7. Ethanol-induced changes in protein tyrosine phosphorylation in the plasma membrane domains. (A–F) IgE-sensitized BMMCs were pretreated or not with the indicated concentrations of ethanol for 15 min and then non-activated (A–D) or activated with antigen (E and F; 100 ng/ml) for 5 min. Then the cells were solubilized in 1% Brij-96-containing lysis buffer and fractionated on sucrose density gradient. Individual fractions were collected from the top of the gradient (fraction 1), size fractionated by SDS-PAGE

and examined for tyrosine phosphoproteins by immunoblotting (IB) with PY-20-HRP conjugate (PY-20) or with antibodies specific for PAG, LYN, and NTAL). Positions of PAG, LYN, and NTAL are indicated by arrows on the left. Fractions (1–3) containing detergent-resistant membranes are marked (DRM). Numbers on the right indicate positions of molecular weight markers in kDa. Representative immunoblots from three to four independent experiments are shown. (G–I) All immunoblots were analyzed by densitometry, and the relative amounts of PAG (G), LYN (H), and NTAL (I) and their tyrosine phosphorylated forms (PY-20) in DRMs were determined. Means ± S.E. were calculated and the statistical significance of intergroup differences was determined.

doi:10.1371/journal.pone.0144596.g007

antigen for 5 min. For these studies we selected proteins involved in tyrosine phosphorylation of the FcεRI subunits (LYN and SYK), regulation of calcium response (LAT and PLCγ), and transcriptional regulation of cytokines (STAT5, ERK, AKT). We found that in non-activated cells, Mβ alone and/or ethanol either had no effect (SYK, LAT, pLCγ1, STAT5, and AKT) or slightly but significantly increased phosphorylation of the target (ERK). In antigen-activated cells, pretreatment with Mβ alone and/or ethanol reduced tyrosine phosphorylation of several target proteins (SYK, LAT, STAT5, and AKT). When pPLCγ1 was analyzed, only ethanol and Mβ+ethanol showed inhibitory effects, whereas in the case of pERK, only ethanol alone was inhibitory.

Activity of mouse LYN kinase is regulated by tyrosine phosphorylation of Tyr 507 (a negative regulator; Fig 8D) and Tyr 416 (a positive regulator; Fig 8E). To determine whether Mβ and/or ethanol interfere with phosphorylation of these tyrosines, we performed immunoblotting with LYN-tyrosine-specific antibodies. We found that pretreatment of cells with 0.5% ethanol enhanced phosphorylation at LYN-Tyr 507 15 min after FcεRI triggering. Mβ together with ethanol increased phosphorylation of LYN-Tyr 507 at all intervals. In contrast, LYN-Tyr 416 did not exhibit any significant changes in phosphorylation after Mβ and/or ethanol exposure and antigen activation. These data suggest that ethanol could inhibit FcεRI activation by enhancing tyrosine phosphorylation of LYN-Tyr 507.

Pretreatment with ethanol and/or cholesterol removal does not interfere with FcεRI expression but affects its internalization

Previous studies with other cell types showed that ethanol interferes with internalization of plasma membrane receptors, their trafficking, endocytosis, and recycling [49–51]. FcεRI is rapidly internalized upon antigen triggering [52,53]. Next, we therefore compared internalization of antigen-aggregated FcεRI in BMMCs pretreated or not with ethanol and/or Mβ. Data presented in Fig 9A indicate that 15 min pretreatment with 0.5% ethanol and/or 2 mM Mβ had no effect on the surface expression of the FcεRI and KIT. When the cells were pretreated with ethanol and/or Mβ and then permeabilized and stained for total IgE, no significant differences in the amount of internalized IgE were determined in non-activated cells. In cells activated with antigen for 15 min, IgE was internalized, and pretreatment with ethanol together with Mβ significantly reduced the internalization. Pretreatment with ethanol or Mβ alone had no significant effect on internalization of the antigen-IgE-receptor complexes (Fig 9B and 9C).

Ethanol suppresses IgE-mediated PCA in mice

Finally, we examined whether ethanol could have an inhibitory effect on mast cells under *in vivo* conditions. We used PCA in which local activation of mast cells results in increased vascular permeability, as visibly manifested by leakage of the Evans blue dye into the reaction site of the ear. This leakage was not affected by intraperitoneal administration of 0.5 ml PBS containing 5% ethanol (Fig 10A and 10B; compare 0% and 5%) 30 min before the antigen. In contrast, in mice that were injected with 10% or 20% ethanol in PBS, the vascular permeability of the

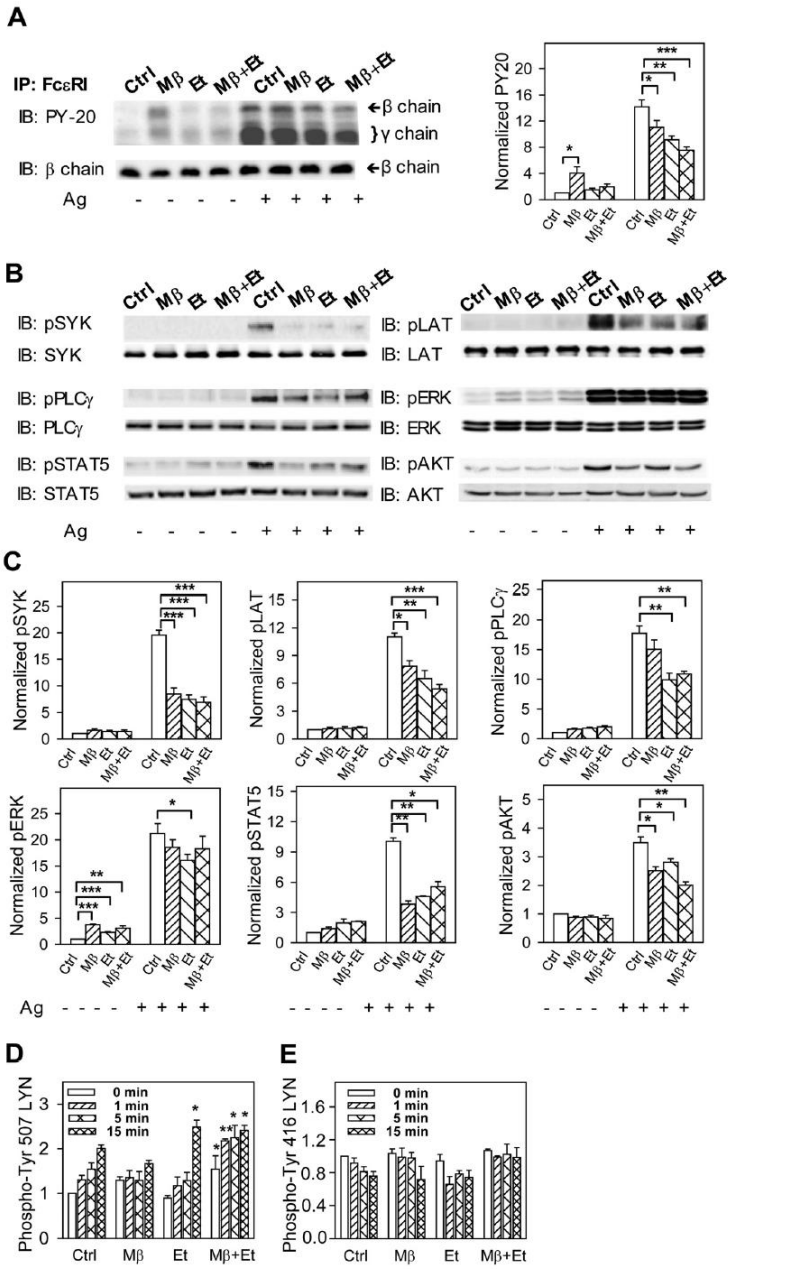

Fig 8. Pretreatment with ethanol inhibits tyrosine phosphorylation of FcεRI β and γ subunits and some other proteins involved in FcεRI signaling. (A) IgE-sensitized cells were preincubated for 15 min with BSS-BSA alone (Ctrl) or supplemented with ethanol (0.5%) and/or Mβ and then activated or not with antigen (100 ng/ml) in the presence or absence of the compounds. After 5 min the cells were solubilized in 0.2% Triton X-100 and FcεRI was immunoprecipitated (IP) from postnuclear supernatants. The

immunoprecipitates were resolved by SDS-PAGE and analyzed by immunoblotting with PY-20-HRP conjugate. For loading controls, the same membrane was stripped and re-blotted with FcεRI-β-chain-specific antibody. Representative immunoblots from three to five independent experiments are shown on the left. The immunoblots were analyzed by densitometry and the fold increase in tyrosine FcεRI-β and -γ chain phosphorylation, normalized to non-activated cells and the amount of FcεRI-β chain, is also shown on the right. (B) IgE-sensitized cells were incubated and activated as above. Five min after triggering the cells were solubilized, size fractionated, and tyrosine phosphorylated proteins were detected by immunoblotting with the phosphoprotein-specific antibodies. Antibodies for the corresponding proteins were used for detection of loading controls. Representative immunoblots from three to four independent experiments are shown. (C) The immunoblots were analyzed by densitometry. Fold increases of protein tyrosine phosphorylation, normalized to control (Ctrl) non-activated cells and the corresponding protein loads are shown. (D and E) IgE-sensitized cells were incubated with the drugs as in A and then activated with antigen (100 ng/ml) in the presence of the drugs for the indicated time intervals. The cells were solubilized, size fractionated, and LYN phosphorylated on Tyr 507 (D) or Tyr 416 (E) was detected by immunoblotting with the corresponding antibodies. After stripping, the membranes were developed for LYN used as a loading control. Fold increase in protein tyrosine phosphorylation, normalized to non-activated cells (Ctrl) and protein load, is also shown. Means ± SEs and the statistical significance of differences in A, C, E, and D were calculated from three to five independent experiments.

doi:10.1371/journal.pone.0144596.g008

ears was attenuated, as evaluated by the extent of Eva blue staining (Fig 10A, 10% and 20%) and amounts of Evans blue extracted from the ears (Fig 10B). The difference in PCA between mice injected with 0.5 ml PBS alone or 0.5 ml PBS containing 10% or 20% ethanol was significant (Fig 10B). No significant intergroup differences were noticed when control ears (not sensitized with IgE) were evaluated. The data suggest that ethanol inhibits FcεRI-induced mast cell activation *in vivo*.

Discussion

Data presented in this study show that short-term exposure of BMMCs to nontoxic concentrations of ethanol inhibits FcεRI-mediated degranulation, calcium response, and production of several cytokines (TNF-α, IL-6, and IL-13) in a dose-dependent manner. To understand the molecular mechanism of the inhibitory effect of ethanol on these activation events we examined various candidate targets. Several lines of evidence suggest that ethanol interferes with the function of FcεRI-cholesterol signalosomes and support the lipid-centric theory of ethanol action in this system, at least at the early stages of cell activation

First, pretreatment of the cells with 4-MP, an inhibitor of alcohol dehydrogenase, together with ethanol had no effect on the inhibitory action of ethanol on degranulation. Thus, inhibition of mast cell activation seems to be caused by ethanol itself and not its metabolites. This conclusion is supported by the finding that up to 2 hours exposure to 2% ethanol in BSS-BSA at 37°C was not toxic to BMMCs. It should also be noted that the cells in this study were pretreated with ethanol only for 15 min before activation, which makes less likely that metabolites are formed and affect signaling pathways.

Second, antigen-mediated degranulation, calcium response, and production of cytokines were also inhibited by Mβ. In cells treated with Mβ, the inhibitory effect of ethanol on degranulation, and IgE receptor internalization was potentiated. Interestingly, when the cells were pretreated with Mβ saturated with cholesterol, the inhibitory effect of ethanol on calcium response was reduced. These data suggest that cholesterol is involved in the inhibitory effect of ethanol.

Third, production of ROS after FcεRI triggering was also inhibited by ethanol in a dose-dependent manner and treatment together with Mβ potentiated the inhibitory effect of ethanol. These findings are in accord with previous data showing that lowering cellular cholesterol by Mβ in hepatocytes inhibits ROS production [54]. Interestingly, exposure of the cells to sMβ enhanced ROS production, and the inhibitory effect of ethanol was abolished, confirming that cholesterol interferes with the inhibitory activity of ethanol.

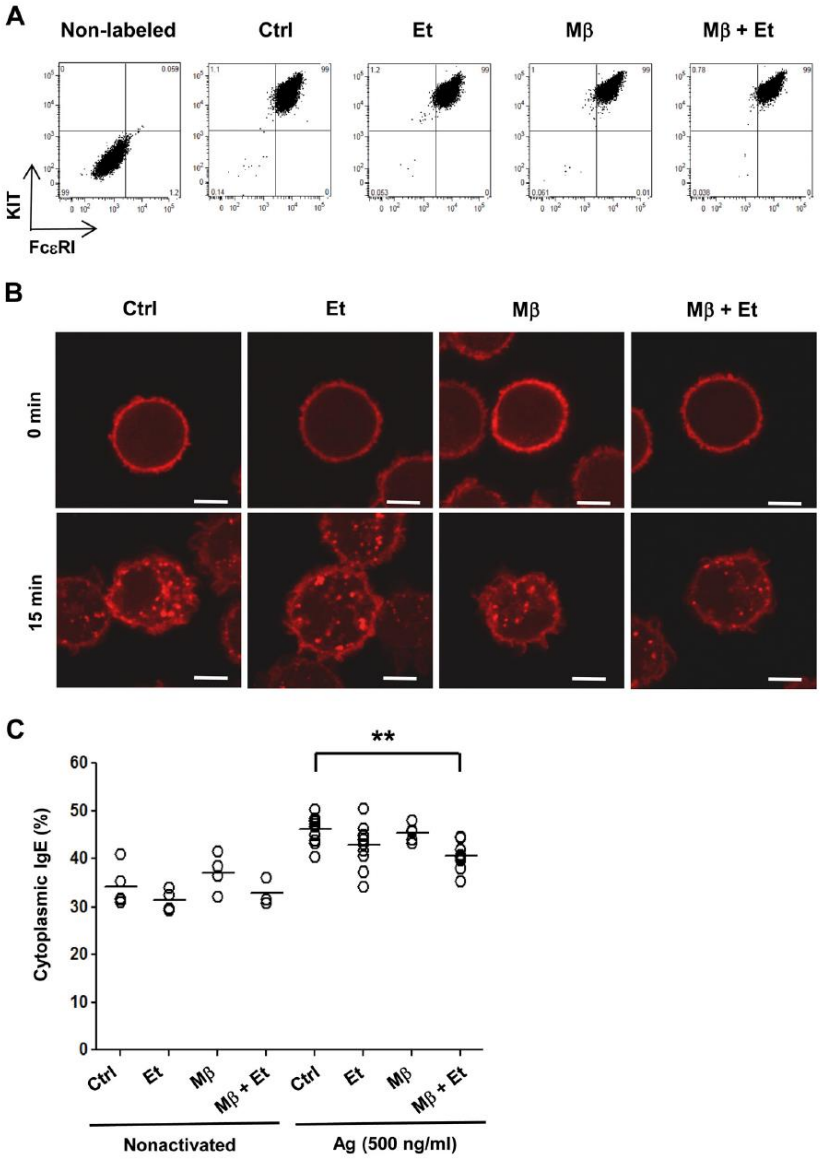

Fig 9. Pretreatment with ethanol and cholesterol removal do not interfere with the FcεRI expression but affect its internalization. (A) The cells were incubated or not for 15 min with BSS-BSA alone (Ctrl) or supplemented with ethanol (0.5%) and/or Mβ (2 mM) and then stained for surface KIT and FcεRI by direct immunofluorescence followed by flow cytometry analysis. (B) IgE-sensitized cells were incubated with the drugs as above and activated or not with antigen (500 ng/ml). After 15 min the cells were fixed, permeabilized, labeled for IgE and analyzed by confocal microscopy. Bars = 5 μm. (C) Distribution of IgE in individual cells was evaluated and the fraction of IgE detected in the cytoplasm was determined. Each spot represents one cell, bars indicate means. Statistical significance of intergroup differences is also indicated.

doi:10.1371/journal.pone.0144596.g009

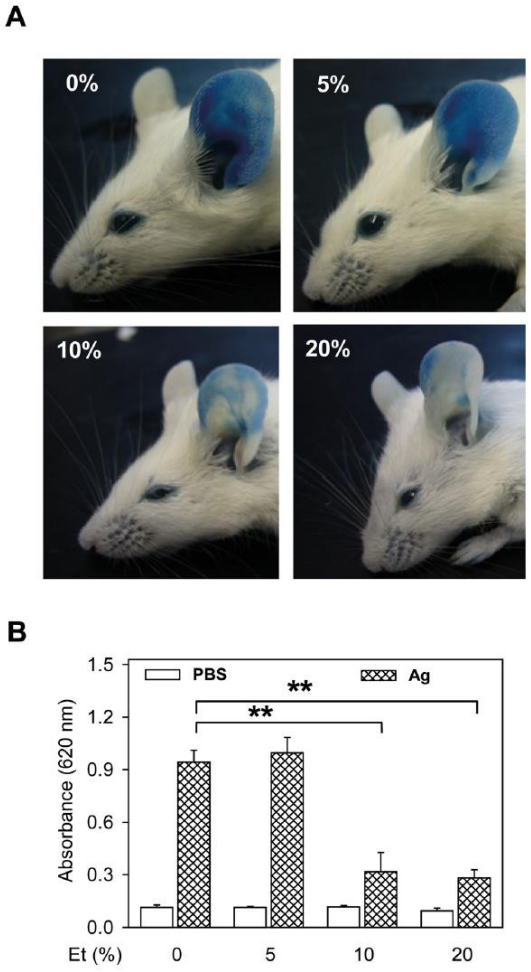

Fig 10. Inhibitory effect of ethanol on mast cell-mediated PCA. PCA was performed as described in Materials and methods. Sensitizing IgE in PBS and PBS alone were injected into left and right ears, respectively. (A) Representative photographs of ears of the mice injected intraperitoneally with 0.5 ml (per mouse weighing 20 g) PBS alone (0%) or with 0.5 ml of PBS containing 5%, 10%, or 20% ethanol, followed by intravenous administration of Evans blue and antigen in PBS. (B) Quantitative data for ear-tissue extracted Evans blue from left (IgE) and right (PBS) ears in mice treated as above. Means ± SEs were calculated from 3–4 animals in each group. Statistically significant differences between control mice injected with PBS alone and mice injected with 10% or 20% ethanol in PBS are shown.

doi:10.1371/journal.pone.0144596.g010

Fourth, immunoprecipitation and immunoblotting analyses showed that ethanol inhibits tyrosine phosphorylation of FcεRI β and γ subunits in antigen-activated cells. Phosphorylation of these targets is the first biochemically well-defined step after FcεRI triggering and depends on the topography and activity of protein tyrosine kinase LYN and protein tyrosine phosphatases in the vicinity of the FcεRI [55,56]. The impaired tyrosine phosphorylation of the FcεRI β and γ subunits could explain reduced tyrosine phosphorylation of the downstream substrates,

including SYK, LAT, PLCγ, AKT, and STAT5 in ethanol-treated cells. Tyrosine phosphorylation of these substrates was also inhibited by Mβ, but no clear additive effect of ethanol and Mβ was observed. This could be related to a similar mechanism of inhibition of both drugs. The reduced phosphorylation of FcεRI by ethanol was neither caused by reduced phosphorylation of the positive regulatory Tyr 416 of LYN nor by enhanced phosphorylation of the negative regulatory Tyr 507 of LYN, which showed enhanced phosphorylation only 15 min after activation. Surprisingly, when Mβ and ethanol were used together, enhanced Tyr 507 phosphorylation was observed at all time intervals after activation and even in non-activated cells. Tyr 507 is phosphorylated by CSK, which is presumably anchored to the plasma membrane via phosphorylated PAG [32]. However, our study did not show enhanced tyrosine phosphorylation of PAG in the cells pretreated with ethanol. The enhanced phosphorylation of Tyr 507 of LYN could be related to our recent findings that PAG is both a positive and negative regulator of FcεRI signaling and that in mast cells there are some other not yet discovered anchors of CSK [32]. Enhanced phosphorylation of LYN Tyr 507 in cells pretreated with ethanol alone, but not in cells treated with Mβ alone, was not accompanied by the corresponding inhibition of SYK phosphorylation, which was observed in cells pretreated with both ethanol alone and Mβ alone. Thus, rather than changes in activity of the LYN kinase, ethanol and Mβ could interfere with formation of the FcεRI signalosome in which cholesterol could play a key role and in which kinases and phosphatases are at equilibrium in nonactivated cells [55]. Nanoscale changes in lateral organization of proteins and lipids in the plasma membrane and enhanced actin polymerization have recently been described in ethanol-pretreated cells [57]. In fact, there could be a direct cross-talk between ethanol and cholesterol, as was noticed in other systems. For example, Furlow and Diamond showed that the interplay between membrane cholesterol and ethanol contributes to alterations of the membrane fluidity, viscosity, and redistribution of surface molecules, which affects neutrophil adhesion, rolling, and tethering behavior [58].

Fifth, internalization of antigen-aggregated FcεRI was significantly inhibited by 15 min pretreatment with Mβ and ethanol. In our previous study we found that cholesterol removal by Mβ enhanced antigen-mediated clustering of the FcεRI [48]. These findings, together with a previous report that aggregated FcεRI can be endocytosed by a clathrin-independent mechanism that appears to be mediated by membrane structures enriched in cholesterol [52], suggest that Mβ and ethanol prevent internalization of the receptor aggregates, which remain for prolonged time intervals on the cell surface.

The capacity of externally added cholesterol to reduce the inhibitory effect of ethanol on calcium and ROS responses are more compatible with the lipid-centric theory than the protein-centric theory of the inhibitory effect of ethanol. How exactly ethanol interacts with lipids and/or how it affects lipid-protein interactions is not known but could involve direct interaction of ethanol with cholesterol [59] and the ability of ethanol to mediate and modify organization of the lipid bilayer structures [7,37]. However, our data do not rule out the possibility that ethanol-protein interactions are also involved in the inhibitory effect of ethanol as was observed in other systems [12,60–62]. This could explain different effects of enhanced cholesterol levels on the inhibitory action of ethanol in various signaling pathways. For example, the observed decrease in the inhibitory effect of ethanol on calcium or ROS responses in cells with enhanced cholesterol levels could reflect the reduced penetration of ethanol through lipid bilayers with increased rigidity caused by cholesterol [63]. On the other hand, ethanol could act directly as an inhibitor of some enzymes involved at later stages of degranulation; this could be an explanation of our finding that degranulation was not protected from the inhibitory effect of ethanol in cells pretreated with sMβ. In this context, Lisboa et al showed that phosphatidic acid produced by phospholipase D (PLD) plays an important role in promoting IgE-dependent

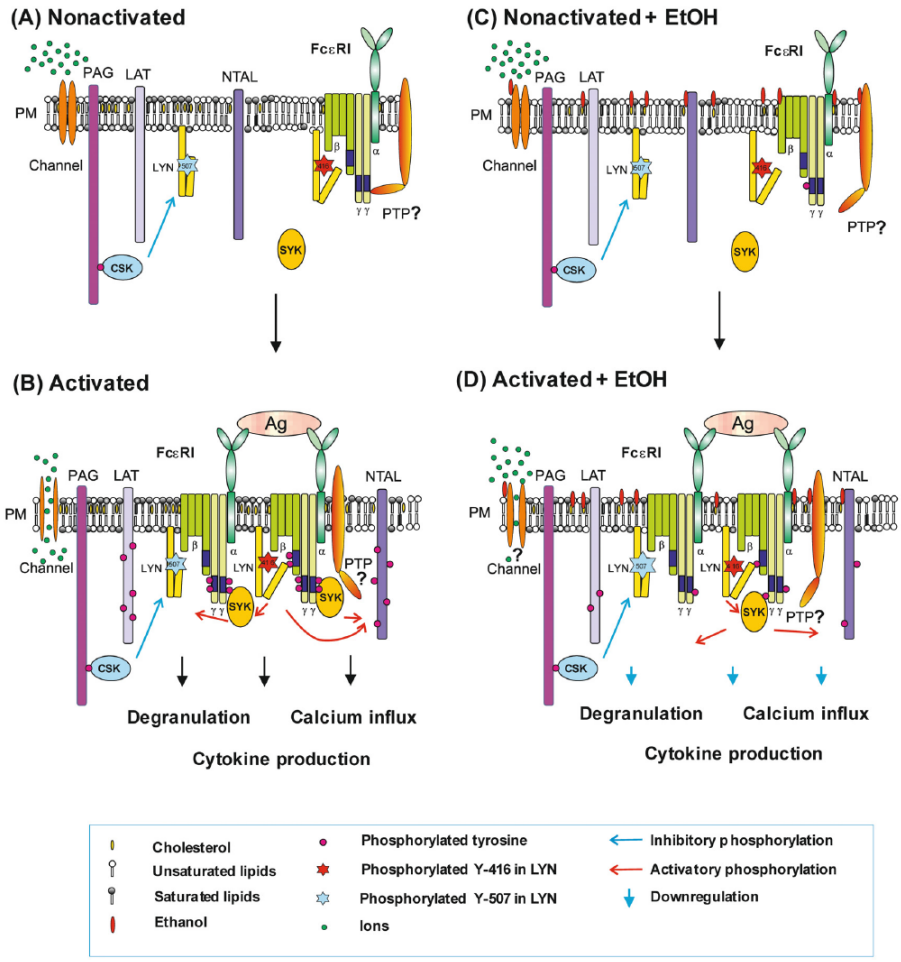

Fig 11. Model of FcεRI-mediated activation in ethanol-pretreated mast cells. In nonactivated cells (A), the topography of FcεRI and other signaling molecules, such as SRC family kinase LYN, protein tyrosine phosphatase (PTP), and adaptor proteins (LAT, PAG, and NTAL), prevents signaling. An important role in this process is played by the plasma membrane cholesterol. Aggregation of the FcεRI-IgE complexes by multivalent antigen (B) induces topographical changes that lead to formation of the FcεRI signalosome and enhanced tyrosine phosphorylation of the FcεRI β and γ subunits by LYN and SYK kinases. This results in enhanced degranulation, calcium response, cytokine production and numerous other events. In the cells exposed to ethanol and/or with reduced amount of cholesterol (C), the topography of plasma membrane molecules is slightly modified, resulting in increased tyrosine phosphorylation of some signaling molecules even in nonactivated cells. Aggregation of the receptor in ethanol-treated cells leads to suboptimal topographical changes resulting in reduced tyrosine phosphorylation of the FcεRI β and γ subunits by LYN and SYK kinases and/or enhanced activity of the corresponding phosphatases (D). This leads to reduced degranulation, calcium response, cytokine production and other events. Ethanol could also bind directly to some cytoplasmic or plasma membrane proteins, such as ion channel proteins, and in this way inhibit the cell signaling.

doi:10.1371/journal.pone.0144596.g011

signaling events within lipid microdomains in mast cells [64]. As a tool they used 1-butanol, which subverts production of phosphatidic acid to the biologically inert phosphatidyl butanol. Similarly, the presence of ethanol could lead to production of phosphatidyl ethanol instead of phosphatidic acid [65] and in this way inhibit FcεRI signaling. However, our and others' data

suggest that ethanol inhibits FcεRI signaling by another mechanism. We found that the inhibitory effect of ethanol on calcium response and ROS production was blocked by exposure of the cells to sMβ, which is unlikely to change production of PA and/or activity of PLD. Furthermore, it has been recently found that mice deficient in PLD1 and PLD2, which do not produce any PA, show no changes in early signaling events after FcεRI triggering [66].

Model of ethanol action on mast cells and their activation by antigen is shown in Fig 11. Exposure of the cells to ethanol leads to changes in properties of plasma membrane and topography of plasma membrane components, resulting in the observed increase in basal tyrosine phosphorylation of some membrane proteins, including FcεRI. When IgE-sensitized and ethanol-treated cells are activated by antigen, tyrosine phosphorylation of the FcεRI β and γ subunits is reduced reflecting suboptimal topography and/or reduced activity of LYN and SYK kinases and/or enhanced activity of protein tyrosine phosphatases in the vicinity of the receptor. Ethanol could also bind to ion channels or some other plasma membrane or cytoplasmic proteins and in this way inhibit various signaling events, including degranulation, calcium response and production of cytokines.

The inhibitory effect of ethanol on mast cell activation was confirmed by experiments *in vivo* in which mast cells were sensitized locally by IgE, and ethanol and antigen was administered intraperitoneally and intravenously, respectively. The results of PCA assays, which reflect the activity of mast cells [67] support previous findings indicating that excessive ethanol consumption is associated with increased risk of infection [68]. Experimental studies with animal and human subjects given ethanol in a controlled setting showed suppression of the innate immunity and inflammation [69–71]. Attention was focused mainly on the inhibitory effect of ethanol on activation of macrophages [72,73], monocytes [74] and T cells [20,75–77]. Although previous studies also indicated that mast cells could be the target of ethanol [24,25], this is the first study showing that ethanol inhibits the earliest events in FcεRI signaling and demonstrate the inhibitory effect of ethanol on mast cells *in vivo*.

Conclusions

In this study we found that 15 min treatment with non-toxic concentrations of ethanol *in vitro* inhibited antigen-induced tyrosine phosphorylation of the FcεRI β and γ subunits, SYK kinase, NTAL adaptor protein, PLCγ, calcium response, production of ROS, degranulation, and expression of cytokine genes in a dose-dependent manner. Early activation events were also inhibited by Mβ, suggesting that cholesterol could be involved. The role of cholesterol in the inhibitory effect of ethanol was supported by the finding that sMβ reduced the inhibitory effect of ethanol on calcium and ROS responses. The data support the lipid-centric theory of ethanol action on the initial stages of FcεRI signaling. The inhibitory effect of ethanol on mast cell activation was also observed in a mouse PCA model *in vivo*, explaining previous findings of the reduced inflammatory response associated with enhanced consumption of ethanol.

Acknowledgments

The authors thank Hana Mrazova and Romana Budovicova for technical and secretary assistance.

Author Contributions

Conceived and designed the experiments: LD MB PD. Performed the experiments: LD TP IH LP VB MB MT. Analyzed the data: LD TP IH LP VB MB MT PD. Contributed reagents/materials/analysis tools: LD PD. Wrote the paper: LD VB IH PD.

References

1. Peoples RW, Li C, Weight FF. Lipid vs protein theories of alcohol action in the nervous system. Annu Rev Pharmacol Toxicol. 1996; 36: 185–201. doi: 10.1146/annurev.pa.36.040196.001153 PMID: 8725387
2. Meyer HH. Zur theorie der alkoholnarkose. I. Mitt. welche eigenschaft der anästhetika bedingt ihre narkotische wirkung? Arch Exp Pathol Pharmakol. 1899; 42: 109–108.
3. Meyer KH. Contribution to the theory of narcosis. Trans Faraday Soc. 1937; 33: 1062–1068.
4. Chin JH, Goldstein DB. Effects of low concentrations of ethanol on the fluidity of spin-labeled erythrocyte and brain membranes. Mol Pharmacol. 1977; 13: 435–441. PMID: 876032
5. Chen SY, Yang B, Jacobson K, Sulik KK. The membrane disordering effect of ethanol on neural crest cells in vitro and the protective role of GM1 ganglioside. Alcohol. 1996; 13: 589–595. S0741832996000730. PMID: 8949954
6. Rowe ES. Thermodynamic reversibility of phase transitions. Specific effects of alcohols on phosphatidylcholines. Biochim Biophys Acta. 1985; 813: 321–330. PMID: 3970925
7. Gray E, Karslake J, Machta BB, Veatch SL. Liquid general anesthetics lower critical temperatures in plasma membrane vesicles. Biophys J. 2013; 105: 2751–2759. S0006-3495(13)01233-2. doi: 10.1016/j.bpj.2013.11.005 PMID: 24359747
8. Ly HV, Longo ML. The influence of short-chain alcohols on interfacial tension, mechanical properties, area/molecule, and permeability of fluid lipid bilayers. Biophys J. 2004; 87: 1013–1033. doi: 10.1529/biophysj.103.034280 PMID: 15298907
9. Seeman P. The membrane actions of anesthetics and tranquilizers. Pharmacol Rev. 1972; 24: 583–655. PMID: 4565956
10. Franks NP, Lieb WR. Molecular mechanisms of general anaesthesia. Nature. 1982; 300: 487–493. PMID: 6755267
11. Franks NP, Lieb WR. Partitioning of long-chain alcohols into lipid bilayers: implications for mechanisms of general anesthesia. Proc Natl Acad Sci U S A. 1986; 83: 5116–5120. PMID: 3460084
12. Ronald KM, Mirshahi T, Woodward JJ. Ethanol inhibition of N-methyl-D-aspartate receptors is reduced by site-directed mutagenesis of a transmembrane domain phenylalanine residue. J Biol Chem. 2001; 276: 44729–44735. doi: 10.1074/jbc.M102800200 PMID: 11572853
13. Ren H, Zhao Y, Dwyer DS, Peoples RW. Interactions among positions in the third and fourth membrane-associated domains at the intersubunit interface of the N-methyl-D-aspartate receptor forming sites of alcohol action. J Biol Chem. 2012; 287: 27302–27312. doi: 10.1074/jbc.M111.338921 PMID: 22715100
14. Borghese CM, Storustovu S, Ebert B, Herd MB, Belelli D, Lambert JJ, et al. The δ subunit of γ-aminobutyric acid type A receptors does not confer sensitivity to low concentrations of ethanol. J Pharmacol Exp Ther. 2006; 316: 1360–1368. doi: 10.1124/jpet.105.092452 PMID: 16272217
15. Brayton RG, Stokes PE, Schwartz MS, Louria DB. Effect of alcohol and various diseases on leukocyte mobilization, phagocytosis and intracellular bacterial killing. N Engl J Med. 1970; 282: 123–128. doi: 10.1056/NEJM197001152820303 PMID: 4982606
16. Gluckman SJ, MacGregor RR. Effect of acute alcohol intoxication on granulocyte mobilization and kinetics. Blood. 1978; 52: 551–559. PMID: 678671
17. Szabo G, Dolganiuc A, Dai Q, Pruett SB. TLR4, ethanol, and lipid rafts: a new mechanism of ethanol action with implications for other receptor-mediated effects. J Immunol. 2007; 178: 1243–1249. 178/3/1243. PMID: 17237368
18. Rimland D, Hand WL. The effect of ethanol on adherence and phagocytosis by rabbit alveolar macrophages. J Lab Clin Med. 1980; 95: 918–926. PMID: 7381298
19. Karavitis J, Murdoch EL, Deburghgraeve C, Ramirez L, Kovacs EJ. Ethanol suppresses phagosomal adhesion maturation, Rac activation, and subsequent actin polymerization during FcγR-mediated phagocytosis. Cell Immunol. 2012; 274: 61–71. doi: 10.1016/j.cellimm.2012.02.002 PMID: 22381996
20. Ghare S, Patil M, Hote P, Suttles J, McClain C, Barve S, et al. Ethanol inhibits lipid raft-mediated TCR signaling and IL-2 expression: potential mechanism of alcohol-induced immune suppression. Alcohol Clin Exp Res. 2011; 35: 1435–1444. doi: 10.1111/j.1530-0277.2011.01479.x PMID: 21463338
21. Pruett SB, Schwab C, Zheng Q, Fan R. Suppression of innate immunity by acute ethanol administration: a global perspective and a new mechanism beginning with inhibition of signaling through TLR3. J Immunol. 2004; 173: 2715–2724. 173/4/2715 [pii]. PMID: 15294990
22. Mandrekar P, Dolganiuc A, Bellerose G, Kodys K, Romics L, Nizamani R, et al. Acute alcohol inhibits the induction of nuclear regulatory factor κ B activation through CD14/toll-like receptor 4, interleukin-1, and tumor necrosis factor receptors: a common mechanism independent of inhibitory κ B α

degradation? Alcohol Clin Exp Res. 2002; 26: 1609–1614. doi: 10.1097/01.ALC.0000036926.46632.57 PMID: 12436048

23. Patel M, Keshavarzian A, Kottapalli V, Badie B, Winship D, Fields JZ. Human neutrophil functions are inhibited in vitro by clinically relevant ethanol concentrations. Alcohol Clin Exp Res. 1996; 20: 275–283. PMID: 8730218

24. Toivari M, Maki T, Suutarla S, Eklund KK. Ethanol inhibits IgE-induced degranulation and cytokine production in cultured mouse and human mast cells. Life Sci. 2000; 67: 2795–2806. S0024320500008638. PMID: 11105996

25. Kennedy RH, Pelletier JH, Tupper EJ, Hutchinson LM, Gosse JA. Estrogen mimetic 4-tert-octylphenol enhances IgE-mediated degranulation of RBL-2H3 mast cells. J Toxicol Environ Health A. 2012; 75: 1451–1455. doi: 10.1080/15287394.2012.722184 PMID: 23116450

26. Rivera J, Kinet J-P, Kim J, Pucillo C, Metzger H. Studies with a monoclonal antibody to the β subunit of the receptor with high affinity for immunoglobulin E. Mol Immunol. 1988; 25: 647–661. PMID: 2971137

27. Rudolph AK, Burrows PD, Wabl MR. Thirteen hybridomas secreting hapten-specific immunoglobulin E from mice with Ig^a or Ig^b heavy chain haplotype. Eur J Immunol. 1981; 11: 527–529. PMID: 6790293

28. Tolar P, Tumová M, Dráber P. New monoclonal antibodies recognizing the adaptor protein LAT. Folia Biol (Praha). 2001; 47: 215–217.

29. Dráberová L, Amoui M, Dráber P. Thy-1-mediated activation of rat mast cells: the role of Thy-1 membrane microdomains. Immunology. 1996; 87: 141–148. PMID: 8666426

30. Volná P, Lebduška P, Dráberová L, Šímová S, Heneberg P, Boubelík M, et al. Negative regulation of mast cell signaling and function by the adaptor LAB/NTAL. J Exp Med. 2004; 200: 1001–1013. PMID: 15477348

31. Kovárová M, Tolar P, Arudchandran R, Dráberová L, Rivera J, Dráber P. Structure-function analysis of Lyn kinase association with lipid rafts and initiation of early signaling events after Fcε receptor I aggregation. Mol Cell Biol. 2001; 21: 8318–8328. PMID: 11713268

32. Draberova L, Bugajev V, Potuckova L, Halova I, Bambouskova M, Polakovicova I, et al. Transmembrane adaptor protein PAG/CBP is involved in both positive and negative regulation of mast cell signaling. Mol Cell Biol. 2014; 34: 4285–4300. doi: 10.1128/MCB.00983-14 PMID: 25246632

33. DiVirgilio F, Steinberg TH, Swanson JA, Silverstein SC. Fura-2 secretion and sequestration in macrophages. A blocker of organic anion transport reveals that these processes occur via a membrane transport system for organic anions. J Immunol. 1988; 140: 915–920. PMID: 3339244

34. Carpenter AE, Jones TR, Lamprecht MR, Clarke C, Kang IH, Friman O, et al. CellProfiler: image analysis software for identifying and quantifying cell phenotypes. Genome Biol. 2006; 7: R100. doi: 10.1186/gb-2006-7-10-r100 PMID: 17076895

35. Christian AE, Haynes MP, Phillips MC, Rothblat GH. Use od cyclodextrins for manipulating cellular cholesterol content. J Lipid Res. 1997; 38: 2264–2272. PMID: 9392424

36. Li TK, Theorell H. Human liver alcohol dehydrogenase: inhibition by pyrazole and pyrazole analogs. Acta Chem Scand. 1969; 23: 892–902. PMID: 4308830

37. Setiawan I, Blanchard GJ. Ethanol-induced perturbations to planar lipid bilayer structures. J Phys Chem B. 2014; 118: 537–546. doi: 10.1021/jp410305m PMID: 24372563

38. Loftsson T, Magnusdottir A, Masson M, Sigurjonsdottir JF. Self-association and cyclodextrin solubilization of drugs. J Pharm Sci. 2002; 91: 2307–2316. doi: 10.1002/jps.10226 PMID: 12379916

39. Nishijo J, Moriyama S, Shiota S. Interactions of cholesterol with cyclodextrins in aqueous solution. Chem Pharm Bull (Tokyo). 2003; 51: 1253–1257.

40. Zidovetzki R, Levitan I. Use of cyclodextrins to manipulate plasma membrane cholesterol content: evidence, misconceptions and control strategies. Biochim Biophys Acta. 2007; 1768: 1311–1324. doi: 10.1016/j.bbamem.2007.03.026 PMID: 17493580

41. Grutzkau A, Smorodchenko A, Lippert U, Kirchhof L, Artuc M, Henz BM. LAMP-1 and LAMP-2, but not LAMP-3, are reliable markers for activation-induced secretion of human mast cells. Cytometry A. 2004; 61: 62–68. doi: 10.1002/cyto.a.20068 PMID: 15351990

42. Yeligar SM, Harris FL, Hart CM, Brown LA. Ethanol induces oxidative stress in alveolar macrophages via upregulation of NADPH oxidases. J Immunol. 2012; 188: 3648–3657. doi: 10.4049/jimmunol.1101278 PMID: 22412195

43. Kim MJ, Nepal S, Lee ES, Jeong TC, Kim SH, Park PH. Ethanol increases matrix metalloproteinase-12 expression via NADPH oxidase-dependent ROS production in macrophages. Toxicol Appl Pharmacol. 2013; 273: 77–89. doi: 10.1016/j.taap.2013.08.005 PMID: 23978445

44. Kim MJ, Nagy LE, Park PH. Globular adiponectin inhibits ethanol-induced reactive oxygen species production through modulation of NADPH oxidase in macrophages: involvement of liver kinase B1/AMP-

activated protein kinase pathway. Mol Pharmacol. 2014; 86: 284–296. doi: 10.1124/mol.114.093039 PMID: 24850909

45. Swindle EJ, Coleman JW, DeLeo FR, Metcalfe DD. FcεRI- and Fcγ receptor-mediated production of reactive oxygen species by mast cells is lipoxygenase- and cyclooxygenase-dependent and NADPH oxidase-independent. J Immunol. 2007; 179: 7059–7071. PMID: 17982097

46. Kuehn HS, Swindle EJ, Kim MS, Beaven MA, Metcalfe DD, Gilfillan AM. The phosphoinositide 3-kinase-dependent activation of Btk is required for optimal eicosanoid production and generation of reactive oxygen species in antigen-stimulated mast cells. J Immunol. 2008; 181: 7706–7712. 181/11/7706. PMID: 19017959

47. Kraft S, Kinet JP. New developments in FcεRI regulation, function and inhibition. Nat Rev Immunol. 2007; 7: 365–378. PMID: 17438574

48. Surviladze Z, Dráberová L, Kovárová M, Boubelík M, Dráber P. Differential sensitivity to acute cholesterol lowering of activation mediated via the high-affinity IgE receptor and Thy-1 glycoprotein. Eur J Immunol. 2001; 31: 1–10. PMID: 11169432

49. Dalton SR, Wiegert RL, Casey CA. Receptor-mediated endocytosis by the asialoglycoprotein receptor: effect of ethanol administration on endosomal distribution of receptor and ligand. Liver Int. 2003; 23: 484–491. PMID: 14986823

50. Methner DN, Mayfield RD. Ethanol alters endosomal recycling of human dopamine transporters. J Biol Chem. 2010; 285: 10310–10317. doi: 10.1074/jbc.M109.029561 PMID: 20133946

51. Pascual-Lucas M, Fernandez-Lizarbe S, Montesinos J, Guerri C. LPS or ethanol triggers clathrin- and rafts/caveolae-dependent endocytosis of TLR4 in cortical astrocytes. J Neurochem. 2014; 129: 448–462. doi: 10.1111/jnc.12639 PMID: 24345077

52. Fattakhova G, Masilamani M, Borrego F, Gilfillan AM, Metcalfe DD, Coligan JE. The high-affinity immunoglobulin-E receptor FcεRI is endocytosed by an AP-2/clathrin-independent, dynamin-dependent mechanism. Traffic. 2006; 7: 673–685. PMID: 16637889

53. Cleyrat C, Darehshouri A, Anderson KL, Page C, Lidke DS, Volkmann N, et al. The architectural relationship of components controlling mast cell endocytosis. J Cell Sci. 2013; 126: 4913–4925. doi: 10.1242/jcs.128876 PMID: 23986485

54. Nourissat P, Travert M, Chevanne M, Tekpli X, Rebillard A, Le Moigne-Muller G, et al. Ethanol induces oxidative stress in primary rat hepatocytes through the early involvement of lipid raft clustering. Hepatology. 2008; 47: 59–70. doi: 10.1002/hep.21958 PMID: 18038449

55. Heneberg P, Draberova L, Bambouskova M, Pompach P, Draber P. Down-regulation of protein tyrosine phosphatases activates an immune receptor in the absence of its translocation into lipid rafts. J Biol Chem. 2010; 285: 12787–12802. doi: 10.1074/jbc.M109.052555 PMID: 20157115

56. Bugajev V, Bambousková M, Dráberová L, Dráber P. What precedes the initial tyrosine phosphorylation of the high affinity IgE receptor in antigen-activated mast cell? FEBS Lett. 2010; 584: 4949–4955. doi: 10.1016/j.febslet.2010.08.045 PMID: 20828563

57. Tobin SJ, Cacao EE, Hong DW, Terenius L, Vukojevic V, Jovanovic-Talisman T. Nanoscale effects of ethanol and naltrexone on protein organization in the plasma membrane studied by photoactivated localization microscopy (PALM). PLoS One. 2014; 9: e87225. doi: 10.1371/journal.pone.0087225 PMID: 24503624

58. Furlow M, Diamond SL. Interplay between membrane cholesterol and ethanol differentially regulates neutrophil tether mechanics and rolling dynamics. Biorheology. 2011; 48: 49–64. doi: 10.3233/BIR-2011-0583 PMID: 21515936

59. Daragan VA, Voloshin AM, Chochina SV, Khazanovich TN, Wood WG, Avdulov NA, et al. Specific binding of ethanol to cholesterol in organic solvents. Biophys J. 2000; 79: 406–415. doi: 10.1016/S0006-3495(00)76302-8 PMID: 10866966

60. Salous AK, Ren H, Lamb KA, Hu XQ, Lipsky RH, Peoples RW. Differential actions of ethanol and trichloroethanol at sites in the M3 and M4 domains of the NMDA receptor GluN2A (NR2A) subunit. Br J Pharmacol. 2009; 158: 1395–1404. doi: 10.1111/j.1476-5381.2009.00397.x PMID: 19788495

61. Das J, Pany S, Rahman GM, Slater SJ. PKC ε has an alcohol-binding site in its second cysteine-rich regulatory domain. Biochem J. 2009; 421: 405–413. doi: 10.1042/BJ20082271 PMID: 19432558

62. Olsen RW, Li GD, Wallner M, Trudell JR, Bertaccini EJ, Lindahl E, et al. Structural models of ligand-gated ion channels: sites of action for anesthetics and ethanol. Alcohol Clin Exp Res. 2014; 38: 595–603. doi: 10.1111/acer.12283 PMID: 24164436

63. Polley A, Vemparala S. Partitioning of ethanol in multi-component membranes: effects on membrane structure. Chem Phys Lipids. 2013; 166: 1–11. doi: 10.1016/j.chemphyslip.2012.11.005 PMID: 23220048

64. Lisboa FA, Peng Z, Combs CA, Beaven MA. Phospholipase d promotes lipid microdomain-associated signaling events in mast cells. J Immunol. 2009; 183: 5104–5112. doi: 10.4049/jimmunol.0802728 PMID: 19794068

65. Jenkins GM, Frohman MA. Phospholipase D: a lipid centric review. Cell Mol Life Sci. 2005; 62: 2305–2316. doi: 10.1007/s00018-005-5195-z PMID: 16143829

66. Zhu M, Zou J, Li T, O'Brien SA, Zhang Y, Ogden S, et al. Differential Roles of Phospholipase D Proteins in FcεRI-Mediated Signaling and Mast Cell Function. J Immunol. 2015. doi: 10.4049/jimmunol.1500665

67. Zhou JS, Xing W, Friend DS, Austen KF, Katz HR. Mast cell deficiency in Kit(W-sh) mice does not impair antibody-mediated arthritis. J Exp Med. 2007; 204: 2797–2802. doi: 10.1084/jem.20071391 PMID: 17998392

68. Happel KI, Nelson S. Alcohol, immunosuppression, and the lung. Proc Am Thorac Soc. 2005; 2: 428–432. doi: 10.1513/pats.200507-065JS PMID: 16322595

69. Gluckman SJ, Dvorak VC, MacGregor RR. Host defenses during prolonged alcohol consumption in a controlled environment. Arch Intern Med. 1977; 137: 1539–1543. PMID: 921440

70. Szabo G, Chavan S, Mandrekar P, Catalano D. Acute alcohol consumption attenuates interleukin-8 (IL-8) and monocyte chemoattractant peptide-1 (MCP-1) induction in response to ex vivo stimulation. J Clin Immunol. 1999; 19: 67–76. PMID: 10080106

71. Boe DM, Nelson S, Zhang P, Bagby GJ. Acute ethanol intoxication suppresses lung chemokine production following infection with Streptococcus pneumoniae. J Infect Dis. 2001; 184: 1134–1142. doi: 10.1086/323661 PMID: 11598836

72. Dolganiuc A, Bakis G, Kodys K, Mandrekar P, Szabo G. Acute ethanol treatment modulates Toll-like receptor-4 association with lipid rafts. Alcohol Clin Exp Res. 2006; 30: 76–85. doi: 10.1111/j.1530-0277.2006.00003.x PMID: 16433734

73. Dai Q, Pruett SB. Ethanol suppresses LPS-induced Toll-like receptor 4 clustering, reorganization of the actin cytoskeleton, and associated TNF-α production. Alcohol Clin Exp Res. 2006; 30: 1436–1444. doi: 10.1111/j.1530-0277.2006.00172.x PMID: 16899048

74. Mandrekar P, Catalano D, Szabo G. Inhibition of lipopolysaccharide-mediated NFκB activation by ethanol in human monocytes. Int Immunol. 1999; 11: 1781–1790. PMID: 10545482

75. Bagasra O, Howeedy A, Dorio R, Kajdacsy-Balla A. Functional analysis of T-cell subsets in chronic experimental alcoholism. Immunology. 1987; 61: 63–69. PMID: 2953674

76. Glassman AB, Bennett CE, Randall CL. Effects of ethyl alcohol on human peripheral lymphocytes. Arch Pathol Lab Med. 1985; 109: 540–542. PMID: 3838884

77. Brodie C, Domenico J, Gelfand EW. Ethanol inhibits early events in T-lymphocyte activation. Clin Immunol Immunopathol. 1994; 70: 129–136. S0090122984710208 [pii]. PMID: 8299228

1.8 NEW REGULATORY ROLES OF GALECTIN-3 IN HIGH-AFFINITY IgE RECEPTOR SIGNALING

Mol Cell Biol. 36(9):1366-82, 2016

In this study we utilized RNAi-based HTS to identify new regulators of mast cell Ag-mediated activation via FcεRI. We selected 144 genes for screen and identified 15 potential regulators of mast cell degranulation. We chose Gal3 for detail functional analysis. Gal3 negatively regulated mast cell degranulation and cytokine expression. FcεRI signaling in cells with decreased expression of Gal3 was upregulated on the level of SYK kinase, suggesting involvement of Gal3 in early signaling upon FcεRI triggering. We found that Gal3 did not affect phosphorylation of FcεRI receptor subunits but regulated receptor ubiquitination and internalization. Next, Gal3 positively regulated adhesion and motility of mast cells on fibronectin, that is likely to be caused by Gal3-controled surface β1-integrin expression in non-activated and also in Ag-activated mast cells. By contrast Gal3 negatively regulated mast cell chemotaxis towards Ag that is at least by part caused by negative regulatory function of Gal3 in chemokine production.

AMERICAN SOCIETY FOR MICROBIOLOGY | Molecular and Cellular Biology

New Regulatory Roles of Galectin-3 in High-Affinity IgE Receptor Signaling

Monika Bambouskova,[a] Iva Polakovicova,[a] Ivana Halova,[a] Gautam Goel,[b,c] Lubica Draberova,[a] Viktor Bugajev,[a] Aivi Doan,[b,c] Pavol Utekal,[a] Agnes Gardet,[b,c] Ramnik J. Xavier,[b,c] Petr Draber[a]

Department of Signal Transduction, Institute of Molecular Genetics, Academy of Sciences of the Czech Republic, Prague, Czech Republic[a]; Center for Computational and Integrative Biology, Massachusetts General Hospital, Harvard Medical School, Boston, Massachusetts, USA[b]; Broad Institute of Harvard University and Massachusetts Institute of Technology, Cambridge, Massachusetts, USA[c]

Aggregation of the high-affinity receptor for IgE (FcεRI) in mast cells initiates activation events that lead to degranulation and release of inflammatory mediators. To better understand the signaling pathways and genes involved in mast cell activation, we developed a high-throughput mast cell degranulation assay suitable for RNA interference experiments using lentivirus-based short hairpin RNA (shRNA) delivery. We tested 432 shRNAs specific for 144 selected genes for effects on FcεRI-mediated mast cell degranulation and identified 15 potential regulators. In further studies, we focused on galectin-3 (Gal3), identified in this study as a negative regulator of mast cell degranulation. FcεRI-activated cells with Gal3 knockdown exhibited upregulated tyrosine phosphorylation of spleen tyrosine kinase and several other signal transduction molecules and enhanced calcium response. We show that Gal3 promotes internalization of IgE-FcεRI complexes; this may be related to our finding that Gal3 is a positive regulator of FcεRI ubiquitination. Furthermore, we found that Gal3 facilitates mast cell adhesion and motility on fibronectin but negatively regulates antigen-induced chemotaxis. The combined data indicate that Gal3 is involved in both positive and negative regulation of FcεRI-mediated signaling events in mast cells.

Mast cells are important immune cells involved in multiple biological processes (1, 2). Under pathological conditions, they are responsible for IgE-mediated hyperreactivity and participate in severe diseases, such as allergy and asthma (3). Antigen (Ag)-mediated mast cell activation leads to the release of secretory granules containing a variety of preformed mediators (e.g., histamine and proteases), *de novo* synthesis of cytokines and chemokines, and enhanced production of arachidonic acid metabolites (4, 5). The principal surface receptor involved in mast cell activation is the high-affinity receptor for IgE (FcεRI), which belongs to the family of multichain immune recognition receptors. FcεRI is a tetrameric complex formed by an IgE-binding α subunit, a signal-amplifying β subunit, and a homodimer of disulfide-linked γ subunits. Each FcεRI β and γ subunit contains one immunoreceptor tyrosine-based activation motif (ITAM), which, after tyrosine phosphorylation, serves as a docking site for other signaling molecules, such as the SRC family kinase LYN or spleen tyrosine kinase (SYK). These two enzymes, together with other kinases, then phosphorylate various adaptor proteins, including linker of activated T cells 1 (LAT1) and LAT2 (also known as non-T cell activation linker [NTAL]). These adaptors are involved in activation of phospholipase Cγ (PLCγ) and subsequent signal transduction events, leading to calcium response and degranulation (6). FcεRI signaling is a complex process that depends on the magnitude of receptor aggregation and a balance between positive and negative signals that determine the extent of the response (7, 8). Although signaling pathways leading to mast cell activation have been extensively studied in recent years, they are far from being completely understood.

In recent years, RNA interference (RNAi) technology has become an indispensable tool in the elucidation of protein functions. RNAi-based high-throughput screening techniques have contributed significantly to identification of signal transduction pathway components in multiple systems (9–12). In this study, we took advantage of a lentiviral delivery method to transduce otherwise minimally transfectable mast cells and to induce knockdown (KD) of selected genes. We developed a short hairpin RNA (shRNA)-based high-throughput screening system to identify new regulators of FcεRI signaling and tested 432 shRNAs specific for 144 selected genes for their effects on FcεRI-mediated mast cell degranulation. Using this method, we identified 11 negative and 4 positive potential regulators of mast cell degranulation. Detailed analysis of one such regulator, galectin-3 (Gal3), revealed previously unrecognized functions of Gal3 in FcεRI signaling.

MATERIALS AND METHODS

Antibodies and reagents. The following antibodies and their conjugates were used: mouse IgE monoclonal antibody (MAb) specific for 2,4,6-trinitrophenol (TNP), clone IGEL b4 1 (13), SYK-specific MAb (14), rabbit anti-IgE (15), FcεRI β subunit-specific MAb (JRK) (16), mouse IgE MAb specific for dinitrophenol (DNP) clone SPE-7 (Sigma-Aldrich), rat anti-KIT–allophycocyanin conjugate (17-1171) and hamster anti-FcεRI-α–fluorescein isothiocyanate (FITC) conjugate (eBioscience; 11-5898), rabbit anti-pSYK (2710) and mouse anti-phosphorylated c-Jun N-terminal kinase (anti-pJNK) (Cell Signaling; 9255S), rabbit anti-GRB2 (sc-255), actin (sc-8432), pAKT (sc-7985), extracellular signal-regulated kinase (ERK) (sc-93), pERK (sc-7976), CBL (sc-170), pCBL (sc-26140),

Received 26 January 2016 **Accepted** 16 February 2016

Accepted manuscript posted online 29 February 2016

Citation Bambouskova M, Polakovicova I, Halova I, Goel G, Draberova L, Bugajev V, Doan A, Utekal P, Gardet A, Xavier RJ, Draber P. 2016. New regulatory roles of galectin-3 in high-affinity IgE receptor signaling. Mol Cell Biol 36:1366–1382. doi:10.1128/MCB.00064-16.

Address correspondence to Petr Draber, draberpe@img.cas.cz.

Supplemental material for this article may be found at http://dx.doi.org/10.1128/MCB.00064-16.

pPLCγ1 (sc-12943), JNK1 (sc-571), Gal3 (sc-20157), galectin-1 (Gal1) (sc-28248), PLCγ1 (sc-81), goat anti-AKT1 (sc-1618), rat MAb specific for lysosomal-associated protein 1 (LAMP1) (sc-19992), horseradish peroxidase (HRP)-conjugated goat anti-mouse IgG, goat anti-rabbit IgG, and donkey anti-goat IgG (Santa Cruz Biotechnology), phosphotyrosine-specific MAb PY-20–HRP conjugate (610012), rabbit antiphosphotyrosine (anti-pY) (610010), and V450-conjugated rat anti-mouse LAMP1 (560648) (BD Biosciences), mouse MAb specific for ubiquitinated proteins (FK2 clone; Affinity Research Products; PW8810), anti-β1-integrin antibodies (HM β1-1 and 9EG7; BD Pharmingen), secondary antibodies anti-rabbit, anti-mouse, and anti-rat IgG conjugated to Alexa Fluor 488 (AF488) or AF568 (Invitrogen), AF488-conjugated anti-hamster IgG (Life Technologies), Fcγ-specific anti-rat IgG (Jackson ImmunoResearch Laboratories), and Fura-2 AM- and AF488-conjugated phalloidin (Life Technologies). TNP-bovine serum albumin (BSA) conjugate (15 to 25 mol TNP/mol BSA) was produced as described previously (17). Mouse recombinant Gal3 was obtained from R&D Systems. DNP-human serum albumin (HSA) conjugate (30 to 40 mol DNP/mol HSA) and all other reagents were obtained from Sigma-Aldrich if not otherwise specified.

Mice, cells, and lentiviral transduction. Mouse bone marrow mast cells (BMMCs) were derived from femurs and tibias of 8- to 10-week-old BALB/c mice bred, maintained, and used in accordance with the Institute of Molecular Genetics guidelines (permit number 12135/2010-17210) and national guidelines (2048/2004-1020). The cells were cultured in RPMI 1640 medium supplemented with 100 U/ml penicillin, 100 μg/ml streptomycin, 71 μM 2-mercaptoethanol, minimum essential medium (MEM) nonessential amino acids, 0.7 mM sodium pyruvate, 2.5 mM L-glutamine, 12 mM D-glucose, recombinant mouse stem cell factor (SCF) (15 ng/ml; PeproTech EC), mouse recombinant interleukin 3 (IL-3) (20 ng/ml; PeproTech EC), and 10% fetal calf serum (FCS). A stable cell line derived from BMMCs (BMMCL [18]) was donated by M. Hibbs (Ludwig Institute for Cancer Research, Melbourne, Australia) (19). The cells exhibited strong Ca^{2+} (15) and degranulation (18) response after activation by Ag. The cells were cultured in medium as described above but in the absence of SCF. Lentiviruses for infections were prepared by mixing 1.5-ml aliquots of Opti-MEM medium (Invitrogen) with 21 μl of ViraPower Lentiviral Packaging Mix (Invitrogen), 14 μg of lentiviral construct, and 105 μl of polyethylenimine (1 mg/ml; 25 kDa; linear form; Polysciences). The mixture was incubated for 20 min at room temperature before it was added to HEK-293FT packaging cells in medium for cultivation of BMMCs in a 150-cm^2 tissue culture flask. Forty-eight hours later, virus-containing medium was filtered through 45-μm-pore-size nitrocellulose filters (Merck Millipore) and used directly for BMMC infection in the presence of 1 μg/ml protamine. The next day, the cells were subjected to the new virus load. Two days later, the cells were transferred to fresh medium containing 3 μg/ml puromycin (Apollo Scientific) for selection of positive transductants. A set of murine shRNAs targeting *Lgals3* cloned into the pLKO.1 or pLKO_TRC005 vector (TRCN0000301479 [shRNA_1], TRCN0000054863 [shRNA_2], TRCN0000054867 [shRNA_3], TRCN0000301547 [shRNA_4], and TRCN0000301480 [shRNA_5]) was purchased from the RNAi Consortium (Broad Institute, Cambridge, MA). The cells were transduced with individual shRNAs or with a pool of shRNAs prepared by mixing shRNA_1, shRNA_2, shRNA_3, and shRNA_5, in equimolar ratios to obtain 14 μg of constructs transfected into packaging cells. The pool of shRNAs gave results similar to those with individual shRNAs but allowed us to scale up the experiments. Therefore, most of the pilot experiments were performed with individual shRNAs and confirmed with cells transduced with the shRNA pool.

Degranulation and Ca^{2+} response. BMMCs were sensitized with TNP-specific IgE (1 μg/ml) in SCF- and IL-3-free culture medium for 16 h. The cells were then washed in buffered saline solution (BSS) (135 mM NaCl, 5 mM KCl, 1.8 mM $CaCl_2$, 5.6 mM glucose, 20 mM HEPES, pH 7.4) supplemented with 0.1% BSA (BSSA) and activated with Ag (TNP-BSA). The extent of degranulation was evaluated by determining the concentration of β-glucuronidase, as previously described (20). An Infinite 200M (Tecan) plate reader at 355-nm excitation and 460-nm emission wavelengths was used. In some experiments, cells were pretreated with lactose for 30 min prior to activation; lactose was also present during the activation. Alternatively, cells were incubated with recombinant Gal3 for 30 min prior to activation. For analysis of calcium response, cells were loaded with Fura-2 AM as described previously (20). Kinetic measurements of intracellular Ca^{2+} were determined by spectrofluorometry using an Infinite 200M plate reader with excitation wavelengths at 340 and 380 nm and with constant emission at 510 nm.

shRNA screening and high-throughput degranulation assay. Genes for RNAi screening were selected on the basis of their expression in mast cells, as determined by microarray gene expression profiling using an Affymetrix Gene Titan HT MG-430 PM 24-array plate, as previously described (21), and/or a BioGPS gene portal (http://biogps.org/), together with estimated functions of their products in early signaling events/calcium signaling, cytoskeleton dynamics, cell adhesion/migration, and/or other plasma membrane functions (see Table S1 in the supplemental material). The lentivirus-based shRNA library containing 432 shRNA sequences specific for 144 genes was obtained from the RNAi Consortium (see Table S1 in the supplemental material). For shRNA screening in BMMCL, the following protocol was established. Cells were cultured in Iscove's modified Dulbecco's medium supplemented with mouse recombinant IL-3 (30 ng/ml) and 10% FCS. Each plate with samples contained in-plate negative-control shRNAs targeting irrelevant sequences, green fluorescent protein (GFP) (TRCN0000072181 and TRCN0000072186) or red fluorescent protein (RFP) (TRCN0000072212 and TRCN0000072209), and positive-control shRNAs targeting STIM1 (shRNA_5; TRCN0000175139) or SYK (shRNA_3; TRCN0000234763). Rows containing in-plate negative and positive controls were shuffled in different plates to minimize potential edge effects. On day 1, cells were seeded in 96-well flat-bottom plates (5×10^5 per well) and transduced with lentiviruses at a multiplicity of infection (MOI) of 15 in medium supplemented with Polybrene at the optimal concentration of 8 μg/ml. The plates were centrifuged at 830 × *g* for 1 h and then incubated for 16 h at 37°C. On day 2, the medium containing viruses was changed for fresh medium, and on day 4, fresh medium supplemented with puromycin (5 μg/ml) was added. The medium containing puromycin was replenished every 3 days. The β-glucuronidase assay was performed more than 14 days after the start of puromycin selection. Before the assay, puromycin was removed for 24 h, and the cells were sensitized for 4 h with DNP-specific IgE (1 μg/ml) in medium depleted of IL-3. The cells (approximately 10^5) were then washed in BSSA and split into two parts for analysis of nonactivated and Ag-activated samples (25 μl of cell suspension per well). Activation was triggered by addition of 25 μl of Ag (DNP-HSA; 10 ng/ml final concentration). This relatively low concentration of Ag allowed us to score both positive and negative regulatory hits. The cells were activated for 30 min at 37°C, and β-glucuronidase released from the cells was determined in 20 μl of cell supernatants by mixing with 28 μl of 4-methylumberylliferyl-β-D-glucuronide substrate (Invitrogen), 50 μM final concentration. The cell pellets were then lysed by the addition of 20 μl Triton X-100 at a final concentration of 1% in BSSA to each well and incubated at 37°C for 30 min. The total β-glucuronidase content was analyzed in 20 μl of cell lysate as described above, with the exception that a SpectraMax Gemini reader (Molecular Devices) was used. Degranulation was enumerated as the percentage of the β-glucuronidase activity in the supernatant from the total β-glucuronidase activity in the supernatant and lysate. Transduced cells were assayed to obtain a minimum of 3 replicates meeting quality control criteria for data analysis. Data were collected from two independent lentiviral transductions (runs). The extent of gene expression knockdown was analyzed in cells transduced in the second screen run using reverse transcription-quantitative PCR (RT-qPCR).

shRNA screen data analysis. Data collected from degranulation assays were filtered using the following quality control criteria for each well: (i) β-glucuronidase activity detected in the well was above the measure-

ment noise level (>10,000 relative fluorescence units [RFU]) and (ii) the β-glucuronidase released from nonactivated cells was less than 30% of the mean β-glucuronidase release from activated in-plate negative controls. Subsequently, the data from each well were Z-normalized to the mean degranulation of activated in-plate negative controls and are shown as a degranulation ratio. As a quality control for each plate, the following criteria were used: (i) the mean degranulation of activated in-plate negative controls reached at least 18% and (ii) the degranulation of activated in-plate SYK positive controls showed at least 1.5 times the standard deviation (SD) (on a Z-normalized scale) difference from the mean degranulation of activated in-plate negative controls. The Z-score for each shRNA was determined using the mean degranulation and SD of activated in-plate negative controls, and average Z-scores were calculated using all the replicates in each run. The statistical significance of differences in shRNA Z-scores versus the Z-score of negative controls was computed using a Mann-Whitney test. To limit potential false-negative results from the assay that showed significant variability ($Z' = 0.37$), we evaluated the effects of shRNAs in two independent runs. Based on this evaluation, we selected the shRNAs with average Z-scores greater than ±1 and reproducible effects with P values of <0.05 across two runs; we also accepted P values of <0.075 across two runs with at least one P value of <0.05 to define shRNA hits. shRNAs with effects with opposite directionalities were excluded from the list of potential mast cell regulators.

RNA isolation and RT-qPCR. RNA was isolated using an RNeasy minikit (Qiagen) when single samples were isolated. For RNA isolation from 96-well plates, a Macherey-Nagel kit for 96-well extraction was used according to the manufacturer's instructions. RNA was reverse transcribed using either an iScript cDNA synthesis kit (Bio-Rad) or Moloney murine leukemia virus (MMLV) reverse transcriptase (Invitrogen) according to the manufacturer's protocol. RT-qPCRs were performed in 384-well plates using a PCR mastermix supplemented with 0.2 M trehalose, 1 M 1,2-propanediol, and SYBR green I as described previously (22). RT-qPCRs were performed in a LightCycler 480 (Roche Diagnostics). All assays were performed at least in duplicate, and reaction mixtures in 10-μl volumes were processed under the following cycling conditions: initial 3-min denaturation at 95°C, followed by 50 cycles at 95°C for 10 s, 60°C for 20 s, and 72°C for 20 s. A melting-curve analysis was carried out from 72°C to 97°C with 0.2°C increments; threshold cycle (C_T) values for each sample were determined by automated threshold analysis. Data from shRNA-transduced cells from the RNAi screen were normalized to glyceraldehyde-3-phosphate dehydrogenase (GAPDH) mRNA levels of negative controls present in each 96-well plate with the transduced cells. Primer pairs specific for positive controls and hits in the screen are listed in Table S2 in the supplemental material. For analysis of cytokine and chemokine mRNAs, cells were not activated or activated with Ag (TNP-BSA; 100 ng/ml; 1 h). Genes for GAPDH, actin, and ubiquitin were used as reference genes, and the expression levels of all mRNAs were normalized to the geometric mean of the expression of the reference genes. The relative increase in the expression level of a cytokine was normalized to the level of expression by nonactivated pLKO.1 control cells in each experiment. Primer pairs used for analysis of cytokine and chemokine mRNAs have been listed elsewhere (20).

Cloning and mast cell transfection. For experiments with transient Gal3 overexpression, a plasmid encoding human Gal3 (hGal3) (23), kindly provided by F.-T. Liu (University of California, Davis, CA), was used for amplification of hGal3 sequence using the forward primer 5′-aa agaattcgccaccATGGCAGACAATTTTTCGCT -3′ (the EcoRI restriction site is underlined, and the coding sequence is in uppercase) and the reverse primer 5′-tttggatccttTATCATGGTATATGAAGCAC-3′ (the BamHI restriction site is underlined, and the coding sequence is in uppercase). The amplified DNA was cloned, using EcoRI and BamHI restriction sites, into a pEGFP-N1 expression vector (Clontech Laboratories Inc.; 6085-1). Mouse Gal3 (mGal3) was obtained by PCR amplification from cDNA produced as described above and cloned into the pCDH-CMV-MCS-EF1-Puro (Systembio; pCDH) lentiviral expression vector using NheI and NotI restriction sites. For PCR, the following primers were used: 5′-aaaaagctagcgccaccATGGCAGACAGCTTTTCGCT-3′ (forward; the NheI restriction site is underlined) and 5′-tttttgcggccgcTTAGATCATGG CGTGGTTAG-3′ (reverse; the NotI restriction site is underlined). All the constructs were verified by DNA sequencing. A plasmid with hGal3 was introduced into BMMCs by Amaxa nucleofection according to the manufacturer's instructions. A plasmid with mGal3 was used for production of lentiviruses as described above and introduced into the cells by lentiviral transduction followed by puromycin selection.

PGD_2 production. IgE-sensitized BMMCs were seeded at 2×10^5 cells per well in 100 μl of BSSA in 96-well flat-bottom culture plates. The cells were activated with Ag (TNP-BSA; 100 ng/ml; 25 min). Cell-free supernatants were collected and assessed for prostaglandin D_2 (PGD_2) using a competitive enzyme immunoassay according to the manufacturer's instructions (Cayman Chemicals). To be read within the range of the respective standard curves, supernatants of nonactivated and activated cells were diluted 1/10 and 1/40, respectively.

Immunoblotting and immunoprecipitation. Whole-cell extracts from nonactivated or Ag (TNP-BSA)-activated cells were prepared by solubilizing pelleted cells in sodium dodecyl sulfate (SDS) sample buffer (24), followed by sonication and denaturation of samples at 97°C for 5 min. Proteins were size fractionated by SDS-polyacrylamide gel electrophoresis (PAGE), electrophoretically transferred onto nitrocellulose, and analyzed by immunoblotting with protein- or phosphoprotein-specific antibodies. For FcεRI immunoprecipitation, cells were pelleted and solubilized in ice-cold lysis buffer containing 25 mM Tris-HCl, pH 8.0, 140 mM NaCl, 1 mM Na_3VO_4, 2 mM EDTA, 100-fold-diluted protease inhibitor cocktail (Sigma-Aldrich; P8340), 1 mM phenylmethylsulfonyl fluoride, and 0.2% Triton X-100. After 30 min incubation on ice, the lysates were spun down (16,000 × *g*; 5 min; 4°C), and IgE complexes in postnuclear supernatants were immunoprecipitated with rabbit anti-IgE antibody prebound to UltraLink-immobilized protein A (Thermo Scientific). Immunoprecipitates were size fractionated as described above and immunoblotted with phosphotyrosine-specific PY-20–HRP conjugate or with antibody specific for ubiquitinated proteins. Bound primary antibodies were detected with HRP-conjugated secondary antibodies. HRP signal was detected with chemiluminescence reagent (25) and quantified with a luminescent image analyzer (LAS 3000; Fuji Photo Film). Aida software (Raytest GmbH) was used for signal quantification.

Flow cytometry analysis. To analyze surface levels of FcεRI and KIT receptor, labeling was performed as described previously (20). For analysis of internalized IgE, IgE-sensitized BMMCs were activated or not with different concentrations of Ag (TNP-BSA) for various times at 37°C. Activation was stopped by centrifugation at 4°C (300 × *g*; 4 min), and samples were split into two; one half was subjected to acid stripping by a 10-min incubation in 0.5 M NaCl and 0.2 M acetic acid (pH 2.7) on ice to remove surface-accessible IgE, as previously described (26). All the samples were then fixed for 20 min in 2% paraformaldehyde, washed in PBS, and then permeabilized in 0.05% Triton X-100 for 10 min. IgE was stained using AF-conjugated anti-mouse Ig (cross-reacting with IgE) in PBS-1% BSA. After labeling, the cells were washed 3 times with PBS and analyzed with an LSRII flow cytometer (BD Biosciences). Median fluorescence intensities were determined and further processed using FlowJo software (TreeStar, Ashland, OR). To quantify surface expression of β1-integrin and its activated epitope 9EG7, BMMCs were activated or not with Ag (TNP-BSA; 100 ng/ml; 3 min). The cells were then exposed to the anti-β1-integrin antibody HM β1-1 or 9EG7 for 30 min on ice, followed by a 30-min incubation with the corresponding AF488-conjugated anti-hamster or anti-rat (Fcγ-specific) secondary antibody, respectively. After 30 min of incubation on ice, the cells were washed in ice-cold PBS and analyzed as described above. For analysis of surface LAMP1, BMMCs were activated or not with various concentrations of Ag (TNP-BSA; 10 min; 37°C). Activation was stopped by centrifugation at 4°C. The cells were then resuspended in 50 μl of PBS-1% BSA containing 200-fold-diluted

V450-conjugated rat anti-mouse LAMP1 and stained on ice for 30 min. After washing with PBS, the cells were analyzed as described above.

Confocal microscopy. Eight-well multitest microscopy slides (MP Biomedicals) were coated with CellTak (8 μl in 1 ml of PBS; BD Biosciences). The cells were left to attach to coated slides for 15 min in BSSA and then activated with Ag (TNP-BSA; 100 ng/ml; 37°C). After activation, the cells were fixed with 3% paraformaldehyde in PBS for 30 min and permeabilized with 0.1% Triton X-100 for 30 min. After washing with PBS, free binding sites were blocked with 1% BSA and subsequently labeled with specific antibodies, followed by AF-conjugated secondary antibodies. IgE was detected with AF-conjugated donkey anti-mouse Ig-specific antibody. After labeling, the cells were washed and mounted in 50% (wt/vol) glycerol in PBS, pH 8.5, supplemented with 0.1% p-phenylenediamine and 1 μg/ml Hoechst 33258 to label nuclei. For F-actin staining, cells were permeabilized with L-α-lysophosphatidylcholine (80 μg/ml) and simultaneously labeled with 10 μg/ml of AF488-conjugated phalloidin for 1 h in PBS-1% BSA. Samples were examined with a confocal laser scanning microscope (Leica TCS SP5) equipped with a 63× (numerical aperture, 1.4) oil immersion objective. In each experiment, images were acquired at identical microscope settings. Image analyses were performed using a pipeline generated in CellProfiler cell image analysis software (Broad Institute, Cambridge, MA) (27). For examination of protein distribution, 20 to 40 cells were identified using nuclei, and signals from fluorescently labeled proteins were segmented into 4 concentric rings centered on the nucleus. The fluorescent intensity of each cell was determined, and the fraction of the fluorescence in 3 inner rings (cytoplasmic) was calculated.

Cell adhesion, motility, and chemotaxis. IgE-sensitized BMMCs were loaded with calcein-AM and transferred into wells of a 96-well plate (Thermo Scientific) coated with fibronectin at a concentration of 10 μg/ml (28). After activation with Ag (TNP-BSA; 100 ng/ml; 30 min), unbound cells were washed out using a microplate washer (HydroSpeed; Tecan), and bound cells were determined using an Infinite 200M fluorometer with excitation and emission filters at 485 nm and 538 nm, respectively. Analysis of cell motility on fibronectin after activation with PGE_2 was performed as described previously (29). Ag (TNP-BSA; 250 ng/ml)- or PGE_2 (100 nM)-mediated chemotactic responses were evaluated using 24-well Transwell chambers (Corning) with 8-μm polycarbonate filters, as described previously (28). Cells migrating into lower compartments within the 8-h incubation period were counted using an Accuri C6 flow cytometer (Becton Dickinson). Cell migration toward PGE_2 (100 ng/ml) was performed in the same way, except that the cells were not sensitized with IgE. In some experiments, the supernatants from IgE-sensitized and Ag-activated (TNP-BSA; 100 ng/ml; 6 h) BMMCs at a concentration of 2×10^6/ml were used as a source of chemoattractants for unsensitized cells.

Data analysis. All experiments were repeated independently as indicated in the figure legends. Averages or representative results from all repeats are shown. Unless otherwise indicated, the significance of intergroup differences was evaluated by Student's *t* test.

RESULTS

Search for new regulators of FcεRI signaling using an RNAi-based high-throughput degranulation assay. To identify new regulators of FcεRI signaling, we developed an shRNA high-throughput mast cell degranulation assay using BMMCL. The cells were transduced with shRNA lentiviruses, followed by puromycin selection (Fig. 1A). Our optimized protocol included infection of the cells at an MOI of 15 in the presence of Polybrene at 8 μg/ml. Two weeks after selection, the cells were sensitized with Ag-specific IgE and activated with Ag, and the amount of β-glucuronidase released from preformed secretory granules was assessed by enzymatic assay (Fig. 1B). shRNAs targeting GFP and RFP were used as negative controls, and shRNAs targeting STIM1 and SYK were used as positive controls. STIM1 shRNAs led to 50 to 80% knockdown efficiency and up to a 5-fold decrease in degranulation, and SYK shRNAs led to more than 70% knockdown of gene expression and up to a 5-fold decrease in degranulation (Fig. 1C and D). Notably, the STIM1 shRNAs that had smaller effects on STIM1 expression levels also had poorer effects on mast cell degranulation. SYK shRNAs were used to calculate the Z′ factor as 0.37, which is considered acceptable for screening for RNAi cell-based assays (30).

For screening, we selected 144 genes that are expressed in mast cells and could be involved in FcεRI signaling. The list included genes with potential roles in early signaling events/calcium signaling, cytoskeleton dynamics, cell adhesion/migration, and/or other plasma membrane functions. As shown in Table S1 in the supplemental material, we tested 432 lentivirus-encoded shRNAs, with 3 different shRNAs targeting each gene. As the Z′ factor of the assay did not pass the 0.5 threshold to be considered an excellent screening assay, we collected data from two independent transduction runs. In each run, we collected at least 3 degranulation assays that passed quality control criteria (see Materials and Methods) to increase confidence in the identification of potential mast cell regulators. To limit potential false-negative results from the assay that showed significant variability (Z′ factor = 0.37), we used a *P* value of <0.05 (Mann-Whitney test) across two runs, and we also accepted a *P* value of <0.075 across two runs with at least one *P* value of <0.05 for shRNAs with an average Z-score greater than ± 1. To limit potential false-positive results, the effect of each shRNA had to pass statistical significance using the above *P* values in the two independent runs. Using these criteria, we identified potential regulators with consistent effects on shRNA levels on mast cell degranulation: 10 hits using a *P* value of <0.05 across two runs and 5 hits using a *P* value of <0.075 across two runs with at least one *P* value of <0.05. Data collection and the subsequent processes of quality control and hit calling are summarized in Fig. 1E. Average Z-scores and average degranulation ratios calculated for all shRNAs in both screen runs, together with an analysis of gene expression of the identified hits from the second run, are shown in Table S1 in the supplemental material. Among 15 potential regulators, 11 were negative regulators and 4 were positive regulators of cell degranulation (Table 1). The effects of all shRNAs on degranulation in the second screen run are shown in Fig. 1F. Among the negative regulatory genes, the KD of the *Lgals3* gene, encoding Gal3, increased cell degranulation in all 3 tested shRNAs, displaying 1.67 ± 0.03-fold change in mast cell degranulation ($P < 0.05$). This was a surprising finding, because previous studies using BMMCs from mice with Gal3 knockout (KO) suggested that Gal3 is a positive regulator of mast cell degranulation (31). We therefore focused on deciphering the mechanism of the negative regulatory role of Gal3 in mast cell activation.

Negative regulatory role of Gal3 in FcεRI-mediated mast cell degranulation, cytokine expression, and PGD_2 production. To confirm the negative regulatory role of Gal3 in mast cell degranulation, we expanded the number of shRNAs and analyzed their effects on Gal3 expression (Fig. 2A and B) and degranulation (Fig. 2C) in BMMCL. The results were compared to those obtained with cells transduced with an empty vector (pLKO.1). The data obtained showed that inhibition of degranulation was mediated by different shRNAs targeting Gal3. Next, we transduced BMMCs with individual shRNAs or pooled shRNA_1, shRNA_2, shRNA_3, and shRNA_5. Because of the similarity of the data obtained with these two approaches, we pooled the data and la-

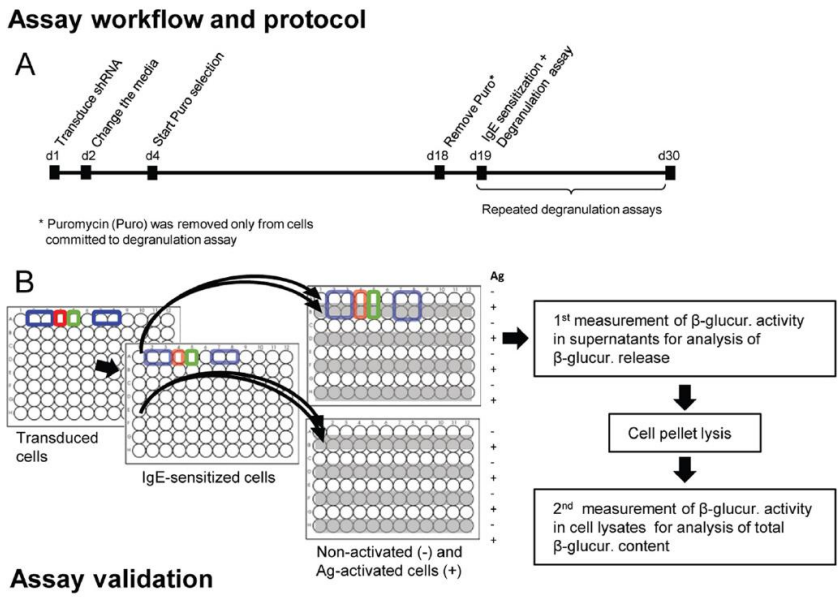
Assay workflow and protocol
A
Transduce shRNA
Change the media
Start Puro selection
Remove Puro*
IgE sensitization +
Degranulation assay
d1
d2
d4
d18
d19
d30
Repeated degranulation assays
* Puromycin (Puro) was removed only from cells committed to degranulation assay
B
Ag
Transduced cells
IgE-sensitized cells
Non-activated (-) and Ag-activated cells (+)
1st measurement of β-glucur. activity in supernatants for analysis of β-glucur. release
Cell pellet lysis
2nd measurement of β-glucur. activity in cell lysates for analysis of total β-glucur. content

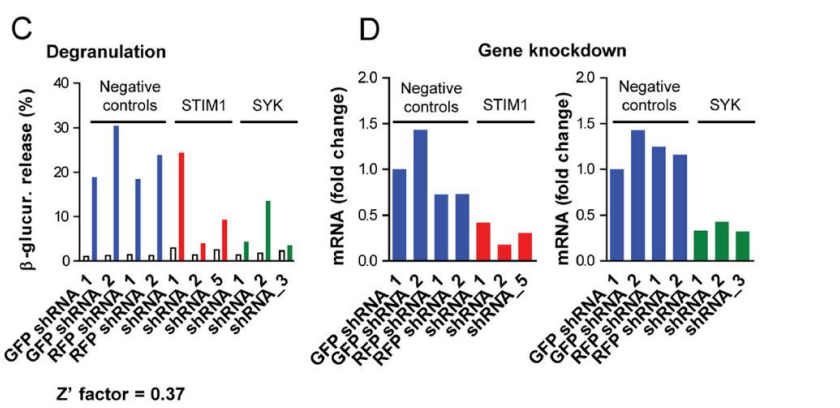
Assay validation
C
Degranulation
β-glucur. release (%)
Negative controls
STIM1
SYK
GFP shRNA 1
GFP shRNA 2
RFP shRNA 1
RFP shRNA 2
shRNA 1
shRNA 2
shRNA_5
shRNA 1
shRNA 2
shRNA_3
D
Gene knockdown
mRNA (fold change)
Negative controls
STIM1
SYK
Z' factor = 0.37

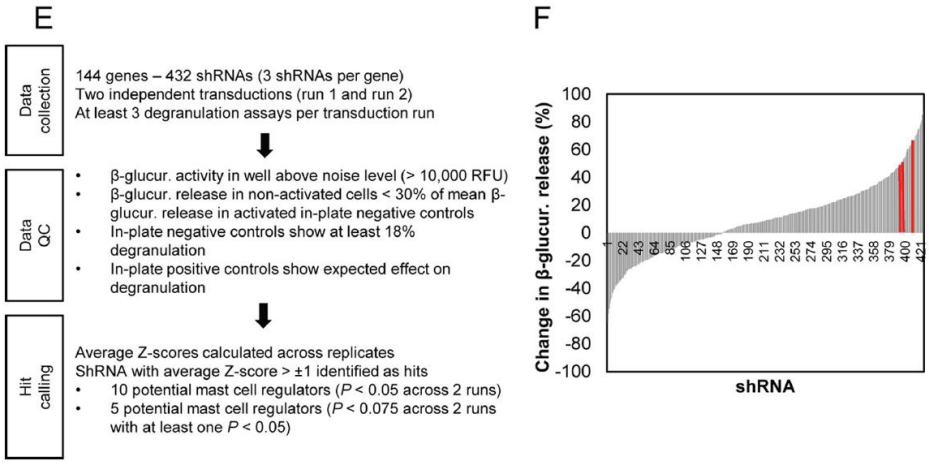
Data collection and hit calling workflow
E
Data collection
144 genes – 432 shRNAs (3 shRNAs per gene)
Two independent transductions (run 1 and run 2)
At least 3 degranulation assays per transduction run
Data QC
β-glucur. activity in well above noise level (> 10,000 RFU)
β-glucur. release in non-activated cells < 30% of mean β-glucur. release in activated in-plate negative controls
In-plate negative controls show at least 18% degranulation
In-plate positive controls show expected effect on degranulation
Hit calling
Average Z-scores calculated across replicates
ShRNA with average Z-score > ±1 identified as hits
10 potential mast cell regulators (P < 0.05 across 2 runs)
5 potential mast cell regulators (P < 0.075 across 2 runs with at least one P < 0.05)
F
Change in β-glucur. release (%)
shRNA

TABLE 1 Potential regulators of mast cell degranulation identified in shRNA screening in mast cells

Symbol	NCBI gene ID	GenBank accession no.	Official full name	Fold change in degranulation (mean ± SD)[a]
Negative regulators				
Adora2b	11541	NM_007413.2	Adenosine A2b receptor	1.75 ± 0.76
Basp1	70350	NM_027395.1	Brain acid-soluble protein 1	1.4 ± 0.36
Cyfip2	76884	NM_133769.1	Cytoplasmic FMR1-interacting protein 2	1.26 ± 0.19
Diap1	13367	NM_007858.2	Diaphanous homolog 1	1.65 ± 0.42
Lgals3	16854	NM_010705.3	Lectin, galactose binding, soluble 3	1.67 ± 0.03
Lpxn	107321	NM_134152.1	Leupaxin	1.38 ± 0.35
Mctp1	78771	XM_127419.3	Multiple C2 domains, transmembrane 1	1.6 ± 0.36
Plscr1	22038	NM_011636.2	Phospholipid scramblase 1	1.65 ± 0.32
S100a10	20194	NM_009112.2	S100 calcium binding protein A10	1.52 ± 0.27
Spn	20737	NM_009259.3	Sialophorin	1.33 ± 0.07
Tjp1	21872	NM_009386.1	Tight-junction protein 1	1.27 ± 0.06
Positive regulators				
Add2	11519	NM_013458.2	Adducing 2 (beta)	0.67 ± 0.1
Coro7	78885	NM_030205.2	Coronin 7	0.46 ± 0.18
Dock8	76088	NM_028785.3	Dedicator of cytokinesis 8	0.52 ± 0.27
Ier2	15936	NM_010499.4	Immediate-early response 2	0.42 ± 0.17

[a] Most effective shRNAs for each gene across both runs ($P < 0.05$). The following genes had nonsignificant or inconsistent effects on mast cell degranulation: genes encoding Adcy7, Adora3, Ahnak, Akap2, Alox5ap, Arap3, Arhgdia, Arhgdib, Arhgef1, Avil, Bcap31, Bsg, Cab39, Cd151, Cd200r1, Cd200r3, Cd200r4, Cd244, Cd274, Cd276, Cd300a, Cd300lb, Cd93, Cd96, Cd97, Cd99, Cdc42, Cdh2, Cfl1, Coro1a, Cotl1, Csk, Cyfip1, Cytip, Darc, Dock10, Dock11, Dstn, Dusp19, Efhd1, Efhd2, Enah, Fcer1a, Fcer1g, Fermt3, Fert2, Fgfr1op2, Frmd4a, Git2, Gng5, Gp1ba, Gp49a, Gpr34, Grb2, Ier3, Ifitm1, Ifitm2, Inpp5b, Inpp5d, Itgb7, Kcnn4, Kit, Lamp2, Laptm5, Lasp1, Lgals1, Lims1, Lpar6, Lst1, March8, Ms4a2, Msn, Mtss1, Nckap1, Nckap1l, Nckipsd, Ninj1, P2rx7, P2ry14, Pdcd1lg2, Pdlim5, Pdzk1ip1, Pecam1, Pfn1, Plec, Plek, Prnp, Ptger3, Ptp4a1, Ptp4a2, Ptp4a3, Ptpn1, Ptpn11, Ptpn12, Ptpn18, Ptpn2, Ptpn3, Ptpn9, Rab1, Rab27b, Rac2, Rap1a, Rassf5, Rdx, Rnf128, Rock1, S100a6, Scin, Sema4d, Sh3bgrl3, Shc1, Sla, Spna2, Spnb2, Svil, Tagln2, Tjp2, Tln1, Tmem123, Tmem158, Tmem66, Tspan13, Tspan31, Tspan4, Tspan5, Tspan8, Twf2, Tyrobp, and Vcl. For details, see Table S1 in the supplemental material.

beled the cells Gal3 KD. BMMCs with Gal3 KD exhibited ≥70% decrease of Gal3 expression at the level of both mRNA (Fig. 2D) and protein (Fig. 2E). They also exhibited enhanced Ag-induced degranulation (Fig. 2F). The expression of other galectins was not affected by transduction with Gal3-targeted shRNAs (see Fig. S1A in the supplemental material), with the exception of Gal1 mRNA, which was upregulated up to 2-fold at the mRNA level but not at the protein level (see Fig. S1B in the supplemental material). When the cells were activated with thapsigargin, an inhibitor of sarcoplasmic/endoplasmic reticulum Ca^{2+} ATPase, the differences in degranulation between BMMCs with Gal3 KD and pLKO.1 controls were not significant, suggesting that Gal3 is not involved in the mechanism of granule release and acts upstream of calcium signaling (Fig. 2G). BMMCs with Gal3 KD had normal surface expression of FcεRI and KIT (Fig. 2H), suggesting that lentiviral transduction, puromycin selection, and Gal3 KD had no effect on the expression of these two receptors in nonactivated mast cells.

Cell activation and degranulation are accompanied by enhanced surface expression of LAMP1 secretory granule/lysosomal marker (32). In agreement with data evaluating β-glucuronidase release, Ag (TNP-BSA)-activated BMMCs with Gal3 KD showed significantly higher levels of surface LAMP1 than pLKO.1 controls (Fig. 2I). Similarly, we found that cells with Gal3 KD activated with DNP-HSA showed more LAMP1 expression than control cells, especially when activated with low concentrations of Ag (see Fig. S2 in the supplemental material). To further confirm the role of Gal3 in mast cell activation, we next examined mast cell activation in cells overexpressing Gal3. BMMCs were transiently transfected with a plasmid encoding Gal3 fused to enhanced green fluorescent protein (EGFP) (pEGFP-hGal3) or a control plasmid (Fig. 2J), and LAMP1 surface expression was analyzed in EGFP-positive cells. The data presented in Fig. 2K show that when activated with Ag (10 to 500 ng/ml), Gal3-overexpressing cells exhibited significantly decreased LAMP1 surface expression compared with control cells; this supports our findings of a negative regulatory role of Gal3 in FcεRI signaling.

Gal3 in BMMCs showed mainly cytoplasmic localization, with some in the nucleus and on the plasma membrane (see Fig. S3 in the supplemental material). Upon Ag activation, Gal3 localization did not change. To test whether Gal3 acts on mast cell degranulation via its lectin function, we attempted to block its lectin activity with lactose. However, as shown in Fig. S4A in the supplemental material, lactose had no effect on Ag-induced degranulation. Al-

FIG 1 High-throughput degranulation assay protocol and shRNA screening in mast cells. (A) Time axis of lentiviral transduction of BMMCL, selection in puromycin (Puro) and degranulation assay in one transduction run. (B) Assay design and protocol for high-throughput degranulation assay. Appropriate numbers of cells (~10^5) were transferred from the culture plate (transduced cells) to a new plate and sensitized with IgE (IgE-sensitized cells). The cells were split into two parts for nonactivated samples (Ag^-) or Ag-activated samples (shaded; Ag^+). The positions of 4 negative controls (blue), positive-control shRNAs targeting STIM1 (red), and SYK (green) are indicated. After 30 min of activation, β-glucuronidase (β-glucur.) was measured in cell-free supernatants and in lysates from cell pellets. (C) Degranulation of control shRNAs. Representative results from pilot experiments are shown. The cells were transduced with negative-control shRNAs targeting irrelevant sequences (2 GFP and 2 RFP; blue) or positive-control shRNAs targeting STIM1 (red) or SYK (green). The Z′ factor for the screening assay is also shown. (D) RT-qPCR analysis of gene KD of STIM1 and SYK from cells in panel C. (E) Schematic workflow of data collection, criteria for data quality control (QC), and hit calling. (F) Overview of all individual shRNAs in the second run of the screen ranked according to percent inhibition or activation in the degranulation assay. The red bars indicate the positions of all shRNAs targeting *Lgals3*.

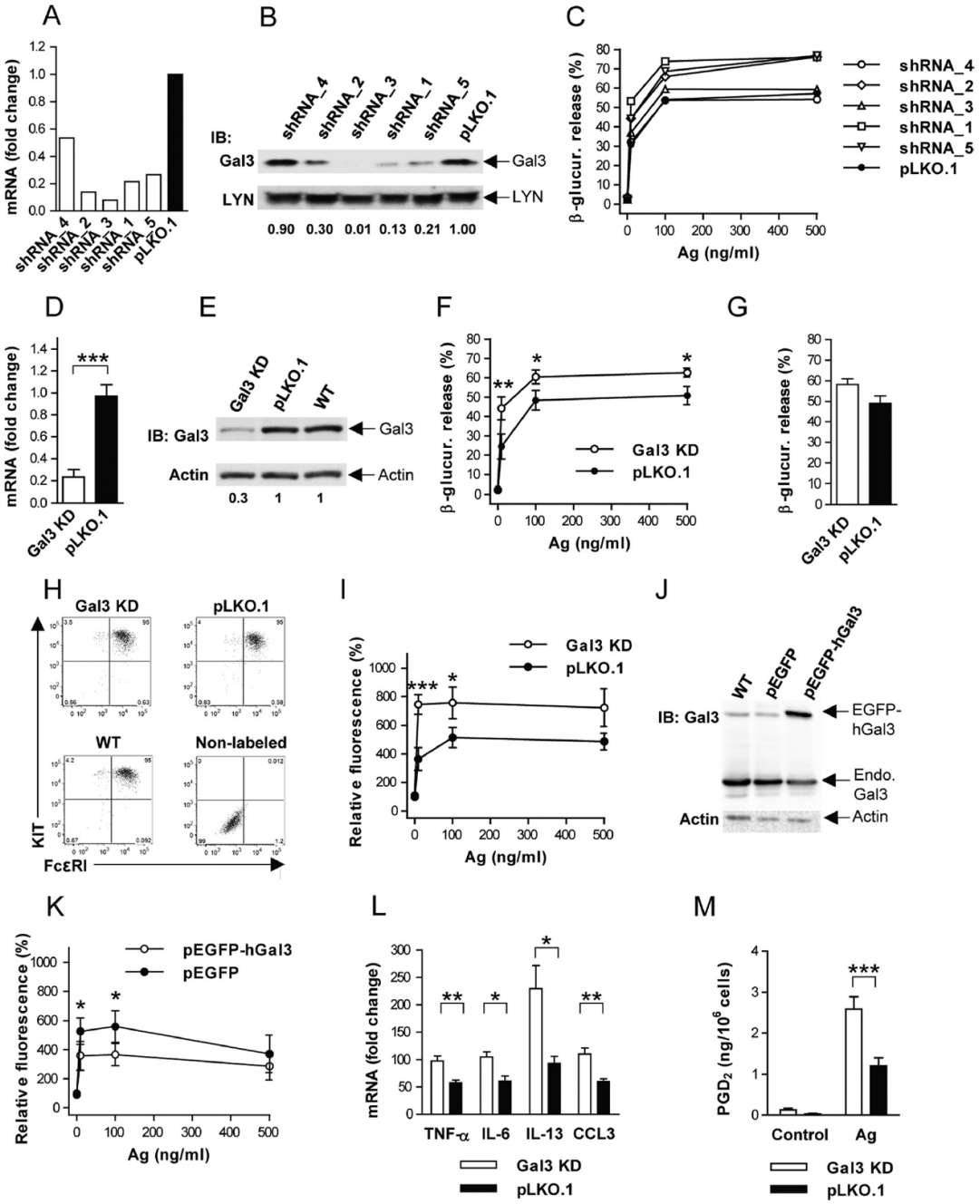

FIG 2 Upregulated Ag-induced activation of BMMCs with Gal3 KD. (A) RT-qPCR quantification of Gal3 mRNA expression in BMMCL transduced with shRNAs targeting Gal3 or pLKO.1 control vector. The data are representatives of 3 independent experiments. (B) Quantification of Gal3 protein expression by immunoblotting (IB) in whole-cell lysates prepared from cells transduced as in panel A. The numbers under the blot indicate the relative amounts of Gal3 normalized to the relative amounts of LYN, used as a loading control, and Gal3 in pLKO.1 control cells. The results are representative of 3 independent experiments. (C) BMMCs, transduced as in panel A, were sensitized with IgE and activated for 30 min with various concentrations of Ag, and β-glucuronidase release was determined. The data are representative of the results of 3 independent experiments. (D) RT-qPCR quantification of Gal3 mRNA expression in BMMCs with Gal3 KD and in pLKO.1 control cells. Means and standard errors (SE) are shown ($n = 7$). (E) Quantification of Gal3 protein expression by IB in whole-cell lysates prepared from BMMCs transduced as in panel D; nontransduced cells are labeled as wild type (WT). The numbers under the blots are as in panel B; however, actin was used as a loading control. The data are representative of the results of 3 independent experiments. (F) BMMCs transduced as in panel

ternatively, BMMCs with Gal3 KD were incubated or not for 30 min with recombinant mouse Gal3 prior to activation. The data in Fig. S4B in the supplemental material show that externally added Gal3 was ineffective in restoring the Gal3 KD phenotype.

Mast cells are potent producers of cytokines, chemokines, and other soluble mediators involved in immune responses. Therefore, we also investigated the role of Gal3 in these processes. Compared with control pLKO.1 cells, BMMCs with Gal3 KD produced significantly more mRNA for tumor necrosis factor alpha (TNF-α), IL-6, and IL-13, as well as chemokine C-C motif ligand 3 (CCL3), upon Ag stimulation (Fig. 2L). Production of PGD_2 was also significantly increased in BMMCs with Gal3 KD (Fig. 2M).

Together, our data from gene expression knockdown and overexpression experiments in primary mast cells are consistent with the results from our shRNA screen in BMMCL and confirm the negative regulatory role of endogenous Gal3 in Ag-induced mast cell activation.

Negative regulatory role of Gal3 in F-actin dynamics, calcium response, and phosphorylation of signal transduction molecules. Consistent with increased degranulation, BMMCs with Gal3 KD exhibited significantly higher calcium response to Ag than pLKO.1 control cells (Fig. 3A). To determine whether Gal3 mediates its effect on mast cell degranulation by affecting negative regulation mediated by the actin cytoskeleton, we analyzed the F-actin levels in Ag-stimulated BMMCs with Gal3 KD and control cells by confocal microscopy. As shown in Fig. 3B and C, Ag-stimulated BMMCs with Gal3 KD exhibited reduced levels of F-actin compared to control cells.

Next, we examined global tyrosine phosphorylation using confocal microscopy. Nonactivated BMMCs with Gal3 KD and pLKO.1 control cells showed comparable levels and localization of tyrosine-phosphorylated proteins (Fig. 4A, left, and B). However, Ag-activated cells with Gal3 KD showed more intense phosphotyrosine staining than control pLKO.1 cells (Fig. 4A, right, and B). We also examined phosphorylation of key signaling molecules in the FcεRI pathway by immunoblotting. Analysis with antibodies specific for phosphorylated SYK, PLCγ1, and AKT (Fig. 4C) after 5 min of activation with various concentrations of Ag (10 or 100 ng/ml) and antibodies specific for pJNK (Fig. 4D) after 15 min of activation with Ag (100 ng/ml) showed significantly upregulated phosphorylation of the target proteins in activated BMMCs with Gal3 KD compared with pLKO.1 controls. No significant differences in phosphorylation of ERK were found between these two cell types after FcεRI triggering (Fig. 4C). In nonactivated cells with Gal3 KD, the phosphorylation of AKT and ERK was significantly increased, suggesting that Gal3 also affects signaling pathways in the resting cells. These results demonstrate that Gal3 is involved in downregulation of early FcεRI activation events, including phosphorylation of key signaling molecules and calcium response.

Gal3 regulates IgE internalization and trafficking to endolysosomes. Previous studies have shown that T cells lacking Gal3 exhibited enhanced T cell receptor (TCR) activation events and that these changes were connected to the impaired downregulation and internalization of TCRs (33). FcεRI is rapidly internalized upon its aggregation with IgE-multivalent Ag complexes (34). Therefore, we next compared internalization of the Ag-aggregated FcεRI in BMMCs with Gal3 KD and control cells. To quantitatively determine intracellular IgE, we used flow cytometry to measure the fraction of total IgE remaining on the cell surface after acid wash stripping. We found that upon activation with Ag at concentrations of 500 ng/ml and 1 μg/ml, BMMCs with Gal3 KD showed less acid-resistant and intracellular IgE than pLKO.1 controls (Fig. 5A).

Internalized IgE-FcεRI complexes have been shown to be delivered into LAMP1-positive endolysosomes (35). To determine the involvement of Gal3 in this process, we next examined trafficking of IgE-FcεRI complexes. In nonactivated cells, IgE staining was almost exclusively associated with plasma membranes in both BMMCs with Gal3 KD and pLKO.1 control cells (Fig. 5B). Thirty minutes after Ag activation, a fraction of IgE in pLKO.1 cells moved into vesicular structures. In contrast, BMMCs with Gal3 KD showed IgE staining with a diffuse pattern, with IgE predominantly localized near the plasma membrane. We quantified the amount of IgE localized in the vesicles inside the cells after 30 min of Ag activation and found that significantly less IgE was associated with intracellular structures in cells with Gal3 KD than in controls (Fig. 5C). The combined data indicate that Gal3 facilitates internalization of IgE-FcεRI complexes upon Ag triggering and facilitates the trafficking of internalized IgE into the LAMP1-positive lysosomal compartments.

Gal3 is involved in regulation of FcεRI ubiquitination. The internalization and sorting of FcεRI into endosomal compartments is a ubiquitin-dependent process (36). We speculated that aberrant IgE internalization and trafficking in BMMCs with Gal3 KD could be coupled with impaired ubiquitination of FcεRI. To test this hypothesis, we immunoprecipitated IgE-FcεRI complexes from BMMCs with Gal3 KD or pLKO.1 control cells and evaluated the ubiquitination of the FcεRI β and γ subunits upon Ag activation. We found that FcεRI β and γ subunits in BMMCs with Gal3 KD had less ubiquitination than those in control cells (Fig. 6A to C). We also prepared BMMCs overexpressing mGal3-Myc after lentiviral transduction and selection of puromycin-resistant cells, but the level of mGal3-Myc expression was rather

D were sensitized with IgE and activated with various concentrations of Ag for 30 min, and β-glucuronidase was determined. Means ± SE are shown ($n = 7$). (G) BMMCs transduced as in panel D were activated for 30 min with 1 μM thapsigargin, and β-glucuronidase release was determined. Means and SE are shown ($n = 7$). (H) Representative flow cytometry plots showing expression of surface FcεRI and KIT in BMMCs transduced as in panel D. Nontransfected cells are labeled as WT. The control fluorescence profile of BMMCs is denoted nonlabeled. (I) BMMCs transduced as in panel D were sensitized with IgE and activated with various concentrations of Ag for 10 min. Increased surface expression of LAMP1 was determined by flow cytometry. Means ± SE are shown ($n = 4$). (J) BMMCs were transfected with empty pEGFP vector or pEGFP-hGal3 to overexpress Gal3. Gal3 protein expression was analyzed by IB in whole-cell lysates with anti-Gal3 antibody. Actin is shown as a loading control. The arrows indicate the positions of endogenous Gal3, exogenous EGFP-hGal3 fusion protein, and actin. Nontransfected cells are labeled as WT. (K) BMMCs were transfected as in panel J, and surface expression of LAMP1 was determined by flow cytometry. Means ± SE are shown ($n = 6$). (L) Cytokine and chemokine mRNA expression. BMMCs were transduced as in panel D, sensitized with IgE, and activated with Ag (100 ng/ml) for 1 h. mRNAs encoding TNF-α, IL-6, IL-13, and CCL3 were quantified by RT-qPCR. The fold increase in mRNA expression after Ag stimulation was normalized to nonactivated pLKO.1 control cells. Means and SE are shown ($n = 7$). (M) PGD_2 production. BMMCs were transduced as in panel D, sensitized with IgE, and activated with Ag (100 ng/ml) for 25 min. The amount of PGD_2 in cell-free supernatants was determined by immunoassay. Means and SE are shown ($n = 5$). *, $P < 0.05$; **, $P < 0.01$; ***, $P < 0.001$.

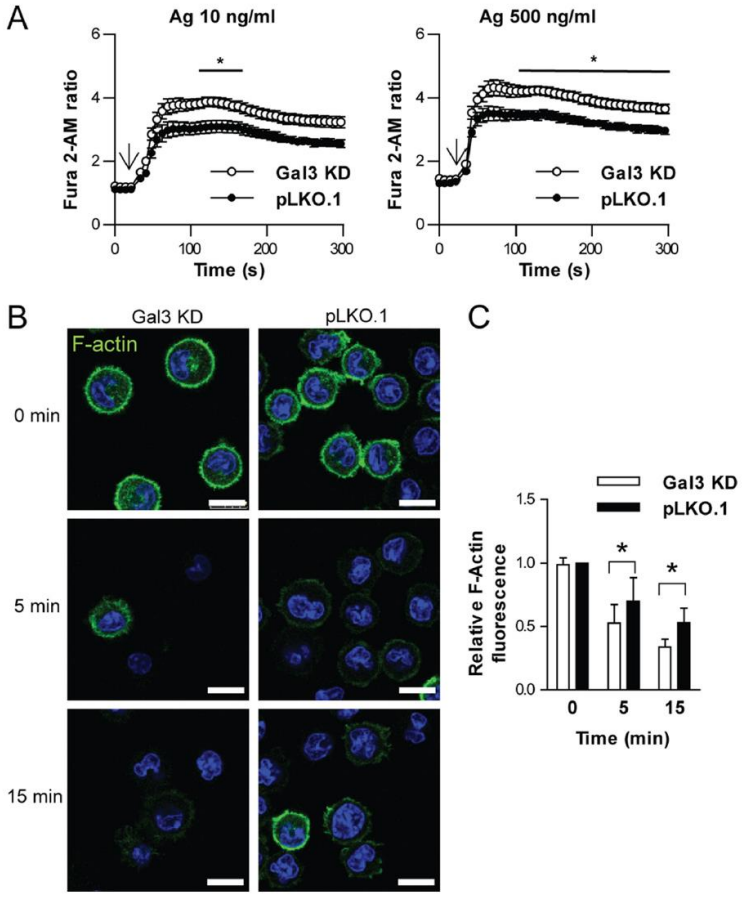

FIG 3 Calcium mobilization and F-actin dynamics. (A) Intracellular calcium mobilization. BMMCs with Gal3 KD or pLKO.1 control cells were sensitized with IgE and loaded with Fura 2-AM. The cells were then activated with Ag at a concentration of 10 ng/ml (left) or 500 ng/ml (right), and increases in calcium response were monitored by measuring fluorescence ratios. The arrows indicate the time points of Ag addition, and the bars above the curves represent statistically significant differences between cells with Gal3 KD and pLKO.1 controls. Means ± SE are shown ($n = 6$). (B) F-actin response. IgE-sensitized BMMCs as in panel A were activated with Ag (100 ng/ml) for the indicated times. After fixation, the cells were permeabilized and stained for F-actin with AF488-conjugated phalloidin. The images were acquired by confocal microscopy. Scale bars, 10 μm. (C) Statistical evaluation of F-actin fluorescence in cells, as in panel B; 5 to 20 cells were analyzed in each experiment. Means and SE were calculated from the results of 4 independent experiments. *, $P < 0.05$.

moderate in several independent experiments and did not result in significant differences in ubiquitination of FcεRI β and γ subunits in these cells compared to cells transduced with empty pCDH vector (Fig. 6D to F). Interestingly, no significant differences in tyrosine phosphorylation of β and γ FcεRI subunits were found between BMMCs with Gal3 KD and pLKO.1 control cells (Fig. 6G and H). CBL, an E3-ubiquitin ligase, is rapidly phosphorylated after Ag stimulation and is involved in FcεRI ubiquitination (37, 38). Therefore, we also investigated whether phosphorylation of CBL is dependent on the presence of Gal3. As shown in Fig. 6I to J, similar levels of CBL phosphorylation were found in cells with Gal3 KD and pLKO.1 controls. Thus, changes in phosphorylation of CBL do not explain the observed defect in FcεRI ubiquitination in BMMCs with Gal3 KD.

Regulatory role of Gal3 in mast cell adhesion, motility, and chemotaxis. Gal3 affects cell adhesion, motility, and migration in various cell types (39, 40). Previous studies have shown adhesion of BMMCs to fibronectin (41). Therefore, we investigated whether Gal3 KD interferes with the adhesion and motility of mast cells on fibronectin-coated surfaces. We found that Gal3 had no effect on binding of nonactivated cells to fibronectin-coated surfaces (Fig. 7A). However, after Ag activation, cells with Gal3 KD showed significantly decreased binding to fibronectin compared to pLKO.1 control cells.

Upon Ag stimulation of mast cells, β1-integrin, a receptor for fibronectin, adopts an activated conformation with higher affinity for fibronectin (42). To determine whether defects in adhesion and motility of BMMCs with Gal3 KD on fibronectin are related to changes in β1-integrin activation, we tested the levels of activated β1-integrin by flow cytometry with antibody against the 9EG7 epitope. Our data show that nonactivated BMMCs with Gal3 KD expressed almost doubled the levels of activated β1-integrin compared with control cells (Fig. 7B). After Ag activation, levels of activated β1-integrin increased in pLKO.1 control cells

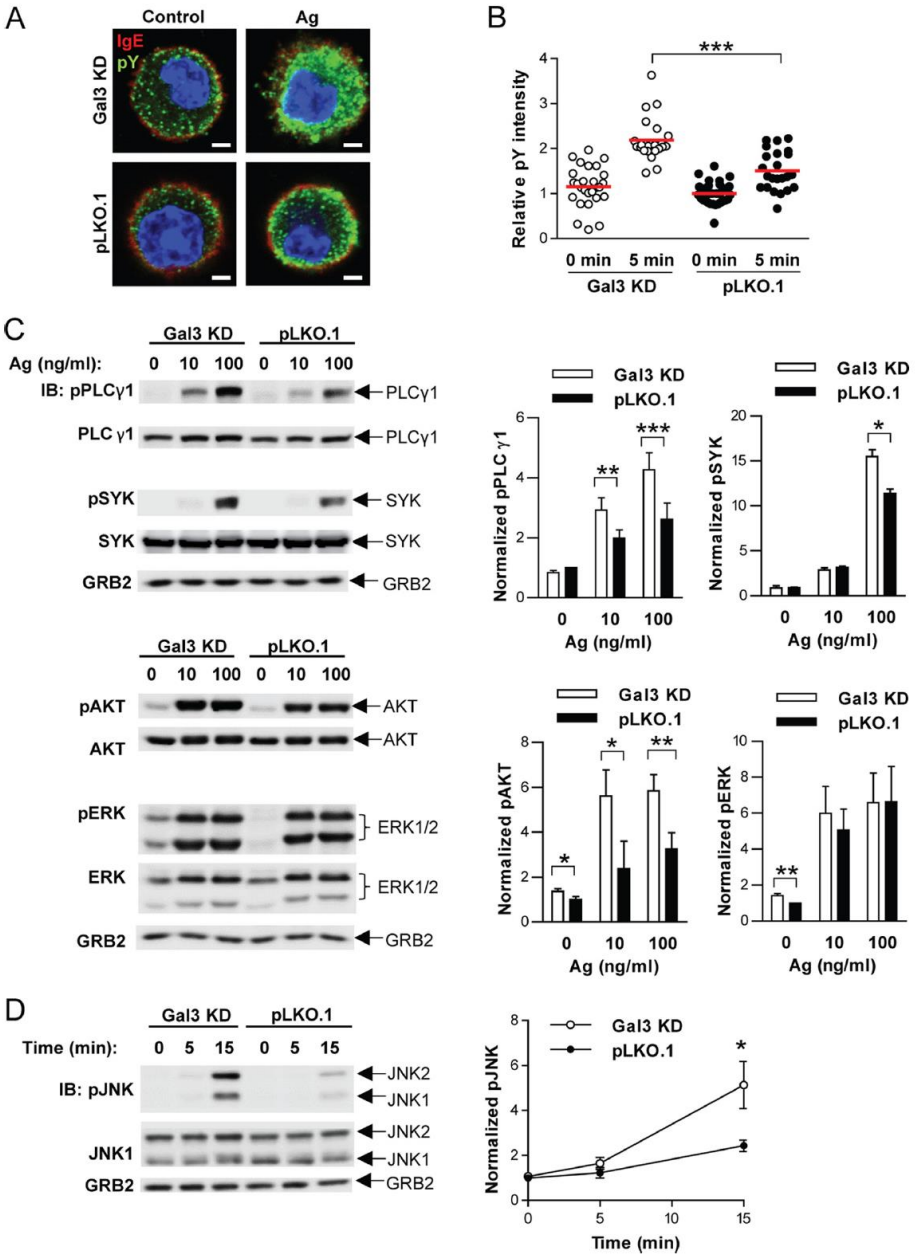

FIG 4 Early activation events in BMMCs with Gal3 KD. (A) Global tyrosine phosphorylation in BMMCs with Gal3 KD (top) or pLKO.1 controls (bottom). Cells were sensitized with IgE and either not activated (Control) or Ag activated (Ag) (100 ng/ml) for 5 min. After activation, the cells were fixed, permeabilized, and stained with anti-IgE, followed by AF568-mouse Ig-specific secondary-antibody conjugate (red) and anti-pY antibody followed by AF488-rabbit Ig-specific secondary antibody conjugate (green). Bars, 2 μm. (B) Evaluation of differences in pY fluorescence in cells as in panel A. Each dot represents one cell. Means are indicated by red bars. A statistically significant difference between BMMCs with Gal3 KD and pLKO.1 controls is indicated. (C) Phosphoprotein analysis. BMMCs with Gal3 KD or pLKO.1 controls were sensitized with IgE and activated with various concentrations of Ag for 5 min. SDS-PAGE-separated whole-cell lysates were analyzed with various phosphosite-specific antibodies (pPLCγ1, pSYK, pAKT, and pERK), as indicated. For loading controls the membranes were analyzed by immunoblotting with the corresponding protein-specific antibodies. GRB2 is shown as another loading control. (Left) Representative immunoblots from at least 3 experiments. (Right) Densitometry analysis of the corresponding immunoblots, in which signals from tyrosine-phosphorylated proteins in activated cells were normalized to the signal in nonactivated pLKO.1 control cells and loading control proteins. Means and SE were calculated from the results of three independent experiments. The statistical significance of differences between cells with Gal3 KD and pLKO.1 controls is also shown. (D) BMMCs were processed and analyzed as in panel C, with the modification that cells were activated with Ag (100 ng/ml) for various times. Phosphorylation of JNK1/2 was determined by immunoblotting with pJNK antibody. For loading controls, the membranes were analyzed by immunoblotting with JNK1- and GRB2-specific antibodies. Means ± SE are shown ($n = 3$). *, $P < 0.05$; **, $P < 0.01$; ***, $P < 0.001$.

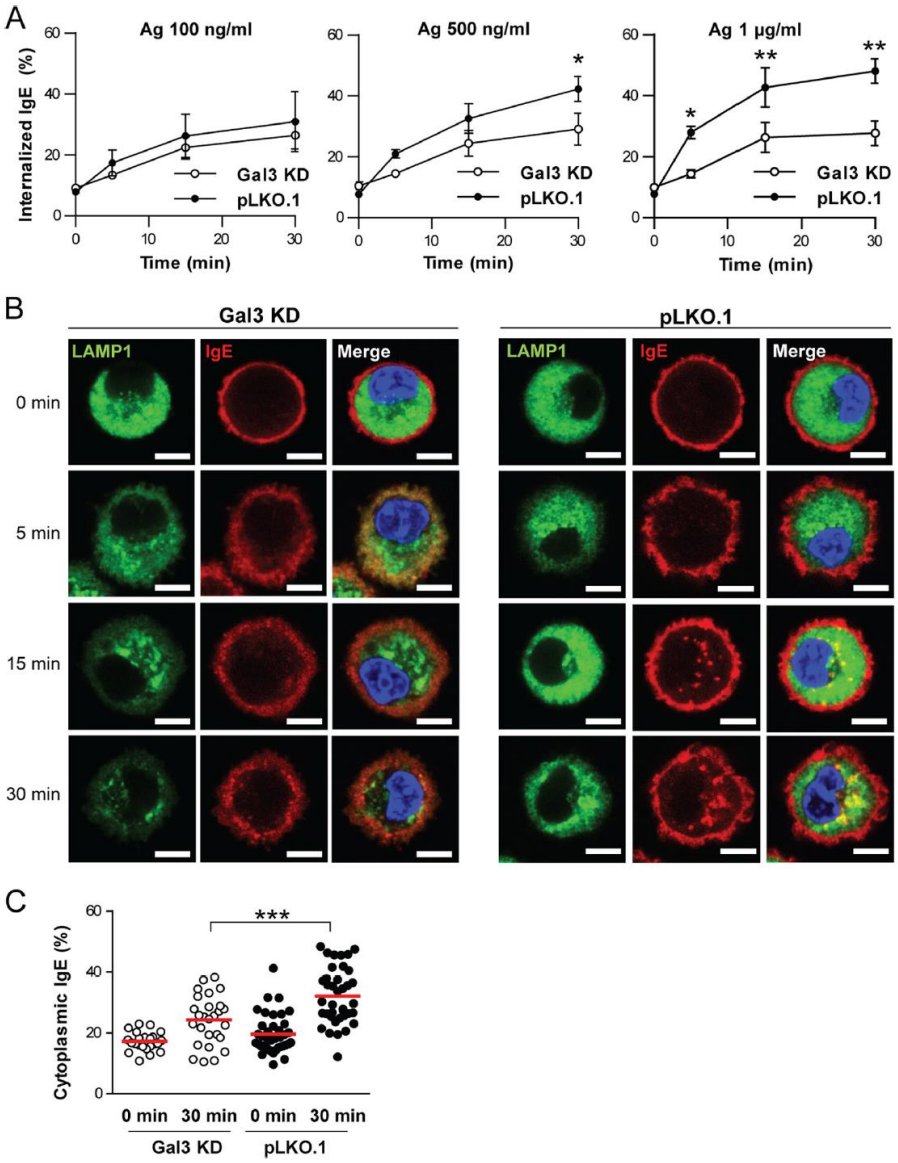

FIG 5 Gal3-regulated IgE internalization and trafficking to endolysosomes. (A) IgE internalization in BMMCs with Gal3 KD and control pLKO.1 cells. The cells were sensitized with IgE and activated with various concentrations of Ag (100 ng/ml, 500 ng/ml, or 1 μg/ml). At various time intervals after triggering (0, 5, 15, or 30 min), surface IgE was removed by acid stripping, and the cells were fixed and permeabilized. IgE levels were quantified with anti-IgE antibody by flow cytometry. Means ± SEs from the results of 3 independent experiments are shown. (B) Representative confocal images of IgE and LAMP1 localization in BMMCs transduced as in panel A (left, Gal3 KD; right, pLKO.1 controls). The cells were sensitized with IgE and not activated (0 min) or activated with Ag (100 ng/ml) for various times (5, 15, or 30 min), fixed, permeabilized, and stained with anti-IgE, followed by AF568–mouse Ig-specific secondary antibody conjugate (red) and anti-LAMP1-specific antibody and then by AF488-secondary antibody conjugate (green). Bars, 5 μm. (C) Quantitative analysis of IgE distribution in nonactivated (0 min) and Ag-activated (30 min) cells from experiments, as in panel B. IgE fluorescence was analyzed as described in Materials and Methods and plotted as a percentage of cytoplasmic IgE. Each point represents one cell from 2 independent experiments; the red bars represent the means. *, $P < 0.05$; **, $P < 0.01$; ***, $P < 0.001$.

but remained unchanged in BMMCs with Gal3 KD. One explanation of these findings could be deregulated β1-integrin internalization in the absence of Gal3. Therefore, we examined total β1-integrin on the cell surface. We found that BMMCs with Gal3 KD expressed significantly larger amounts of β1-integrin on the plasma membrane and, when activated with Ag, β1-integrin rapidly internalized to a greater extent in BMMCs with Gal3 KD than in control pLKO.1 cells (Fig. 7C).

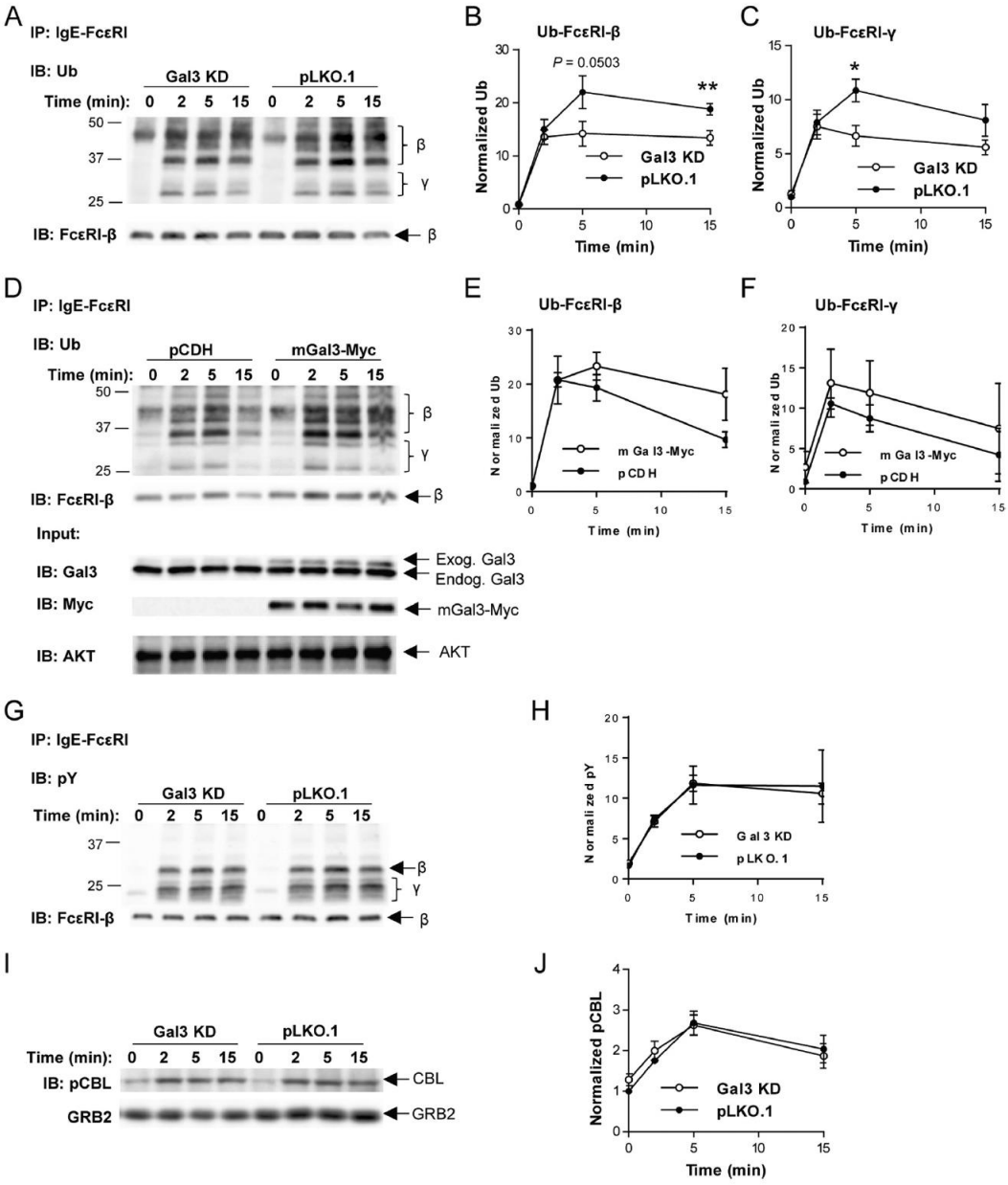

FIG 6 Gal3 promotes ubiquitination of FcεRI β and γ subunits without affecting phosphorylation of FcεRI and CBL. (A to C) BMMCs with Gal3 KD or pLKO.1 controls were sensitized with IgE and activated with Ag (100 ng/ml) for the indicated times. (A) IgE-FcεRI complexes were immunoprecipitated with IgE-specific polyclonal antiserum. Immunoprecipitates (IPs) were size separated by SDS-PAGE, and ubiquitination was determined by IB with an antibody specific for ubiquitinated proteins (Ub). The positions of molecular weight standards and the FcεRI β and γ subunits are indicated on the left and right, respectively. (B and C) Quantification of FcεRI β (B) and γ (C) subunit ubiquitination from data in panel A. Densitometry data for the subunit ubiquitination were normalized to the number of β subunits used as loading controls and nonactivated pLKO.1 controls. (D to F) BMMCs were transduced with mGal3-Myc or empty pCDH vector, puromycin-resistant cells were selected, and FcεRI subunit ubiquitination was analyzed as in panel A. Expression of Gal3 (endogenous and exogenous) and mGal3-Myc was detected with anti-Gal3 and anti-Myc antibodies, respectively. GRB2 was also analyzed as another loading control. (E and F) Quantification of FcεRI β (E) and γ (F) subunit ubiquitination from data in panel D was performed as described above, except that densitometry data were normalized to nonactivated empty pCDH controls. (G and H) The FcεRI IPs were obtained as in panel A, and samples were analyzed for tyrosine phosphorylation of the FcεRI β and γ subunits with the phosphotyrosine-specific antibody PY-20–HRP (pY). Quantification of the subunit phosphorylation was performed by densitometry of the blots as in panel G, and data were normalized to the number of FcεRI β subunits and pLKO.1 controls. (I and J) Phosphorylation of CBL in BMMCs with Gal3 KD or pLKO.1 controls. Cells were activated as in panel A, and whole-cell lysates were size separated by SDS-PAGE and analyzed by immunoblotting with pCBL-specific antibody; because of poor performance of anti-CBL, GRB2 was used as a loading control (I). Quantification of pCBL was performed by densitometry of the blots as in panel I, and data were normalized to the amount of GRB2 and nonactivated pLKO.1 controls. (B, C, E, F, H, and J) Means ± SE calculated from the results of at least 3 independent experiments. *, $P < 0.05$; **, $P < 0.01$.

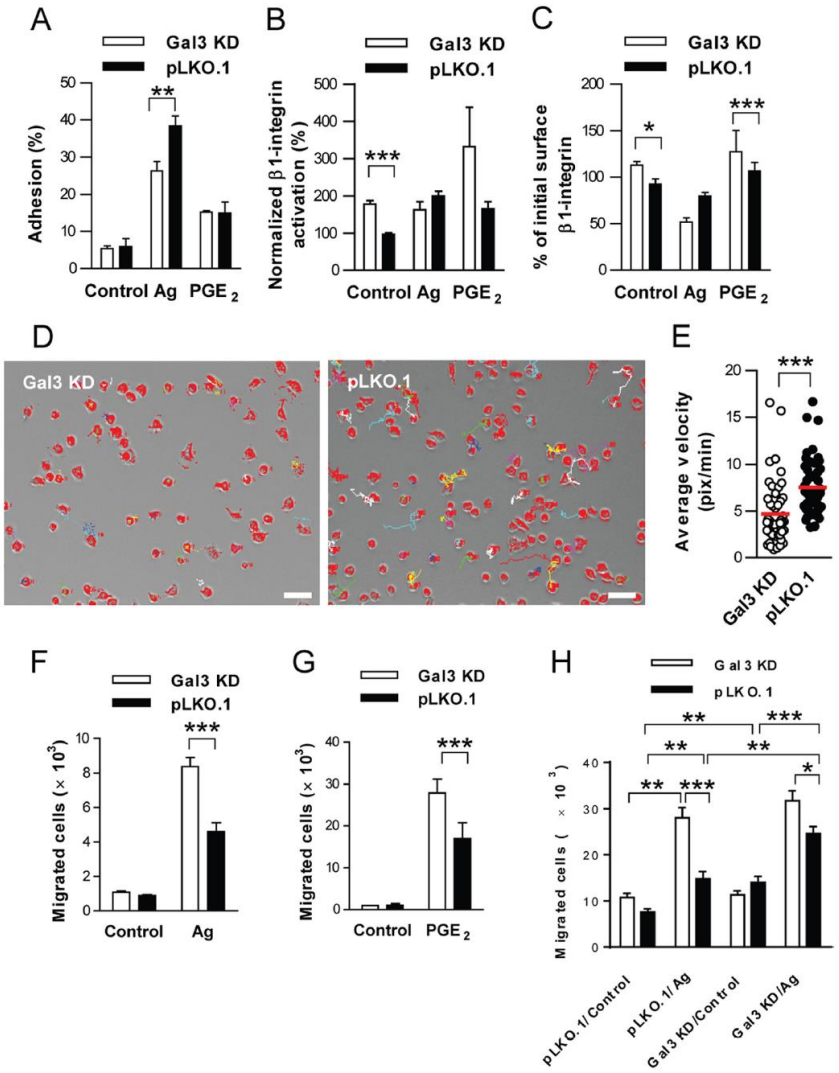

FIG 7 Involvement of Gal3 in BMMC motility, adhesion, and chemotaxis. (A) Cell adhesion to fibronectin-coated surfaces was analyzed in BMMCs with Gal3 KD or pLKO.1 controls. The cells were sensitized with IgE, loaded with calcein, and left to attach to a fibronectin-coated surface for 30 min. After activation with Ag (100 ng/ml) or PGE_2 (100 nM) for 30 min, the fraction of attached cells was determined. Means and SE are shown ($n = 5$). (B) Activation of β1-integrin in cells sensitized with IgE and, after washing, activated with Ag (100 ng/ml) or PGE_2 (100 nM) for 3 min. Surface expression of activated β1-integrin was determined with an antibody specific for the open conformation of β1-integrin and by flow cytometry. Means and SE are shown ($n = 7$). (C) Detection of total surface β1-integrin in cells sensitized with IgE and activated with Ag (100 ng/ml) or PGE_2 (100 nM) for 3 min. Surface expression of β1-integrin was determined by flow cytometry. Means and SE are shown ($n = 7$). (D) Motility was evaluated in cells attached to a fibronectin-coated surface for 15 min and activated with PGE_2 (100 nM). Cell movement was recorded at 1-min intervals. Representative cell trajectories over 30 min are indicated in colors. Bars, 50 μm. (E) Quantification of average velocity in relative units (pixels per min) in cells analyzed as in panel B. Each point represents one cell; the data are from two independent experiments; the red bars represent means. (F and G) Migration of IgE-sensitized BMMCs with Gal3 KD or pLKO.1 controls toward Ag (100 ng/ml) (F) or PGE_2 (100 nM) (G). (H) Migration of nonsensitized BMMCs with Gal3 KD or pLKO.1 control toward supernatants obtained from IgE-sensitized BMMCs with Gal3 KD or pLKO.1 controls activated for 6 h with Ag (TNP-BSA; 100 ng/ml) or without Ag (Control). Means and SE are shown ($n = 3$). *, $P < 0.05$; **, $P < 0.01$; ***, $P < 0.001$.

To examine motility, we activated the cells with PGE_2, a potent inducer of mast cell migration (43). Figure 7D shows representative trajectories of PGE_2-activated BMMCs with Gal3 KD or control cells recorded in 1-min intervals for a total of 30 min. Trajectories of BMMCs with Gal3 KD showed impaired motility compared with control cells. When quantified, the differences were significant (Fig. 7E).

Next we examined whether Gal3 is involved in fibronectin-

independent chemotaxis toward Ag and PGE_2. As shown in Fig. 7F and G, BMMCs with Gal3 KD showed significantly increased migration toward Ag and PGE_2, respectively, compared with their control counterparts. In the absence of chemoattractants, no differences in migration were observed between the two cell types. To find out how the production of cytokines and chemokines by activated BMMCs accounts for migration of BMMCs with Gal3 KD toward Ag, we let the cells migrate toward supernatants from Ag-activated BMMCs with normal Gal3 expression or with Gal3 KD (Fig. 7H). We recorded increased migration of BMMCs toward supernatants from both nonactivated and Ag-activated cells with Gal3 KD. The combined data suggest that Gal3 is involved in stabilizing β1-integrin on the plasma membranes of mast cells and facilitates proper cell adhesion and motility on fibronectin. On the other hand, Gal3 inhibits fibronectin-independent cell chemotaxis toward Ag, in part by regulating the release of chemoattractants from mast cell products.

DISCUSSION

In this study, we utilized RNAi screening to gain new insights into FcεRI signaling in mast cells. We focused on genes with unknown or poorly understood functions in mast cell activation. Based on the screen, we identified several potential negative and positive regulators of mast cell degranulation and focused on understanding the regulatory mechanism of one of them, Gal3.

RNAi screening in differentiated immune cells has historically been complicated by difficulties with transfection. To overcome this problem, we established a screening protocol based on lentiviral shRNA delivery. We used BMMCL, a mouse mast cell line that preserved a high growth rate following lentiviral transduction and exhibited stable expression of mast cell surface receptors, including FcεRI and KIT (data not shown). Among several functional assays that we examined, we chose Ag-induced degranulation for its robustness and specificity. The performance of the assay is considered acceptable for screening by high-throughput standards, with a Z′ factor of 0.37; Z′ factors of cell-based RNAi screens are generally lower than the optimal values of 0.5 to 1 (30). To improve evaluation of the results, we included a control-based Z-normalization step to compare degranulation assays whose magnitudes showed inherent variation between experiments. Another crucial step in data analysis was proper quality control filtering of technical replicates. The major indicator of per plate data quality was the inhibition of degranulation induced by positive-control shRNA targeting SYK. Following shRNA transductions, among 144 genes, we identified 15 candidates that showed reproducibility and consistency across screen runs. To our knowledge, none of these genes except *Plscr1* and *Lgals3* have been studied in mast cells yet. *Plscr1* was shown to play a role in degranulation of a rat basophilic leukemia cell line (44), and *Lgals3* was found to be a positive regulator of mast cell degranulation in studies with BMMCs from mice with Gal3 knockout (see below). In further analysis, we focused on *Lgals3*, encoding Gal3, which showed strong effects on degranulation by scoring with all three shRNAs used in the screen. The inhibitory effect of Gal3 was confirmed in primary BMMCs.

Gal3 belongs to the family of galectins, animal lectins that bind β-galactosides and have a unique structure containing a highly conserved C-terminal carbohydrate recognition domain and a proline-rich N-terminal sequence. The N-terminal sequence facilitates oligomerization of Gal3 up to pentamers and can be further organized into complex structures called lattices (45, 46). Gal3 plays various roles in immune processes during parasitic infections and allergic inflammation, affecting cytokine production, participating in recruitment of immune cells to inflammatory sites, and regulating Th2 responses (47–50). Gal3 was originally identified as an IgE-binding protein (51) and has been studied in several cell types, including BMMCs (31, 52). Here, we show that Gal3 is a negative regulator of FcεRI-induced cell degranulation at a wide range of Ag concentrations. The fact that most profound differences in degranulation were observed when the cells were activated with low doses of Ag suggests that Gal3 participates in setting the FcεRI activation threshold.

Previous studies showed decreased degranulation and production of IL-4 upon Ag stimulation of BMMCs derived from C57BL/6 mice with Gal3 KO. However, Gal3-deficient cells showed normal tyrosine phosphorylation of LYN, SYK, PLCγ1, and LAT1 (31), suggesting that Gal3 has no effect on early activation events after FcεRI triggering. In contrast, in our study, we found enhanced tyrosine phosphorylation of SYK, PLCγ1, JNK, and AKT but not FcεRI β and γ subunits. This indicates that Gal3 in BMMCs with Gal3 KD interferes with events immediately after tyrosine phosphorylation of the FcεRI subunits, and this leads to enhanced degranulation and calcium response. The observed discrepancy could not be explained simply by the genetic background of BMMCs used in this study (BALB/c) and the previous study with Gal3 KO cells, because we found enhanced degranulation in BMMCs with Gal3 KD derived from both BALB/c and C57BL/6 mice (our unpublished data). However, the observed discrepancy could be explained by the use of different methodologies of gene ablation, KO versus KD (53). During development, gene ablation can be compensated for by genetic mechanisms that are in many cases poorly understood (21, 54, 55). Previous studies in mice with Gal3 KO showed involvement of Gal3 in regulating cell differentiation and morphogenesis, which could contribute, among other things, to changes in mast cell physiology (49, 56). Inducible and conditional *in vivo* gene targeting of Gal3 in mast cells will be required to understand the basis of the different results obtained with BMMCs with Gal3 KO or KD. Moreover, differences in the methodology of BMMC derivation from bone marrow and in culture conditions may also significantly contribute to different mast cell phenotype alterations (57).

It has been suggested that Gal3 prolongs receptor signaling by restricting receptor movement within the membrane and by delaying its removal by constitutive endocytosis (58). Internalization of FcεRI, as well as some sphingolipids, is triggered by their extensive cross-linking and immobilization (59, 60). Recently, Gal3 was identified as a driver of endocytosis of clathrin-independent carriers, including glycosphingolipids and integrins (61). Based on our data, we propose that Gal3 facilitates FcεRI internalization. Our data suggest that aberrant trafficking of aggregated FcεRI in cells with Gal3 KD is accompanied by enhanced FcεRI-mediated signaling. Consistent with these findings, it has been shown that intracellular-trafficking pathways of plasma membrane receptors can determine the outcome of receptor signaling (62–64). In this connection it should be noted that we observed enhanced F-actin depolymerization in FcεRI-activated BMMCs with Gal3 KD compared to controls. This indicates that Gal3 is a positive regulator of actin polymerization, and this finding could explain enhanced degranulation in cells with Gal3 KD because F-actin is a negative regulator of FcεRI-mediated degranulation (65, 66).

Receptor ubiquitination modulates its internalization and sorting for degradation (67). In LAMP1-positive compartments, IgE-FcεRI complexes are committed for degradation, or in some cases, recycling of IgE to the cell surface can occur (68, 69). Our data show that Gal3 is one of the regulators participating in proper sorting of the aggregated FcεRI to LAMP1-positive compartments. We note that Gal3 is not likely to affect the rate of IgE degradation at early stages of activation (up to 15 min), since the same levels of FcεRI were obtained by immunoprecipitation experiments. Furthermore, we found that Gal3 does not affect FcεRI ITAM phosphorylation. This is consistent with a finding that phosphorylation of FcεRI ITAMs is dispensable for receptor ubiquitination (70). We propose that Gal3 promotes ubiquitination of FcεRI and in this way contributes to downregulation of some of the downstream FcεRI-mediated signaling pathways. Previous studies have shown that overexpression of CBL ubiquitin ligase in mast cells inhibits Ag-mediated signaling (71). We analyzed CBL tyrosine residue 700, which is phosphorylated by SRC family kinases and SYK (72), and found that FcεRI ubiquitination promoted by Gal3 did not require enhanced CBL phosphorylation at this site. We cannot exclude the possibility that Gal3 affects phosphorylation of other sites on CBL or accessibility of CBL to FcεRI signalosomes or other components of the CBL interactome, such as SHIP or CIN85 (73). How exactly Gal3 regulates ubiquitination of FcεRI remains to be elucidated.

Gal3 functions are mainly attributed to its glycan binding activity (46, 61, 74). However, we did not observe any effect of lactose, an inhibitor of Gal3 lectin binding, on BMMC degranulation and adhesion to fibronectin (data not shown). Similarly, the effect of Gal3 KD was not reversed by treatment of the cells with recombinant Gal3. This suggests that Gal3 functions in mast cells, as documented in this work, by its intracellular interactions, which are not mediated by its lectin binding activity or are not accessible to externally added lactose. In this regard, it should be noted that Gal3 has been shown to interact with several nonglycosylated molecules through protein-protein interactions (75, 76).

We have also demonstrated that Gal3 is involved in regulating surface expression and internalization of β1-integrin in BMMCs. Our data show that Gal3 participates in regulation of the level of β1-integrin on the cell surface in resting cells and stabilizes the β1-integrin on the surface upon Ag activation. Similarly, Gal3 was shown to interact with β1-integrin and drive its internalization (61, 77). Rapid displacement of β1-integrin from the cell surface observed after Ag activation of BMMCs with Gal3 KD can lead to inefficient interactions between the plasma membrane and fibronectin-coated surfaces. The motility of the cells upon PGE_2 stimulation could be affected by Gal3 at the level of β1-integrin activation, as β1-integrin was not internalized upon PGE_2, but its activation was affected by the expression level of Gal3. These defects were specific to fibronectin-mediated events, since the general ability of BMMCs with Gal3 KD to migrate toward chemoattractants was increased. It is possible that enhanced production of cytokines and PGD_2 observed in cells with Gal3 KD acts by autocrine mechanisms on enhanced chemotaxis toward Ag, as has been described previously (78). The upregulated migration of mast cells toward supernatants from activated BMMCs with Gal3 KD confirms the contribution of mast cell-produced chemoattractants. However, since PGE_2 alone is not known to trigger mast cell degranulation or cytokine production (79), the upregulated migration of the cells with Gal3 KD toward PGE_2 suggests involvement of other mechanisms. This conclusion is supported by elevated phosphorylation of AKT and ERK in nonactivated cells with Gal3 KD.

In conclusion, our data obtained in shRNA-based RNAi screening in activated mast cells allowed us to identify several potential new regulators of FcεRI-mediated mast cell degranulation. Detailed analysis of one of them, Gal3, showed that Gal3 in Ag-activated mast cells is involved in regulation of F-actin depolymerization, surface FcεRI internalization, and trafficking, and through these activities could affect a variety of mast cell signaling pathways.

ACKNOWLEDGMENTS

We thank H. Mrazova for technical assistance.

This work was supported by project P302/12/G101 from the Czech Science Foundation. M.B. and I.P. were supported in part by the Faculty of Science, Charles University, Prague. R.J.X. was supported by the Helmsley Charitable Trust, CCFA, and National Institutes of Health (DK43351).

We report no conflicting financial interests.

FUNDING INFORMATION

This work, including the efforts of Ramnik Xavier, was funded by HHS | National Institutes of Health (NIH) (DK43351). This work, including the efforts of Ramnik Xavier, was funded by Crohn's and Colitis Foundation of America (CCFA). This work, including the efforts of Petr Draber, was funded by Czech Science Foundation (P302/12/G101). This work, including the efforts of Monika Bambouskova and Iva Polakovicova, was funded by Přírodovědecká Fakulta, Univerzita Karlova (Faculty of Science, Charles University). This work, including the efforts of Ramnik Xavier, was funded by Leona M. and Harry B. Helmsley Charitable Trust (Helmsley Charitable Trust).

REFERENCES

1. **Galli SJ, Grimbaldeston M, Tsai M.** 2008. Immunomodulatory mast cells: negative, as well as positive, regulators of immunity. Nat Rev Immunol **8**:478–486. http://dx.doi.org/10.1038/nri2327.
2. **Galli SJ, Nakae S, Tsai M.** 2005. Mast cells in the development of adaptive immune responses. Nat Immunol **6**:135–142. http://dx.doi.org/10.1038/ni1158.
3. **Galli SJ, Tsai M.** 2012. IgE and mast cells in allergic disease. Nat Med **18**:693–704. http://dx.doi.org/10.1038/nm.2755.
4. **Moon TC, Befus AD, Kulka M.** 2014. Mast cell mediators: their differential release and the secretory pathways involved. Front Immunol **5**:569. http://dx.doi.org/10.3389/fimmu.2014.00569.
5. **Kalesnikoff J, Galli SJ.** 2008. New developments in mast cell biology. Nat Immunol **9**:1215–1223. http://dx.doi.org/10.1038/ni.f.216.
6. **Gilfillan AM, Rivera J.** 2009. The tyrosine kinase network regulating mast cell activation. Immunol Rev **228**:149–169. http://dx.doi.org/10.1111/j.1600-065X.2008.00742.x.
7. **Suzuki R, Leach S, Liu W, Ralston E, Scheffel J, Zhang W, Lowell CA, Rivera J.** 2014. Molecular editing of cellular responses by the high-affinity receptor for IgE. Science **343**:1021–1025. http://dx.doi.org/10.1126/science.1246976.
8. **Bugajev V, Bambousková M, Dráberová L, Dráber P.** 2010. What precedes the initial tyrosine phosphorylation of the high affinity IgE receptor in antigen-activated mast cell? FEBS Lett **584**:4949–4955. http://dx.doi.org/10.1016/j.febslet.2010.08.045.
9. **Zhang J, Mendoza M, Guiraldelli MF, Barbu EA, Siraganian RP.** 2010. Small interfering RNA screen for phosphatases involved in IgE-mediated mast cell degranulation. J Immunol **184**:7178–7185. http://dx.doi.org/10.4049/jimmunol.0904169.
10. **Liao J, Jijon HB, Kim IR, Goel G, Doan A, Sokol H, Bauer H, Herrmann BG, Lassen KG, Xavier RJ.** 2014. An image-based genetic assay identifies genes in T1D susceptibility loci controlling cellular antiviral immunity in mouse. PLoS One **9**:e108777. http://dx.doi.org/10.1371/journal.pone.0108777.
11. **Sharma S, Quintana A, Findlay GM, Mettlen M, Baust B, Jain M,**

Nilsson R, Rao A, Hogan PG. 2013. An siRNA screen for NFAT activation identifies septins as coordinators of store-operated Ca^{2+} entry. Nature 499:238–242. http://dx.doi.org/10.1038/nature12229.
12. Zhang SL, Yeromin AV, Zhang XH, Yu Y, Safrina O, Penna A, Roos J, Stauderman KA, Cahalan MD. 2006. Genome-wide RNAi screen of Ca^{2+} influx identifies genes that regulate Ca^{2+} release-activated Ca^{2+} channel activity. Proc Natl Acad Sci U S A 103:9357–9362. http://dx.doi.org/10.1073/pnas.0603161103.
13. Rudolph AK, Burrows PD, Wabl MR. 1981. Thirteen hybridomas secreting hapten-specific immunoglobulin E from mice with Ig^a or Ig^b heavy chain haplotype. Eur J Immunol 11:527–529. http://dx.doi.org/10.1002/eji.1830110617.
14. Tolar P, Dráberová L, Dráber P. 1997. Protein tyrosine kinase Syk is involved in Thy-1 signaling in rat basophilic leukemia cells. Eur J Immunol 27:3389–3397. http://dx.doi.org/10.1002/eji.1830271238.
15. Kovářová M, Tolar P, Arudchandran R, Dráberová L, Rivera J, Dráber P. 2001. Structure-function analysis of Lyn kinase association with lipid rafts and initiation of early signaling events after Fcε receptor I aggregation. Mol Cell Biol 21:8318–8328. http://dx.doi.org/10.1128/MCB.21.24.8318-8328.2001.
16. Rivera J, Kinet J-P, Kim J, Pucillo C, Metzger H. 1988. Studies with a monoclonal antibody to the β subunit of the receptor with high affinity for immunoglobulin E. Mol Immunol 25:647–661. http://dx.doi.org/10.1016/0161-5890(88)90100-9.
17. Schmitt-Verhulst AM, Pettinelli CB, Henkart PA, Lunney JK, Shearer GM. 1978. H-2-restricted cytotoxic effectors generated in vitro by the addition of trinitrophenyl-conjugated soluble proteins. J Exp Med 147:352–368. http://dx.doi.org/10.1084/jem.147.2.352.
18. Hájková Z, Bugajev V, Dráberová E, Vinopal S, Dráberová L, Janáček J, Dráber P, Dráber P. 2011. STIM1-directed reorganization of microtubules in activated mast cells. J Immunol 186:913–923. http://dx.doi.org/10.4049/jimmunol.1002074.
19. Hibbs ML, Tarlinton DM, Armes J, Grail D, Hodgson G, Maglitto R, Stacker SA, Dunn AR. 1995. Multiple defects in the immune system of *Lyn*-deficient mice, culminating in autoimmune disease. Cell 83:301–311. http://dx.doi.org/10.1016/0092-8674(95)90171-X.
20. Draberova L, Bugajev V, Potuckova L, Halova I, Bambouskova M, Polakovicova I, Xavier RJ, Seed B, Draber P. 2014. Transmembrane adaptor protein PAG/CBP is involved in both positive and negative regulation of mast cell signaling. Mol Cell Biol 34:4285–4300. http://dx.doi.org/10.1128/MCB.00983-14.
21. Polakovicova I, Draberova L, Simicek M, Draber P. 2014. Multiple regulatory roles of the mouse transmembrane adaptor protein NTAL in gene transcription and mast cell physiology. PLoS One 9:e105539. http://dx.doi.org/10.1371/journal.pone.0105539.
22. Horáková H, Polakovičová I, Shaik GM, Eitler J, Bugajev V, Dráberová L, Dráber P. 2011. 1,2-Propanediol-trehalose mixture as a potent quantitative real-time PCR enhancer. BMC Biotechnol 11:41. http://dx.doi.org/10.1186/1472-6750-11-41.
23. Hsu DK, Zuberi RI, Liu FT. 1992. Biochemical and biophysical characterization of human recombinant IgE-binding protein, an S-type animal lectin. J Biol Chem 267:14167–14174.
24. Laemmli UK. 1970. Cleavage of structural proteins during the assembly of the head of bacteriophage T4. Nature 227:680–685. http://dx.doi.org/10.1038/227680a0.
25. Haan C, Behrmann I. 2007. A cost effective non-commercial ECL-solution for Western blot detections yielding strong signals and low background. J Immunol Methods 318:11–19. http://dx.doi.org/10.1016/j.jim.2006.07.027.
26. Cleyrat C, Darehshouri A, Anderson KL, Page C, Lidke DS, Volkmann N, Hanein D, Wilson BS. 2013. The architectural relationship of components controlling mast cell endocytosis. J Cell Sci 126:4913–4925. http://dx.doi.org/10.1242/jcs.128876.
27. Carpenter AE, Jones TR, Lamprecht MR, Clarke C, Kang IH, Friman O, Guertin DA, Chang JH, Lindquist RA, Moffat J, Golland P, Sabatini DM. 2006. CellProfiler: image analysis software for identifying and quantifying cell phenotypes. Genome Biol 7:R100. http://dx.doi.org/10.1186/gb-2006-7-10-r100.
28. Hálová I, Dráberová L, Bambousková M, Machyna M, Stegurová L, Smrž D, Dráber P. 2013. Crosstalk between tetraspanin CD9 and transmembrane adaptor protein non-T cell activation linker (NTAL) in mast cell activation and chemotaxis. J Biol Chem 288:9801–9814. http://dx.doi.org/10.1074/jbc.M112.449231.
29. Bambousková M, Hájkovà Z, Dráber P, Dráber P. 2014. Microscopy assays for evaluation of mast cell migration and chemotaxis. Methods Mol Biol 1192:161–176. http://dx.doi.org/10.1007/978-1-4939-1173-8_12.
30. Birmingham A, Selfors LM, Forster T, Wrobel D, Kennedy CJ, Shanks E, Santoyo-Lopez J, Dunican DJ, Long A, Kelleher D, Smith Q, Beijersbergen RL, Ghazal P, Shamu CE. 2009. Statistical methods for analysis of high-throughput RNA interference screens. Nat Methods 6:569–575. http://dx.doi.org/10.1038/nmeth.1351.
31. Chen HY, Sharma BB, Yu L, Zuberi R, Weng IC, Kawakami Y, Kawakami T, Hsu DK, Liu FT. 2006. Role of galectin-3 in mast cell functions: galectin-3-deficient mast cells exhibit impaired mediator release and defective JNK expression. J Immunol 177:4991–4997. http://dx.doi.org/10.4049/jimmunol.177.8.4991.
32. Grutzkau A, Smorodchenko A, Lippert U, Kirchhof L, Artuc M, Henz BM. 2004. LAMP-1 and LAMP-2, but not LAMP-3, are reliable markers for activation-induced secretion of human mast cells. Cytometry A 61:62–68.
33. Chen HY, Fermin A, Vardhana S, Weng IC, Lo KF, Chang EY, Maverakis E, Yang RY, Hsu DK, Dustin ML, Liu FT. 2009. Galectin-3 negatively regulates TCR-mediated CD4+ T-cell activation at the immunological synapse. Proc Natl Acad Sci U S A 106:14496–14501. http://dx.doi.org/10.1073/pnas.0903497106.
34. Fattakhova G, Masilamani M, Borrego F, Gilfillan AM, Metcalfe DD, Coligan JE. 2006. The high-affinity immunoglobulin-E receptor FcεRI is endocytosed by an AP-2/clathrin-independent, dynamin-dependent mechanism. Traffic 7:673–685. http://dx.doi.org/10.1111/j.1600-0854.2006.00423.x.
35. Fattakhova GV, Masilamani M, Narayanan S, Borrego F, Gilfillan AM, Metcalfe DD, Coligan JE. 2009. Endosomal trafficking of the ligated FcεRI receptor. Mol Immunol 46:793–802. http://dx.doi.org/10.1016/j.molimm.2008.09.002.
36. Molfetta R, Gasparrini F, Peruzzi G, Vian L, Piccoli M, Frati L, Santoni A, Paolini R. 2009. Lipid raft-dependent FcεRI ubiquitination regulates receptor endocytosis through the action of ubiquitin binding adaptors. PLoS One 4:e5604. http://dx.doi.org/10.1371/journal.pone.0005604.
37. Lafont F, Simons K. 2001. Raft-partitioning of the ubiquitin ligases Cbl and Nedd4 upon IgE-triggered cell signaling. Proc Natl Acad Sci U S A 98:3180–3184. http://dx.doi.org/10.1073/pnas.051003498.
38. Ota Y, Beitz LO, Scharenberg AM, Donovan JA, Kinet JP, Samelson LE. 1996. Characterization of Cbl tyrosine phosphorylation and a Cbl-Syk complex in RBL-2H3 cells. J Exp Med 184:1713–1723. http://dx.doi.org/10.1084/jem.184.5.1713.
39. Liu W, Hsu DK, Chen HY, Yang RY, Carraway KL III, Isseroff RR, Liu FT. 2012. Galectin-3 regulates intracellular trafficking of EGFR through Alix and promotes keratinocyte migration. J Investig Dermatol 132:2828–2837. http://dx.doi.org/10.1038/jid.2012.211.
40. Hsu DK, Chernyavsky AI, Chen HY, Yu L, Grando SA, Liu FT. 2009. Endogenous galectin-3 is localized in membrane lipid rafts and regulates migration of dendritic cells. J Investig Dermatol 129:573–583. http://dx.doi.org/10.1038/jid.2008.276.
41. Dastych J, Costa JJ, Thompson HL, Metcalfe DD. 1991. Mast cell adhesion to fibronectin. Immunology 73:478–484.
42. Bazzoni G, Shih DT, Buck CA, Hemler ME. 1995. Monoclonal antibody 9EG7 defines a novel β1 integrin epitope induced by soluble ligand and manganese, but inhibited by calcium. J Biol Chem 270:25570–25577. http://dx.doi.org/10.1074/jbc.270.43.25570.
43. Kuehn HS, Jung MY, Beaven MA, Metcalfe DD, Gilfillan AM. 2011. Prostaglandin E_2 activates and utilizes mTORC2 as a central signaling locus for the regulation of mast cell chemotaxis and mediator release. J Biol Chem 286:391–402. http://dx.doi.org/10.1074/jbc.M110.164772.
44. Amir-Moazami O, Alexia C, Charles N, Launay P, Monteiro RC, Benhamou M. 2008. Phospholipid scramblase 1 modulates a selected set of IgE receptor-mediated mast cell responses through LAT-dependent pathway. J Biol Chem 283:25514–25523. http://dx.doi.org/10.1074/jbc.M705320200.
45. Ahmad N, Gabius HJ, Andre S, Kaltner H, Sabesan S, Roy R, Liu B, Macaluso F, Brewer CF. 2004. Galectin-3 precipitates as a pentamer with synthetic multivalent carbohydrates and forms heterogeneous cross-linked complexes. J Biol Chem 279:10841–10847. http://dx.doi.org/10.1074/jbc.M312834200.
46. Rabinovich GA, Toscano MA. 2009. Turning 'sweet' on immunity: galectin-glycan interactions in immune tolerance and inflammation. Nat Rev Immunol 9:338–352. http://dx.doi.org/10.1038/nri2536.

47. **Bhaumik P, St-Pierre G, Milot V, St-Pierre C, Sato S.** 2013. Galectin-3 facilitates neutrophil recruitment as an innate immune response to a parasitic protozoa cutaneous infection. J Immunol **190:**630–640. http://dx.doi.org/10.4049/jimmunol.1103197.
48. **Jia W, Kidoya H, Yamakawa D, Naito H, Takakura N.** 2013. Galectin-3 accelerates M2 macrophage infiltration and angiogenesis in tumors. Am J Pathol **182:**1821–1831. http://dx.doi.org/10.1016/j.ajpath.2013.01.017.
49. **MacKinnon AC, Farnworth SL, Hodkinson PS, Henderson NC, Atkinson KM, Leffler H, Nilsson UJ, Haslett C, Forbes SJ, Sethi T.** 2008. Regulation of alternative macrophage activation by galectin-3. J Immunol **180:**2650–2658. http://dx.doi.org/10.4049/jimmunol.180.4.2650.
50. **Hsu DK, Yang RY, Pan Z, Yu L, Salomon DR, Fung-Leung WP, Liu FT.** 2000. Targeted disruption of the galectin-3 gene results in attenuated peritoneal inflammatory responses. Am J Pathol **156:**1073–1083. http://dx.doi.org/10.1016/S0002-9440(10)64975-9.
51. **Cherayil BJ, Weiner SJ, Pillai S.** 1989. The Mac-2 antigen is a galactose-specific lectin that binds IgE. J Exp Med **170:**1959–1972. http://dx.doi.org/10.1084/jem.170.6.1959.
52. **Dhirapong A, Lleo A, Leung P, Gershwin ME, Liu FT.** 2009. The immunological potential of galectin-1 and -3. Autoimmun Rev **8:**360–363. http://dx.doi.org/10.1016/j.autrev.2008.11.009.
53. **Thyagarajan T, Totey S, Danton MJ, Kulkarni AB.** 2003. Genetically altered mouse models: the good, the bad, and the ugly. Crit Rev Oral Biol Med **14:**154–174. http://dx.doi.org/10.1177/154411130301400302.
54. **Wright J, Morales MM, Sousa-Menzes J, Ornellas D, Sipes J, Cui Y, Cui I, Hulamm P, Cebotaru V, Cebotaru L, Guggino WB, Guggino SE.** 2008. Transcriptional adaptation to Clcn5 knockout in proximal tubules of mouse kidney. Physiol Genomics **33:**341–354. http://dx.doi.org/10.1152/physiolgenomics.00024.2008.
55. **Reaume AG, de Sousa PA, Kulkarni S, Langille BL, Zhu D, Davies TC, Juneja SC, Kidder GM, Rossant J.** 1995. Cardiac malformation in neonatal mice lacking connexin43. Science **267:**1831–1834. http://dx.doi.org/10.1126/science.7892609.
56. **Nangia-Makker P, Honjo Y, Sarvis R, Akahani S, Hogan V, Pienta KJ, Raz A.** 2000. Galectin-3 induces endothelial cell morphogenesis and angiogenesis. Am J Pathol **156:**899–909. http://dx.doi.org/10.1016/S0002-9440(10)64959-0.
57. **Lantz CS, Huff TF.** 1995. Differential responsiveness of purified mouse c-kit+ mast cells and their progenitors to IL-3 and stem cell factor. J Immunol **155:**4024–4029.
58. **Partridge EA, Le RC, Di Guglielmo GM, Pawling J, Cheung P, Granovsky M, Nabi IR, Wrana JL, Dennis JW.** 2004. Regulation of cytokine receptors by Golgi N-glycan processing and endocytosis. Science **306:**120–124. http://dx.doi.org/10.1126/science.1102109.
59. **Andrews NL, Pfeiffer JR, Martinez AM, Haaland DM, Davis RW, Kawakami T, Oliver JM, Wilson BS, Lidke DS.** 2009. Small, mobile FcεRI receptor aggregates are signaling competent. Immunity **31:**469–479. http://dx.doi.org/10.1016/j.immuni.2009.06.026.
60. **Oliver C, Fujimura A, Silveira E Souza AM, de Orlandini CR, Siraganian RP, Jamur MC.** 2007. Mast cell-specific gangliosides and FcεRI follow the same endocytic pathway from lipid rafts in RBL-2H3 cells. J Histochem Cytochem **55:**315–325.
61. **Lakshminarayan R, Wunder C, Becken U, Howes MT, Benzing C, Arumugam S, Sales S, Ariotti N, Chambon V, Lamaze C, Loew D, Shevchenko A, Gaus K, Parton RG, Johannes L.** 2014. Galectin-3 drives glycosphingolipid-dependent biogenesis of clathrin-independent carriers. Nat Cell Biol **16:**595–606. http://dx.doi.org/10.1038/ncb2970.
62. **Sigismund S, Argenzio E, Tosoni D, Cavallaro E, Polo S, Di Fiore PP.** 2008. Clathrin-mediated internalization is essential for sustained EGFR signaling but dispensable for degradation. Dev Cell **15:**209–219. http://dx.doi.org/10.1016/j.devcel.2008.06.012.
63. **Benzing C, Rossy J, Gaus K.** 2013. Do signalling endosomes play a role in T cell activation? FEBS J **280:**5164–5176. http://dx.doi.org/10.1111/febs.12427.
64. **Obata Y, Toyoshima S, Wakamatsu E, Suzuki S, Ogawa S, Esumi H, Abe R.** 2014. Oncogenic kit signals on endolysosomes and endoplasmic reticulum are essential for neoplastic mast cell proliferation. Nat Commun **5:**5715. http://dx.doi.org/10.1038/ncomms6715.
65. **Frigeri L, Apgar JR.** 1999. The role of actin microfilaments in the down-regulation of the degranulation response in RBL-2H3 cells. J Immunol **162:**2243–2250.
66. **Tolarová H, Dráberová L, Heneberg P, Dráber P.** 2004. Involvement of filamentous actin in setting the threshold for degranulation in mast cells. Eur J Immunol **34:**1627–1636. http://dx.doi.org/10.1002/eji.200424991.
67. **Sigismund S, Woelk T, Puri C, Maspero E, Tacchetti C, Transidico P, Di Fiore PP, Polo S.** 2005. Clathrin-independent endocytosis of ubiquitinated cargos. Proc Natl Acad Sci U S A **102:**2760–2765. http://dx.doi.org/10.1073/pnas.0409817102.
68. **Furuichi K, Rivera J, Buonocore LM, Isersky C.** 1986. Recycling of receptor-bound IgE by rat basophilic leukemia cells. J Immunol **136:**1015–1022.
69. **Greer AM, Wu N, Putnam AL, Woodruff PG, Wolters P, Kinet JP, Shin JS.** 2014. Serum IgE clearance is facilitated by human FcεRI internalization. J Clin Invest **124:**1187–1198. http://dx.doi.org/10.1172/JCI68964.
70. **Molfetta R, Gasparrini F, Santoni A, Paolini R.** 2010. Ubiquitination and endocytosis of the high affinity receptor for IgE. Mol Immunol **47:**2427–2434. http://dx.doi.org/10.1016/j.molimm.2010.06.003.
71. **Paolini R, Molfetta R, Beitz LO, Zhang J, Scharenberg AM, Piccoli M, Frati L, Siraganian R, Santoni A.** 2002. Activation of Syk tyrosine kinase is required for c-Cbl-mediated ubiquitination of FcεRI and Syk in RBL cells. J Biol Chem **277:**36940–36947. http://dx.doi.org/10.1074/jbc.M204948200.
72. **Feshchenko EA, Langdon WY, Tsygankov AY.** 1998. Fyn, Yes, and Syk phosphorylation sites in c-Cbl map to the same tyrosine residues that become phosphorylated in activated T cells. J Biol Chem **273:**8323–8331. http://dx.doi.org/10.1074/jbc.273.14.8323.
73. **Schmidt MH, Dikic I.** 2005. The Cbl interactome and its functions. Nat Rev Mol Cell Biol **6:**907–918. http://dx.doi.org/10.1038/nrm1762.
74. **Demetriou M, Granovsky M, Quaggin S, Dennis JW.** 2001. Negative regulation of T-cell activation and autoimmunity by Mgat5 N-glycosylation. Nature **409:**733–739. http://dx.doi.org/10.1038/35055582.
75. **Dumic J, Dabelic S, Flogel M.** 2006. Galectin-3: an open-ended story. Biochim Biophys Acta **1760:**616–635. http://dx.doi.org/10.1016/j.bbagen.2005.12.020.
76. **Shimura T, Takenaka Y, Tsutsumi S, Hogan V, Kikuchi A, Raz A.** 2004. Galectin-3, a novel binding partner of β-catenin. Cancer Res **64:**6363–6367. http://dx.doi.org/10.1158/0008-5472.CAN-04-1816.
77. **Furtak V, Hatcher F, Ochieng J.** 2001. Galectin-3 mediates the endocytosis of β-1 integrins by breast carcinoma cells. Biochem Biophys Res Commun **289:**845–850. http://dx.doi.org/10.1006/bbrc.2001.6064.
78. **Kitaura J, Kinoshita T, Matsumoto M, Chung S, Kawakami Y, Leitges M, Wu D, Lowell CA, Kawakami T.** 2005. IgE- and IgE+Ag-mediated mast cell migration in an autocrine/paracrine fashion. Blood **105:**3222–3229. http://dx.doi.org/10.1182/blood-2004-11-4205.
79. **Kuehn HS, Radinger M, Brown JM, Ali K, Vanhaesebroeck B, Beaven MA, Metcalfe DD, Gilfillan AM.** 2010. Btk-dependent Rac activation and actin rearrangement following FcεRI aggregation promotes enhanced chemotactic responses of mast cells. J Cell Sci **123:**2576–2585. http://dx.doi.org/10.1242/jcs.071043.